

# STUDY OF HIGH SPIN STATES IN NUCLEI NEAR SPHERICAL AND DEFORMED SHELL GAPS

*By*

**MD ALI ASGAR**

Enrolment No: PHYS04201204007

Variable Energy Cyclotron Centre, Kolkata

*A thesis submitted to the  
Board of Studies in Physical Sciences*

*In partial fulfillment of requirements  
for the Degree of  
DOCTOR OF PHILOSOPHY*

*of*

**HOMI BHABHA NATIONAL INSTITUTE**

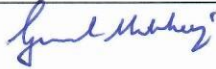
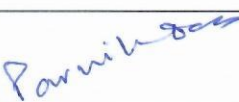


August, 2018

# Homi Bhabha National Institute<sup>1</sup>

## Recommendations of the Viva Voce Committee

As members of the Viva Voce Committee, we certify that we have read the dissertation prepared by Md. ALI ASGAR entitled "STUDY OF HIGH SPIN STATES IN NUCLEI NEAR SPHERICAL AND DEFORMED SHELL GAPS" and recommend that it may be accepted as fulfilling the thesis requirement for the award of Degree of Doctor of Philosophy.

Chairman – Dr. S.R. Banerjee		Date: 27/11/2018
Guide / Convener – Dr. Gopal Mukherjee		Date: 27/11/18
Co-guide - <Name> (if any) XXXXXXXXXXXXXXXXXXXXXXXX		Date: XXXX
Examiner – Prof. Ajay Kr. Singh		Date: 27.11.18
Member 1- Prof. Asimananda Goswami		Date: 27.11.2018
Member 2- Dr. Parnika Das		Date: 27/11/2018

Final approval and acceptance of this thesis is contingent upon the candidate's submission of the final copies of the thesis to HBNI.

I hereby certify that I have read this thesis prepared under my direction and recommend that it may be accepted as fulfilling the thesis requirement.

Date: 27/11/2018

Place: Kalkate



<Signature>

Guide

<sup>1</sup> This page is to be included only for final submission after successful completion of viva voce.

## STATEMENT BY AUTHOR

This dissertation has been submitted in partial fulfillment of requirements for an advanced degree at Homi Bhabha National Institute (HBNI) and is deposited in the Library to be made available to borrowers under rules of the HBNI.

Brief quotation from this dissertation are allowable without special permission, provided that accurate acknowledgement of source is made. Requests for permission for extended quotation from or reproduction of this manuscript in whole or in part may be granted by the Competent Authority of HBNI when in his or her judgment the proposed use of the material is in the interests of scholarship. In all other instances, however, permission must be obtained from the author.

*Md. Ali Asgar*

Md. Ali Asgar

## DECLARATION

I, hereby declare that the investigation presented in the thesis has been carried out by me. The work is original and has not been submitted earlier as a whole or in part for a degree/diploma at this or any other Institution/University.

*Md. Ali Asgar*

Md. Ali Asgar

# List of Publications arising from the thesis

## Journal

1. “Return of backbending in  $^{169}\text{Tm}$  and the effect of the  $N = 98$  deformed shell gap”, **Md.A. Asgar**, T. Roy, G. Mukherjee, A. Dhal, Soumik Bhattacharya, S. Bhattacharyya, C. Bhattacharya, S. Bhattacharya, A. Chaudhuri, K. Banerjee, S. Kundu, S. Manna, R. Pandey, J. K. Meena, R. Palit, S. Biswas, S. Saha, J. Sethi, P. Singh, and D. Choudhury, *Phys. Rev. C*, **2017**, 95, 031304(R)(1-5).

## Conferences

1. “Degree of Alignment of the Angular Momentum of Nuclei Produced in Inelastic Excitation”, **Md.A. Asgar** and G. Mukherjee, *Proceedings of the DAE-BRNS Symp. on Nucl. Phys.*, **2017**, 62, 104-105.
2. “Geant4 Simulation of VECC array for Nuclear Spectroscopy (VENUS) and HPGe detector of NDPCI”, **Md.A. Asgar**, G. Mukherjee, T. Roy, Soumik Bhattacharya, C. Bhattacharya, A. Dhal, D. Mahato and S. Bhutani, *Proceedings of the DAE-BRNS Symp. on Nucl. Phys.*, **2016**, 61, 950-951.
3. “Nuclear structure study at low spin in  $^{169}\text{Tm}$ ”, **Md.A. Asgar**, A. Dhal, T. Roy, G. Mukherjee, Soumik Bhattacharya, S. Bhattacharyya, C. Bhattacharya, S. Bhattacharya, A. Chaudhuri, K. Banerjee, S. Kundu, S. Manna, R. Pandey, and J.K. Meena, *Proceedings of the DAE-BRNS Symp. on Nucl. Phys.*, **2015**, 60, 80-81.
4. “High spin gamma ray spectroscopy of  $^{196}\text{Tl}$ ”, **Md.A. Asgar**, T. Roy, G. Mukherjee, H. Pai, S. Bhattacharyya, M.R Gohil, C. Bhattacharya, R. Palit, S. Saha, J. Sethi, T. Trivedi, Shital, Thakur, B.S Naidu, S.V Jadav, R. Donthi and A. Goswami, *Proceedings of the DAE-BRNS Symp. on Nucl. Phys.*, **2015**, 60, 172-173.

5. “Geant4 simulation of a large volume segmented clover detector”, **Md.A. Asgar**, T. Roy, G. Mukherjee, and C. Bhattacharya, *Proceedings of the DAE-BRNS Symp. on Nucl. Phys.*, **2015**, 60, 960-961.
6. “Target Coulex and the Production of Po Isotopes by Fusion Evaporation Reaction”, **Md.A. Asgar**, T. Roy, G. Mukherjee, Soumik Bhattacharya, S. Bhattacharyya, C. Bhattacharya, S. Bhattacharya, A. Chaudhuri, K. Banerjee, S. Kundu, S. Manna, R. Pandey, and J.K. Meena R. Palit, S. Biswas, S. Saha, J. Sethi, P. Singh, and D. Choudhury, *Proceedings of the DAE Symp. on Nucl. Phys.*, **2014**, 59, 246-247.
7. “Characterization of a segmented clover detector”, **Md.A. Asgar**, T. Roy, G. Mukherjee, Soumik Bhattacharya, Abhirup Chaudhuri, V. Srivastava, S. Bhattacharyya, S. Bhattacharya, C. Bhattacharya, T.K. Ghosh, K. Banerjee, S. Kundu, R. Pandey, T.K. Rana, P. Roy, S. Manna, J.K. Sahoo, J.K. Meena, A.K. Saha, R. Mondal Saha, P. Mukhopadhyay, A. Choudhury, and I. Shaik, *Proceedings of the DAE Symp. on Nucl. Phys.*, **2014**, 59, 882-883.

## Other publications

### (Journal)

1. “Observation of multiple doubly degenerate bands in  $^{195}\text{Tl}$ ”, T. Roy, G. Mukherjee, **Md.A. Asgar**, S. Bhattacharyya, Soumik Bhattacharya, C. Bhattacharya, S. Bhattacharya, T.K. Ghosh, K. Banerjee, Samir Kundu, T.K. Rana, P. Roy, R. Pandey, J. Meena, A. Dhal, R. Palit, S. Saha, J. Sethi, Shital Thakur, B.S. Naidu, S.V. Jadav, R. Dhonti, H. Pai, and A. Goswami, *Phys. Lett. B*, **2018**, 782, 768-772.
2. “Effect of clustering on the emission of light charged particles”, S. Kundu, C. Bhattacharya, T. K. Rana, S. Bhattacharya, R. Pandey, K. Banerjee, Pratap Roy, J. K. Meena, G. Mukherjee, T. K. Ghosh, S. Mukhopadhyay, A. K. Saha, J. K. Sahoo, R.

- Mandal Saha, V. Srivastava, M. Sinha, and **Md.A. Asgar**, *Eur. Phys. J. A*, **2018**, 54, 63-70.
3. “Deformed band structures at high spin in  $^{200}\text{Tl}$ ”, Soumik Bhattacharya, S. Bhattacharyya, S. Das Gupta, H. Pai, G. Mukherjee, R. Palit, F. R. Xu, Q. Wu, A. Shrivastava, **Md.A. Asgar**, R. Banik, T. Bhattacharjee, S. Chanda, A. Chatterjee, A. Goswami, V. Nanal, S. K. Pandit, S. Saha, J. Sethi, T. Roy, and S. Thakur, *Phys. Rev. C*, **2017**, 95, 014301(1-15).
  4. “Direct evidence of fadeout of collective enhancement in nuclear level density”, K. Banerjee, Pratap Roy, Deepak Pandit, Jhilam Sadhukhan, S. Bhattacharya, C. Bhattacharya, G. Mukherjee, T.K. Ghosh, S. Kundu, A. Sen, T.K. Rana, S. Manna, R. Pandey, T. Roy, A. Dhal, **Md.A. Asgar** and S. Mukhopadhyay, *Phys. Lett. B*, **2017**, 772, 105-109.
  5. “Fragment emission mechanism in the  $^{32}\text{S}+^{12}\text{C}$  reaction”, R. Pandey, S. Kundu, C. Bhattacharya, K. Banerjee, T.K. Rana, S. Manna, G. Mukherjee, J.K. Meena, A. Chaudhuri, T. Roy, P. Roy, **Md.A. Asgar**, V. Srivastava, A. Dey, M. Sinha, T.K. Ghosh, S. Bhattacharya, S.K. Pandit, K. Mahata, P. Patle, S. Pal, A. Shrivastava and V. Nanal, *Phys. Rev. C*, **2017**, 95, 064603(1-7).
  6. “Fission fragment mass distributions in reactions populating  $^{200}\text{Pb}$ ”, A. Chaudhuri, A. Sen, T. K. Ghosh, K. Banerjee, Jhilam Sadhukhan, S. Bhattacharya, P. Roy, T. Roy, C. Bhattacharya, **Md.A. Asgar**, A. Dey, S. Kundu, S. Manna, J. K. Meena, G. Mukherjee, R. Pandey, T. K. Rana, V. Srivastava, R. Dubey, Gurpreet Kaur, N. Saneesh, P. Sugathan, and P. Bhattacharya, *Phys. Rev. C*, **2016**, 94, 024617(1-5).
  7. “Experimental investigation of  $T = 1$  analog states of  $^{26}\text{Al}$  and  $^{26}\text{Mg}$ ”, Vishal Srivastava, C. Bhattacharya, T. K. Rana, S. Manna, S. Kundu, S. Bhattacharya, K. Banerjee, P. Roy, R. Pandey, G. Mukherjee, T. K. Ghosh, J. K. Meena, T. Roy, A. Chaudhuri, M.

- Sinha, A. K. Saha, **Md.A. Asgar**, A. Dey, Subinit Roy, and Md. M. Shaikh, *Phys. Rev. C*, **2016**, 93, 044601(1-3).
8. “A new high-spin isomer in  $^{195}\text{Bi}$ ”, T. Roy, G. Mukherjee, N. Madhavan, T.K. Rana, Soumik Bhattacharya, **Md.A. Asgar**, I. Bala, K. Basu, S.S. Bhattacharjee, C. Bhattacharya, S. Bhattacharya, S. Bhattacharyya, J. Gehlot, S.S. Ghugre, R.K. Gurjar, A. Jhingan, R. Kumar, S. Muralithar, S. Nath, H. Pai, R. Palit, R. Raut, R.P. Singh, A.K. Sinha, and T. Varughese, *Eur. Phys. J. A*, **2015**, 51, 153-160.
  9. “Experimental study of  $^{26}\text{Al}$  through the  $1n$  pick-up reaction  $^{27}\text{Al}(d, t)$ ”, Vishal Srivastava, C. Bhattacharya, T. K. Rana, S. Manna, S. Kundu, S. Bhattacharya, K. Banerjee, P. Roy, R. Pandey, G. Mukherjee, T. K. Ghosh, J. K. Meena, T. Roy, A. Chaudhuri, M. Sinha, A. K. Saha, **Md.A. Asgar**, A. Dey, Subinit Roy, and Md. M. Shaikh, *Phys. Rev. C*, **2015**, 91, 054611(1-7).
  10. “No influence of a  $N = 126$  neutron-shell closure in fission-fragment mass distributions”, A. Chaudhuri, T. K. Ghosh, K. Banerjee, S. Bhattacharya, Jhilaam Sadhukhan, S. Kundu, C. Bhattacharya, J. K. Meena, G. Mukherjee, A. K. Saha, **Md.A. Asgar**, A. Dey, S. Manna, R. Pandey, T. K. Rana, P. Roy, T. Roy, V. Srivastava, P. Bhattacharya, D. C. Biswas, B. N. Joshi, K. Mahata, A. Shrivastava, R. P. Vind, S. Pal, B. R. Behera, and Varinderjit Singh, *Phys. Rev. C*, **2015**, 92, 041601(R)(1-5).

### (Conferences)

1. “High spin structure and neutron alignments in  $^{197}\text{Tl}$ ”, S. Nandi, G. Mukherjee, H. Pai, T. Roy, **Md.A. Asgar**, A. Dhal, R. Banik, Soumik Bhattacharya, A. Saha, S. S. Alam, S. Bhattacharyya, C. Bhattacharya, Pratap Roy, T.K. Ghosh, S. Kundu, K. Banerjee, T.K. Rana, R. Pandey, S. Manna, A. Sen, S. Pal, S. Mukhopadhyay, D. Pandit, D. Mondal, T. Bhattacharjee, A. Dey, J.K. Meena, A.K. Saha, J.K. Sahoo, R. Mandal Saha, A.

- Choudhury, and S.R. Banerjee, *Proceedings of the DAE-BRNS Symp. on Nucl. Phys.*, **2017**, 62, 80-81.
2. “Decay measurements of  $^{43}\text{K}(\beta^-)^{43}\text{Ca}$  by HRS and TAS”, A. Dhal, G. Mukherjee, M. Bhattacharjee, V. Naik, S. Mukhopadhyay, D. Pandit, S. Pal, D. Mondal, P. Karmakar, T. Roy, **Md.A. Asgar**, Soumik Bhattacharya, S. Bhattacharyya, C. Bhattacharya, S.R. Banerjee, and A. Chakrabarti, *EPJ Web of Conferences*, **2017**, 146, 10013(1-4).
  3. “Deformed structure based on  $\nu i_{13/2}$  orbital in  $^{199}\text{Hg}$ ”, Soumik Bhattacharya, S. Bhattacharyya, R. Banik, S. Das Gupta, A. Dhal, G. Mukherjee, S. S. Alam, **Md.A. Asgar**, T. Roy, T. Bhattacharje, A. Saha, S. Mukhopadhyay, Debasish Mondal, Deepak Pandit, Surajit Pal and S. R. Banerjee, *Proceedings of the DAE Symp. on Nucl. Phys.*, **2017**, 62, 118-119.
  4. “Probing Hoyle analogue state in  $^{16}\text{O}$ ”, S. Manna, T. K. Rana, C. Bhattacharya, S. Kundu, K. Banerjee, Pratap Roy, R. Pandey, V. Srivastava, A. Chaudhury, A. Sen, T. K. Ghosh, T. Roy, A. Dhal, G. Mukherjee, **Md.A. Asgar**, M. Sinha, A. Dey, J. K. Meena and S. Bhattacharya, *Proceedings of the DAE Symp. on Nucl. Phys.*, **2017**, 62, 364-365.
  5. “Mass distribution for  $^{210}\text{Po}$  at  $E^* \sim 30$  MeV”, A. Sen, T.K.Ghosh, K. Banerjee, C Bhattacharya, S. Bhattacharya, S. Kundu, G. Mukherje, **A. Asgar**, A. Dey, A. Dhal, M.Khan, J. K. Meena, S. Manna, R. Pandey, T.K. Rana, Pratap Roy, T.Roy, V. Srivastava, P. Bhattacharya, *Proceedings of the DAE Symp. on Nucl. Phys.*, **2017**, 62, 388-389.
  6. “Fragment mass distributions in fusion fission of  $^{213}\text{At}$ ”, A. Sen, T.K.Ghosh, K. Banerjee, C Bhattacharya, S. Bhattacharya, S. Kundu, G. Mukherjee, **A. Asgar**, A. Dey, A. Dhal, M.Khan, J. K. Meena, S. Manna, R. Pandey, T.K. Rana, Pratap Roy, T.Roy, V. Srivastava, and P. Bhattacharya, *Proceedings of the DAE Symp. on Nucl. Phys.*, **2017**, 62, 534-535.

7. “Study of the nucleus  $^{25}\text{Mg}$ ”, Vishal Srivastava, C. Bhattacharya, T. K. Rana, S. Manna, S. Kundu, S. Bhattacharya, K. Banerjee, Pratap Roy, R. Pandey, G. Mukherjee, T. K. Ghosh, J. K. Meena, T. Roy, A. Chaudhuri, M. Sinha, A. K. Saha, **Md.A. Asgar**, A. Dey, Subinit Roy, and Md. Moin Shaikh, *Proceedings of the DAE Symp. on Nucl. Phys.*, **2017**, 62, 572-573.
8. “Study of multi-quasiparticle band structures in  $^{197}\text{Tl}$  using  $\alpha$  beam”, G. Mukherjee, S. Nandi, H. Pai, T. Roy, **Md.A. Asgar**, A. Dhal, R. Banik, Soumik Bhattacharya, A. Saha, S. S. Alam, S. Bhattacharyya, C. Bhattacharya, Pratap Roy, T. K. Ghosh, S. Kundu, K. Banerjee, T. K. Rana, R. Pandey, S. Manna, A. Sen, S Pal, S Mukhopadhyay, D. Pandit, D. Mondal, T. Bhattacharjee, A. Dey, J. K. Meena, A. K. Saha, J. K. Sahoo, R. Mondal Saha, A. Choudhury, and S.R Banerjee, *Proceedings of the DAE-BRNS Symp. on Nucl. Phys.*, **2016**, 61, 270-271.
9. “Oblate band structure based on  $\pi h_{9/2}$  orbital in  $^{199}\text{Tl}$ ”, Soumik Bhattacharya, S. Bhattacharyya, R. Banik, G. Mukherjee, S. Das Gupta, S. S. Alam, A. Dhal, **Md.A. Asgar**, T. Roy, A. Saha, T. Bhattacharjee, S. Mukhopadhyay, D. Pandit, D. Mondal, S. Pal, and S. R. Banerjee, *Proceedings of the DAE-BRNS Symp. on Nucl. Phys.*, **2016**, 61, 188-189.
10. “Decay Study of Neutron-rich  $^{43}\text{K}$  using Total Absorption TAGS and High Resolution HRGS Gamma Spectroscopy Methods”, A. Dhal, G. Mukherjee, M. Bhattacharjee, V. Naik, S. Mukhopadhyay, D. Pandit, S. Pal, D. Mondal, P. Karmakar, T. Roy, **Md.A. Asgar**, Soumik Bhattacharya, S. Bhattacharyya, C. Bhattacharya, S. R. Banerjee, and A. Chakrabarti, *Proceedings of the DAE-BRNS Symp. on Nucl. Phys.*, **2016**, 61, 96-97.
11. “VECC array for NUClear Spectroscopy VENUS”, Soumik Bhattacharya, R. Banik, S. S. Alam, A. Saha, **Md.A. Asgar**, T. Roy, A. Chowdhury, I. Sheikh, P. Mukhopadhyay, A. Dhal, T. Bhattacharjee, S. Bhattacharyya, G. Mukherjee, S. Mukhopadhyay, D. Mondal,

- D. Pandit, S. Pal, and S.R. Banerjee, *Proceedings of the DAE-BRNS Symp. on Nucl. Phys.*, **2016**, 61, 98-99.
12. “Half-life and  $\beta$ -feeding measurements of  $^{217}\text{Po}$  by  $\gamma$ -spectroscopy method”, A. Dhal, R. Ghosh, A. G. Nair, G. Mukherjee, **Md.A. Asgar**, T. Roy, T. K. Rana, T. K. Ghosh, K. Banerjee, S. Kundu, R. Pandey, Pratap Roy, S. Manna, A. Sen, A. Dey, J. K. Meena, J. K. Sahoo, A. K. Saha, R. Banik, Soumik Bhattacharya, A. Saha, S. S. Alam, D. Mondal, D. Pandit, S. Mukhopadhyay, S. Pal, T. Bhattacharjee, S. Bhattacharyya, C. Bhattacharya, and S. R. Banerjee, *Proceedings of the DAE-BRNS Symp. on Nucl. Phys.*, **2016**, 61, 266-267.
  13. “Study of nuclear structure in odd-odd  $^{122,124}\text{I}$ ”, S. S. Alam, A. Saha, T. Bhattacharjee, D. Banerjee, **Md.A. Asgar**, R. Banik, S. Bhattacharyya, Soumik Bhattacharya, A. Dhal, D. Mondal, G. Mukherjee, S. Mukhopadhyay, S. Pal, D. Pandit, T. Roy, and S. R. Banerjee, *Proceedings of the DAE-BRNS Symp. on Nucl. Phys.*, **2016**, 61, 316-317.
  14. “Search for fadeout of collectivity in nuclear level density”, K. Banerjee, Pratap Roy, C. Bhattacharya, T. K. Ghosh, A. Sen, S. Bhattacharya, S. Kundu, T. K. Rana, G. Mukherjee, R. Pandey, S. Manna, T. Roy, **Md.A. Asgar**, A. Dey, D. Pandit, and S. Mukhopadhyay, *Proceedings of the DAE-BRNS Symp. on Nucl. Phys.*, **2016**, 61, 374-375.
  15. “Further evidence of the absence of the shell effects in fission fragment mass distribution in  $^{210}\text{Po}$ ”, A. Sen, T. K. Ghosh, K. Banerjee, C. Bhattacharya, S. Bhattacharya, S. Kundu, G. Mukherjee, **Md.A. Asgar**, P. Bhattacharya, A. Dey, A. Dhal, M. Khan, J. K. Meena, R. Mondal Saha, S. Manna, R. Pandey, T. K. Rana, Pratap Roy, T. Roy, J. K. Sahoo, A. K. Saha, and V. Srivastava, *Proceedings of the DAE-BRNS Symp. on Nucl. Phys.*, **2016**, 61, 378-379.

16. “Study of higher excited states of  $^{26}\text{Al}$ ”, V. Srivastava, C. Bhattacharya, T. K. Rana, S. Manna, S. Kundu, S. Bhattacharya, K. Banerjee, P. Roy, R. Pandey, G. Mukherjee, T. K. Ghosh, J. K. Meena, T. Roy, A. Chaudhuri, M. Sinha, A. K. Saha, **Md.A. Asgar**, A. Dey, Subinit Roy, and Md. Moin Shaikh, *Proceedings of the DAE-BRNS Symp. on Nucl. Phys.*, **2016**, 61, 514-515.
17. “Excited states of  $^{26}\text{Al}$  studied via the reaction  $^{27}\text{Al}(d,t)$ ”, Vishal Srivastava, C. Bhattacharya, T. K. Rana, S. Manna, S. Kundu, S. Bhattacharya, K. Banerjee, P. Roy, R. Pandey, G. Mukherjee, T. K. Ghosh, J. K. Meena, T. Roy, A. Chaudhuri, M. Sinha, A. K. Saha, **Md.A. Asgar**, A. Dey, Subinit Roy and Md. Moin Shaikh, *EPJ Web of Conferences*, **2016**, 117, 07022(1-6).
18. “Shears Band based on a large multi-qp configuration in  $^{195}\text{Tl}$ ”, T. Roy, H. Pai, **Md.A. Asgar**, G. Mukherjee, A. Dhal, and C. Bhattacharya, *Proceedings of the DAE-BRNS Symp. on Nucl. Phys.*, **2015**, 60, 262-263.
19. “Search for high-spin isomers near  $N = 50$  shell closure”, Purnima Singh, R. Palit, D. Choudhury, S. Biswas, S. Saha, J. Sethi, C. Ghosh, H. C. Jain , P. C. Srivastava, S. Mukhopadhyay, D. C. Biswas, L. S. Danu, **A. Asgar**, G. Mukherjee, R. Raut, S. S. Ghugre, A . K. Sinha, S. K. Tandel6, and S. Muralithar, *Proceedings of the DAE-BRNS Symp. on Nucl. Phys.*, **2015**, 60, 298-299.
20. “Study of one proton pick-up reaction  $^{27}\text{Al}(d,^3\text{He})$ ”, Vishal Srivastava, C. Bhattacharya, T.K. Rana1 , S. Manna, S. Kundu, S. Bhattacharya, K. Banerjee, P. Roy, R. Pandey, G. Mukherjee, T.K. Ghosh, J.K. Meena, T. Roy, A. Chaudhuri, M. Sinha, A. K. Saha, **Md.A. Asgar**, A. Dey, Subinit Roy , and Md. Moin Shaikh, *Proceedings of the DAE-BRNS Symp. on Nucl. Phys.*, **2015**, 60, 342-343.
21. “Effect of neutron shell closure in fission fragment mass distributions of  $^{206,210}\text{Po}$ ”, A. Chaudhuri, T. K. Ghosh, K. Banerjee, S. Bhattacharya, Jhilam Sadhukhan, S. Kundu,

- C. Bhattacharya, J. K. Meena, G. Mukherjee, A. K. Saha, **Md.A. Asgar**, A. Dey, S. Manna, R. Pandey, T. K. Rana, P. Roy, T. Roy, V. Srivastava, P. Bhattacharya, D. C. Biswas, B. N. Joshi, K. Mahata, A. Shrivastava, R. P. Vind, S. Pal, B. R. Behera, and Varinderjit Singh, *Proceedings of the DAE-BRNS Symp. on Nucl. Phys.*, **2015**, 60, 360-361.
22. “Study of fusion-fission dynamics of  $^{200}\text{Pb}$  through fission fragment mass distribution”, A. Chaudhuri, T. K. Ghosh, K. Banerjee, S. Bhattacharya, P. Roy<sup>1</sup>, T. Roy<sup>1</sup>, C. Bhattacharya, S. Kundu<sup>1</sup>, J. K. Meena<sup>1</sup>, G. Mukherjee, **Md.A. Asgar**, A. Dey, S. Manna, R. Pandey, T. K. Rana, A. Sen, M. Sinha, V. Srivastava, P. Bhattacharya, R. Dubey, N. Saneesh, P. Sugathan, and Gurpreet Kaur, *Proceedings of the DAE-BRNS Symp. on Nucl. Phys.*, **2015**, 60, 506-507.
23. “Deformation of  $^{28}\text{Si}^*$  produced via p on  $^{27}\text{Al}$ ”, S. Kundu, C. Bhattacharya, T. K. Rana, S. Bhattacharya, K. Banerjee, P. Roy, J. K. Meena, G. Mukherjee, T. K. Ghosh, R. Pandey, A. Dey, R. Saha, S. Mukhopadhyay, A. K. Saha, J. K. Sahoo, R. Mandal Saha, V. Srivastava, M. Sinha, and **M.A. Asgar**, *Proceedings of the DAE-BRNS Symp. on Nucl. Phys.*, **2015**, 60, 514-515.
24. “Role of fusion fission process on fragment emission mechanism in  $^{32}\text{S}+^{12}\text{C}$  reaction”, R. Pandey, C. Bhattacharya, S. Kundu, K. Banerjee, S. Manna, T. K. Rana, J. K. Meena, T. Roy, A. Chaudhuri, **Md.A. Asgar**, V. Srivastava, A. Dey, M. Sinha, G. Mukherjee, P. Roy, T. K. Ghosh, S. Bhattacharya, A. Srivastava, K. Mahata, S. K. Pandit, P. Patle, S. Pal, and V. Nanal, *Proceedings of the DAE-BRNS Symp. on Nucl. Phys.*, **2015**, 60, 544-545.
25. “Rotational Bands in  $^{195}\text{Tl}$ ”, T. Roy, H. Pai, **Md.A. Asgar**, G. Mukherjee, S. Bhattacharya, M. R. Gohil, T. Bhattacharjee, C. Bhattacharya, R. Palit, S. Saha, J. Sethi, T. Trivedi, Shital Thakur, B. S. Naidu, S. V. Jadav, R. Donthi, A. Goswami, and S. Chanda, *Proceedings of the DAE Symp. on Nucl. Phys.*, **2014**, 59, 88-89.

26. "A New Isomer in  $^{195}\text{Bi}$  Identified at the Focal Plane of HYRA", T. Roy, G. Mukherjee, **Md.A. Asgar**, Soumik Bhattacharya, H. Pai, T.K Rana, S. Bhattacharyya, C. Bhattacharya, S. Bhattacharya, N. Madhavan, S. Nath, R.P. Singh, A. Jhingan, S. Muralithar, R. Kumar, J. Ghelot, T. Varughese, I. Bala, R.K. Gurjar, A.K. Sinha, S.S. Ghugre, R. Raut, S.S. Bhattacharjee, K. Basu, and R. Palit, *Proceedings of the DAE Symp. on Nucl. Phys.*, **2014**, 59, 126-127.
27. "Mass distribution in  $^{238}\text{U}(^{32}\text{S},f)$  reaction", L. S. Danu, B. K. Nayak, D. C. Biswas, B. V. John, A. Saxena, E. T. Mirgule, S. Mukhopadhyay, Y. K. Gupta, B. N. Joshi, G. Prajapati, V. V. Desai, S. V. Suryanarayana, A. Goswami, P. K. Joshi, S. K. Tandel, R. Palit, S. Saha, J. Sethi, S. Biswas, D. Choudhury, P Singh, R. G. Pillay, V. Nanal, T. Roy, **Md Ali Asgar**, P. V. Madhusudhana Rao, Naveen Kumar, and U. Garg, *Proceedings of the DAE-BRNS Symp. on Nucl. Phys.*, **2014**, 59, 368-369.

## Chapters in books and lectures notes

N. A.

*Md. Ali Asgar*

Md. Ali Asgar

Dedicated to my parents

# ACKNOWLEDGEMENTS

Throughout my research career, I got valuable suggestions, advices, supports and inspiration from several people. First of all, I would like to express my sincere appreciation and gratitude to my supervisor Dr. Gopal Mukherjee whose constant and valuable guidance, suggestions and supports helped me to learn some skillful experimental techniques and the necessary attitudes to solve scientific problems. During this period, his constant advices and inspiration motivated me to look at things from different perspectives and his constant supervision helped me in the development of this thesis.

I am very much indebted to the directors of VECC, Prof. Dinesh Kumar Srivastava, Prof. Alok Chakrabarti and Shri Amitava Roy for providing an appropriate working atmosphere and the facility which helped me immensely during my research work. At the same time I am extremely grateful to Prof. Jan-e Alam, Dean, HBNI, VECC, for his suggestions and help during my Ph. D work.

I am extremely grateful to Prof. Sailajananda Bhattacharya, Prof. Sudhee Ranjan Banerjee, Dr. Chandana Bhattacharya, Dr. Parnika Das, Dr. Sarmishtha Bhattacharyya, Dr. Tilak Kumar Ghosh, Prof. Asimananda Goswami (SINP, Kolkata) and Dr. Rudrajyoti Palit (TIFR, Mumbai) for their encouragement, suggestions and kind support.

I would like to give my sincere thanks to Dr. K. Banerjee, Dr. S. Kundu, Dr. T.K. Rana, Dr. Pratap Roy, Dr. Supriya Mukhopadhyay, Dr. Deepak Pandit, Dr. Surajit Pal, Dr. T. Bhattacharjee, Dr. A. Dhal, S. Manna, R. Pandey, A. Sen, D. Mondal, A. Dey, J.K. Meena, A. Choudhury, P. Mukherjee, A.K Saha, J.K Sahoo, R. Mandal Saha. They helped me in various experiments.

The effort of the operators of the accelerators at VECC and TIFR, and all the participating members in the INGA Collaboration are gratefully acknowledged. I also acknowledge the effort of all the members participating in VENUS array setup at VECC. I also thank Mr. A. Mahadkar, member of target making laboratory of TIFR, for target preparation.

My special thanks to Tanmoy da (Dr. Tanmoy Roy), Soumik da (Soumik Bhattacharya), Hari da (Dr. Haridas Pai) and Subhendu da (Dr. Subhendu Rajbanshi) for their suggestions, criticisms and constant help throughout my Ph. D work.

It is my great pleasure to have friends like Debasish, Sarwar, Noor, Utsab, Arunabha and my juniors Rana, Rajendra, Pingal, Somnath, Snigdha, Pabrisa, Ashik, Ranabir, Safikul, Dipak, Homenath, Ajit, Soumen, Mahfuzur, Santanu, Sumit, Mitali, Shreyasi and Sanchari.

I am very grateful to my parents, brothers and sisters for their constant support throughout my Ph. D work.

*Md. Ali Asgar*

Md. Ali Asgar

# Contents

<b>Synopsis</b>	<b>xxi</b>
<b>List of Figures</b>	<b>xxxix</b>
<b>List of Tables</b>	<b>xli</b>
<b>1 Introduction</b>	<b>1</b>
<b>2 Nuclear Models</b>	<b>10</b>
2.1 Liquid drop model . . . . .	10
2.2 Shell model . . . . .	12
2.3 Collective model . . . . .	14
2.4 Nilsson model . . . . .	17
2.5 Strutinsky Shell correction . . . . .	23
2.6 Cranked Shell model . . . . .	25
2.7 Total Routhian Surface (TRS) calculations . . . . .	27

<b>3</b>	<b>Experimental Technique</b>	<b>29</b>
3.1	Generation of High Spin Nuclear States . . . . .	29
3.1.1	Fusion evaporation reaction . . . . .	30
3.1.2	Decay of compound nucleus . . . . .	32
3.1.3	Inelastic excitation . . . . .	33
3.2	$\gamma$ -ray detection processes . . . . .	34
3.2.1	Photoelectric effect . . . . .	34
3.2.2	Compton scattering . . . . .	35
3.2.3	Pair production . . . . .	37
3.3	HPGe detector . . . . .	37
3.4	Clover detector . . . . .	38
3.5	Indian National Gamma Array (INGA) at TIFR . . . . .	43
3.6	VENUS array setup at VECC . . . . .	45
<b>4</b>	<b>GEANT4 Simulation</b>	<b>49</b>
4.1	Geant4 Simulation of HPGe Single Crystal, Clover and VENUS array . . . . .	49
4.1.1	HPGe Single Crystal . . . . .	50
4.1.2	Clover . . . . .	53
4.1.3	VENUS array . . . . .	55
<b>5</b>	<b>Experimental Data Analysis</b>	<b>62</b>

5.1	Energy and Efficiency Calibration . . . . .	62
5.2	Construction of Level Scheme . . . . .	64
5.2.1	Coincidence relation and relative intensity of $\gamma$ -rays . . . . .	64
5.3	Spin and Parity Assignment of Nuclear Levels . . . . .	66
5.3.1	$\gamma$ -ray selection rules . . . . .	66
5.3.2	Determination of multipolarity of $\gamma$ -ray transitions . . . . .	67
5.3.3	Linear polarization of $\gamma$ -ray transitions . . . . .	77
5.4	Some useful quantities for the interpretation of experimental data . . . . .	86
5.4.1	Quasi-particle aligned angular momentum . . . . .	87
5.4.2	Experimental quasi-particle Routhian . . . . .	88
5.4.3	Moment of inertia . . . . .	88
5.4.4	Experimental B(M1)/B(E2) ratio . . . . .	89
5.4.5	Calculated B(M1)/B(E2) ratio . . . . .	90
<b>6</b>	<b>Study of Band Structures in <math>^{169}\text{Tm}</math></b>	<b>92</b>
6.1	Introduction . . . . .	92
6.2	Experiment and Data Analysis . . . . .	94
6.3	Experimental Results . . . . .	94
6.4	Discussion . . . . .	102
6.4.1	Band crossing in $^{169}\text{Tm}$ . . . . .	103

6.4.2	Possible octupole correlation in $^{169}\text{Tm}$ . . . . .	108
6.5	Conclusion . . . . .	112
<b>7</b>	<b>High spin nuclear structures in odd-odd <math>^{196}\text{Tl}</math></b>	<b>114</b>
7.1	Introduction . . . . .	114
7.2	Experiment and Data Analysis . . . . .	115
7.3	Experimental Results . . . . .	116
7.4	Discussion . . . . .	129
7.5	TRS calculations . . . . .	137
7.6	Conclusion . . . . .	139
<b>8</b>	<b>High spin <math>\gamma</math>-spectroscopy of <math>^{207}\text{Po}</math></b>	<b>141</b>
8.1	Introduction . . . . .	141
8.2	Experiment and Data Analysis . . . . .	142
8.3	Results and Discussion . . . . .	143
8.3.1	Low lying states . . . . .	153
8.3.2	Possible Magnetic Rotational band . . . . .	155
8.4	Conclusion . . . . .	158
<b>9</b>	<b>Summary and Future Outlook</b>	<b>160</b>
9.1	Summary . . . . .	160
9.2	Future outlook . . . . .	165

# SYNOPSIS

## Introduction

In this thesis work, the high-spin states in  $^{169}\text{Tm}$  ( $Z = 69$ ),  $^{196}\text{Tl}$  ( $Z = 81$ ) and  $^{207}\text{Po}$  ( $Z = 84$ ) nuclei were experimentally investigated using the gamma-ray spectroscopic technique. Nucleus is a many-body quantal system which is a fascinating laboratory to test the quantum mechanical laws and symmetries. Because of the finite size and finite number of nucleons in a nuclear system, it can have both collective as well as single particle excitations when energy is pumped into a nuclear system. The modes of excitation depend on the factors like, nuclear shape and the available nucleonic orbitals near the proton and the neutron Fermi levels. The nuclei with proton and/or neutron numbers close to the spherical shell gaps at 2, 8, 20, 28, 50 and 126 (for neutron only) are mostly spherical in nature while the near mid-shell nuclei with proton and neutron numbers away from these shell closures are deformed in their ground state. For a spherical nucleus, the excited states consist of irregular sequence of levels characterizing the single particle (proton and neutron) excitations to different nucleonic orbitals, whereas, in case of a deformed nucleus, the excited states are the regular sequences of levels characteristics of collective excitation of nucleus due to rotation of a deformed quantal system. However, due to the presence of high- $j$  ( $j$  is the total angular momentum quantum number of a nucleonic state) single particle orbitals near the shell gaps may polarize a nucleus to a deformed shape due to their shape-driving effect. On the other hand, in case of a deformed nucleus, the Coriolis force of the rotation can break the paired state of the nucleons giving rise to band-crossing in nucleus due to particle alignment. Such interplay of single particle and collective degrees of freedom not only generates interesting high-spin phenomena in nuclei but also helps to understand the nature and strength of the underlying internucleon forces.

Among the nuclei studied under this thesis work, the  $^{169}\text{Tm}$  is situated in the deformed rare-earth region. In case of odd-A Thulium isotopes with  $Z = 69$ , the proton Fermi level lies near the mid-shell region of the two magic numbers at  $Z = 50$  and  $Z = 82$ . As they are situated in the deformed rare-earth region, these nuclei are well deformed in their ground state. The lighter nuclei are reported to be triaxial and the heavier ones ( $A > 163$ ) are axially deformed. Rotational bands observed in  $^{157}\text{Tm}$  [1] indicate that the deformation in Tm isotopes set in even at neutron number  $N = 88$ . For the heavier odd-A Tm isotopes around  $N = 98$ , apart from the ground state rotational band based on the configuration of odd-proton occupying the  $[411]1/2^+$  Nilsson orbital, other rotational bands built on different single-particle proton orbitals have also been observed [2, 3, 4, 5, 6]. The band crossing due to the Coriolis decoupling of the  $i_{13/2}$  neutron pair has been reported for the  $\pi[411]1/2^+$  bands in  $^{165,167}\text{Tm}$  isotopes [2, 3]. The nature of alignment of these two neighboring isotopes shows contrasting behavior. In case of  $^{165}\text{Tm}$ , a sharp back bending and in  $^{167}\text{Tm}$  a smooth or gradual up-bending are reported. The high spin data on  $^{169}\text{Tm}$  [4, 5] and heavier isotopes are, however, limited to below the band crossing region and a systematic comparison of the effect of the neutron Fermi level on the alignment behaviour could not be made. Moreover, the Nilsson orbitals  $[541]1/2^-$  and  $[411]1/2^+$ , situated near the proton Fermi level of Tm isotopes, are originated from  $\pi h_{9/2}$  and  $\pi d_{3/2}$  orbitals, respectively. These are  $\Delta l = 3$  and  $\Delta j = 3$  orbitals which may be the good candidates for octupole correlation in nuclei. Therefore, the high spin states in  $^{169}\text{Tm}$  have been studied to investigate the above features in heavy Tm isotopes.

For the Thallium nuclei with  $Z = 81$ , the proton Fermi level lies near the  $Z = 82$  spherical shell closure and, hence, the ground state of the Tl isotopes are spherical. However, due to the large shape driving effect of the  $\pi h_{9/2}$  orbital, the high (low)  $\Omega$  components of this orbital comes down in energy with oblate (prolate) deformation and intrudes near the proton Fermi level of Tl below the  $Z = 82$  shell gap. On the other hand, in case of Tl isotopes in  $A = 190$  region with neutron Fermi level near the high-j  $\nu i_{13/2}$  orbital also has a large shape driving effect.

Hence, due to the combined effect of these two shape-driving orbitals, rotational bands based on the  $\pi h_{9/2} \otimes \nu i_{13/2}$  configuration, indicating induced deformation, have been observed in the odd-odd Tl isotopes in this region [7, 8, 9, 10] at moderate excitation energies. The prolate and oblate shape driving effect of the  $\nu i_{13/2}$  orbital depends on whether the neutron Fermi level is close to the low or high- $\Omega$  components of  $i_{13/2}$  orbital. Therefore, it is important to identify and determine the nature of the band structures built on different configurations in the Tl isotopes. However, data on the odd-odd Tl nuclei are very limited. Moreover, the complex and exotic modes of generation of angular momentum have been reported in some of the odd-odd Tl nuclei. For neutron number  $N = 113$ , a triaxial shape is indicated at higher excitation energy from the observation of Chiral doublet bands in  $^{194}\text{Tl}$  [11] for the 4-quasiparticle (qp) configuration. This is possibly due to the opposite shape driving effects of the proton and the neutron orbitals. On the other hand, Magnetic Rotational (MR) band has also been identified in the same nucleus with a configuration based on  $\pi h_{9/2}^2 s_{1/2}^{-1} \otimes \nu i_{13/2}^{-2} p_{3/2}$  [12]. In  $^{198}\text{Tl}$  [13, 14], the chiral band is reported for the 2-quasiparticle configuration,  $\pi h_{9/2} \otimes \nu i_{13/2}$ , at relatively lower spin compared to the chiral band in  $^{194}\text{Tl}$ . Therefore, in order to get a better understanding on the band structures based on different configurations, the high spin states in odd-odd  $^{196}\text{Tl}$  nucleus have been studied. This will also provide information on the effect of the neutron numbers in inducing triaxial shapes in odd-odd Tl nuclei in this region. The existing data on the high-spin states in  $^{196}\text{Tl}$  [9] are very scarce. Apart from the  $\pi h_{9/2} \otimes \nu i_{13/2}$  band which is limited to below the particle alignment region, the spin and parities of the other states are not known, so configuration assignment could not be done. In the present thesis work, the study of the high spin spectroscopy of  $^{196}\text{Tl}$  provided better information to get a new insight about the odd-odd Tl nuclei.

In case of  $^{207}\text{Po}$  nucleus with  $Z = 84$  and  $N = 123$ , the proton and the neutron fermi levels lie just above and below the heaviest known shell closures at  $Z = 82$  and  $N = 126$ , respectively. The available high-j orbitals near the proton and neutron Fermi levels are  $f_{5/2}$ ,  $f_{7/2}$ ,  $h_{9/2}$  and

$i_{13/2}$ . Because of the proximity of the spherical shell closures the heavier Polonium isotopes ( $N > 114$ ) are spherical and the high spin excited states of these isotopes are mostly generated by single particle excitation [15, 16, 17, 18, 19]. The properties of the excited states of the heavier Po isotopes are interpreted by the coupling of the doubly closed  $^{208}\text{Pb}$  ( $Z = 82$ ,  $N = 126$ ) core with the valence proton particles and neutron holes outside the core [16, 17, 18, 19]. An even-even core of nearest isotope can also be considered and the experimental results could be used for testing the nuclear shell model. Systematic investigations of the effect of the coupling of the high- $j$  orbitals with the doubly closed Pb core can be done for these nuclei.

## Experiments

The high-spin states in  $^{169}\text{Tm}$  and  $^{196}\text{Tl}$  nuclei were produced by  $^{169}\text{Tm}(^{32}\text{S}, ^{32}\text{S}')^{169}\text{Tm}^*$  inelastic reaction and  $^{185,187}\text{Re}(^{13}\text{C}, \text{xn})^{196}\text{Tl}$  fusion-evaporation reaction, respectively. The 164-MeV  $^{32}\text{S}$  and 75-MeV  $^{13}\text{C}$  beams were delivered from the 14-UD BARC-TIFR Pelletron (Pelletron LINAC Facility), Mumbai. The emitted  $\gamma$ -rays were detected using the Indian National Gamma Array (INGA) at TIFR. It consisted of 19 and 15 numbers of Compton-suppressed clover HPGe detectors for the  $^{169}\text{Tm}$  and  $^{196}\text{Tl}$  experiments, respectively. A digital data acquisition system based on Pixie-16 modules with a sampling rate of 100 MHz [21, 22], was used to record time-stamped  $\gamma - \gamma$  coincidence data. The high-spin states in  $^{207}\text{Po}$  were populated via  $^{208}\text{Pb}(\alpha, 5\text{n})^{207}\text{Po}$  fusion-evaporation reaction at a beam energy of 60 MeV from K-130 cyclotron at VECC, Kolkata. The  $\gamma$ -rays were detected using the VENUS (VECC array for Nuclear Spectroscopy) setup at VECC [23], consisted of 6 Compton-suppressed clover detectors in the horizontal plane. A VME data acquisition system was used to collect the  $\gamma - \gamma$  coincidence data.

# Geant4 simulation of HPGe detector and array

For in-depth understanding of the details of the response of the clover detectors, a simulation code in the Monte Carlo Geant4 [24] platform has been developed [25, 26]. The simulation was performed for a single-crystal HPGe detector, a clover detector and of the VENUS array. Exact geometry as per the manufacturers (Canberra Inc.) specification was obtained for each clover with BGO Compton suppressor and heavy-metal collimator. The array geometry, as per the experimental situation for  $^{207}\text{Po}$  experiment was also generated.  $\gamma$ -ray energy spectra for  $^{137}\text{Cs}$  and  $^{60}\text{Co}$  sources, absolute photo-peak efficiencies and peak-to-total (P/T) ratio at different modes such as single-crystal, sum-of-four-crystal, add-back and Compton suppressed were obtained. Good agreement between simulated and measured values of add-back factors were achieved.

## Data analysis

Data analysis was done using MARCOS [22], LAMPS [27] and RADWARE [28] software packages.  $\gamma$ - $\gamma$  coincidence relations, obtained from  $\gamma$ - $\gamma$  matrices and  $\gamma$ - $\gamma$ - $\gamma$  cubes, and intensity relations were used to construct the level schemes of the nuclei of interest. Definite spin and parity of a nuclear level was assigned by measuring the multipolarity and type (E/M) of the gamma-rays emitted from that level. Multipolarity of a  $\gamma$ -ray was measured from the  $\gamma$ -ray angular distributions and Directional Correlation from Oriented states (DCO) ratios. Angular distribution data of a  $\gamma$ -ray transition are fitted using the relation:

$$W(\theta) = a_0(1 + a_2P_2(\cos\theta) + a_4P_4(\cos\theta)) \quad (1)$$

where the coefficients  $a_2$  and  $a_4$  depends on the multipolarity of the  $\gamma$ -ray transition.  $P_2(\cos\theta)$  and  $P_4(\cos\theta)$  are the Legendre polynomials. For DCO ratio measurement, asymmetric  $\gamma$ - $\gamma$

matrices were formed from the coincidence events in which the x-axis contains the data from the  $-23^\circ$  ( $\theta_1$ ) detectors and the y-axis contains the data from the  $90^\circ$  ( $\theta_2$ ) detectors in the INGA array setup and for VENUS array  $\theta_1$  and  $\theta_2$  were  $30^\circ$  and  $90^\circ$  respectively. The DCO ratio of a  $\gamma$ -transition ( $\gamma_1$ ) is obtained from the ratio of its intensities (I) gated by a transitions with known multipolarity ( $\gamma_2$ ) at the above two angles from the above DCO matrix, using the relation,

$$R_{DCO} = \frac{I_{\gamma_1} \text{ at } \theta_1, \text{ gated by } \gamma_2 \text{ at } \theta_2}{I_{\gamma_1} \text{ at } \theta_2, \text{ gated by } \gamma_2 \text{ at } \theta_1} \quad (2)$$

In the present experiments, for the same multiplicities of  $\gamma_1$  and  $\gamma_2$ , the value of  $R_{DCO} = 1$  whereas, for a pure dipole transition gated by a stretched quadrupole transition  $R_{DCO} \sim 0.5$ . Parities of the nuclear states were assigned from the knowledge of the type (E/M) of the emitted  $\gamma$ -rays which were confirmed by measuring the Integrated Polarization Directional Correlation (IPDCO) ratios. The data from the  $90^\circ$  detectors were only used for  $\gamma - \gamma$  matrix to extract the IPDCO ratios. Measuring the intensities of the perpendicular ( $N_\perp$ ) and the parallel ( $N_\parallel$ ) scattered  $\gamma$ -rays with respect to the reaction plane, IPDCO ratios can be obtained using the following relation:

$$\Delta_{IPDCO} = \frac{a(E_\gamma)N_\perp - N_\parallel}{a(E_\gamma)N_\perp + N_\parallel} \quad (3)$$

where  $a(E_\gamma)$  ( $= N_\parallel/N_\perp$ ) is a correction factor related to the geometrical asymmetry of the detector array and its value has been obtained using the  $^{133}\text{Ba}$  and  $^{152}\text{Eu}$  radioactive sources. A positive or negative value of  $\Delta_{IPDCO}$  indicates that the transition is electric or magnetic type, respectively.

## Theoretical calculations

In order to understand and interpret the data on the deformed rotational bands in  $^{169}\text{Tm}$  and  $^{196}\text{Tl}$ , theoretical model calculations in the frame work of Cranked Shell Model (CSM) formalism

with BCS pairing have been performed. The single particle energies for protons and neutrons were calculated in the deformed mean field basis using deformed Woods-Saxon potential. The total Routhian surfaces (TRS) were calculated using the Strutinsky shell correction method for several values of the deformation parameters  $\beta_2, \gamma$  and  $\beta_4$  for different rotational frequencies  $\hbar\omega$ . For a particular  $\hbar\omega$ , the values of  $\beta_2, \gamma$  and  $\beta_4$  corresponding to the minimum of the TRS gives the calculated shape of a nucleus at that frequency.

## Results

Total 16 new  $\gamma$ -ray transitions have been identified and placed in the new level scheme of  $^{169}\text{Tm}$ . The ground-state  $[411]1/2^+$  band has been extended up to the excitation energy ( $E_x$ ) of 2.5 MeV and spin ( $J$ ) of  $31/2\hbar$ . Band crossing, due to the alignment of a pair of neutrons, is observed in this band for the first time in  $^{169}\text{Tm}$ . The plot of aligned angular momentum vs. rotational frequency clearly indicates a sharp backbending in  $^{169}\text{Tm}$  similar to  $^{165}\text{Tm}$  but in sharp contrast to the smooth upbending in  $^{167}\text{Tm}$  [2, 3]. This indicates that the interaction strength between the 1-qp ground-state band and 3-qp band is larger in case of  $N = 98$  isotope  $^{167}\text{Tm}$  compared to that in  $^{167,169}\text{Tm}$ . The TRS calculations show very similar prolate deformation for these three isotopes for that configuration with  $\beta_2 \sim 0.28$ . However, the calculated single-neutron Routhians clearly show a much larger interaction strength of  $\sim 125$  keV for  $^{167}\text{Tm}$  compared to  $V = 20$  and  $V = 10$  for  $^{165}\text{Tm}$  and  $^{169}\text{Tm}$ , respectively. It is concluded that the different band crossing phenomena in these three isotopes are due to a significantly large deformed shell gap at  $\beta_2 \sim 0.28$  for neutron number  $N = 98$ , which has been confirmed later on from the mass and decay data measurements of Eu isotopes [29]. The results of this work has been published in referred journal [30].

Several E1 transitions, intertwined between the positive parity ground-state band and a negative parity band based on  $[541]1/2^-$  configuration, have also been observed in this work. These are

compared with the octupole correlated bands in the  $A = 140$  region and concluded the existence of octupole correlation in  $^{169}\text{Tm}$  with reduced strength.

In  $^{196}\text{Tl}$ , the level scheme has been extended up to  $E_x = 5.1$  MeV and  $J = 22\hbar$  with the placement of several newly observed  $\gamma$ -rays in this work compared to those reported in Ref. [9]. Moreover, definite spin and parity assignments were done in this work for the side bands and hence, proper configuration has been assigned to these bands. With the new observation, the  $\pi h_{9/2} \otimes \nu i_{13/2}$  band could be extended beyond the band crossing and a systematic comparison of alignment frequency and aligned angular momentum could be made for the odd-odd Tl isotopes. It has been observed that the behaviour of the odd-odd Tl nuclei remain almost identical before the band crossing but they behave differently after the band crossing [31]. It is also interesting that no clear indication of chirality or MR band could be observed in  $^{196}\text{Tl}$ , where as these were reported for the isotopes  $^{194,198}\text{Tl}$ .

In the present study of  $^{207}\text{Po}$ , a new level scheme has been obtained which extends up to  $E_x = 6.87$  MeV and  $J = 49/2\hbar$ . The lower-lying excited states could be interpreted as the odd-neutron in  $i_{13/2}$  orbital coupled with the different states in even-even  $^{206}\text{Po}$  nucleus. A comparison with the other isotopes provides the information on the position of this  $i_{13/2}$  orbital as a function of neutron number. The higher lying states are generated due to the multi-particle excitations in the single-particle orbitals. No evidence of collective states could be observed for up to 5-qp excitations. However, a MR band has been identified for the first time in this nucleus with 5-qp configuration at  $E_x = 4.8$  MeV with the observation of a regular sequence of M1(+E2) transitions.

## Conclusion

The high spin states in  $^{169}\text{Tm}$ ,  $^{196}\text{Tl}$  and  $^{207}\text{Po}$  were studied in this thesis work using  $\gamma$ -ray spectroscopic technique. The INGA and VENUS detector setup at TIFR, Mumbai and at VECC,

Kolkata, with clover HPGe detectors were used for the detection of  $\gamma$ -rays. The existence of a deformed shell gap at neutron number  $N = 98$  and its effect on the band crossing could be established qualitatively from the study of  $^{169}\text{Tm}$ . A quantitative estimate of the interaction strength was also calculated and compared for the three isotopes. Possible existence of octupole correlation with reduced strength was also determined in this odd-proton nucleus. The effect of intruder proton and high- $j$  neutron orbitals in breaking the nuclear spherical symmetry has been studied in the odd-odd nucleus  $^{196}\text{Tl}$  from the observation of several rotational band structures. Also, no evidence of chiral bands has been seen in this nucleus indicating that as the high- $j$   $i_{13/2}$  orbital is completely filled, a triaxial shape, necessary for chiral bands, may not be realized for  $N > 114$ . In case of the odd-neutron nucleus  $^{207}\text{Po}$ , it has been found that the nucleus remain near spherical even at higher angular momentum with up to 5-qp excitation. An MR band has been observed for such multi-qp configuration comprising of 2 proton particles and 3 neutron holes.

Although important results on the deformation and the role of single-particle orbitals in determining the high spin structure of different types of nuclei have been achieved in this thesis work, however, the present study also paves the way for some new investigation. It would be interesting to study the band structures in the neutron rich Tm isotopes beyond the band crossing to get a more complete picture of the band interaction phenomena as a function of neutron number. Moreover, the octupole correlation in the neutron deficient Tm isotopes with neutron number  $N \sim 88$  may be studied where it is expected to show enhanced octupole correlation. Also, the lifetimes of the excited states may be measured to get the quantitative information on the deformation of different configuration as well as the possible shape change after band crossing for the  $\pi h_{9/2} \otimes \nu i_{13/2}$  band in  $^{196}\text{Tl}$  and to establish the MR band in  $^{207}\text{Po}$ .

# List of Figures

1.1	Crossing of g-band with s-band has been shown. The experimental data (open circle) of $^{162}\text{Er}$ [35, 36] have been fitted with parabolic curves corresponding to the rotational model as given in equation (1.1). High-spin data of $^{162}\text{Er}$ up to $44\hbar$ of spin are available in Ref. [37]. . . . .	3
1.2	A schematic diagram illustrating the back-bending and up-bending types of band crossings due to the pair breaking of valence nucleons in time-reversed orbits. . .	4
1.3	(a) Back-bending and (b) up-bending types of band crossings in the ground-state bands of $^{165}\text{Tm}$ and $^{167}\text{Tm}$ , respectively, as a function of rotational frequency are shown. The filled and open circles represent the signature partners of the rotational bands. Experimental data for plot (a) are taken from Ref. [2] and for plot (b), data are taken from Ref. [3]. . . . .	4
1.4	A schematic diagram illustrating the coupling between the particle and hole angular momenta for magnetic rotation. . . . .	7
1.5	The nuclei $^{169}\text{Tm}$ , $^{196}\text{Tl}$ and $^{207}\text{Po}$ studied in this thesis work are shown in red boxes in nuclear chart. Basic diagram of this figure is taken from Ref. [54]. . . .	8
2.1	Various nuclear shapes in $(\beta_2 - \gamma)$ plane using Lund convention [62]. . . . .	15

2.2	Nilsson diagram of single particle states for proton ( $Z \geq 82$ ) as a function of deformation $e_2$ ( $e_2 = \delta$ )[64]. . . . .	18
2.3	Nilsson diagram of single particle states for neutron ( $82 \geq N \leq 126$ ) as a function of deformation $e_2$ ( $e_2 = \delta$ )[64]. . . . .	19
2.4	Asymptotic quantum numbers $\Lambda$ , $\Sigma$ and $\Omega$ for the Nilsson model are shown. . .	22
3.1	Schematic diagram of fusion evaporation reaction. This figure is taken from Ref. [77]. . . . .	30
3.2	Excitation energy as a function of nuclear spin is shown. This figure is taken from Ref. [77]. . . . .	33
3.3	Relative Probability for each of the three types of $\gamma$ -ray interactions in Ge ( $Z = 32$ ) and Si ( $Z = 14$ ) as a function of energy. This figure is taken from Ref. [78]. . .	36
3.4	Clover HPGe detector at Laboratory. . . . .	39
3.5	Schematic diagram of clover HPGe detector [80]. . . . .	39
3.6	Addback factor as a function of $\gamma$ -ray energy for clover detector. . . . .	41
3.7	FWHM of clover detector as a function of $\gamma$ -ray energy. Solid straight line is the linear fit of the data. . . . .	41
3.8	Absolute efficiency of Clover detector at 10 cm distance from the source . . . . .	42
3.9	INGA setup at TIFR. . . . .	43
3.10	Block diagram for the digital DAQ for 24 Compton suppressed clover detectors. It consists of six Pixie-16 modules, two LVDS level translator modules and one controller arranged in a single Compact PCI/PXI crate [22]. . . . .	44
3.11	VENUS setup at VECC. . . . .	46

3.12	Block diagram for electronics setup for VENUS array at VECC [87]. . . . .	47
4.1	The simulated geometry of the HPGe detector (left) and the sketched diagram of the detector (right). . . . .	51
4.2	Measured and simulated absolute efficiencies of the single-crystal HPGe detector as a function of $\gamma$ -ray energy for 11 cm, 16 cm and 22 cm distances from the source to the detector. The Experimental data (filled symbols) were taken using a $^{152}\text{Eu}$ source. . . . .	52
4.3	Variation of the measured and simulated absolute efficiencies with distance for 1 MeV $\gamma$ -ray (the experimental values of efficiency at 1 MeV are obtained from the fitted efficiency curve). The data are also fitted with the $y = a/r^2$ equation, where, $y = \text{efficiency}$ , $r = \text{distance}$ and $a$ is the fitted parameter. . . . .	52
4.4	Simulated spectrum of an arbitrary $\gamma$ -ray of energy 1511 keV. The spectrum shows the single-escape and the double-escape peaks. . . . .	53
4.5	The construction of clover detector in Geant4 simulation are shown through four steps in figures (a), (b), (c) and (d). . . . .	54
4.6	The geometry of the VENUS array with the ACS as constructed in the Geant4 simulation. . . . .	56
4.7	Absolute efficiency of clover in crystal, sum of four crystals and add-back mode at 10 cm distance. Data are compared with simulation. . . . .	57
4.8	Simulated $^{60}\text{Co}$ spectra with (red) and without (black) ACS in the add-back mode. . . . .	58
4.9	Simulated $^{137}\text{Cs}$ spectra with (red) and without (black) ACS in the add-back mode, compared with the measured $^{137}\text{Cs}$ spectrum (green) with ACS. The measured spectrum shows the room background lines also. . . . .	58

4.10	Upper panel: simulated efficiencies are shown in various modes (inset: adback efficiency compared with measured data) as a function of $\gamma$ -ray energy. Lower panel: measured and simulated adback factors are compared. . . . .	59
4.11	Simulated P/T ratios as a function of $\gamma$ -ray energy are shown for four different cases. . . . .	59
4.12	Hit patterns of $\gamma$ rays for the interaction with the four crystals of clover detector are shown. . . . .	60
5.1	Relative efficiency of INGA as a function of $\gamma$ -ray energy using $^{152}\text{Eu}$ and $^{133}\text{Ba}$ sources. The solid line is the fitted curve with the equation ( 5.3). . . . .	64
5.2	Example of level scheme for $\gamma$ -ray coincidence demonstration. . . . .	65
5.3	Total projection, single- and double- gated $\gamma$ -ray spectra of $^{196}\text{Tl}$ . . . . .	66
5.4	Schematic diagram of $\gamma$ -ray transitions illustrating the effect of $\gamma$ -ray selection rules on allowed multipolarities. . . . .	67
5.5	Calculated angular distributions of pure dipole, quadrupole and octupole $\gamma$ -transitions. . . . .	70
5.6	Calculated angular distributions of mixed (dipole + quadrupole) transition for different mixing ratios. . . . .	70
5.7	Calculated angular distributions of mixed (quadrupole + octupole) transition for different mixing ratios. . . . .	71
5.8	Two emitted $\gamma$ rays, $\gamma_1$ and $\gamma_2$ , separated by a number of intermediate unobserved transitions, are shown in a cascade. The directions of the emitted $\gamma$ rays are shown in terms of spherical angles $\theta$ and $\phi$ with respect to the beam axis in the right side figure. . . . .	72

5.9	Calculated angular distribution of $\gamma$ -ray for different $\sigma/J$ values. . . . .	76
5.10	Angular distribution of (a) 323-keV and (b) 337-keV $\gamma$ -transitions. The solid line (red) is the fitted curve to the experimental data points (circle). . . . .	77
5.11	Calculated contour plot of $a_2$ vs. $a_4$ (red square) for different $\sigma/J$ values in interval of 0.05 for 323 keV stretched quadrupole transition of $^{169}\text{Tm}$ produced via $^{169}\text{Tm}(^{32}\text{S},\text{S}')^{169}\text{Tm}^*$ inelastic reaction has been shown. The experimental angular distribution coefficients (black circle) are compared with the calculation. . . . .	78
5.12	Asymmetry correction factor $a(E_\gamma)$ of (a) INGA and (b) VENUS detector arrays. The solid line is the linear fit. . . . .	80
5.13	(a): Perpendicular counts (black solid line) are less than the parallel counts (red solid line) for 266-, 271-, 285- and 289-keV $\gamma$ -transitions of $^{196}\text{Tl}$ and therefore, these are magnetic in nature. (b): For 663- and 681-keV transitions of $^{196}\text{Tl}$ , perpendicular counts are greater than the parallel counts and therefore, these are electric type. . . . .	80
5.14	Calculated polarization of (a) (M1/E2) mixed $\gamma$ -ray for $\Delta J = 1$ , (b) (E1/M2) mixed $\gamma$ -ray for $\Delta J = 1$ and (c) (M2/E3) mixed $\gamma$ -ray for $\Delta J = 2$ as a function of mixing ratio. . . . .	82
5.15	Calculated polarization of (a) (M1/E2) mixed $\gamma$ -ray for $\Delta J = 0$ and (b) (E1/M2) mixed $\gamma$ -ray for $\Delta J = 0$ as a function of mixing ratio. . . . .	83
5.16	Contour plot of calculated $R_{DCO}$ and polarization for the (a) 337-keV, $17/2^+ \rightarrow 15/2^+$ transition in the band B1 and (b) 235-keV, $13/2 \rightarrow /2^+$ connecting transition between band B1 and B2 of $^{169}\text{Tm}$ . The measured values are shown as experimental points. The values of mixing ratio $\delta$ for the calculated points close to the experimental point are shown. . . . .	85

5.17	A schematic diagram illustrating the kinematic and dynamic moment of inertia.	89
5.18	B(M1)/B(E2) ratios for the bands based on different configurations in $^{165}\text{Tm}$ . The experimental data (black circle) are compared with calculated ones (red solid line). The experimental data are taken from Ref. [2].	91
6.1	Proposed level scheme of $^{169}\text{Tm}$ . The $\gamma$ -rays marked by * symbol are the newly placed transitions.	95
6.2	$\gamma$ -ray spectra of $^{169}\text{Tm}$ obtained by sum of double gates. The gates were put on the transitions in band B1. The new $\gamma$ peaks are marked by asterisks (*).	99
6.3	$\gamma$ -spectra of $^{169}\text{Tm}$ obtained by double gates. The gates were put on (a) the transition in band B1 and a connecting transition between bands B1 and B2, (b) the transitions in band B2 and (c) the transitions in band B3. The new $\gamma$ transitions are marked by asterisks (*).	100
6.4	$\gamma$ -ray spectra of $^{169}\text{Tm}$ obtained by single gates. The gates were put on the transitions in band B2 (a) and in band B3 (b). The new $\gamma$ transitions are marked by asterisks (*).	101
6.5	Quasi-particle aligned angular momenta ( $i_x$ ) as a function of rotational frequency ( $\hbar\omega$ ) for odd-A Tm isotopes. The solid and the open symbols represent signature $\alpha = +1/2$ and $-1/2$ , respectively. Harris parameters $J_0 = 35 \hbar^2/\text{MeV}$ and $J_1 = 43 \hbar^4/\text{MeV}^3$ are taken to subtract a rotor reference value.	103
6.6	TRS calculations of $^{165}\text{Tm}$ (a), $^{167}\text{Tm}$ (b), and $^{169}\text{Tm}$ (c) nuclei at $\hbar\omega = 0.2$ MeV. The contours are 250 keV apart.	105
6.7	Calculated quasi-neutron energy levels for $N = 96, 98$ and $100$ corresponding to $^{165}\text{Tm}$ , $^{167}\text{Tm}$ and $^{169}\text{Tm}$ nuclei.	107

6.8	Plot of the energy difference ( $\delta E$ ) between the positive and negative parity states in bands B1 and B2 in $^{169}\text{Tm}$ compared with that in the parity doublet bands in odd-A nuclei (a) and even-even nuclei (b). . . . .	110
7.1	Proposed level scheme of $^{196}\text{Tl}$ . The $\gamma$ -rays marked by * symbol are the newly placed transitions. . . . .	118
7.2	DCO and IPDCO ratios plots as a function of $\gamma$ -ray energy of the known as well as new $\gamma$ rays in $^{196}\text{Tl}$ . The DCO ratios of the $\gamma$ rays have been obtained with stretched E2 transition gate. . . . .	119
7.3	Coincidence $\gamma$ -spectra corresponding to sum of single gates on 344-, 271- and 236-keV. The upper panel spectrum up to 800 keV and lower panel spectrum is from 800 keV to 1600 keV. New $\gamma$ -transitions are marked by *. . . . .	120
7.4	Double gated $\gamma$ -spectra. Top panel: double gate on 344- and 271-keV, middle panel: double gate on 192- and 319-keV and lower panel: double gate on 244- and 161-keV. . . . .	121
7.5	Coincidence spectrum generated by double gate list of 344-, 108-, 271- and 236-keV $\gamma$ rays. The new $\gamma$ -transitions are marked by *. . . . .	122
7.6	Perpendicular (solid) and parallel (dashed) components of 992-keV $\gamma$ ray are shown. The higher parallel scattering counts than the perpendicular one indicates magnetic type transition. . . . .	123
7.7	Theoretical contour plots of DCO ratio vs. polarization for different possible spin-parity $J_i^\pi \rightarrow J_f^\pi$ assignments as a function of mixing ratio ( $\delta$ ) for the 992-keV $\gamma$ ray. The theoretical calculations are compared with the experimentally measured values. . . . .	124

7.8	Angular distribution of 678-keV $\gamma$ ray decaying from the 2223-keV to 1545-keV state in band B3. Solid line is the fitted curve of the data. . . . .	125
7.9	Theoretical contour plots of DCO ratio vs. polarization for different possible spin-parity $J_i^\pi \rightarrow J_f^\pi$ assignments as a function of mixing ratio ( $\delta$ ) for the 244-keV $\gamma$ ray in band B3. The theoretical calculations are compared with the experimentally measured values. . . . .	130
7.10	Experimental B(M1)/B(E2) ratios (filled symbols) as a function of spin for the $\pi h_{9/2} \otimes \nu i_{13/2}$ yrast band in $^{196}\text{Tl}$ nucleus along with the neighboring odd-odd Tl isotopes. The experimental values are compared with theoretical calculation (solid line) from geometrical model for the $\pi h_{9/2} \otimes \nu i_{13/2}$ configuration in $^{196}\text{Tl}$ . .	131
7.11	Experimental B(M1)/B(E2) ratios (filled symbols) as a function of spin for the bands B2 and B3 in $^{196}\text{Tl}$ . The experimental values are compared with calculations (red solid lines) from geometrical model. . . . .	133
7.12	Aligned angular momenta ( $i_x$ ) as a function of rotational frequency ( $\hbar\omega$ ) for the $\pi h_{9/2} \otimes \nu i_{13/2}$ bands in odd-odd Tl isotopes. The Harris reference parameters are chosen to be $J_0 = 8.0 \hbar^2/\text{MeV}$ and $J_1 = 40.0 \hbar^4/\text{MeV}^3$ . . . . .	134
7.13	Comparison of kinetic moment of inertia ( $J^{(1)}$ ) as a function of spin ( $I$ ) of $\pi h_{9/2} \otimes \nu i_{13/2}$ rotational bands in odd-odd Tl isotopes. . . . .	135
7.14	Comparison of signature splitting $S(I)$ as a function of spin ( $I$ ) of $\pi h_{9/2} \otimes \nu i_{13/2}$ rotational bands in odd-odd Tl isotopes. . . . .	136
7.15	TRS calculations of $^{196}\text{Tl}$ for the ground-state band B1 near band head at $\hbar\omega = 0.11$ MeV. The contours are 250 keV apart. . . . .	137
7.16	TRS calculations of $^{196}\text{Tl}$ for the side band B2 near band head at $\hbar\omega = 0.16$ MeV. The contours are 250 keV apart. . . . .	138

7.17	TRS calculations of $^{196}\text{Tl}$ for the side band B3 near band head at $\hbar\omega = 0.16$ MeV. The contours are 250 keV apart. . . . .	139
8.1	A plot of excitation energy vs. spin for the ground state bands of the odd-A Po isotopes. The data are taken from Ref. [36]. . . . .	142
8.2	Level scheme of $^{207}\text{Po}$ obtained from the present work. . . . .	144
8.3	Coincidence $\gamma$ -spectrum corresponding to sum of single gates on 258-, 757- and 173-keV. New $\gamma$ -transitions are marked by *. . . . .	148
8.4	Coincidence spectrum generated by single gate on 244-keV. The new $\gamma$ -transitions are marked by *. . . . .	149
8.5	Coincidence spectrum generated by single gate on 347-keV. The new $\gamma$ -transitions are marked by *. . . . .	150
8.6	Coincidence spectrum of top panel (a) generated by tight gate on 467-keV and lower panel (b) by tight gate on 465-keV. . . . .	151
8.7	Coincidence spectrum of top panel (a) generated by gate on 258-keV and lower panel (b) by gate on 720-keV. . . . .	152
8.8	DCO (gated by stretched E2 transitions) and IPDCO ratios are plotted as a function of $\gamma$ -ray energy. . . . .	153
8.9	Excitation energies of $13/2^+$ , $25/2^+$ and $29/2^+$ spin-states in odd-A $^{203-209}\text{Po}$ isotopes relative to the excitation energies of the neighboring even-even core Po isotopes. . . . .	154

- 8.10 Relative level energy ( $E - E_0$ ) has been plotted as a function of  $(I - I_0)^2$ .  $E_0$  and  $I_0$  are the band-head energy and spin of band B3. The data points indicated by filled circles are from 5-qp band and the data indicated by filled squares are from 7-qp band. The solid lines are the fitting curves of the data points. . . . . 155
- 8.11 The interaction between the proton particle and neutron hole angular momenta as a function of shears angle for the 5-qp band (B3) based on  $\pi i_{13/2}^2 \otimes \nu(i_{13/2}^{-2} p_{3/2}^{-1})$  configuration, obtained from semiclassical formalism. . . . . 157

# List of Tables

1.1	Details of experiments performed using different accelerator facilities and detector arrays. . . . .	9
5.1	Calculated $R_{DCO}$ for INGA and VENUS setup. In this calculation, $\sigma/J = 0.3$ has been considered. . . . .	74
5.2	Calculated angular coefficients and $R_{DCO}$ for an E2 transition for different $\sigma/J$ values. . . . .	75
6.1	The energy ( $E_\gamma$ ) and intensity ( $I_\gamma$ ) of the $\gamma$ rays of $^{169}\text{Tm}$ along with the corresponding spin and parity of the initial ( $J_i^\pi$ ) and the final ( $J_f^\pi$ ) states and the energy of the initial state ( $E_i$ ). The measured values of $R_{DCO}$ and $\Delta_{IPDCO}$ of the corresponding $\gamma$ rays are also shown. . . . .	96
6.2	Deformation parameters $\beta_2$ , $\beta_4$ and $\gamma$ obtained from TRS calculations for the $[411]1/2^+$ band in Tm isotopes. . . . .	106
6.3	Experimental & calculated crossing frequencies ( $\omega_c$ ) and calculated interaction strengths (V) at the band crossings for the $[411]1/2^+$ band in Tm isotopes. . . .	108

- 7.1 The energy ( $E_\gamma$ ) and intensity ( $I_\gamma$ ) of the  $\gamma$  rays of  $^{196}\text{Tl}$  along with the corresponding spin and parity of the initial ( $J_i^\pi$ ) and the final ( $J_f^\pi$ ) states and the energy of the initial state ( $E_i$ ). The measured values of  $R_{DCO}$  and  $\Delta_{IPDCO}$  of the corresponding  $\gamma$  rays are also shown in the following table. . . . . 125
- 8.1 The energy ( $E_\gamma$ ) and intensity ( $I_\gamma$ ) of the  $\gamma$  rays of  $^{207}\text{Po}$  along with the corresponding spin and parity of the initial ( $J_i^\pi$ ) and the final ( $J_f^\pi$ ) states and the energy of the initial state ( $E_i$ ). The measured values of  $R_{DCO}$  and  $\Delta_{IPDCO}$  of the corresponding  $\gamma$  rays are also shown in the following table. . . . . 145

# Chapter 1

## Introduction

Nucleus is a many-body quantal system which is a fascinating laboratory to test the quantum mechanical laws and symmetries. Because of the finite size and finite number of nucleons in a nuclear system, it can have both collective as well as single particle excitations when energy is pumped into a nuclear system. The modes of excitation of a nucleus depend on, among other things, the factors like, nuclear shape and the available nucleonic orbitals near the proton and the neutron Fermi levels. The nuclei with proton and/or neutron numbers close to the spherical shell gaps at 2, 8, 20, 28, 50 and 126 (for neutron only) are mostly spherical in nature while the near mid-shell nuclei with proton and neutron numbers away from these shell closures are deformed in their ground state. For a spherical nucleus, the excited states consist of irregular sequence of levels characterizing the single particle (proton and neutron) excitations to different nucleonic orbitals, whereas, in case of a deformed nucleus, the excited states are the regular sequences of levels characteristics of collective excitation of nucleus due to rotation of a deformed quantal system. However, due to the presence of high- $j$  ( $j$  is the total angular momentum quantum number of a nucleonic state) single particle orbitals near the shell gaps may polarize a nucleus to a deformed shape due to their shape-driving effect. On the other hand, in case of a deformed nucleus, the Coriolis force of the rotation can break the

paired state of the nucleons giving rise to band-crossing in nucleus due to particle alignment. Such interplay of single particle and collective degrees of freedom not only generates interesting high-spin phenomena in nuclei but also helps to understand the nature and strength of the underlying internucleon forces.

The nuclei, situated in the mid-shell region, are deformed in their ground-state. In these nuclei, collective mode of excitation is the dominant one which is realized mainly through the nuclear rotation and vibration. In case of rotation, rotational bands are observed, which consists of regular sequence of excited states following  $E \propto I(I + 1)$  pattern, where  $E$  and  $I$  are excitation energy and spin, respectively, [32, 33, 34, 35]. Ground-state rotational bands (g-band) are built on 0-, 1- and 2-quasiparticle (qp) configurations for even-even, odd-A and odd-odd deformed nuclei, respectively. A second band with extra 2-qp (s-band) is situated at a higher excitation energy (non-yrast) for lower rotational frequency of the nucleus. With increasing rotational frequency, the energies of the excited states in s-band may be lowered with respect to the excited states in the g-band after a critical rotational frequency ( $\omega_c$ ). This phenomenon is called band crossing between the g-band and the s-band, and the  $\omega_c$  is called crossing frequency. The band crossing occurs due to the breaking of a pair of valence nucleons in time-reversed orbits by the Coriolis force. Due to this pair alignment, a gain in alignment is added to the total angular momentum of the nucleus.

In Fig. 1.1, an example of a band crossing in the even-even  $^{162}\text{Er}$  nucleus has been depicted. In this figure, the spins ( $I$ ) and the corresponding excitation energies ( $E_x$ ) are plotted for the ground state band (open circle). These points are fitted by the rotational model formula

$$E_x = \frac{\hbar^2}{2\mathcal{J}} I(I + 1) \quad (1.1)$$

In this equation,  $\mathcal{J}$  is the moment of inertia. It is not possible to fit all the experimental points by one parabola (of equation (1.1)). The parabolas that fit lower (up to spin  $10\hbar$ ) and higher

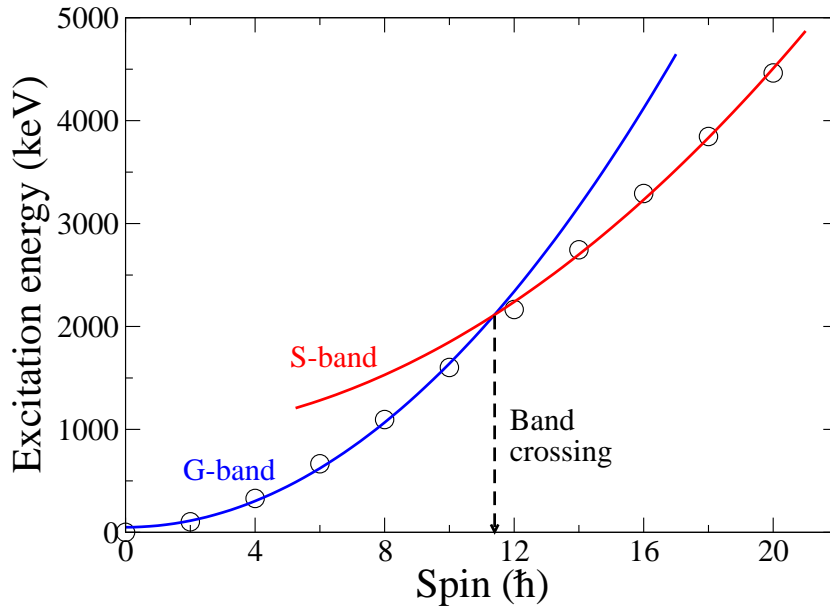


Figure 1.1: Crossing of g-band with s-band has been shown. The experimental data (open circle) of  $^{162}\text{Er}$  [35, 36] have been fitted with parabolic curves corresponding to the rotational model as given in equation (1.1). High-spin data of  $^{162}\text{Er}$  up to  $44\hbar$  of spin are available in Ref. [37].

lying points have different moment of inertia ( $\mathcal{J}$ ) corresponding to two different configurations (0- and 2-qp). The two fitted curves are extended to depict the crossing between the 0-qp and the 2-qp bands. It can also be clearly realized that the excited states in s-band become lower in energy with respect to the excited states of the same spins in g-band after the band crossing.

There are two types of band crossings observed in nuclei, back-bending and up-bending or forward bending [2, 3]. These are pictorially depicted in Fig. 1.2. In the top part of this figure, the spin vs. excitation energy are shown for the g- and the s-band. In the lower part of this figure, the spin values are plotted as a function of the rotational frequency (which is equal to  $E_\gamma/2$ , for the ground state band in even-even nuclei, where  $E_\gamma$  is the  $\gamma$ -ray energy). The band crossing can be identified prominently in such plots, as can be seen in these figures. Depending on the interaction between the ground and the s-band, the plot of spin vs. rotational frequency looks either as back-bending (smaller interaction strength) or up-bending (larger interaction strength). Therefore, it is convenient to use such type of plots to identify the band crossing

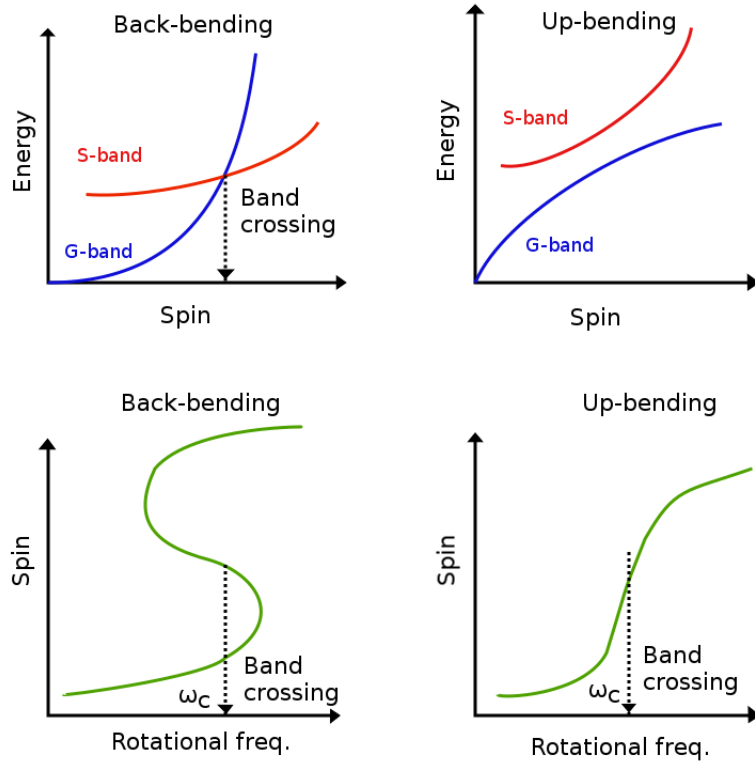


Figure 1.2: A schematic diagram illustrating the back-bending and up-bending types of band crossings due to the pair breaking of valence nucleons in time-reversed orbits.

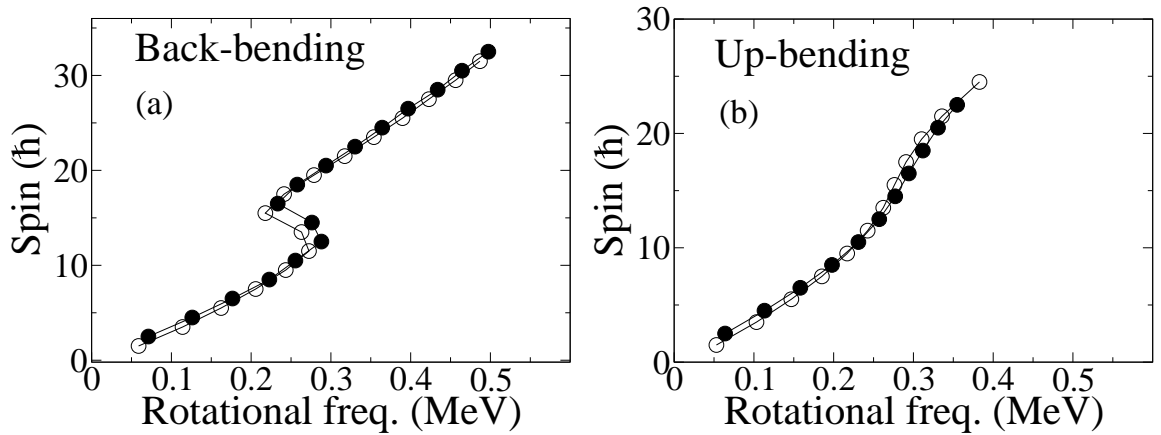


Figure 1.3: (a) Back-bending and (b) up-bending types of band crossings in the ground-state bands of  $^{165}\text{Tm}$  and  $^{167}\text{Tm}$ , respectively, as a function of rotational frequency are shown. The filled and open circles represent the signature partners of the rotational bands. Experimental data for plot (a) are taken from Ref. [2] and for plot (b), data are taken from Ref. [3].

and the nature of the band crossing. The example of two different types of band crossings are shown in Fig. 1.3. In this figure, the experimental data of spin vs. rotational frequency are shown for the two signature partner bands in  $^{165}\text{Tm}$  (left) and  $^{167}\text{Tm}$  (right). It can be seen that the data clearly indicate back-bending for  $^{165}\text{Tm}$  while up-bending for  $^{167}\text{Tm}$ , and hence a larger interaction strength between the g- and the s-bands in case of  $^{167}\text{Tm}$  than  $^{165}\text{Tm}$ .

On the other hand, the shape of the nuclei with the Fermi levels close to the spherical shell closures are near spherical. In these nuclei, single particle excitation is the dominant mode of excitation. For example, because of the proximity of the Fermi levels near the  $Z = 82$  and  $N = 126$  shell closures, the excited states in  $^{209}\text{Bi}$  ( $Z = 83$ ) [38] and  $^{209}\text{Po}$  ( $Z = 84$ ) [19] nuclei are mostly generated by the single particle excitation. The shell model calculation can reproduce the single particle excited states. In the calculation, the excited states are interpreted as the coupling of the doubly magic inert core (e.g.  $^{208}\text{Pb}$ ) with the valence particles outside the core. The excited states are also interpreted as the coupling of the odd particle or hole with the neighboring even-even core. Additional coupling with the other modes like the octupole vibration of the neighboring even-even core is also introduced to reproduce the excited states in nuclei near shell closures. For example, in  $^{207}\text{Tl}$  and  $^{207,209}\text{Pb}$  nuclei, the particle octupole vibration coupling (POVC) was introduced to explain the excited states [39]. Moreover, the proton and the neutron orbitals with  $\Delta l = 3$  and  $\Delta j = 3$ , where  $l$  and  $j$  are the orbital angular momentum and the total angular momentum quantum numbers, respectively, in close proximity induces octupole correlation in nuclei, such as in the Barium, Lanthanum, Cerium, Samarium, etc nuclei in  $A \sim 140$  region [40, 41, 42, 43, 44, 45].

Interesting features are expected for the Tl ( $Z = 81$ ) nuclei, the proton Fermi level of which is situated just below the  $Z = 82$  shell closure. Due to the large shape driving effect, the  $\Omega = 9/2$  component of the high- $j$   $\pi h_{9/2}$  orbital comes down in energy with oblate deformation and intrudes below the  $Z = 82$  shell gap. Therefore, this orbital induces deformation in the lighter odd- $A$  Tl isotopes in  $A \sim 190$  region. Indeed, rotational bands based on this  $\pi h_{9/2}$  orbital have

been observed in odd-A Tl nuclei in this region [46, 47, 48, 49, 50]. On the other hand, in case of odd-odd Tl isotopes in the same mass region, the unique positive parity  $\nu i_{13/2}$  orbital becomes available near the neutron Fermi level. This high-j orbital also has large shape driving effect. Hence, due to the combined effect of these two shape-driving orbitals, rotational bands based on the  $\pi h_{9/2} \otimes \nu i_{13/2}$  configuration, indicating induced deformation, have been observed in the odd-odd Tl isotopes [7, 8, 9, 10, 11, 13]. However, the band crossing phenomena in the odd-odd Tl isotopes are not well studied, except for a few isotopes. Moreover, because of the different possible couplings between proton and neutron orbitals, several excited states with band structures built on them are expected in the odd-odd nuclei.

Magnetic Rotation (MR) is another exotic mode of nuclear excitation, which was discovered in near spherical Pb isotopes in  $A \sim 200$  mass region [51, 52, 53] in early 1990s. The MR bands are consisted of regular sequence of enhanced  $\Delta I = 1$  magnetic dipole (M1) transitions. For these bands, the cross-over E2 transitions are extremely weak, or even unobserved, which reflects that the quadrupole collectivity and, hence, the nuclear deformation ( $\beta_2$ ) is very small. The energies ( $E$ ) and spins ( $I$ ) of the states in these bands follow the  $(E - E_0) \propto (I - I_0)^2$  rotational behaviour, where  $E_0$  and  $I_0$  are the band-head energy and spin, respectively. The reduced transition probability B(M1) of the intraband M1 transitions in MR bands is quite large ( $1 - 10 \mu_N^2$ ) compared to the normal deformed rotational bands. The B(M1) value decreases with increasing spin. The B(M1)/B(E2) ratio is generally large ( $\geq 20 \mu_N^2/e^2b^2$ ) and decreases with spin. This type of band structure is formed by the coupling of high-j particles and holes. Initially, the particle and hole angular momentum vectors are almost perpendicular at low energies near band head and then the step-by-step alignment of the particle and hole angular momenta into the direction of the total angular momentum (see Fig. 1.4) generates the angular momenta of the excited states in this band. As this resembles the closing of the blades of a pair of shears, the MR band is also called shears band. The perpendicular coupling of the particle and hole angular momenta gives minimum angular momentum which corresponds

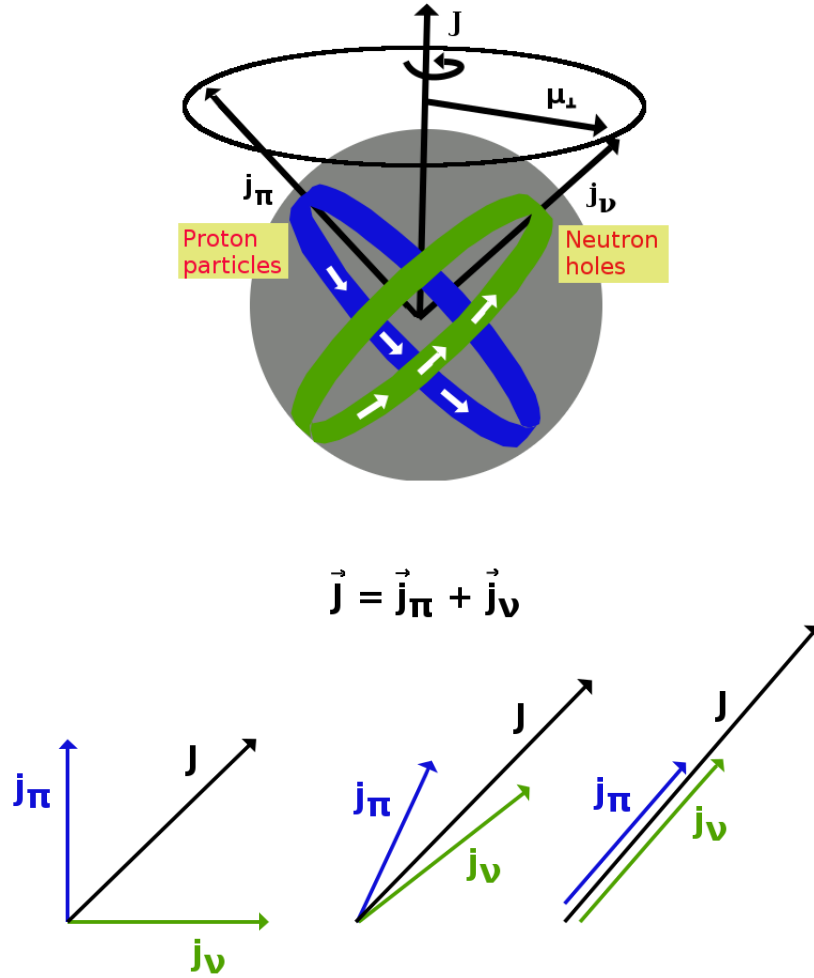


Figure 1.4: A schematic diagram illustrating the coupling between the particle and hole angular momenta for magnetic rotation.

to the band-head spin of MR band, whereas the complete alignment of the particle and hole angular momenta into the direction of the total angular momentum corresponds to the highest spin of the MR band.

In this thesis work, the excited states in  $^{169}\text{Tm}$ ,  $^{196}\text{Tl}$  and  $^{207}\text{Po}$  nuclei have been studied. In which the salient features of the above modes of nuclear excitation are expected. These nuclei are shown in the nuclear chart in Fig. 1.5. It can be seen that while odd-proton nucleus  $^{169}\text{Tm}$  is situated in the mid-shell region, the other two nuclei are close to the shell closures. In case of

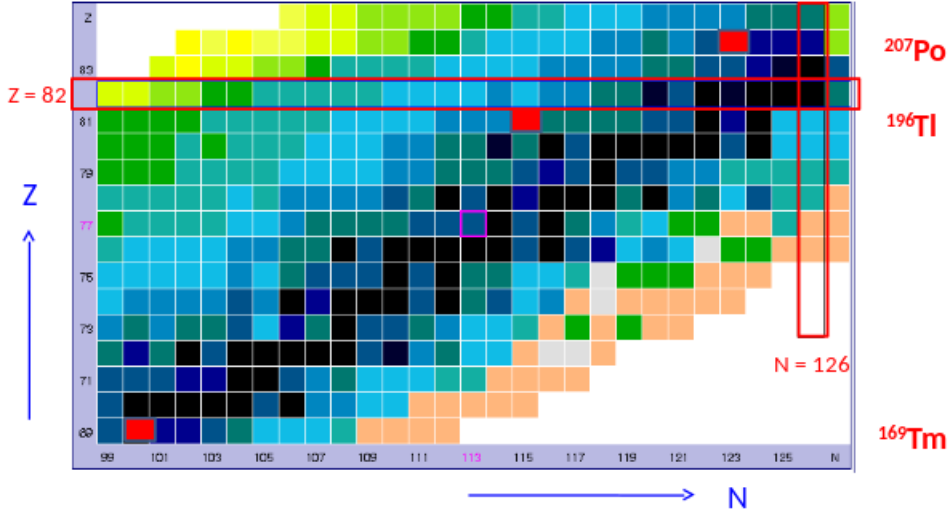


Figure 1.5: The nuclei  $^{169}\text{Tm}$ ,  $^{196}\text{Tl}$  and  $^{207}\text{Po}$  studied in this thesis work are shown in red boxes in nuclear chart. Basic diagram of this figure is taken from Ref. [54].

odd-neutron nucleus,  $^{207}\text{Po}$ , the proton and neutron numbers are close to the heaviest known proton and neutron magic numbers  $Z = 82$  and  $N = 126$ . On the other hand, in case of odd-odd  $^{196}\text{Tl}$ , the proton number is close to the  $Z = 82$  shell closure but the neutron number is near mid-shell.

In order to study the structural phenomena in these nuclei, the gamma-ray spectroscopic method has been employed. The high-spin states in  $^{196}\text{Tl}$  and  $^{207}\text{Po}$  nuclei have been populated by fusion-evaporation reactions and the high-spin states in  $^{169}\text{Tm}$  have been generated by inelastic excitation. The decaying  $\gamma$  rays from the excited states are detected by using the gamma-detector array comprising of a number of Compton-suppressed clover HPGe (High Purity Germanium) detectors. In case of  $^{169}\text{Tm}$  and  $^{196}\text{Tl}$  experiments, INGA (Indian National Gamma Array) at TIFR was used. For  $^{207}\text{Po}$  experiment, VENUS (VECC array for NUclear Spectroscopy) at VECC was used. The details about the experiments and the setup used in this work have been shown in Table 1.1. In addition to the gamma-ray spectroscopic work, the Monte Carlo GEANT4 simulation of the detectors used in this work and of the VENUS array have been performed for in-depth understanding of their response.

Table 1.1: Details of experiments performed using different accelerator facilities and detector arrays.

<b>Nucleus studied</b>	<b>Accelerator used</b>	<b>Reaction used</b>	<b>Beam energy</b>	<b>Detector array used</b>
$^{169}\text{Tm}$	14-UD BARC-TIFR Pelletron Facility, Mumbai	$^{169}\text{Tm}(^{32}\text{S}, ^{32}\text{S}')^{169}\text{Tm}^*$	164 MeV	INGA with 19 Clovers with ACS
$^{196}\text{Tl}$		$^{185,187}\text{Re}(^{13}\text{C}, \text{xn})^{196}\text{Tl}$ (x = 2 & 4)	75 MeV	INGA with 15 Clovers with ACS
$^{207}\text{Po}$	K-130 Cyclotron at VECC, Kolkata	$^{208}\text{Pb}(\alpha, 5\text{n})^{207}\text{Po}$	60 MeV	VENUS with 6 Clovers with ACS

The present thesis has been organized in the following way: After a short introduction in this chapter, the nuclear models, relevant to the present thesis work, have been described briefly in the 2<sup>nd</sup> chapter. The experimental techniques have been discussed in the 3<sup>rd</sup> chapter. GEANT4 simulation of the HPGe single-crystal, clover and VENUS array has been described in the 4<sup>th</sup> chapter. The analysis of the experimental data has been discussed in the 5<sup>th</sup> chapter. The experimental results for  $^{169}\text{Tm}$ ,  $^{196}\text{Tl}$  and  $^{207}\text{Po}$  nuclei and the interpretation of the results have been discussed in the 6<sup>th</sup>, 7<sup>th</sup> and 8<sup>th</sup> chapters, respectively. Finally, summary and future outlook have been presented in the 9<sup>th</sup> chapter.

# Chapter 2

## Nuclear Models

In order to understand the experimentally observed properties of an atomic nucleus, it is necessary to know about the short-range strong nucleon-nucleon interaction inside the nucleus. The exact mathematical form of this type of interaction is still unknown. The various proposed theories do not give full explanation of the different properties of a nucleus. Even if exact nature of the nucleon-nucleon interaction were known, it would have been extremely difficult to solve the Schrodinger equation for the nuclei which are made up of a large number of proton and neutron, because in this case the nuclei will behave as a complicated many-body system. Due to these difficulties, various nuclear models have been proposed for the nucleus. Each of these models can explain some of the nuclear properties. In this chapter, a few of the nuclear models are briefly discussed.

### 2.1 Liquid drop model

Liquid drop model was first proposed by N. Bohr and F. Kalckar in 1937 [55]. Development of the model was based on the experimentally observed macroscopic properties of nucleus, e.g.,

the constant density of nuclear matter, constant binding energy per nucleon, i.e. saturation property of nuclear force and incompressibility which are analogous to some properties of a liquid drop. This model is able to describe some bulk properties of nuclei like binding energy, vibration, rotation and some phenomena of nuclear fission. Later, C.F. von Weizsäcker and H.A. Bethe applied this model to develop a semi-empirical formula [56, 57] for the nuclear binding energy (or nuclear mass) which is given by

$$B.E(A, Z) = a_v A - a_s A^{\frac{2}{3}} - a_c \frac{Z(Z-1)}{A^{\frac{1}{3}}} - a_{asym} \frac{(N-Z)^2}{A} + \delta_p \quad (2.1)$$

where the parameters can be obtained by fitting the experimental data [58]. The values of the parameters are given below.

$a_v = 15.68$  MeV;  $a_s = 18.56$  MeV;  $a_c = 0.717$  MeV;  $a_{asym} = 28.1$  MeV. The pairing energy term  $\delta_p$ , which depends on A only, is given by

$$\begin{aligned} \delta_p &= 34. A^{-\frac{3}{4}} \text{ MeV for even-even nuclei} \\ &= 0 \text{ MeV for even-odd nuclei} \\ &= -34. A^{-\frac{3}{4}} \text{ MeV for odd-odd nuclei} \end{aligned}$$

where N, Z and A are neutron number, proton number and atomic mass number of a nucleus, respectively. In the above formula the first term is the volume energy term which is proportional to the volume, second term is the surface energy which is proportional to the surface area, third term arises due to Coulombic repulsion among the protons, fourth term is due to the asymmetry in neutron and proton numbers and the fifth term is the pairing energy, arises due the pairing effect of protons and neutrons separately.

The above semi-empirical mass formula can reproduce experimental binding energy quite well. Although this model is successful in describing some of the macroscopic properties like binding energies, nucleon separation energies, magnetic moments etc., it fails to explain the sudden change (jump) in those parameters at some specific nucleon numbers like 2, 8, 20, 28, 50, 82 and 126. These nucleon numbers are called magic numbers and the nuclei whose proton and/or neutron number equal to magic number are called magic nuclei. The magic nuclei show extra stability which can not be explained by the liquid drop model. The effect of these magic numbers in nuclear properties can be well explained by another nuclear model called shell model.

## 2.2 Shell model

Shell model provides nuclear shell structure with proper shell gaps at nucleon numbers equals to 2, 8, 20, 28, 50, 82 and 126. These are called magic numbers. Therefore, the nuclei with nucleon numbers equal to the magic numbers show extra stability. The model also predicts nuclear spin, parity, magnetic moment and energy level. In this model, each nucleon of a nucleus is assumed to move independently in an average potential created by all the nucleons of the nucleus. If the short range interaction between two nucleons,  $i$  and  $j$ , is  $v(r_{ij})$ , then the average potential acting on each nucleon is

$$V(r_i) = \left\langle \sum_j v(r_{ij}) \right\rangle \quad (2.2)$$

The corresponding Hamiltonian is

$$\begin{aligned} H &= \sum_i T_i + \sum_{ij} v(r_{ij}) \\ &= \sum_i \left[ T_i + V(r_i) \right] + \sum_{ij} \left[ v(r_{ij}) - V(r_i) \right] \end{aligned} \quad (2.3)$$

where  $V_{res} = \sum_{ij} \left[ v(r_{ij}) - V(r_i) \right]$  is the residual interaction between nucleons. For extreme single particle shell model, this term is neglected. However, exact mathematical form of nuclear potential is still unknown. Various phenomenological potentials are used as the average potential. For spherical harmonic oscillator potential as given by

$$V(r) = \frac{1}{2}m\omega_0^2(r^2 - R^2) \quad (2.4)$$

the energy levels are given by

$$\epsilon_N = \left( N + \frac{3}{2} \right) \hbar\omega_0 \quad (2.5)$$

with

$$N = 2(n - 1) + l, \text{ where } n = 1, 2, 3, \dots \text{ and } l = 0, 1, 2, \dots \quad (2.6)$$

Each level is  $\frac{1}{2}(N + 1)(N + 2)$ -fold degenerate. Here,  $N = 2(n - 1) + l$  is the oscillator quantum number,  $n$  is the radial quantum number,  $l$  is the orbital quantum number and  $\omega_0$  is the oscillator frequency. In the present thesis work, Woods-Saxon potential has been used as the average potential which is given by

$$V(r) = -\frac{V_0}{1 + \exp[(r - R)/a]} \quad (2.7)$$

where  $R \approx r_0 A^{1/3}$  with  $r_0 \approx 1.2$  fm is nuclear radius,  $V_0 \approx 50$  MeV is depth of the potential and  $a \approx 0.5$  fm is the skin thickness parameter.

However, the calculated nucleonic shell structure can not reproduce the experimentally observed magic numbers. Later, Mayer [59] and independently Haxel, Jensen and Sues [60] suggested to include a spin-orbit interaction term  $V_{so}(r)\vec{l}\cdot\vec{s}$  to the central potential. This reproduced successfully the experimentally observed magic numbers. The term  $\vec{l}\cdot\vec{s}$  causes the reordering of

the nucleonic levels. The expectation value of  $\vec{l} \cdot \vec{s}$  is given by

$$\langle \vec{l} \cdot \vec{s} \rangle = \frac{1}{2} [j(j+1) - l(l+1) - s(s+1)] \hbar^2 \quad (2.8)$$

$\vec{j} = \vec{l} + \vec{s}$  is the angular momentum for a nucleon. Therefore, the possible values of  $j$  are  $j = l + \frac{1}{2}$  or  $j = l - \frac{1}{2}$ . Due to the inclusion of  $\vec{l} \cdot \vec{s}$  term to potential, each single-particle level splits into two levels. Now the splitting energy is given by

$$\Delta E = \langle V_{so} \rangle \left[ \langle \vec{l} \cdot \vec{s} \rangle_{j=l+1/2} - \langle \vec{l} \cdot \vec{s} \rangle_{j=l-1/2} \right] = \frac{1}{2} \langle V_{so} \rangle (2l+1) \hbar^2 \quad (2.9)$$

$$\Delta E \propto (2l+1) \quad (2.10)$$

From equation (2.9) it is seen that for an attractive spin-orbit potential (negative value of  $V_{so}$ ) the  $l + \frac{1}{2}$  levels are energetically always below the  $l - \frac{1}{2}$  levels which is consistent with experimental observations. The equation (2.10) shows that the splitting increases with increasing values of  $l$ .

## 2.3 Collective model

The collective model, based on the concept of the collective coherent motion of all the nucleons of a nucleus, was developed by A. Bohr and B. Motelsson [61]. The liquid drop model provides static nuclear properties. However, by including rotation and vibration to the liquid drop model, dynamical properties can be incorporated into a nucleus. In case of dynamical shape and surface oscillations, the radius vector of the deformed nucleus is given by

$$R(\theta, \phi) = R_0 \left[ 1 + \sum_{\lambda=0}^{\infty} \sum_{\mu=-\lambda}^{\lambda} \alpha_{\lambda\mu}^* Y_{\lambda\mu}(\theta, \phi) \right] \quad (2.11)$$

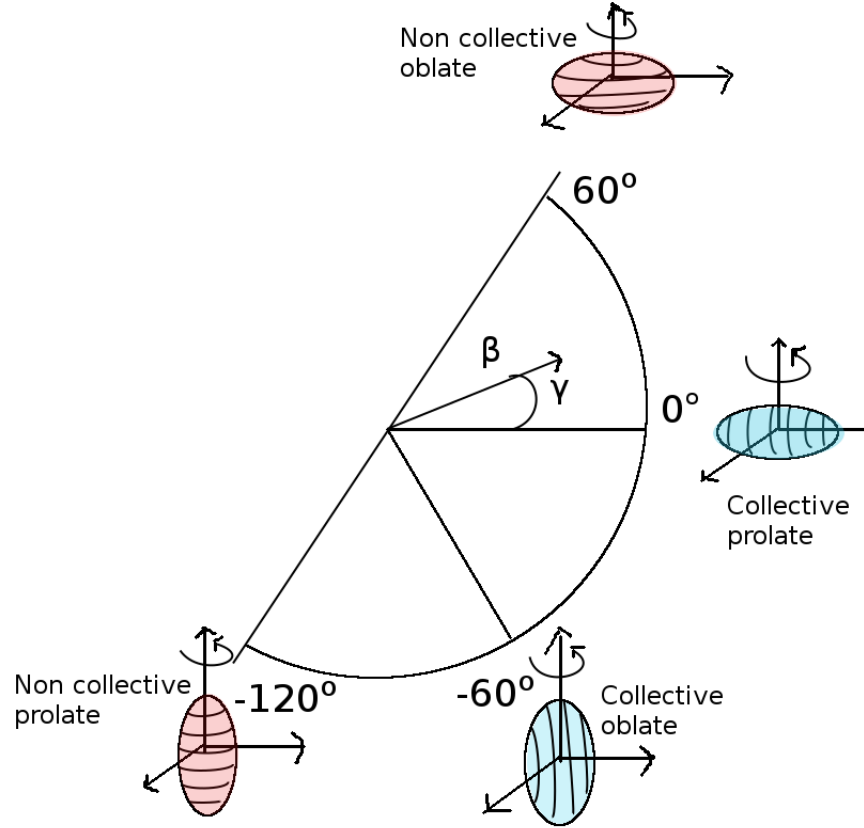


Figure 2.1: Various nuclear shapes in  $(\beta_2 - \gamma)$  plane using Lund convention [62].

where  $R_0$  is the radius of the average spherical shape of nucleus and  $Y_{\lambda\mu}(\theta, \phi)$  are the spherical harmonic functions.  $\alpha_{\lambda\mu}^*$  are the parameters which act as surface coordinates describing the shape of the nuclear surface.  $\lambda$  is the multipolarity corresponding to the different modes of shape vibrations and  $\mu$  is the projection of  $\lambda$ . As  $R(\theta, \phi)$  is invariant under reflection and rotation of the coordinate system, the following property has to be satisfied

$$Y_{\lambda\mu}^* = (-1)^\mu Y_{\lambda-\mu} \quad (2.12)$$

From eq.(2.12), we get

$$\alpha_{\lambda\mu}^* = (-1)^\mu \alpha_{\lambda-\mu} \quad (2.13)$$

The monopole ( $\lambda = 0$ ) term in eq.(2.11) can be neglected because of the incompressibility of nuclear matter. The dipole ( $\lambda = 1$ ) term in eq.(2.11) gives net displacement of the centre of mass of a nucleus and therefore, it does not depend on the action of internal nuclear forces. So, the dipole ( $\lambda = 1$ ) term can also be neglected because of the translational symmetry. Therefore, the quadrupole ( $\lambda = 2$ ) term can be considered as the next lowest mode. In case of quadrupole deformations ( $\lambda = 2$ ), there are five parameters  $\alpha_{\lambda\mu}$  involved. Out of these five parameters, only three parameters are related to the orientation of the nucleus in space and corresponds to three Euler angles. By coinciding the axes of body-fixed system with the principal axes of the mass distribution of the nucleus through proper transformation, the five parameters of  $\alpha_{2\mu}$  reduces to two real independent parameters  $a_{20}$  and  $a_{22} = a_{2-2}$  ( $a_{21} = a_{2-1} = 0$ ). These two parameters can be expressed in terms of so-called Hill-Wheeler [63] coordinates  $\beta_2$  and  $\gamma$  as

$$a_{20} = \beta_2 \cos \gamma \quad (2.14)$$

$$a_{22} = \frac{1}{\sqrt{2}}\beta_2 \sin \gamma \quad (2.15)$$

From eq<sup>n</sup>'s (2.14) and (2.15), we get

$$\sum_{\mu} |\alpha_{2\mu}|^2 = a_{20}^2 + 2a_{22}^2 = \beta_2^2 \quad (2.16)$$

$$R(\theta, \phi) = R_0 \left[ 1 + \beta_2 \sqrt{\frac{5}{16\pi}} (\cos \gamma (3 \cos^2 \theta - 1) + \sqrt{3} \sin \gamma \cos^2 \theta \cos 2\phi) \right] \quad (2.17)$$

The parameters  $\beta_2$  and  $\gamma$  represent the degree of deformation and axial asymmetry, respectively. The increments of the three semi-axes along the  $x$ -,  $y$ - and  $z$ -axes in the body-fixed frame

are given by

$$\delta R_x = R\left(\frac{\pi}{2}, 0\right) - R_0 = R_0 \frac{5}{4\pi} \beta_2 \cos\left(\gamma - \frac{2\pi}{3}\right) \quad (2.18)$$

$$\delta R_y = R\left(\frac{\pi}{2}, \frac{\pi}{2}\right) - R_0 = R_0 \frac{5}{4\pi} \beta_2 \cos\left(\gamma + \frac{2\pi}{3}\right) \quad (2.19)$$

$$\delta R_z = R(0, 0) - R_0 = R_0 \frac{5}{4\pi} \beta_2 \cos \gamma \quad (2.20)$$

For  $\gamma = 0^\circ$  and  $\pm 120^\circ$ , nuclear shape becomes prolate whereas for  $\gamma = \pm 60^\circ$  and  $180^\circ$  nuclear shape is oblate. When  $\gamma$  is not multiple of  $60^\circ$ , nuclear shape corresponds to triaxial shape. Only  $\gamma = 0^\circ$  and  $-60^\circ$  corresponds to collective prolate and oblate shapes, respectively. For quadrupole deformed nucleus, two distinct axially symmetric shapes, prolate and oblate, are possible for different orientations in space. The different nuclear shapes corresponding to the quadrupole deformation in the  $\beta_2 - \gamma$  plane using Lund convention [62] are shown in Fig. 2.1.

## 2.4 Nilsson model

For deformed nucleus, the nuclear potential can be approximated with the anisotropic harmonic oscillator as

$$V = \frac{1}{2}m (\omega_x^2 x^2 + \omega_y^2 y^2 + \omega_z^2 z^2) \quad (2.21)$$

where  $\omega_x$ ,  $\omega_y$  and  $\omega_z$  are the oscillator frequencies along the  $x$ -,  $y$ - and  $z$ - axes, respectively. Though, the deformation changes shape of the potential from spherical to deformed, it is assumed that the volume remains independent of the deformation. Therefore, from the volume conservation, we get

$$\omega_x \omega_y \omega_z = \text{constant} = \tilde{\omega}_0^3 \quad (2.22)$$

where  $\tilde{\omega}_0$  is the oscillator frequency for the spherical potential. For axially deformed nucleus about  $z$ -axis, where  $z$ -axis is the symmetry axis of the nucleus, the oscillator frequencies will

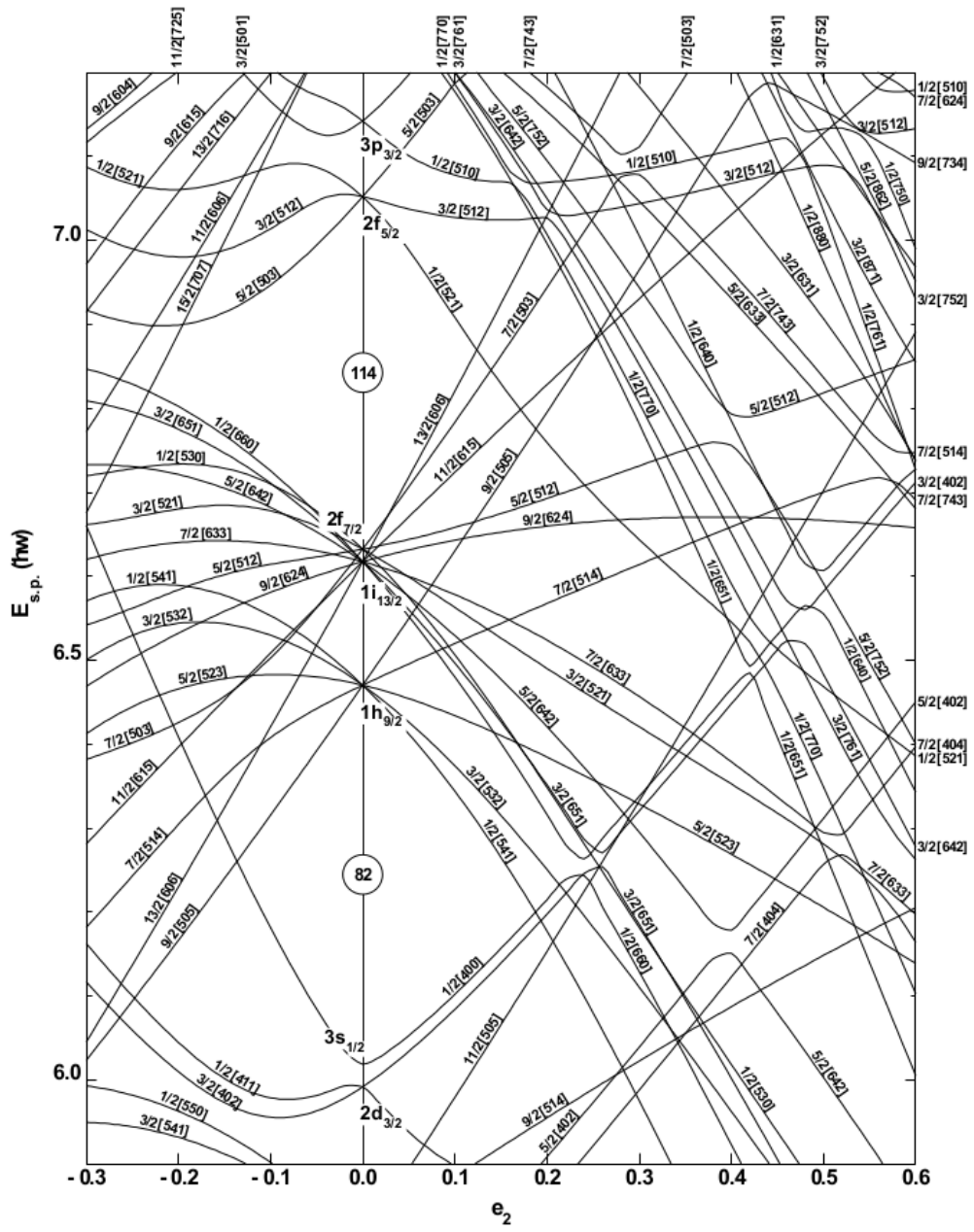


Figure 2.2: Nilsson diagram of single particle states for proton ( $Z \geq 82$ ) as a function of deformation  $e_2$  ( $e_2 = \delta$ )[64].



be transformed as

$$\omega_x = \omega_y = \omega_\perp = \omega_0(\delta) \sqrt{1 + \frac{2}{3}\delta} \quad (2.23)$$

$$\omega_z = \omega_0(\delta) \sqrt{1 - \frac{4}{3}\delta} \quad (2.24)$$

$$\omega_\perp^2 \omega_z = \tilde{\omega}_0^3 \quad (2.25)$$

where  $\delta$  is the deformation parameter.  $\omega_\perp$  and  $\omega_z$  represent the oscillator frequencies of the deformed potential, in the perpendicular and parallel directions to the symmetry axis, respectively. Using the above equations, the relation between  $\tilde{\omega}_0$  and  $\omega_0(\delta)$  is given by

$$\omega_0(\delta) = \tilde{\omega}_0 \left( 1 + \frac{2}{3}\delta^2 \right) \quad (2.26)$$

Again, the deformation parameter  $\delta$  is related to the other deformation parameter,  $\beta_2$  as

$$\delta \approx \frac{3}{2} \sqrt{\frac{5}{4\pi}} \beta_2 \approx 0.95 \beta_2 \quad (2.27)$$

Therefore, the corresponding single-particle Hamiltonian for the axially deformed nucleus can be written as

$$H = \frac{p^2}{2m} + \frac{1}{2}m [\omega_\perp^2(x^2 + y^2) + \omega_z^2 z^2] \quad (2.28)$$

The eigenstates of the Hamiltonian are characterized by the quantum numbers  $n_\perp = n_x + n_y$ ,  $n_z$  and the eigenvalues are given by

$$\epsilon(n_\perp n_z) = (n_\perp + 1)\hbar\omega_\perp + (n_z + \frac{1}{2})\hbar\omega_z \quad (2.29)$$

In order to reproduce the correct nucleonic shell structure, Nilsson added additional terms proportional to  $\vec{l} \cdot \vec{s}$  and  $l^2$  to the anisotropic harmonic oscillator potential [65, 66]. The resulting potential is called modified harmonic oscillator or Nilsson potential. The corresponding Nilsson

Hamiltonian can be written as

$$H = \frac{p^2}{2m} + \frac{1}{2}m [\omega_{\perp}^2(x^2 + y^2) + \omega_z^2 z^2] - \kappa \hbar \tilde{\omega}_0 [2\vec{l} \cdot \vec{s} + \mu(l^2 - \langle l^2 \rangle_N)] \quad (2.30)$$

where  $\kappa$  and  $\mu$  are adjustable coupling parameters. The values of these parameters can be obtained by fitting the experimental data.  $\langle l^2 \rangle_N = \frac{1}{2}N(N+3)$ , where  $N = n_{\perp} + n_z$  is the total oscillator quantum number. The term  $\langle l^2 \rangle_N$  is a constant for each oscillator shell. Due to this term in the Hamiltonian the average energy difference between shells is not affected by the  $l^2$  term.

Nilsson introduced a deformation-dependent oscillator length  $b = \sqrt{\frac{\hbar}{m\omega_0(\delta)}}$  and dimensionless coordinate  $r' = r/b$ . In the new coordinate, the Hamiltonian in eq. (2.30) transforms to

$$H = \hbar\omega_0(\delta) \left[ -\frac{1}{2}\Delta' + \frac{1}{2}r'^2 - \beta_2 r'^2 Y_{20} \right] - \kappa \hbar \tilde{\omega}_0 [2\vec{l} \cdot \vec{s} + \mu(l^2 - \langle l^2 \rangle_N)] \quad (2.31)$$

Plots of single-particle energy levels versus a deformation parameter are generally called Nilsson diagram. Nilsson diagrams corresponding to proton and neutron are shown in Fig. 2.2 and Fig. 2.3, respectively. Each single-particle energy level is labeled by the asymptotic quantum numbers  $[Nn_z\Lambda]\Omega^{\pi}$  where  $\Omega = \Lambda + \Sigma$ .  $N = n_{\perp} + n_z$  is the total oscillator quantum number.  $\Lambda$ ,  $\Sigma$  and  $\Omega$  are the projected angular momenta of the orbital angular momentum  $l$ , the spin  $s$  and the single-particle total angular momentum  $j$  along the symmetry axis of a nucleus, respectively, which are shown in Fig. 2.4. This model provides a description of single-particle motion in a deformed potential and successfully interprets the effect of deformation on the single-particle orbitals.

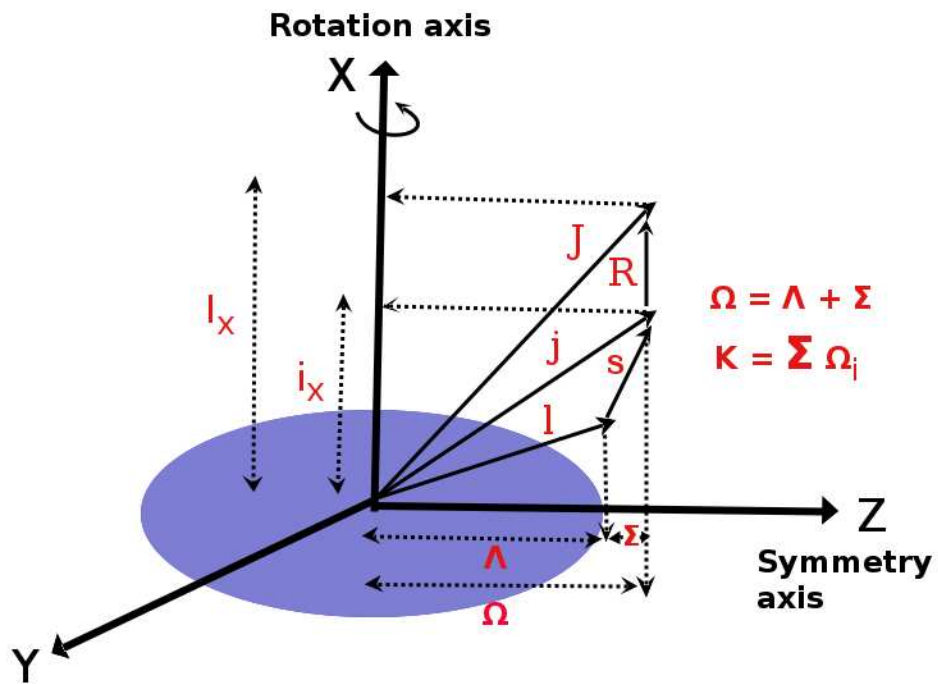


Figure 2.4: Asymptotic quantum numbers  $\Lambda$ ,  $\Sigma$  and  $\Omega$  for the Nilsson model are shown.

## 2.5 Strutinsky Shell correction

Nuclear binding energy can be obtained using liquid drop model as a function of mass number. The calculated binding energy per nucleon varies smoothly with mass number. However, experimental binding energy as a function of mass number shows oscillatory behavior about the smoothly varying liquid drop energy ( $E_{LDM}$ ). According to shell model, nucleonic levels are not uniformly distributed. These levels form a number of shells (groups of closely spaced levels). The oscillation part ( $E_{osc}$ ) arises due to grouping of levels into bunches (shells) and the oscillations show maxima at the shell closures, i.e., at the magic numbers. Therefore, total energy  $E$  of a nucleus can be calculated by adding the smooth part  $E_{LDM}$  from liquid drop model with the oscillatory part  $E_{osc}$  from shell model as

$$E = E_{LDM} + E_{osc} \quad (2.32)$$

The binding energies oscillate according to the shell distribution around an average nucleonic level density. The average level density is responsible for the average behavior of the nuclear binding energy. However, the calculation of this average part of the binding energy in the frame work of shell model does not provide correct value. Therefore, according to Strutinsky prescription [67, 68], the average part and the oscillating part are calculated from the liquid drop model and the shell model, respectively. In order to calculate  $E_{osc}$  part, the shell model energy  $E_{sh}$  is divided into an oscillatory part  $E_{osc}$  and smoothly varying part  $\tilde{E}_{sh}$  as

$$E_{sh} = \sum_{i=1}^A \epsilon_i = E_{osc} + \tilde{E}_{sh} \quad (2.33)$$

where,  $\epsilon_i$  is the energy of the  $i^{th}$  nucleonic level. To calculate  $E_{sh}$ , it is useful to introduce nucleonic level density function,  $g(\epsilon)$ .  $g(\epsilon)d\epsilon$  represents number of nucleonic levels in the energy

interval between  $\epsilon$  to  $d\epsilon$ . In the shell model, level density  $g(\epsilon)$  is written as

$$g(\epsilon) = \sum_i \delta(\epsilon - \epsilon_i) \quad (2.34)$$

If we know  $g(\epsilon)$ , particle number can be calculated by the following relation

$$A = \int_{-\infty}^{\lambda} g(\epsilon) d\epsilon \quad (2.35)$$

where,  $\lambda$  is the Fermi energy and it can be arbitrarily chosen to be between the last filled and the first unfilled level. Now, the shell model energy can be calculated as

$$E_{sh} = \int_{-\infty}^{\lambda} \epsilon g(\epsilon) d\epsilon \quad (2.36)$$

Now, the smooth part of the shell model energy ( $\tilde{E}_{sh}$ ) can be calculated by introducing the continuous function of nucleonic level density  $\tilde{g}(\epsilon)$  which is the smooth part of  $g(\epsilon)$ . The Fermi energy ( $\tilde{\lambda}$ ) corresponding to the smooth part can be calculated as

$$A = \int_{-\infty}^{\tilde{\lambda}} \tilde{g}(\epsilon) d\epsilon \quad (2.37)$$

Therefore, the smooth part of the shell model energy  $\tilde{E}_{sh}$  can be calculated as

$$\tilde{E}_{sh} = \int_{-\infty}^{\tilde{\lambda}} \epsilon \tilde{g}(\epsilon) d\epsilon \quad (2.38)$$

Therefore, the total energy of a nucleus is given by

$$E = E_{LDM} + E_{osc} = E_{LDM} + (E_{sh} - \tilde{E}_{sh}) \quad (2.39)$$

Due to the additional term  $E_{osc}$  in the equation(2.39), in some region of the periodic table the Strutinski averaged energy,  $E$ , has its minimum at a certain value of deformation.

## 2.6 Cranked Shell model

The Nilsson model describes the dependence of the single-particle states on the deformation of a deformed nucleus. In addition to that, in Cranked shell model, a rotation is imposed on a nuclear potential around an axis (conventionally  $x$ -axis) perpendicular to the symmetry axis ( $z$ ) at a fixed rotational frequency  $\omega$ . The Cranked shell model was introduced by Inglis [69, 70] in a semiclassical way. This model provides a microscopic description of the influence of rotation on single-particle motion. The model is very successful in describing the rotational band structures of the rotating nuclei.

The total Hamiltonian of a rotating nucleus in the Cranking model is given by

$$H^\omega = \sum_{i=1}^A h_i^\omega = \sum_{i=1}^A [h_i^0 - \omega j_{ix}] \quad (2.40)$$

where,  $h_i^\omega = h_i^0 - \omega j_{ix}$  is the single particle Hamiltonian in the rotating frame,  $h_i^0$  is the single particle Hamiltonian in the laboratory frame and  $j_{ix}$  is the single particle angular momentum projected onto the rotation axis.  $\omega j_{ix}$  is analogous to Coriolis and centrifugal forces in the rotating frame. The single particle Routhian (energy in the rotating frame of reference) can be obtained by solving the following eigenvalue equation:

$$h^\omega | i^\omega \rangle = e_i^\omega | i^\omega \rangle \quad (2.41)$$

where  $| i^\omega \rangle$  is the single particle eigenfunction in the rotating frame. Therefore, the single particle energy in the laboratory frame is given by

$$\begin{aligned} e_i &= \langle i^\omega | h_i^0 | i^\omega \rangle \\ &= e_i^\omega + \omega \langle i^\omega | j_{ix} | i^\omega \rangle \end{aligned} \quad (2.42)$$

Total energy in the laboratory frame can be obtained as

$$E = \sum_{i=1}^A e_i = \sum_{i=1}^A [e_i^\omega + \omega \langle i^\omega | j_{ix} | i^\omega \rangle] \quad (2.43)$$

Total projection of the nuclear angular momentum on the rotation axis is obtained by

$$I_x = \sum_{i=1}^A \langle i^\omega | j_{ix} | i^\omega \rangle \quad (2.44)$$

Particle aligned angular momentum ( $i_x$ ) is obtained by the slope of the single particle Routhian ( $e_i^\omega$ ) as

$$i_x = \frac{de_i^\omega}{d\omega} = -\langle i^\omega | j_{ix} | i^\omega \rangle \quad (2.45)$$

The time reversal symmetry ( $\pm\Omega$ ) of the Nilsson single particle levels is broken by the incorporation of the Coriolis term ( $\omega j_x$ ) in the cranked Hamiltonian of a rotating nucleus. The two-fold degeneracy is shifted and each level splits into two single particle levels. The cranked Hamiltonian is invariant under the rotation of  $180^\circ$  about the rotation axis, i.e., the two levels belong to eigenstates of the operator  $\mathcal{R}_x$  as

$$\mathcal{R}_x \Psi = e^{-i\pi J_x} \Psi = r \Psi \quad (2.46)$$

with the eigenvalues  $r = e^{-i\pi\alpha}$  where  $\alpha$  is the signature quantum number [71]. This is a good quantum number for rotating nucleus. For even-A nuclei,  $\alpha = 0/1$  and for odd-A nuclei,

$\alpha = \pm\frac{1}{2}$ . It is related to the spin ( $J$ ) of a nuclear level as

$$J = 0, 2, 4, \dots \text{ for } \alpha = 0, r = +1$$

$$J = 1, 3, 5, \dots \text{ for } \alpha = 1, r = -1$$

$$J = 1/2, 5/2, 9/2, \dots \text{ for } \alpha = 1/2, r = -i$$

$$J = 3/2, 7/2, 11/2, \dots \text{ for } \alpha = -1/2, r = +i$$

The splitting of the  $\alpha = 0/1, \pm\frac{1}{2}$  states form two distinct signature partner bands. The favoured and unfavoured signature for a state based on a single-particle orbital corresponding to an odd particle of spin  $j$  is defined as

$$\alpha_f = \frac{1}{2}(-1)^{j-\frac{1}{2}} \quad (2.47)$$

$$\alpha_u = \frac{1}{2}(-1)^{j+\frac{1}{2}} \quad (2.48)$$

For multi-quasi-particle state, favoured signature is defined as

$$\alpha_f = \frac{1}{2} \sum_i (-1)^{j_i - \frac{1}{2}} \quad (2.49)$$

## 2.7 Total Routhian Surface (TRS) calculations

In order to get the quantitative idea about the shape of a nucleus in a particular configuration, Total Routhian Surface (TRS) calculations were performed in the present thesis work. The TRS code of Nazarewicz et al. [72, 73] was used for the calculations. In these calculations, the single-particle energies have been calculated using the following deformed Woods-Saxon

potential

$$V(\vec{r}, \hat{\beta}) = \frac{V_0}{1 + \exp[\text{dist}_\Sigma(\vec{r}, \hat{\beta})/a]} \quad (2.50)$$

where  $\text{dist}_\Sigma(\vec{r}, \hat{\beta})$  is the distance of a point  $\vec{r}$  from the nuclear surface and  $\hat{\beta}$  denotes the set of all deformation parameters. The total Routhian  $E^\omega(Z, N; \hat{\beta})$  of a nucleus is given by

$$E^\omega(Z, N; \hat{\beta}) = E_{LD}^\omega(Z, N; \hat{\beta}) + E_{shell}^\omega(Z, N; \hat{\beta}) + E_{pair}^\omega(Z, N; \hat{\beta}) \quad (2.51)$$

where  $E_{LD}^\omega(Z, N; \hat{\beta})$  is the liquid drop model energy,  $E_{shell}^\omega(Z, N; \hat{\beta})$  is the shell correction energy calculated using Strutinsky shell correction approach and  $E_{pair}^\omega(Z, N; \hat{\beta})$  is the pairing correction energy within the cranking Hartee-Fock-Bogoliubov approach. The TRSs were calculated in the  $\beta_2 - \gamma$  deformation mesh points, with minimization in the hexadecapole deformation  $\beta_4$ , at different rotational frequencies  $\hbar\omega$ , where  $\beta_2$  and  $\gamma$  are the quadrupole deformation parameters. The procedure has been outlined in Refs. [74, 75]. The minima of the contour plots give the nuclear deformation in terms of  $\beta$  and  $\gamma$ . The convention of  $\gamma = 0^\circ$  corresponding to prolate shape and  $\gamma = -60^\circ$  to oblate shape has been used.  $\gamma = \pm 30^\circ$  corresponds to maximum triaxiality.

# Chapter 3

## Experimental Technique

In this chapter, the nuclear reaction mechanisms, experimental methods and the detector setup that have been used to populate and to study the nuclei of interest have been discussed.

### 3.1 Generation of High Spin Nuclear States

In order to investigate the rich variety of the nuclear structural phenomena, it is required to populate the nuclei under extreme conditions such as high excitation energy and high angular momentum. To achieve this condition, the fusion evaporation reaction is the most commonly used reaction. However, other reactions, like inelastic excitation, are also used in some cases. In this thesis work, both the heavy-ion and the light-ion induced fusion evaporation reactions as well as inelastic excitations have been used to populate the excited states in the nuclei of interest.

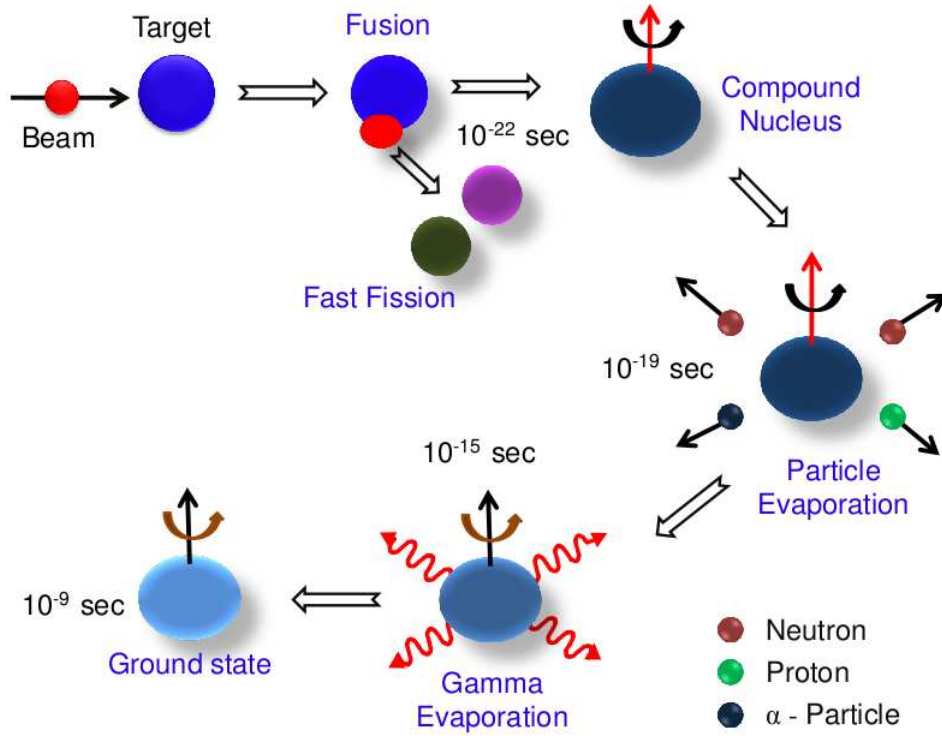


Figure 3.1: Schematic diagram of fusion evaporation reaction. This figure is taken from Ref. [77].

### 3.1.1 Fusion evaporation reaction

Among the different types of nuclear reactions, the fusion evaporation reaction is the most important one which can populate the high spin states in the residual nuclei with relatively large cross-sections. When an accelerated projectile nucleus having an energy greater than the Coulomb energy between the target and the projectile nuclei, collides, the projectile and target nuclei interact and fuse together. After thermodynamic equilibrium occurs within about  $10^{-20}$  seconds, a compound nucleus is formed. Schematic diagram of the formation and decay mechanisms of the compound nucleus have been shown in Fig. 3.1. The amount of angular momentum transferred into the compound nucleus is given by  $l = b \times p$  where  $b$  is the impact parameter and  $p = M_P v = \sqrt{2M_P E_B}$  is the linear momentum of the beam, and  $M_P$  and  $E_B$  are the mass and the kinetic energy of the projectile, respectively. Therefore, higher the beam

energy, the more angular momentum will be transferred into the compound nucleus. Again the higher angular momentum can be achieved depending on the masses and sizes of the colliding projectile and target nuclei. In this reaction, the kinetic energy ( $E_{CM}$ ) of the collision between projectile and target nuclei in the centre of mass frame is converted into excitation energy ( $E_x$ ) of the compound nucleus. The excitation energy of the compound nucleus can be expressed by

$$E_x = Q + E_{CM} \quad (3.1)$$

where  $Q$  is the  $Q$ -value for the formation of the compound nucleus.  $E_{CM}$  is the kinetic energy of the collision in the centre of mass frame.  $Q$  and  $E_{CM}$  can be calculated by the following relation:

$$Q = M_T + M_P - M_{CN} \quad (3.2)$$

$$E_{CM} = \frac{M_T}{M_T + M_P} E_B \quad (3.3)$$

where  $M_T$ ,  $M_P$  and  $M_{CN}$  are the masses of target, projectile and compound nucleus, respectively.  $E_B$  is the beam energy in the laboratory frame. The maximum angular momentum ( $l_{max}$ ) transferred to the compound nucleus in fusion-evaporation reaction can be achieved when the projectile and target nuclei just touch each other. This is given by the following expression:

$$l_{max} = \sqrt{\frac{2\mu R^2}{\hbar^2} (E_{CM} - V_C)} \quad (3.4)$$

where  $\mu = \frac{M_P M_T}{M_P + M_T}$  is the reduced mass for the projectile and the target nuclei.  $R$  is the centre-to-centre distance of the projectile and the target nuclei and is given by [76]

$$R = 1.36(A_P^{\frac{1}{3}} + A_T^{\frac{1}{3}}) + 0.5 \quad (3.5)$$

Unit of  $R$  is fm.  $A_P$  and  $A_T$  are the mass numbers of the projectile and the target nuclei, respectively.  $V_C$  is the Coulomb barrier energy (in MeV) between the projectile and the target nuclei and is given by

$$V_C = 1.44 \frac{Z_P Z_T}{R} \quad (3.6)$$

It is seen from eq. (3.4) that the maximum angular momentum ( $l_{max}$ ) transferred to the compound nucleus depends on reduced mass of the projectile-target combination and the beam energy in CM frame with respect to the Coulomb barrier energy ( $V_C$ ).

### 3.1.2 Decay of compound nucleus

Due to large excitation energy and angular momentum, the compound nucleus becomes very hot and rotates very fast. It typically takes around  $10^{-16}$  seconds to cool down by evaporating particles like neutron, proton and alpha. The probability of emission of the neutron particles is high compared to the charged particles (proton and alpha), because the neutrons do not have to face the Coulomb barrier during evaporation, but in case of proton and alpha, the probability of emission is hindered by Coulomb barrier. The compound nucleus continues to evaporate particles until its excitation energy is less than the particle separation energy. The nucleon separation energy is typically 5-8 MeV. Therefore the compound nucleus loses its excitation energy by around 5-8 MeV by evaporating a nucleon (neutron or proton) and removes 1-2  $\hbar$  amount of angular momentum per nucleon evaporation. When the excitation energy becomes less than the particle separation energy, the compound nucleus stops to evaporate particles and subsequently starts emitting continuous statistical  $\gamma$ -rays which are mainly E1-transitions. For emission of these  $\gamma$ -rays, the residual nuclei, produced from the compound nucleus by evaporating particles, lose very small amount of angular momentum but large amount of excitation energy. After emitting these  $\gamma$ -rays, the residuals reach near the yrast line. The yrast line is consisted of yrast states which have lowest excitation energy for a given angular momentum.

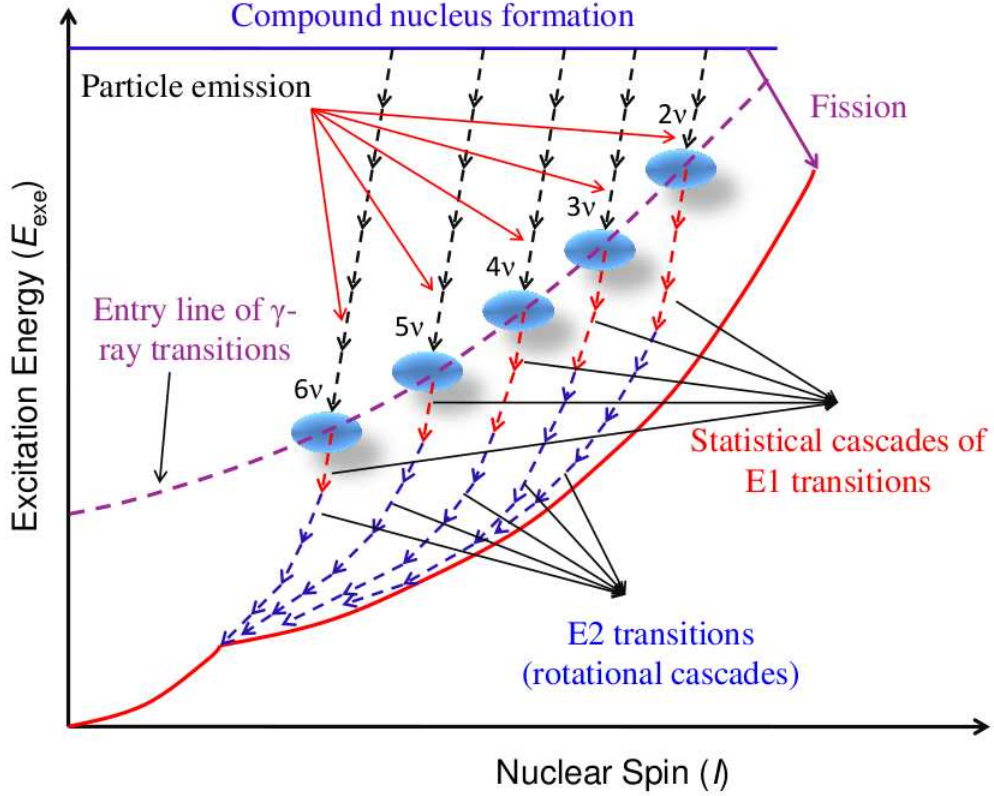


Figure 3.2: Excitation energy as a function of nuclear spin is shown. This figure is taken from Ref. [77].

Along the yrast line the residual nuclei emit the  $\gamma$ -rays which are discrete in nature and finally go to its ground state. If the residual nuclei are deformed rotating nuclei, then the emitted  $\gamma$ -rays are mainly E2 type transitions. The whole process is shown in figure 3.2. In the on-line  $\gamma$ -ray spectroscopic studies, the discrete  $\gamma$ -rays emitted from the residual nuclei in and near the yrast line are detected. These  $\gamma$ -rays carries the information about the structure of the corresponding nucleus around the yrast line.

### 3.1.3 Inelastic excitation

The inelastic excitation is, particularly, employed to generate high spin excited states in nuclei which lie in or near to the stability line. It is difficult or not possible to excite the higher spin

states in these nuclei by fusion evaporation reactions using stable beam-target combinations. In the present work, the excited states in the stable nucleus  $^{169}\text{Tm}$ , have been populated using this method. A heavy-ion beam is normally used to bombard the target material, the excited states of which nucleus are of interest. If the bombarding energy is higher than the Coulomb barrier, the excited states are populated by both Coulomb excitation and nuclear inelastic excitation. For higher beam energies, e.g.  $\sim 15 - 20\%$  above the Coulomb barrier, the Deep Inelastic Collision (DIC) also takes place, in which the transfer of a few particles (proton/neutron) occurs between the target and the projectile nuclei in order to equilibrate the  $N/Z$  of the combined system. DIC with stable target and projectile combination is one of the powerful methods employed to study the excited states of the neutron rich heavy nuclei close to the stability line.

## 3.2 $\gamma$ -ray detection processes

The  $\gamma$ -rays emitted from excited nuclei interact with the detector material by three major processes, photoelectric effect, Compton scattering and pair production. For all these processes, a partial or complete transfer of the  $\gamma$ -ray energy to the electron occurs and the deposited energy in the detector is measured.

### 3.2.1 Photoelectric effect

The photoelectric effect is the most important interaction as far as the  $\gamma$ -ray detection is concerned. This is because the full energy of a  $\gamma$ -ray is deposited into the detector medium by this interaction. In the photoelectric effect, the  $\gamma$ -ray photons interact with the bound atomic electrons and transfer their full energy to the bound electrons. Due to absorption of the  $\gamma$ -ray energy, the electrons become free which are known as photoelectrons. The electron kinetic

energy  $E_e$  is given by

$$E_e = E_\gamma - E_b \quad (3.7)$$

Where  $E_\gamma$  is the  $\gamma$ -ray energy and  $E_b$  is the electron binding energy. The photoelectric cross section depends on the energy of the interacting  $\gamma$ -ray. For sufficiently high  $\gamma$ -ray energy, the most probable origin of photoelectron is the most tightly bound K-shell electron. At  $\gamma$ -ray energy above the K-shell energy, the photoelectric cross section is relatively small and when the  $\gamma$ -ray energy approaches the K-shell energy, the cross section increases significantly. Similarly, for  $\gamma$ -ray energy below the K-shell energy, L, M, etc. shell electrons become available for photoelectric interaction. Besides the  $\gamma$ -ray energy, the photoelectric cross section also strongly depends on the atomic number ( $Z$ ) of the interacting atom of the medium and the cross section increases with atomic number as  $\sigma_{photo} \propto Z^n$ , where  $n$  varies from 4 to 5 over the  $\gamma$ -ray energy region of interest.

### 3.2.2 Compton scattering

The Compton scattering process is the scattering of the incident  $\gamma$ -ray photons with the free electrons of the medium. Inside material, the electrons are bound, however, if the  $\gamma$ -ray energy is high enough compared to the electron binding energy, then the electrons can be considered as nearly free. After scattering,  $\gamma$ -ray transfers a portion of its energy to the electron, which is then known as a recoil electron. Due to the possibility of all the angles of scattering, the amount of energy transferred to the recoil electron varies from zero to a large portion of the  $\gamma$ -ray energy. From the conservation of energy and momentum, energy of the scattered  $\gamma$ -ray can be expressed as:

$$E'_\gamma = \frac{E_\gamma}{1 + \left(\frac{E_\gamma}{m_e c^2}\right)(1 - \cos\theta)} \quad (3.8)$$

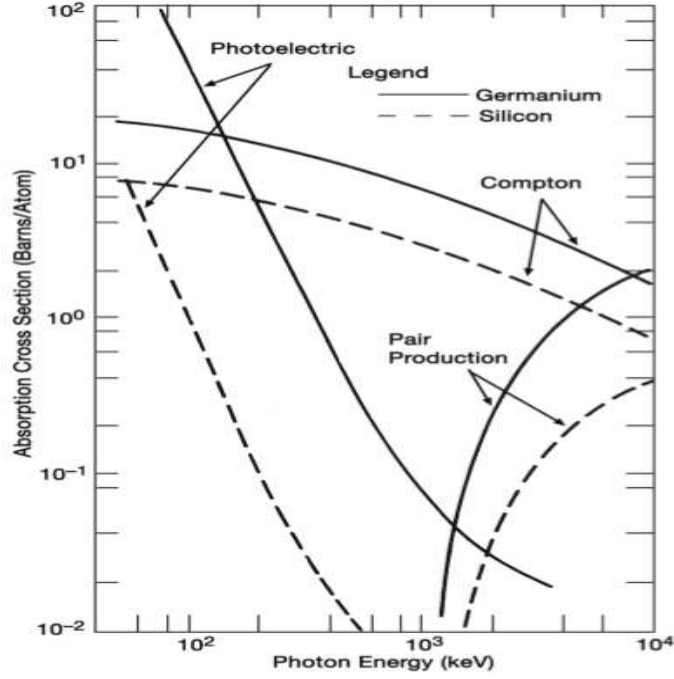


Figure 3.3: Relative Probability for each of the three types of  $\gamma$ -ray interactions in Ge ( $Z = 32$ ) and Si ( $Z = 14$ ) as a function of energy. This figure is taken from Ref. [78].

where  $\theta$  is the scattering angle,  $E_\gamma$  is  $\gamma$ -ray energy and  $m_e c^2$  is the rest mass energy of the recoil electron. The kinetic energy of the recoil electron is given by:

$$\begin{aligned}
 E_e &= E_\gamma - E'_\gamma \\
 &= E_\gamma \frac{\left(\frac{E_\gamma}{m_e c^2}\right)(1 - \cos\theta)}{1 + \left(\frac{E_\gamma}{m_e c^2}\right)(1 - \cos\theta)}
 \end{aligned} \tag{3.9}$$

At  $\theta = 180^\circ$ , the energy transfer to the recoil electron is maximum and this energy is called Compton-edge energy. Due to the partial energy transfer of the  $\gamma$ -ray energy to the electron of the detector medium, always a Compton scattered background appears in the  $\gamma$ -ray spectrum.

### 3.2.3 Pair production

The pair production occurs when the incident  $\gamma$ -ray energy exceeds the twice the rest-mass energy of an electron ( $2m_e c^2 = 1.022$  MeV). In actual situation, the pair production cross section is very low until the  $\gamma$ -ray energy approaches several MeV of energy. Therefore, this process is only dominant one for the high energy  $\gamma$ -rays. Moreover, to satisfy momentum conservation, this process requires a third party, usually a nucleus. In this process, a  $\gamma$ -ray photon is converted into an electron-positron pair. 1.022 MeV of  $\gamma$ -ray energy is required to create the electron-positron pair and the excess energy is transferred to the electron-positron pair as kinetic energy. Pair production cross section depends approximately on the square of the atomic number of the medium. The created positron annihilates after slowing down in the medium and two annihilation  $\gamma$ -ray photons are produced as secondary products of the process.

Variation of absorption cross section of  $\gamma$  rays corresponding to the photoelectric effect, Compton scattering and pair production as a function of  $\gamma$ -ray energy for Ge( $Z = 32$ ) and Si( $Z = 14$ ) materials is shown in Fig. 3.3.

## 3.3 HPGe detector

Germanium detector is preferred than Silicon detector for  $\gamma$ -ray detection due to the higher atomic number of germanium. The cross section of photoelectric effect increases as the atomic number ( $Z$ ) of the materials increases. In case of germanium ( $Z = 32$ ), photoelectric cross section is about 60 times greater than that in silicon ( $Z = 14$ ). The depletion layer of germanium or silicon is used as active area of a solid state detector for  $\gamma$ -ray detection and the width of the depletion layer is normally 2 to 3 mm at high bias voltage which is nearly the breakdown voltage of the materials. The width of the depletion layer depends on impurity concentration

of the germanium or silicon and is written as [79]

$$d = \sqrt{\frac{2\epsilon V}{eN}} \quad (3.10)$$

where  $V$  is the reverse bias voltage,  $N$  is the impurity concentration of the semiconductor material,  $\epsilon$  is the dielectric constant and  $e$  is the electronic charge. As we see from the above relation, width of the depletion layer will increase if the impurity concentration decreases. Now a days fabrication of very high purity germanium with impurity concentration of less than  $10^{10}$  atoms/cm<sup>3</sup> has been achieved. At this impurity concentration, width of the depletion layer is about 10 mm for 1kV reverse bias voltage. This type of germanium detector is called High Purity Germanium (HPGe) detector. Advantage of this detector is that it is not required to keep the detector at low temperature all the time, cooling is required only when the detector is operated at high voltage during experiments. Energy resolution of the HPGe detector is about 2 keV at 1 MeV  $\gamma$ -ray energy. Because of the high energy resolution, the HPGe detectors are preferred for the detection of closely spaced  $\gamma$ -ray peaks.

### 3.4 Clover detector

The Clover detector is a HPGe type detector which is consisted of four crystals. The front face of the detector is tapered at 7 degree to achieve a square shape which looks like a clover leaf. The spacing between the two adjacent crystals is 0.2 mm and each crystal has a bore hole of radius 0.5 cm along its axis. The size of each crystal in this detector is 7 cm (length) x 5 cm (diameter). The detector is housed inside an aluminium vacuum chamber. Clover detector is shown in Fig. 3.4 and its schematic diagram is shown in Fig. 3.5.



Figure 3.4: Clover HPGe detector at Laboratory.

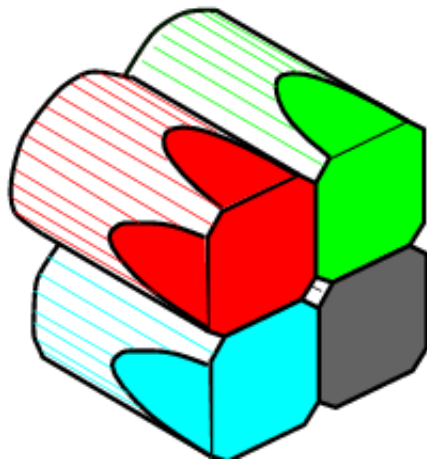


Figure 3.5: Schematic diagram of clover HPGe detector [80].

## Addback factor

In the photoelectric process, energies of the incident  $\gamma$ -rays are completely deposited in any of the four crystals of a clover detector. Due to Compton scattering of  $\gamma$ -ray, only partial energy is deposited in any crystal and the remaining energy of the scattered  $\gamma$ -ray can be absorbed by the other three crystals. Therefore, if we add the counts of the four crystals on event by event basis, we will get full energy  $\gamma$ -peak. This peak contains photoelectric counts as well as Compton scattering counts. This process of adding energies of the four crystals of a clover in an event is known as addback mode. By using addback mode, we can enhance the counts of  $\gamma$ -ray peaks in the  $\gamma$ -ray spectrum. The ratio of the addback mode counts to the sum of the photoelectric counts of the four crystals of a clover is known as addback factor.

$$\text{Addback factor} = \frac{\text{Addback counts of the clover detector}}{\text{Sum of photoelectric counts of the 4 crystals}}$$

The addback factor as a function of  $\gamma$ -ray energy for clover detector has been experimentally obtained using  $^{133}\text{Ba}$  and  $^{152}\text{Eu}$  radioactive sources, as shown in Fig. 3.6. It is seen from the figure that in the low energy region ( $E_\gamma < 150$  keV), the addback factor is  $\sim 1$  because of large photoelectric cross-section. As the  $\gamma$ -energy increases, the addback factor also increases and almost saturates after  $E_\gamma \sim 800$  keV. The addback factor is  $\sim 1.4$  around  $E_\gamma = 1$  MeV and approaches about 1.5 at higher energies.

## Energy resolution

FWHM (Full Width at Half Maximum) is the measure of energy resolution of a detector. FWHM of a clover detector as a function of  $\gamma$ -ray energy has been obtained using  $^{60}\text{Co}$ ,  $^{133}\text{Ba}$  and  $^{152}\text{Eu}$  sources, as shown in Fig. 3.7. The energy resolution in the addback mode is  $\sim 2$  keV at 1 MeV  $\gamma$ -ray energy.

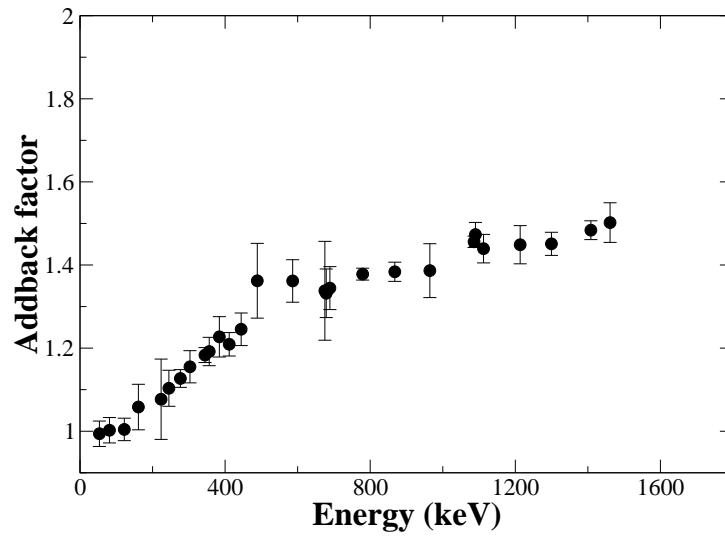


Figure 3.6: Addback factor as a function of  $\gamma$ -ray energy for clover detector.

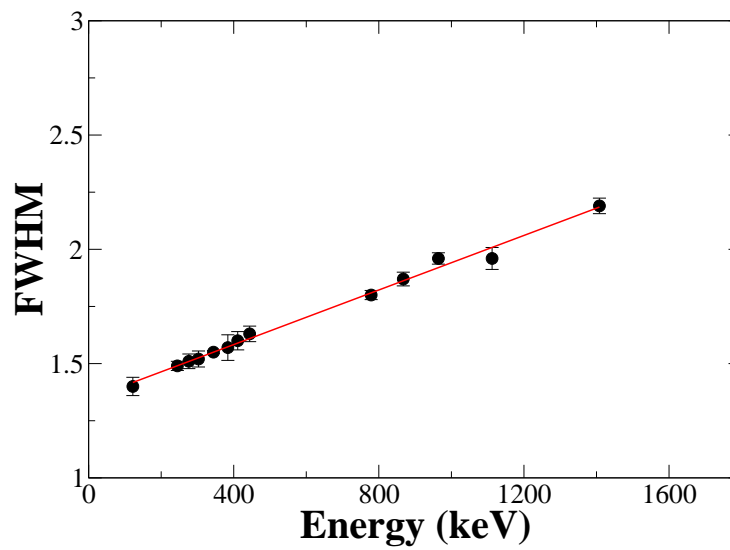


Figure 3.7: FWHM of clover detector as a function of  $\gamma$ -ray energy. Solid straight line is the linear fit of the data.

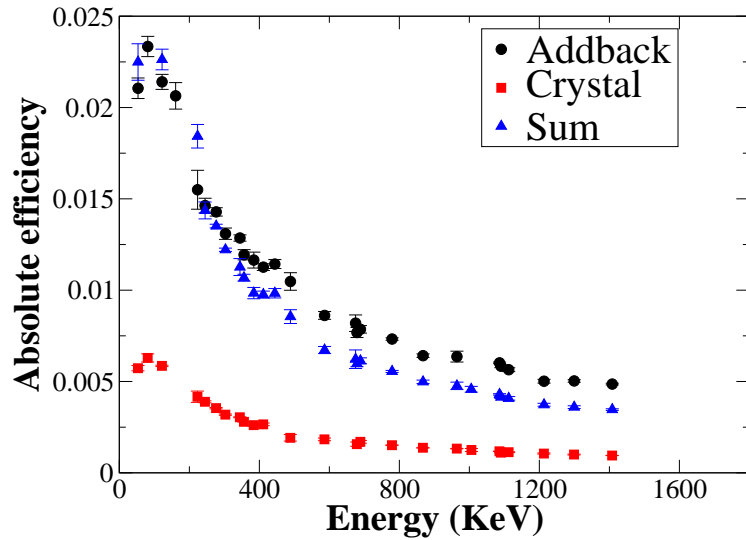


Figure 3.8: Absolute efficiency of Clover detector at 10 cm distance from the source

### Energy efficiency

The measured absolute energy efficiency for different modes, i.e, for crystal, sum-of-four-crystals and addback as a function of  $\gamma$ -ray energy for 10 cm distance from the source has been shown in Fig. 3.8. The addback clover efficiency for 1 MeV energy is  $\sim 0.65\%$  at 10 cm distance from the source.

### Linear polarization of $\gamma$ -ray transitions

Due to the segmented structure of the clover detector, it can be used as a Compton polarimeter. Therefore, the linear polarizations of  $\gamma$ -rays can be experimentally determined to assign parity of nuclear levels.

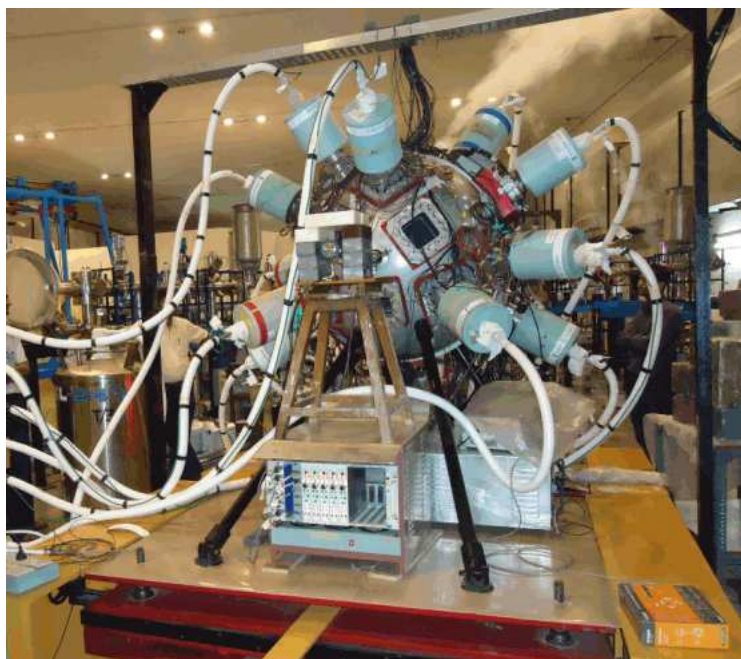


Figure 3.9: INGA setup at TIFR.

### 3.5 Indian National Gamma Array (INGA) at TIFR

The high purity germanium detector array with very good energy resolution and sensitivity is the key instrument for the investigation of variety of nuclear structure by  $\gamma$ -ray spectroscopic technique. The large germanium detector arrays, like Gammasphere [81], INGA [82], Jurogam [83], Exogam [84], Afrodite [85], Tigress [86] etc. with high efficiency and resolving power allow us to observe very weak  $\gamma$ -ray cascades. This can reveal various structural phenomena, e.g., shape coexistence, octupole correlation, magnetic rotation, anti-magnetic rotation, chiral rotation, wobbling motion etc.

The Indian National Gamma Array (INGA) facility in India was initiated by the collaborative effort of Tata Institute of Fundamental Research (TIFR), Inter University Accelerator Center (IUAC), Bhabha Atomic Research Centre (BARC), Saha Institute of Nuclear Physics (SINP), Variable Energy Cyclotron Centre (VECC), UGC DAE Consortium for Scientific Research and many Universities in India. The INGA array, installed at Tata Institute of Fundamental

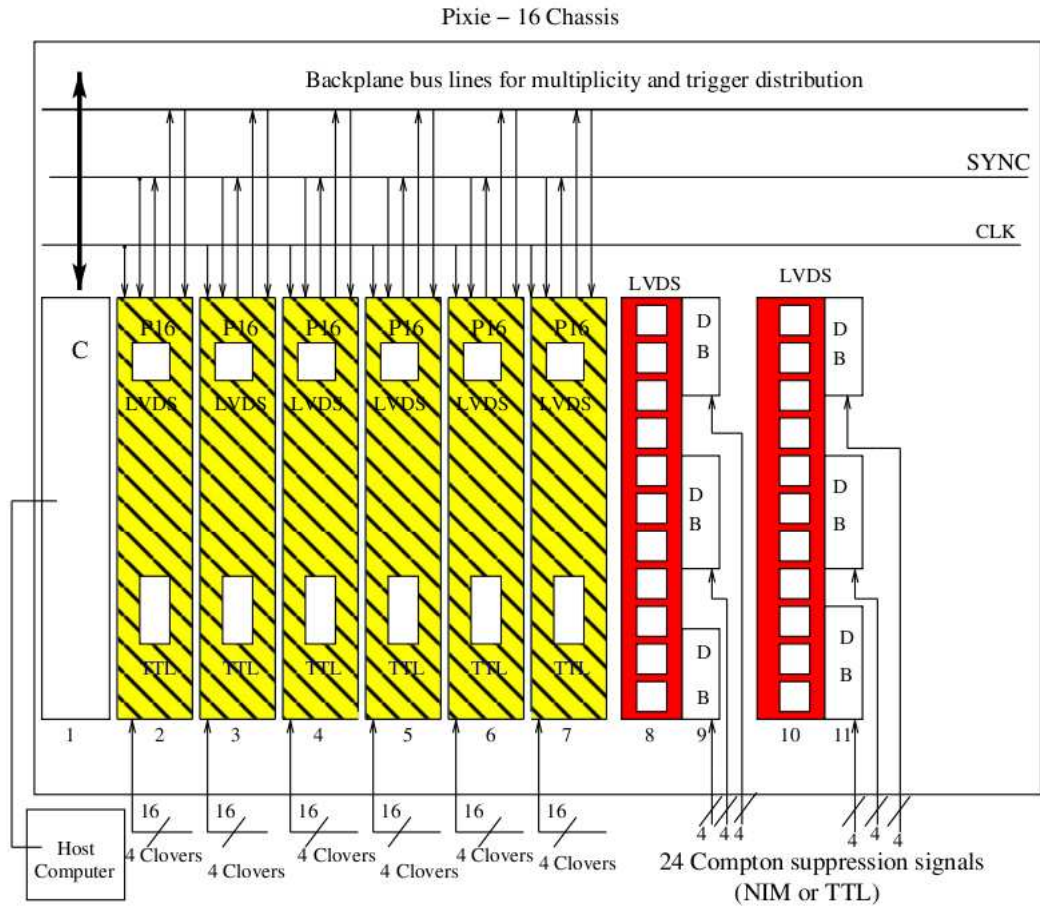


Figure 3.10: Block diagram for the digital DAQ for 24 Compton suppressed clover detectors. It consists of six Pixie-16 modules, two LVDS level translator modules and one controller arranged in a single Compact PCI/PXI crate [22].

Research (TIFR), was used for the present experiments. This array was designed for a maximum of 24 Compton-suppressed HPGe clover detectors arranged in a spherical geometry with six detectors at  $90^\circ$  and three detectors each at  $23^\circ$ ,  $40^\circ$ ,  $65^\circ$ ,  $115^\circ$ ,  $140^\circ$  and  $157^\circ$  with respect to the beam direction. The distance from target to each detector is 25 cm. However, during the experiments to populate the excited states in  $^{196}\text{Tl}$  and  $^{169}\text{Tm}$ , there were 15 and 19 clovers in the array arranged in six different angles, respectively. In the addback mode, the clover has addback factor of  $\sim 1.4$ , peak-to-total ratio of  $\sim 40\%$  and FWHM of  $\sim 2$  keV at  $E_\gamma \sim 1$  MeV. The overall photo-peak efficiency of the array is  $\sim 5\%$  at around 1 MeV for the complete array with 24 clover detectors.

The digital data acquisition (DDAQ) system is consisted of six Pixie-16 modules [21, 22], two LVDS level translator modules, and one controller arranged in a single Compact PCI/PXI crate, shown in Fig. 3.10 through the block diagram. Each Pixie-16 module has sixteen channels and therefore the six Pixie-16 modules have total 96 channels for 24 clover detectors. The details of the DDAQ can be found from Ref. [22]. This DDAQ, based on Pixie-16 modules, has been used for the data collection with a sampling rate of 100 MHz for each detector in the present experiments. The time-stamped  $\gamma - \gamma$  coincidence data were collected when at least two clover detectors were fired within a time window of 150 ns in coincidence mode. Each channel of the clover detectors was vetoed with the respective Compton suppressed BGO shields. Raw data sorting was done by Multi-pARAmeter time-stamped based COincidence Search (MARCOS) code [22], developed at TIFR, Mumbai. The  $\gamma - \gamma$  matrix and  $\gamma - \gamma - \gamma$  cube were formed by MARCOS [22] and RADWARE [28] software packages.

### 3.6 VENUS array setup at VECC

VECC array for NUclear Spectroscopy (VENUS), a detector array, consisting of 6 clover HPGe detectors was set up to perform experiments on high-spin nuclear structure at VECC, Kolkata.



Figure 3.11: VENUS setup at VECC.

Each clover was placed inside anti-Compton shield (ACS) made of BGO scintillator detectors. Two clovers at  $\pm 90^\circ$ , two at  $\pm 150^\circ$  and other two clovers at  $45^\circ$  and  $55^\circ$  angles with respect to the beam direction were placed in the horizontal plane. The detectors were placed at 18 cm distance from target. To improve peak-to-total (PT) ratio by eliminating escaped  $\gamma$ -rays from the clovers, ACS and clover signals were generated. Two  $90^\circ$  detectors were used for measuring polarization of  $\gamma$ -rays. The detectors at  $150^\circ$  and  $90^\circ$  were used to generate  $\gamma - \gamma$  DCO matrix. The experimental setup has been shown in Fig. 3.11.

VME data acquisition system with LAMPS software [27] was used for collecting online data from VENUS array. The 24 preamplifier signals from the 6 clover detectors were processed through the 16-channel Mesytec amplifiers with  $4 \mu s$  shaping time. The amplifiers provide 24 energy signals as well as the corresponding 24 ECL standard timing signals. The energy signals were processed through a 32-channel VME ADC. The ECL timing signals were converted into logic signals through the 16-channel ECL to NIM converters for OR logical operation using the quad logic ORTEC-CO4020 module. OR logical operations of signals of four crystals of each clover detector provide 6 output signals. On the other hand, the BGO signals from the

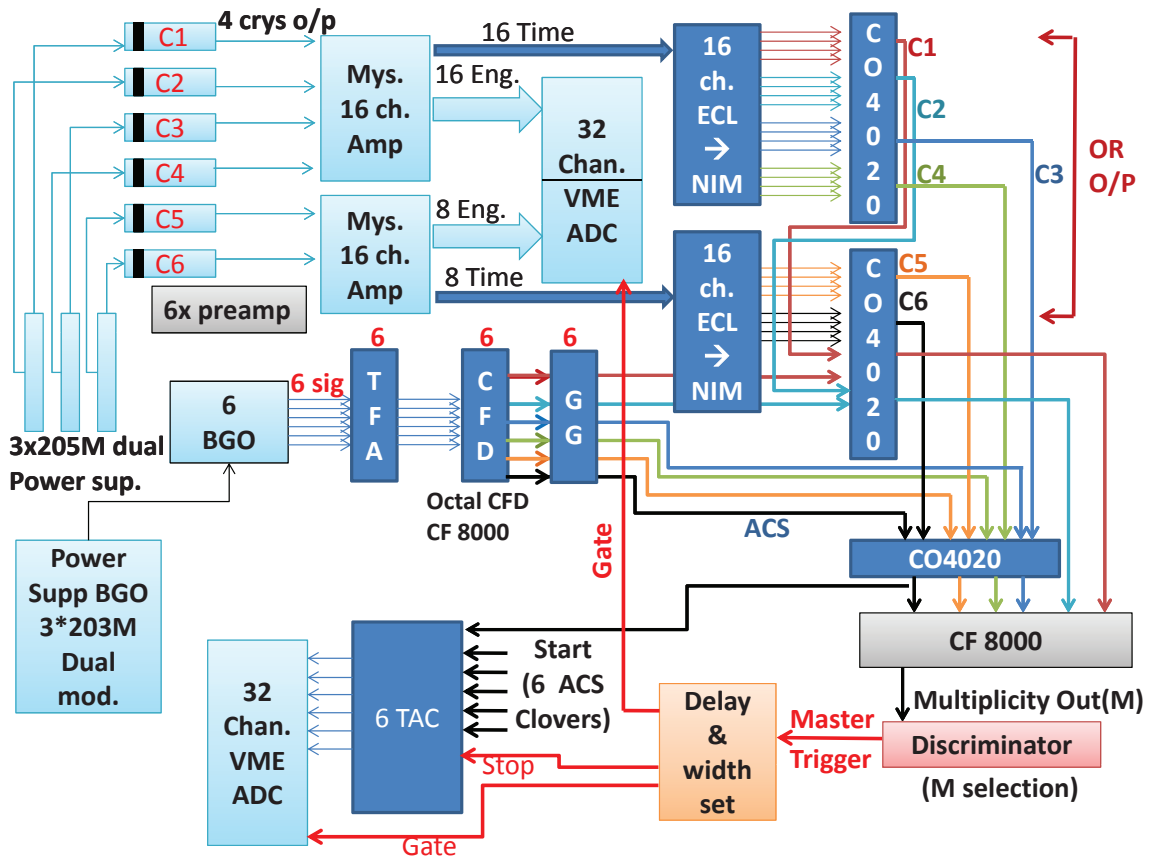


Figure 3.12: Block diagram for electronics setup for VENUS array at VECC [87].

anti-Compton shields of the respective clovers, processed through the TFA and CFD, were used for vetoing the signals from the clover detectors to generate a master trigger to get Compton-suppressed data. Moreover, the time differences of the 6 clover detectors as well as the RF signal of the beam bursts with respect to the master trigger were also recorded on an event by event basis using TAC modules. The singles data ( $M_\gamma \geq 1$ ) and the  $\gamma - \gamma$  coincidence data ( $M_\gamma \geq 2$ ) were collected using CF8000 and Discriminator modules along with the other relevant modules. The whole electronics setup as a block diagram is shown in Fig. 3.12. In the present thesis work, the VENUS array with this electronics setup was used to study  $^{207}\text{Po}$  nucleus which was populated by the fusion evaporation reaction using  $^{208}\text{Pb}$  target and  $\alpha$ -beam of energy 60 MeV from  $K - 130$  cyclotron at VECC, Kolkata.

# Chapter 4

## GEANT4 Simulation

Geant4 (GEometry ANd Tracking - version 4) [24] is a general purpose Monte Carlo simulation toolkit based on object oriented C++ language. This software tool has been developed by an international collaboration to simulate detector geometry, interaction of particles with matter and the trajectories of the interacting particles. It has extensive support of visualization tools, data handling using ROOT [88] software tool and tracking option. It has applications in various fields like high energy particle physics, nuclear physics, material science, space science, medical science, etc. In the present thesis work, a simulation code based on the Geant4 tool has been developed to simulate the geometries of HPGe single-crystal detector, clover detector and VENUS array and the necessary parameters to characterize the detectors and the array.

### 4.1 Geant4 Simulation of HPGe Single Crystal, Clover and VENUS array

In order to understand the  $\gamma$ -ray response of the VENUS detector array for efficiency, hit-pattern, etc and for in-depth understanding of the details of the response of the HPGe detectors,

a simulation code in the Monte Carlo Geant4 platform has been developed [25, 26]. The VENUS array consists of clover HPGe detectors. Each clover detector is composed of four HPGe crystals. Therefore, the simulation was first performed for the case of a separate single crystal HPGe detector, then for a clover HPGe detector and finally, for the VENUS array.

### 4.1.1 HPGe Single Crystal

#### Geometry construction

The simulation was performed for the 25%-efficient single-crystal HPGe detector available at VECC. The exact dimension, geometry and housing of the detector were constructed using the values provided by the supplier. The dimension of the cylindrical-shaped HPGe crystal is 53 mm (diameter) x 60 mm (length) with a dead layer of 0.5 mm. In the front part of the detector, it has a Beryllium window of thickness 0.3 mm and is placed at 6 mm away from the front face of the crystal. The remaining part of the crystal is surrounded by 3 mm thick aluminium cover. The constructed detector and its sketch are shown in Fig. 4.1.

#### Physics processes and data handling

For Geant4 simulation, one of the important parts is the choice of the physics processes for the primary and secondary particles created by the interaction with the detector and surrounding materials. Here the primary particle,  $\gamma$ -ray, interacts with the material by three processes: the photoelectric effect, Compton scattering and pair production. After the interaction, the charged particles (electron and positron) can be produced. Hence, these three types of particles have been incorporated in the simulation. For the charged particles, electron ionization, multiple scattering, bremsstrahlung radiation and positron-annihilation processes have been used in the simulation.

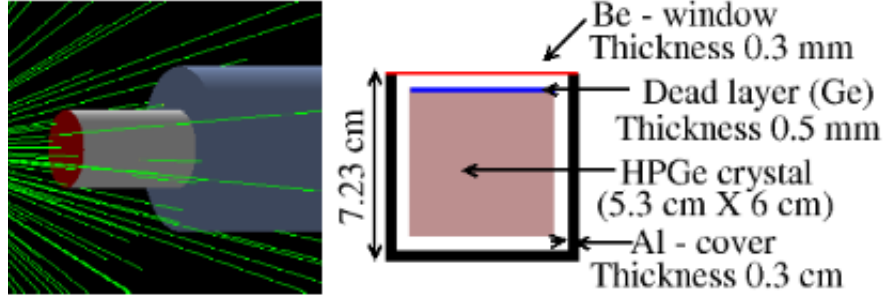


Figure 4.1: The simulated geometry of the HPGe detector (left) and the sketched diagram of the detector (right).

The deposited  $\gamma$ -ray energies in the detector material are collected on an event-by-event basis using the G4UserEventAction class in an output ROOT file. These root files are analysed in the ROOT framework.

## Results and discussion

The detailed experimental results on the characterization of the detector using  $^{60}\text{Co}$ ,  $^{133}\text{Ba}$  and  $^{152}\text{Eu}$  radioactive sources are given in Refs. [89, 90]. The resolution of the detector was measured to be 2.0 keV at 1333 keV. Relative efficiency (with respect to a 3"x3" NaI(Tl) detector at a distance of 25 cm from the source) has been measured as 29.8% (guaranteed value 25%). In the simulation, relative efficiency was obtained as 29.6%. The absolute efficiencies at various distances were also measured and compared with the simulation. These are shown in Fig. 4.2 as a function of  $\gamma$ -ray energy. Excellent agreement between data and simulation has been achieved. The absolute efficiency of the detector at 11 cm has been found to be 0.2% for 1 MeV  $\gamma$ -ray. The variation of the measured and simulated efficiencies of the detector with its distance from the source are shown in Fig. 4.3 for 1 MeV  $\gamma$ -ray. The experimental values of efficiency at 1 MeV are obtained from the fitted efficiency curve. The curve in Fig. 4.3 has been observed to follow the  $a/r^2$  equation (fitted curve) with the value of the constant  $a = 0.26503$

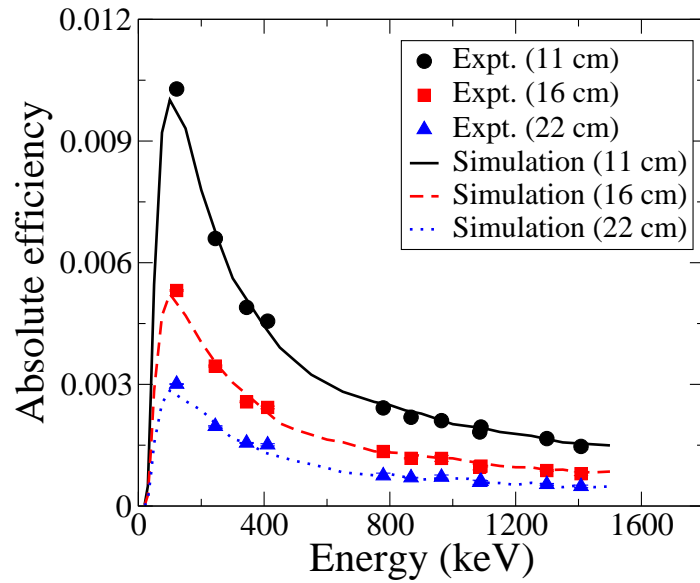


Figure 4.2: Measured and simulated absolute efficiencies of the single-crystal HPGe detector as a function of  $\gamma$ -ray energy for 11 cm, 16 cm and 22 cm distances from the source to the detector. The Experimental data (filled symbols) were taken using a  $^{152}\text{Eu}$  source.

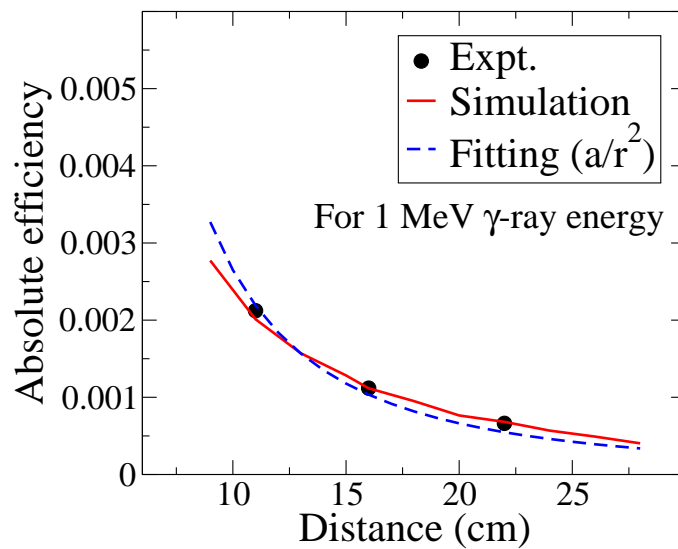


Figure 4.3: Variation of the measured and simulated absolute efficiencies with distance for 1 MeV  $\gamma$ -ray (the experimental values of efficiency at 1 MeV are obtained from the fitted efficiency curve). The data are also fitted with the  $y = a/r^2$  equation, where,  $y = \text{efficiency}$ ,  $r = \text{distance}$  and  $a$  is the fitted parameter.

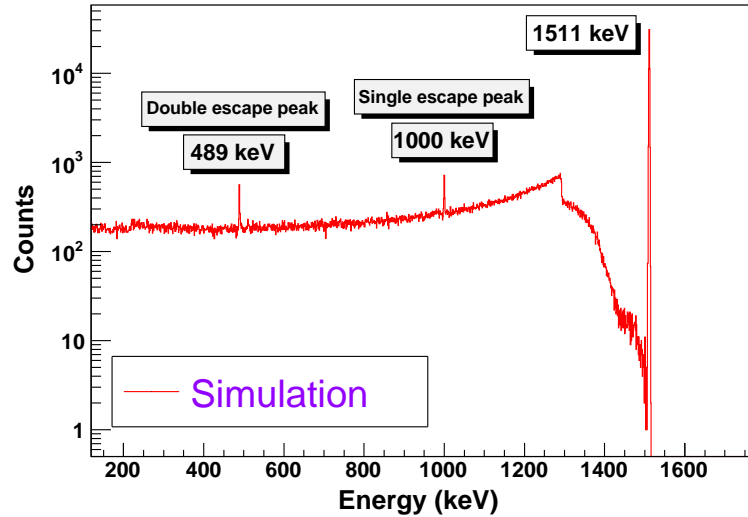


Figure 4.4: Simulated spectrum of an arbitrary  $\gamma$ -ray of energy 1511 keV. The spectrum shows the single-escape and the double-escape peaks.

cm<sup>2</sup>. Due to the small dimension of this detector, the single-escape and double-escape peaks are clearly observed in a simulated arbitrary spectrum of 1511 keV  $\gamma$ -ray energy (see Fig. 4.4).

### 4.1.2 Clover

To understand the response of different parameters of the HPGe clover detector at VECC, nearly exact shape of the detector, as supplied by the manufacturer, has been simulated in Geant4 platform. The simulation for the energy spectra, efficiency and adback factor for the detector has been performed.

#### Geometry construction

The dimension of each crystal in this detector is 7 cm (length) x 5 cm (diameter) and the front side of each crystal is tapered at 7°. The four crystals of the detector are housed inside an aluminium vacuum chamber.

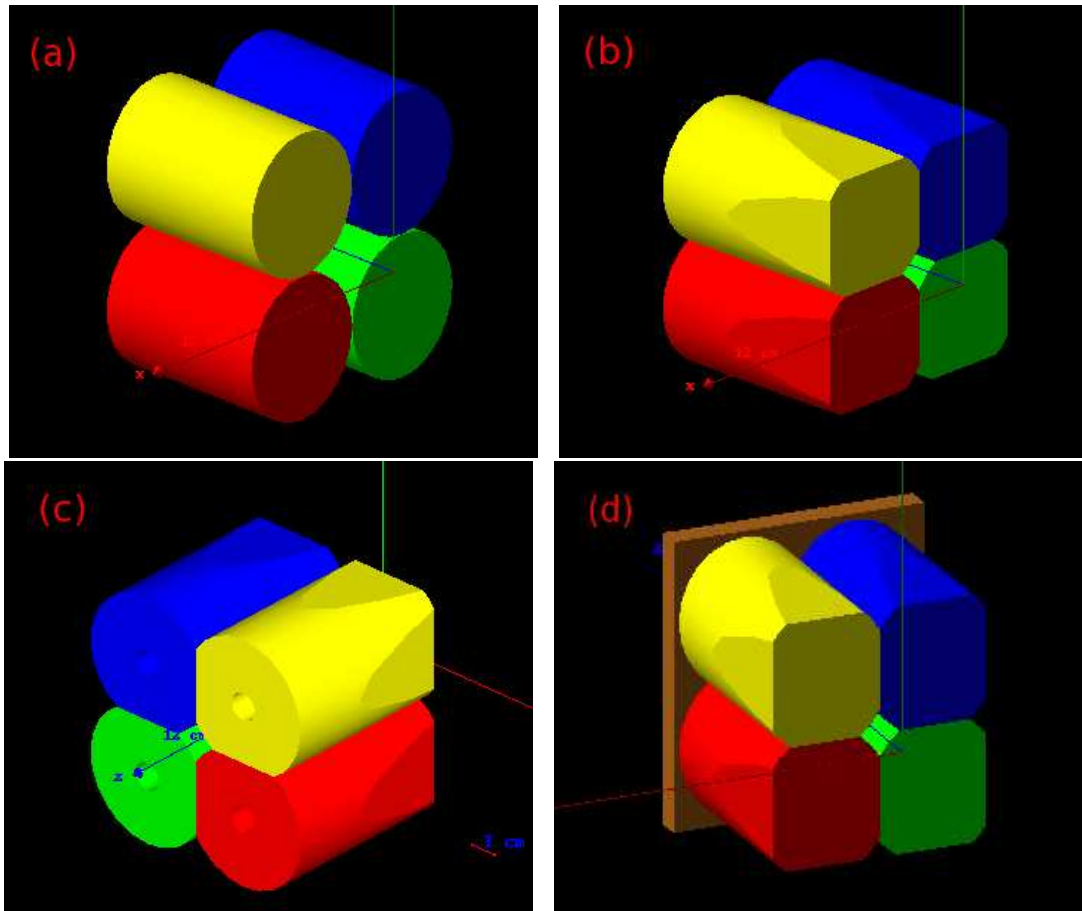


Figure 4.5: The construction of clover detector in Geant4 simulation are shown through four steps in figures (a), (b), (c) and (d).

Initially, to generate clover geometry by Geant4 simulation, four crystals of cylindrical shape, each having 5 cm diameter and 7 cm length, have been considered as shown in Fig. 4.5(a). Two consecutive perpendicular sides of each crystal along its length have been cut to achieve closed-packing of 4 crystals on the same cryostat. Front side of each crystal has been tapered at  $7^\circ$  to make front face square of the combined 4 crystals as shown in Fig. 4.5(b). A bore hole of radius 0.5 cm and length 5.5 cm has been made inside each crystal from behind along its axis as shown in Fig. 4.5(c). For cutting and tapering of the 4 crystals and to make hole inside each crystal, different geometries have been subtracted from the initial cylindrical shape using G4SubtractionSolid class. The 4 crystals are placed on a copper plate of 1 cm thickness to take into account the back scattering events as shown in Fig. 4.5(d). The outer aluminium envelope has been simulated combining trapezoidal and box shape together. Length of trapezoidal shape is 6 cm and that of box shape is 4.2 cm. Each side of square front face of trapezoid is 8.7 cm and each side of box shape is 10.2 cm. Thickness of the trapezoidal part is 0.15 cm and that of box shape is 0.3 cm. The distance from the front face (including the thickness of the Al envelope) of the Al envelope to the crystal front face is 2 cm. Anti-Compton BGO shield and heavy-metal collimator for each clover has also been simulated.

### 4.1.3 VENUS array

Geant4 simulation of the installed VENUS array facility at Variable Energy Cyclotron Centre (VECC), Kolkata has been performed in its experimental configuration. The array consisted of 6 clover HPGe detectors [91] with BGO Anti-Compton shields (ACS) in the horizontal plane. The aim of the present work is to study the simulated response of the array and the individual detectors for radioactive sources in the real experimental situation and its characterization for different parameters, like efficiency, addback factor, peak-to-total ratio etc.

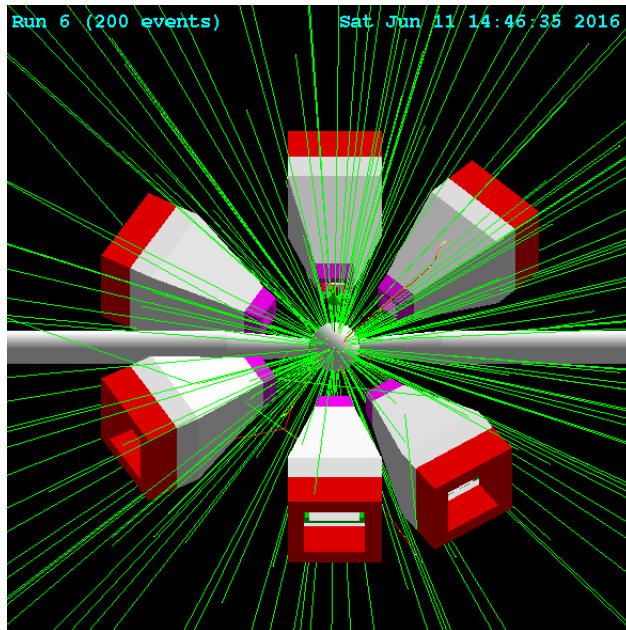


Figure 4.6: The geometry of the VENUS array with the ACS as constructed in the Geant4 simulation.

### Array geometry construction

The geometry includes the clover detectors with the ACS, the beam line and the target chamber. The detectors are placed at  $45^\circ$ ,  $55^\circ$ ,  $\pm 90^\circ$  and  $\pm 150^\circ$  angles with respect to the beam direction. 4 crystals, each of size 7 cm (length) x 5 cm (diameter), are placed on a copper plate of 1 cm thickness to constitute the clover geometry. The whole ensemble is placed inside an aluminium housing. The thickness of the housing in the front side (tapered part) is 0.15 cm and is 0.3 cm for the remaining part. Heavy-metal collimator with proper dimension for each clover have also been considered in the simulation.

A spherical target chamber of 12 cm diameter made up of 0.3 cm thick Al has been considered. The source was placed at the middle of the target chamber. The Distance from source to the heavy-metal collimator of each detector was 18.3 cm and the distance from the source to the HPGe crystal was 28 cm (18.3 cm + 4 cm (length of collimator) + 3.7 cm (distance from the

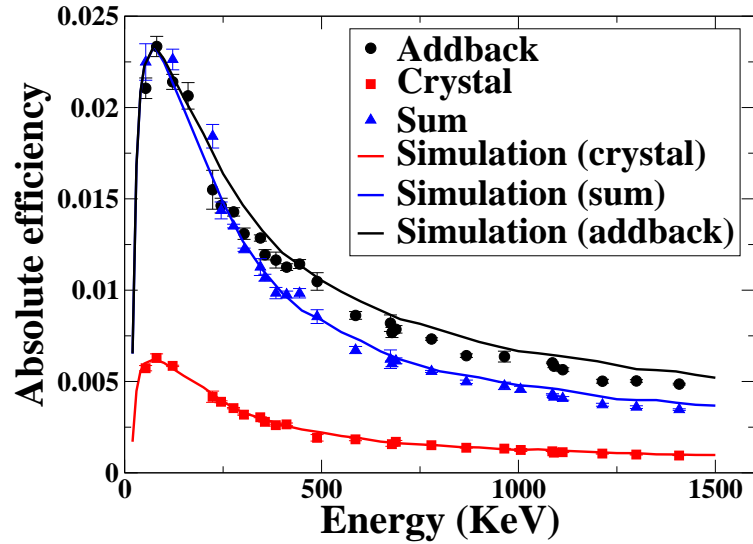


Figure 4.7: Absolute efficiency of clover in crystal, sum of four crystals and add-back mode at 10 cm distance. Data are compared with simulation.

collimator to Al-housing) + 2 cm (distance from Al-housing to HPGe crystal)). The constructed geometry, which resembles the real setup, is shown in Fig. 4.6.

## Results and discussion

$^{137}\text{Cs}$ ,  $^{60}\text{Co}$ ,  $^{133}\text{Ba}$  and  $^{152}\text{Eu}$  sources were used for the characterization of the clover detector and the VENUS array.

**Clover:** At first, clover detector was tested without anti-Compton shields (ACS) using the radioactive sources at 10 cm distance. In this case, measured absolute efficiencies in crystal mode, sum mode and add-back mode are obtained from the detector and compared with the simulation as shown in Fig. 4.7. It can be seen from the figure that an excellent agreement between the experimental data and the simulation has been achieved, which confirms that the clover geometry has been constructed properly using the simulation.

**VENUS:** Simulated spectra of  $^{60}\text{Co}$  and  $^{137}\text{Cs}$  sources with and without ACS for the VENUS array are shown in Fig. 4.8 and Fig. 4.9, respectively. In case of  $^{137}\text{Cs}$  source, measured

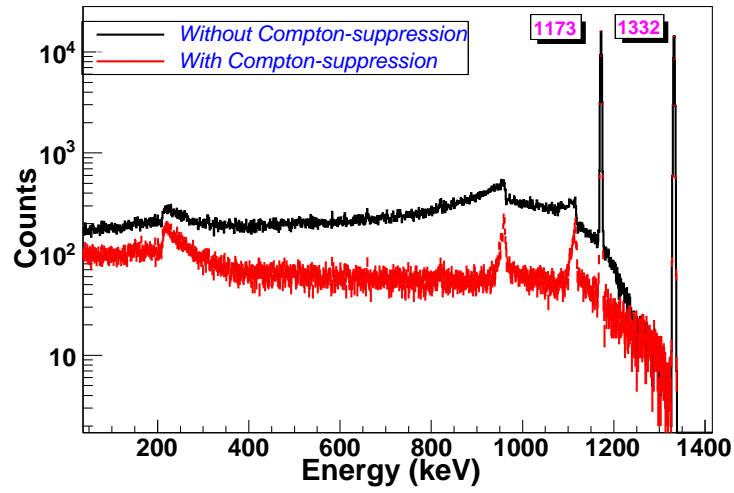


Figure 4.8: Simulated  $^{60}\text{Co}$  spectra with (red) and without (black) ACS in the add-back mode.

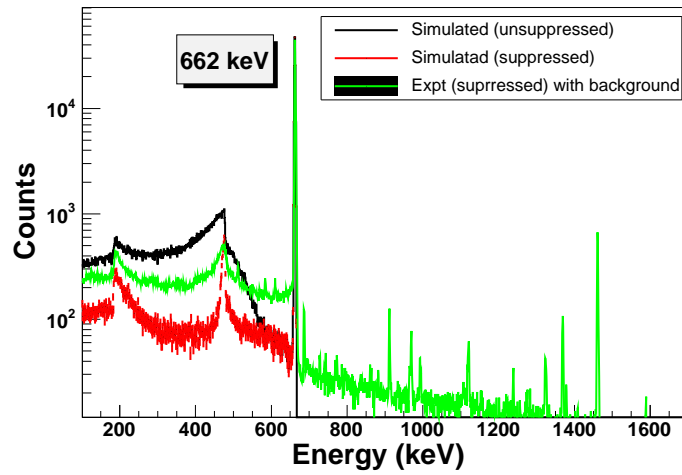


Figure 4.9: Simulated  $^{137}\text{Cs}$  spectra with (red) and without (black) ACS in the add-back mode, compared with the measured  $^{137}\text{Cs}$  spectrum (green) with ACS. The measured spectrum shows the room background lines also.

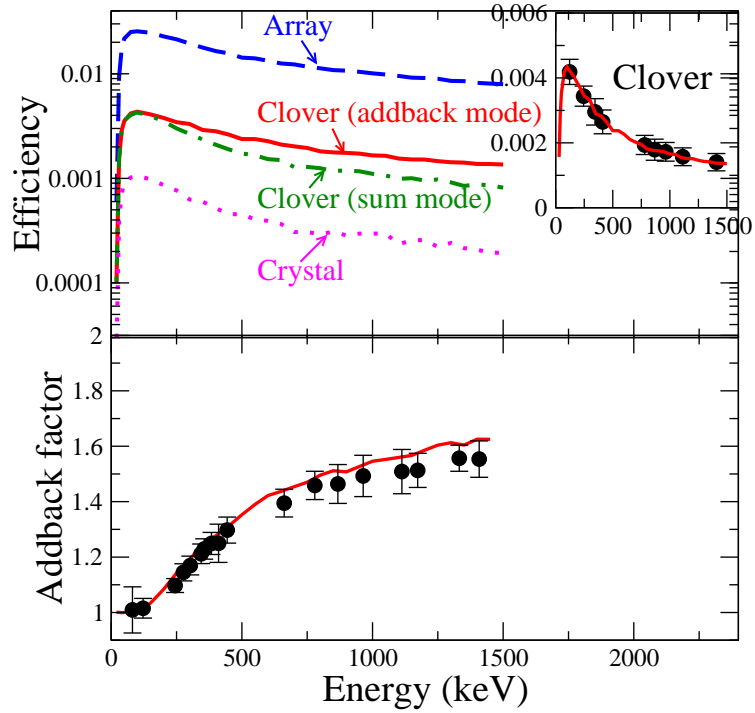


Figure 4.10: Upper panel: simulated efficiencies are shown in various modes (inset: addback efficiency compared with measured data) as a function of  $\gamma$ -ray energy. Lower panel: measured and simulated addback factors are compared.

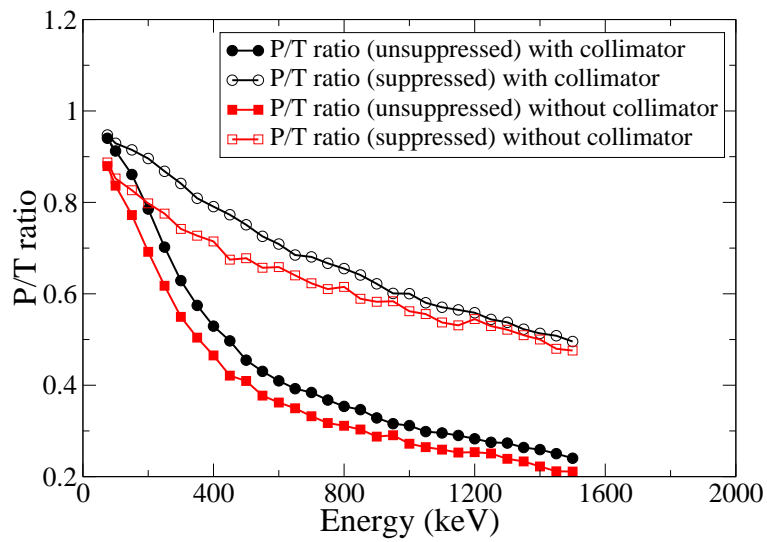


Figure 4.11: Simulated P/T ratios as a function of  $\gamma$ -ray energy are shown for four different cases.

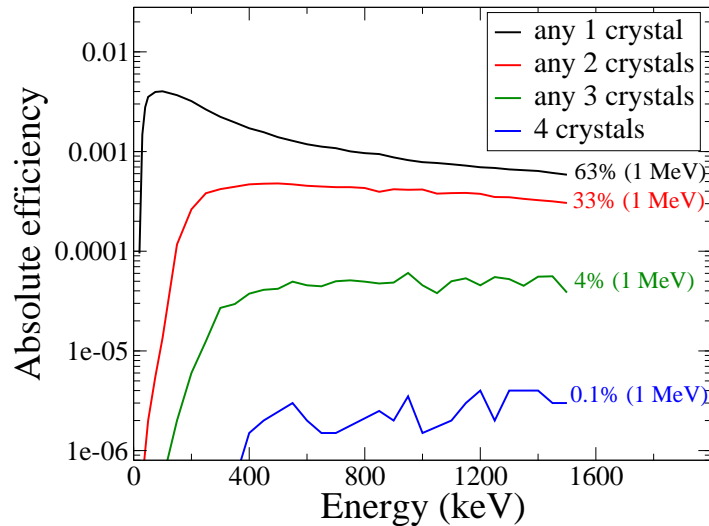


Figure 4.12: Hit patterns of  $\gamma$  rays for the interaction with the four crystals of clover detector are shown.

Compton-suppressed data including room background are also shown with its simulated spectra. The larger Compton background in the measured spectrum is due to the contribution of the room background lines which are not considered in the simulation. Addback factor for the clovers and the efficiencies in the crystal mode, sum mode, add-back mode for each clover and of the array are obtained in the simulation and are shown in Fig. 4.10 as a function of  $\gamma$ -ray energy. Comparison with the measured values are also shown (measured efficiency is normalized with simulation). The absolute efficiencies of the clover addback and array were obtained as  $\sim 0.17\%$  and  $\sim 1.0\%$  at 1 MeV, respectively in the simulation. The peak-to-total (P/T) ratios were also obtained as a function of  $\gamma$ -ray energy and are shown in Fig. 4.11. Nature of hit pattern of  $\gamma$  rays for the interaction with the four crystals of clover detector has been shown in Fig. 4.12. When  $\gamma$  rays incident on clover detector and deposit their total energy inside any one crystal, such number of events, out of the total events, at 1 MeV energy is about 63%. The number of events, out of the total events, for which  $\gamma$  rays deposit their total energy inside any two crystals and inside any three crystals are about 33% and 4% at the same energy,

respectively. However, the number of events for total  $\gamma$ -ray energy deposited inside four crystals is negligible.

# Chapter 5

## Experimental Data Analysis

Data analysis was done using MARCOS code [22], developed at TIFR, LAMPS [27] and RADWARE software packages [28]. The  $\gamma - \gamma$  coincidence relations, obtained by analysing different gated spectra from  $\gamma - \gamma$  matrices and  $\gamma - \gamma - \gamma$  cubes, and intensity relations were used to construct level schemes. Definite spins and parities of the nuclear levels were assigned by measuring multipolarity and type (E/M) of the  $\gamma$  rays emitted from the nuclear excited states, respectively.

### 5.1 Energy and Efficiency Calibration

The pulse height of signal of an incident  $\gamma$ -ray from amplifier is digitized using Analog to Digital Converter (ADC). The digitized number is called channel number of the ADC which is proportional to the energy of the incident  $\gamma$ -ray. Therefore, the energy calibration i.e., the relation between the channel number and the energy can be established using the  $\gamma$ -lines of known radioactive sources to know the energy of unknown  $\gamma$ -ray transitions. The energies and

channel numbers of the known  $\gamma$ -lines are fitted using the following polynomial.

$$E_\gamma = \sum_{i=1}^n (a + b_i x^i) \quad (5.1)$$

where the coefficients  $a$  and  $b_i$  are known as the calibration constants. In case of low energy  $\gamma$ -ray ( $E_\gamma < 200$  keV),  $\sqrt{x}$  term is also included in the above equation. In the present thesis work,  $^{152}\text{Eu}$  and  $^{133}\text{Ba}$  radioactive sources have been used for the energy calibration using the following equation.

$$E_\gamma = a + bx + cx^2 + d\sqrt{x} \quad (5.2)$$

where  $E_\gamma$  and  $x$  are the energy and channel number of the incident  $\gamma$ -ray respectively and  $a$ ,  $b$ ,  $c$  and  $d$  are the calibration constants, which can be obtained from the fitting of the known source data. Using these calibration constants, energy of any unknown  $\gamma$ -ray transition can be obtained just knowing its channel number.

To find the relative intensities of  $\gamma$ -ray transitions, relative efficiency as a function of  $\gamma$ -ray energy is required. The relative efficiency of INGA array, obtained using  $^{152}\text{Eu}$  and  $^{133}\text{Ba}$  sources, is shown in Fig 5.1. The experimental data were fitted with the following equation, using the effit program of the RADWARE package [28].

$$\ln(\epsilon) = \{(A + Bx + Cx^2)^{-G} + (D + Ey + Fy^2)^{-G}\}^{-1/G} \quad (5.3)$$

where  $\epsilon$  is the efficiency,  $x = \ln(\frac{E_\gamma}{100})$ ,  $y = \ln(\frac{E_\gamma}{1000})$  and  $E_\gamma$  is the  $\gamma$ -ray energy in keV.  $A$ ,  $B$ ,  $C$ ,  $D$ ,  $E$ ,  $F$  and  $G$  are the fitting parameters. The values of the fitted parameters for the efficiency data are  $A = 4.366(23)$ ,  $B = 0.16(8)$ ,  $C = 0.0$ ,  $D = 3.273(13)$ ,  $E = -0.55(4)$ ,  $F = 0.09(4)$  and  $G = 15.0(0)$ .

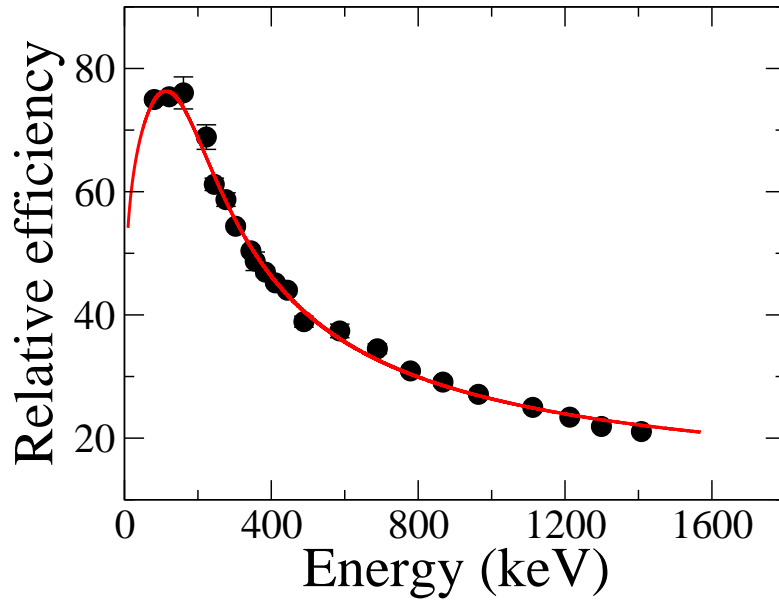


Figure 5.1: Relative efficiency of INGA as a function of  $\gamma$ -ray energy using  $^{152}\text{Eu}$  and  $^{133}\text{Ba}$  sources. The solid line is the fitted curve with the equation ( 5.3).

## 5.2 Construction of Level Scheme

### 5.2.1 Coincidence relation and relative intensity of $\gamma$ -rays

In Fig. 5.2, an example of level scheme is shown. This can be constructed from the coincidence relation among the different  $\gamma$ -rays using  $\gamma - \gamma$  matrix and  $\gamma - \gamma - \gamma$  cube. If we put gate on  $\gamma_2$  energy, then  $\gamma_1, \gamma_3, \gamma_4, \gamma_6$  and  $\gamma_8$   $\gamma$ -lines will appear in the coincidence spectrum. If we put double gate on  $\gamma_1$  and  $\gamma_7$ , then only  $\gamma_5$  and  $\gamma_6$  will appear in the double gated coincidence spectrum. In this way by analysing the single and double gated coincidence spectra, coincidence relation among the different  $\gamma$ -rays can be established. In the fusion evaporation reaction the intensity of the  $\gamma$ -rays decreases with increasing excitation energy. Therefore, in order to construct the level scheme, the intensity balance at each energy level is needed to maintain the proper ordering of the  $\gamma$ -rays in the level scheme.

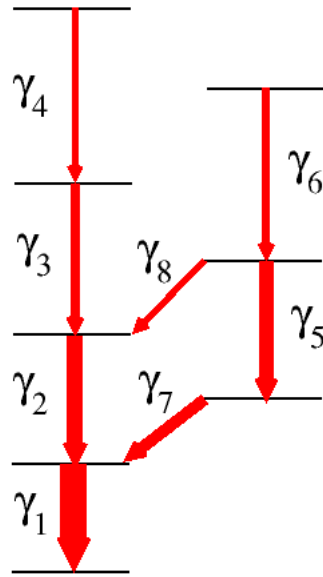


Figure 5.2: Example of level scheme for  $\gamma$ -ray coincidence demonstration.

In case of  $^{169}\text{Tm}$  and  $^{196}\text{Tl}$ , the level schemes were constructed by analysing several double- and single-gated spectra projected from the matrix and the cube but the level scheme of  $^{207}\text{Po}$  was constructed using only single-gated spectra due to limited number of detectors. The relative intensity of each  $\gamma$ -ray was obtained by putting a single gate on a low-lying strong transition from the matrix. Total projection, single- and double- gated  $\gamma$ -ray spectra of  $^{196}\text{Tl}$  are shown in Fig. 5.3. From this figure, it is seen that the number of peaks in the gated spectra are less than in the total projection spectrum. The peaks marked by the red dotted lines are seen in the total projection spectrum, however, they are absent in the single- and double-gated spectra. Moreover, the peaks indicated by the blue dotted lines are clearly seen in the total projection and single-gated spectra, however, they completely disappear in the double-gated spectrum. In this way, we can eliminate the  $\gamma$  rays from a spectrum which are not in coincidence with the  $\gamma$  rays used for gates and hence, the  $\gamma - \gamma$  coincidence relations can be established.

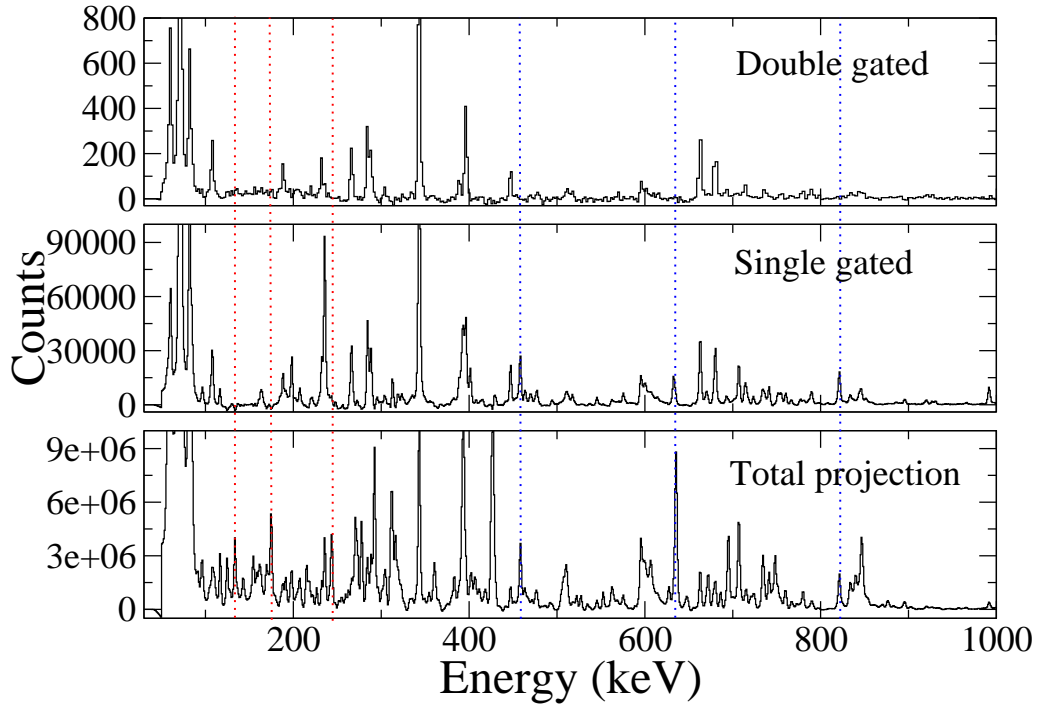


Figure 5.3: Total projection, single- and double- gated  $\gamma$ -ray spectra of  $^{196}\text{Tl}$ .

## 5.3 Spin and Parity Assignment of Nuclear Levels

Spins and parities of the nuclear levels are assigned by determining the multipolarity and type (E/M) of the  $\gamma$ -rays decaying from the levels through the measurements of angular distribution, DCO ratio and polarization.

### 5.3.1 $\gamma$ -ray selection rules

The allowed multipolarity (L) and type (E/M) of a  $\gamma$ -ray in the transition from  $J_i^{\pi_i}$  to  $J_f^{\pi_f}$  are determined by the  $\gamma$ -ray selection rules. Therefore, by measuring the multipolarity and type of a  $\gamma$ -ray, we can easily assign spin-parity of the initial nuclear level, from which the  $\gamma$ -ray decays, if the spin-parity of the final nuclear level is known. The selection rules, which dictate

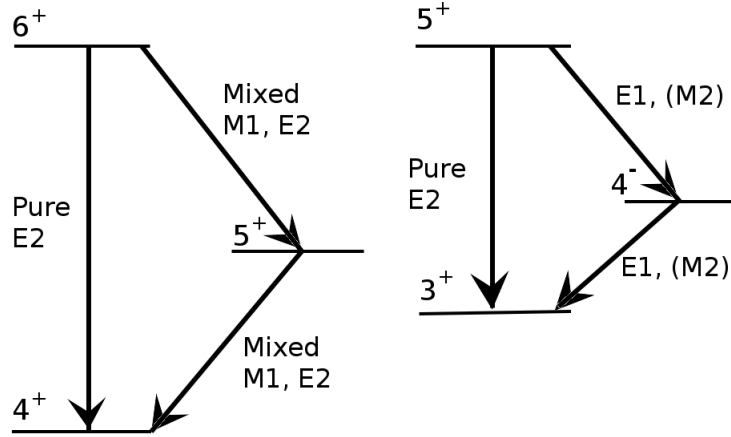


Figure 5.4: Schematic diagram of  $\gamma$ -ray transitions illustrating the effect of  $\gamma$ -ray selection rules on allowed multiplicities.

the allowed multipolarity ( $L$ ) and type (E/M) are:

$$|J_i - J_f| \leq L \leq J_i + J_f \quad (5.4)$$

$$\pi_i \pi_f = (-1)^L \text{ for electric type (E)} \quad (5.5)$$

$$\pi_i \pi_f = (-1)^{L+1} \text{ for magnetic type (M)} \quad (5.6)$$

An example of  $\gamma$ -ray transitions with multiplicities are shown in Fig. 5.4. The figure illustrates the effect of the  $\gamma$ -ray selection rules on allowed multiplicities of  $\gamma$ -ray transitions.

### 5.3.2 Determination of multipolarity of $\gamma$ -ray transitions

The multipolarity of a  $\gamma$ -ray transition is determined by measuring angular distribution and DCO ratio. These are described in the following sections.

## Angular distribution of $\gamma$ -ray transition

Study of angular distribution of  $\gamma$ -rays emitted from nuclear oriented states is used to determine multipolarity of the  $\gamma$ -rays. Excited states of nuclei produced in heavy-ion fusion-evaporation reactions are well aligned relative to the beam direction. Therefore, the  $\gamma$ -rays decaying from these states exhibit characteristic angular distributions depending upon the multiplicities of the  $\gamma$ -rays and the spins of the nuclear excited states involved. In case of complete alignment of the nuclear excited states, the angular distribution of  $\gamma$ -rays [92, 93] is expressed as

$$W(\theta) = \sum_{k=0}^{\lambda} a_k^{max} P_k(\cos \theta) \quad \text{where } k = 0, 2, 4, \dots \quad (5.7)$$

where  $P_k(\cos \theta)$  are the Legendre polynomials and  $a_k^{max}$  are the angular coefficients for the completely aligned nuclear state, which are expressed as

$$a_k^{max}(J_i L_1 L_2 J_f) = \frac{1}{1 + \delta^2} [f_k(J_f L_1 L_1 J_i) + 2\delta f_k(J_f L_1 L_2 J_i) + \delta^2 f_k(J_f L_2 L_2 J_i)] \quad (5.8)$$

where

$$f_k(J_f L_1 L_2 J_i) = B_k(J_i) F_k(J_f L_1 L_2 J_i) \quad (5.9)$$

$$B_k = \sqrt{2J+1} (-1)^J (J0J0|k0) \text{ for integral spin} \quad (5.10)$$

$$B_k = \sqrt{2J+1} (-1)^{J-1/2} (J1/2J-1/2|k0) \text{ for half integral spin} \quad (5.11)$$

$$F_k(J_f L_1 L_2 J_i) = (-1)^{J_f - J_i - 1} \sqrt{(2L_1 + 1)(2L_2 + 1)} (L_1 1 L_2 - 1 | k 0) W(J_i J_i L_1 L_2; k J_f) \quad (5.12)$$

$(J0J0|k0)$ ,  $(J1/2J-1/2|k0)$  and  $(L_1 1 L_2 - 1 | k 0)$  are Clebsch Gordan coefficients.  $W(J_i J_i L_1 L_2; k J_f)$  is a Racah coefficient. The mixing ratio between  $L_1$  and  $L_2$  multiplicities is given by

$$\delta = \frac{(J_f || L_2 || J_i)}{(J_f || L_1 || J_i)} \quad (5.13)$$

In the actual cases, the nuclear oriented states are partially aligned. Therefore, the angular coefficients are expressed as

$$a_k(J_i L_1 L_2 J_f) = \alpha_k(J_i) a_k^{max}(J_i L_1 L_2 J_f) \quad (5.14)$$

Where  $\alpha_k(J_i) = \frac{\rho_k(J_i)}{B_k(J_i)}$  is the attenuation coefficient of alignment.  $\rho_k(J)$  is the degree of alignment of  $J$ -spin state and is expressed as,

$$\rho_k(J) = \sqrt{2J+1} \sum_m (-1)^{J-m} (JmJ-m|k0) P_m(J) \quad (5.15)$$

$P_m$  is the  $m^{th}$  substate population parameter and is expressed as,

$$P_m(J) = \frac{\exp(-\frac{m^2}{2\sigma^2})}{\sum_{m'=-J}^J \exp(-\frac{m'^2}{2\sigma^2})} \quad (5.16)$$

where  $\sigma$  is the measure of the alignment of the nuclear  $m$ -substates and is usually expressed in terms of  $\sigma/J$ . Only when the condition  $P_m(J) = P_{-m}(J)$  is satisfied, the nuclear state is considered aligned. In case of  $\sigma/J \sim 0$ , it corresponds to complete alignment. As the value of  $\sigma/J$  increases, the degree of alignment decreases. In the actual cases, the nuclear oriented states are partially aligned. Therefore, the angular distribution of a  $\gamma$ -ray decaying from the partially aligned nuclear state can be expressed as

$$W(\theta) = \sum_{k=0}^{\lambda} a_k P_k(\cos \theta) = a_0 + a_2 P_2(\cos \theta) + a_4 P_4(\cos \theta) + \dots + a_k P_k(\cos \theta) \quad (5.17)$$

where  $k = 0, 2, 4, \dots, \lambda$

In Fig. 5.5, the calculated angular distributions of pure dipole, quadrupole and octupole  $\gamma$ -ray transitions are shown. The calculated angular distributions of mixed (dipole + quadrupole)

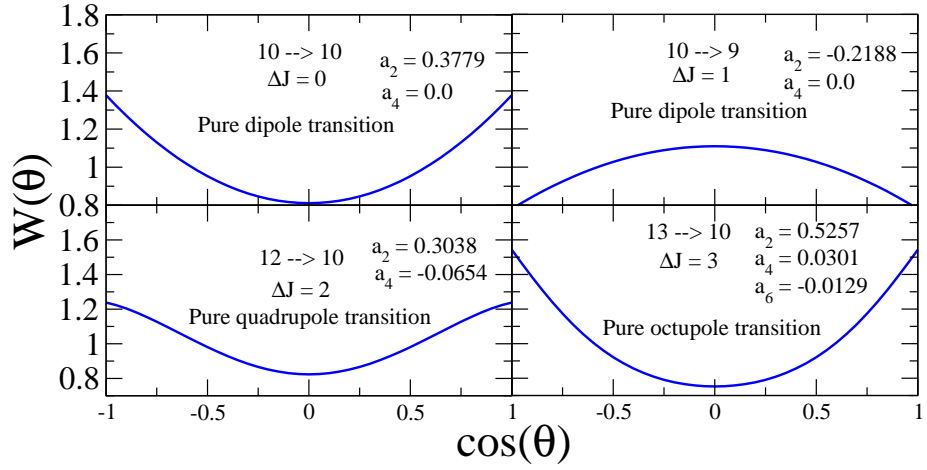


Figure 5.5: Calculated angular distributions of pure dipole, quadrupole and octupole  $\gamma$ -transitions.

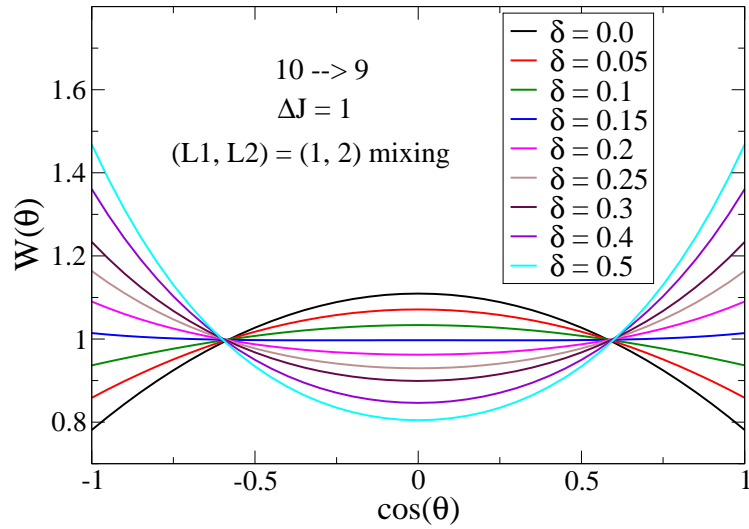


Figure 5.6: Calculated angular distributions of mixed (dipole + quadrupole) transition for different mixing ratios.

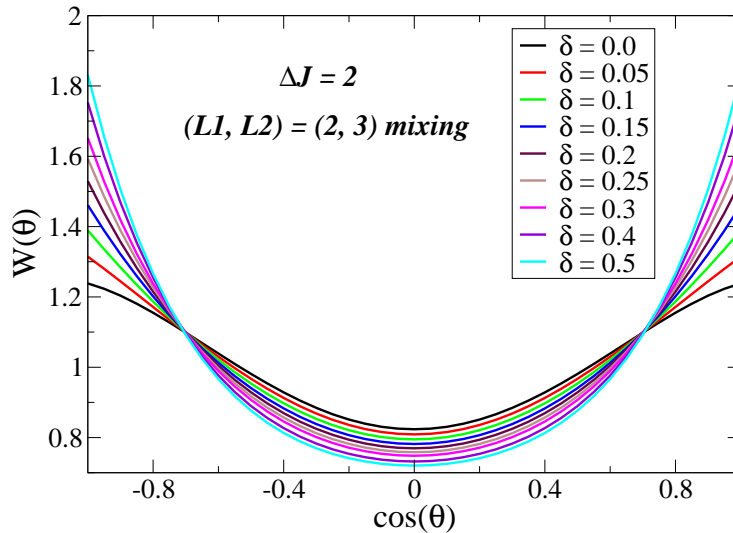


Figure 5.7: Calculated angular distributions of mixed (quadrupole + octupole) transition for different mixing ratios.

and (quadrupole + octupole)  $\gamma$  rays for different mixing ratios ( $\delta$ ) are shown in Fig. 5.6 and Fig. 5.7, respectively.

### Directional Correlation from the Oriented (DCO) states ratio

Due to the contamination of  $\gamma$ -rays in the singles data and limited number of angle combination of detector array, multipolarities of the  $\gamma$ -ray transitions are obtained from the angular correlation analysis using the method of Directional Correlation from the Oriented (DCO) states ratio, following the prescriptions in Ref. [94]. For DCO ratio measurement, an angle-dependent asymmetric  $\gamma - \gamma$  matrix was formed using the coincidence data from the  $-23^\circ$  ( $\theta_1$ ) detectors and the  $90^\circ$  ( $\theta_2$ ) detectors in the INGA array setup and for the VENUS array,  $\theta_1$  and  $\theta_2$  were  $-30^\circ$  and  $90^\circ$ , respectively. The DCO ratio of a  $\gamma$ -transition ( $\gamma_1$ ) is obtained from the ratio of its intensities ( $I_\gamma$ ) gated by a transition ( $\gamma_2$ ) with known multipolarity at the above two angles from the above DCO matrix. This ratio is obtained from the experimental data using

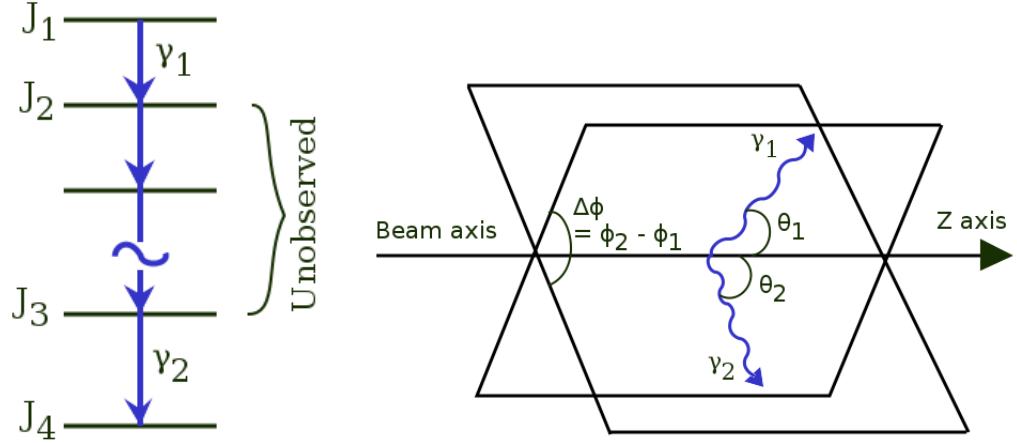


Figure 5.8: Two emitted  $\gamma$  rays,  $\gamma_1$  and  $\gamma_2$ , separated by a number of intermediate unobserved transitions, are shown in a cascade. The directions of the emitted  $\gamma$  rays are shown in terms of spherical angles  $\theta$  and  $\phi$  with respect to the beam axis in the right side figure.

the following relation:

$$R_{DCO} = \frac{I_{\gamma_1} \text{ at } \theta_1, \text{ gated by } \gamma_2 \text{ at } \theta_2}{I_{\gamma_1} \text{ at } \theta_2, \text{ gated by } \gamma_2 \text{ at } \theta_1} \quad (5.18)$$

In the present geometry of INGA and VENUS arrays, theoretical value of DCO ratio of a  $\gamma$ -transition gated by the same multipolarity transition is unity whereas DCO ratio of pure dipole transition gated by stretched quadrupole transition is  $\sim 0.5$  and that of stretched quadrupole transition gated by pure dipole transition is  $\sim 2$ .

Theoretical DCO ratio is calculated using the following directional  $\gamma - \gamma$  correlation function [95, 96] for two  $\gamma$ -rays in a cascade (see Fig. 5.8).

$$W(\Omega_1, \Omega_2) = \sum_{k_1 k_2 k, q_1 q_2 q} (-1)^{k_1+k_2} \sqrt{2J_1+1} \rho_q^k(J_1) A_{k_1}^{k_2 k}(\gamma_1) A_{k_2}(\gamma_2) U_{k_2} \\ \times 4\pi(2k_2+1)^{-1/2} \begin{pmatrix} k_2 & k_1 & k \\ q_2 & q_1 & q \end{pmatrix} Y_{k_1 q_1}(\Omega_1) Y_{k_2 q_2}(\Omega_2) \quad (5.19)$$

$$R_{DCO} = \frac{W(\Omega_1, \Omega_2)}{W(\Omega_2, \Omega_1)} \quad (5.20)$$

where the  $\gamma$ -rays  $\gamma_1$  and  $\gamma_2$  are emitted in the direction  $\Omega_1 = (\theta_1, \phi_1)$  and  $\Omega_2 = (\theta_2, \phi_2)$ , respectively, which are shown in Fig. 5.8. The polarization of the  $\gamma$ -rays is assumed not to be detected, implying that  $k_1$  and  $k_2$  are both even. For only dipole and quadrupole radiations, the  $k_1, k_2$  and  $k$  will take the values:  $k_1 \leq 4, k_2 \leq 4$  and  $|k_1 - k_2| \leq k \leq (k_1 + k_2)$ . For dipole, quadrupole and octupole radiations, the  $k_1, k_2$  and  $k$  will take the values:  $k_1 \leq 8, k_2 \leq 8$  and  $|k_1 - k_2| \leq k \leq (k_1 + k_2)$ . The statistical tensor  $\rho_q^k(J_1)$  describes the initial state orientation of the ensemble of nuclei. For an axially symmetric orientation  $q = 0$  and we may use instead the orientation parameters  $B_k(J_1) = \rho_0^k(J_1)(2J_1 + 1)^{1/2}$ .  $Y_{k_1 q_1}(\Omega_1)$  and  $Y_{k_2 q_2}(\Omega_2)$  are the spherical harmonics for  $\gamma_1$  and  $\gamma_2$  respectively.  $U_{k_2}$  is the deorientation coefficients which describe the deorientation due to the unobserved intermediate transitions.  $A_{k_1}^{k_2 k}(\gamma_1)$  is the correlated directional distribution coefficients for the first  $\gamma$ -transition relative to the second  $\gamma$ -transition and  $A_{k_2}(\gamma_2)$  is the directional distribution coefficients for the second  $\gamma$ -transition. Definitions of the coefficients are given below:

$$A_{k_2}(\gamma_2) = (1 + \delta_2^2)^{-1} [F_{k_2}(J_4 L_2 L_2 J_3) + 2\delta_2 F_{k_2}(J_4 L_2 L'_2 J_3) + \delta_2^2 F_{k_2}(J_4 L'_2 L'_2 J_3)] \quad (5.21)$$

for a mixture of two multipoles  $L_2$  and  $L'_2$  with a mixing ratio  $\delta_2$ .

The ordinary F-coefficients are defined by

$$F_{k_2}(J_4 L_2 L'_2 J_3) = (-1)^{J_3 + J_4 - 1} [(2L_2 + 1)(2L'_2 + 1)(2J_3 + 1)(2k_2 + 1)]^{1/2} \\ \times \begin{pmatrix} L_2 & L'_2 & k_2 \\ 1 & -1 & 0 \end{pmatrix} \begin{Bmatrix} L_2 & L'_2 & k_2 \\ J_3 & J_3 & J_4 \end{Bmatrix} \quad (5.22)$$

The generalized A-coefficients are defined by

$$A_{k_1}^{k_2 k}(\gamma_1) = (1 + \delta_1^2)^{-1} [F_{k_1}^{k_2 k}(J_2 L_1 L_1 J_1) + 2\delta_1 F_{k_1}^{k_2 k}(J_2 L_1 L'_1 J_1) + \delta_1^2 F_{k_1}^{k_2 k}(J_2 L'_1 L'_1 J_1)] \quad (5.23)$$

Table 5.1: Calculated  $R_{\text{DCO}}$  for INGA and VENUS setup. In this calculation,  $\sigma/J = 0.3$  has been considered.

Gate: $\Delta J$ , Multipolarity	$\Delta J$ , Multipolarity	$R_{\text{DCO}}$ (INGA) ( $\theta_1 = -23^\circ, \theta_2 = 90^\circ$ )	$R_{\text{DCO}}$ (VENUS) ( $\theta_1 = -30^\circ, \theta_2 = 90^\circ$ )
2, Quadrupole	2, Quadrupole	1.0	1.0
2, Quadrupole	1, Dipole	0.50	0.52
2, Quadrupole	1, Dipole+Quadrupole	0.13 to 1.46	0.16 to 1.40
2, Quadrupole	0, Dipole	1.09	1.08
2, Quadrupole	0, Dipole+Quadrupole	0.40 to 1.13	0.45 to 1.11
1, Dipole	2, Quadrupole	2.0	1.92

where

$$\begin{aligned}
 F_{k_1}^{k_2 k} (J_2 L_1 L'_1 J_1) &= (-1)^{k+k_2+L'_1+1} [(2L_1+1)(2L'_1+1)(2J_1+1)(2J_2+1)(2k_1+1) \\
 &\quad \times (2k_2+1)(2k+1)]^{1/2} \begin{pmatrix} L_1 & L'_1 & k_1 \\ 1 & -1 & 0 \end{pmatrix} \begin{Bmatrix} J_2 & L_1 & J_1 \\ J_2 & L'_1 & J_1 \\ k_2 & k_1 & k \end{Bmatrix} \quad (5.24)
 \end{aligned}$$

for a mixture of two multipoles  $L_1$  and  $L'_1$  with a mixing ratio  $\delta_1$ .

The calculated DCO ratios gated by  $\gamma$ -rays of different multiplicities considering  $\sigma/J = 0.3$  for INGA and VENUS arrays are shown in Table 5.1.

### Dependence of angular coefficients and DCO ratio on $\sigma/J$ value

The multipolarity of a  $\gamma$  ray can be deduced from the angular distribution of the  $\gamma$  ray or from the Directional Correlation of Oriented (DCO) state ratio. However, in either case, the nuclear m-substates must be aligned in a particular direction, normally perpendicular to the beam direction. For a nucleus with poor alignment, the decay  $\gamma$  ray may not show a good angular distribution pattern. The degree of alignment is given by the spin alignment parameter  $\sigma/J$ ,

Table 5.2: Calculated angular coefficients and  $R_{\text{DCO}}$  for an E2 transition for different  $\sigma/J$  values.

$\sigma/J$	$a_2$	$a_4$	$R_{\text{DCO}}$ gated by stretched E1 $\gamma$
0.1	0.422	-0.188	2.698
0.2	0.388	-0.141	2.463
0.3	0.331	-0.086	2.119
0.4	0.261	-0.045	1.782
0.5	0.198	-0.024	1.539
0.6	0.151	-0.013	1.383

where  $\sigma$  is the width of the m-substate population distribution,  $P_m(J)$ . The smaller the value of  $\sigma/J$ , the better is the alignment.

The heavy-ion induced fusion evaporation reaction is one of the common method to populate the high spin states in nuclei. It has been observed that it is one of the better reactions in which good alignment is obtained. In these types of reactions, the nominal value of  $\sigma/J$  is taken around 0.3. However, the value of  $\sigma/J$  depends on the reaction, used to populate excited states. The degree of alignment is expected to be less (larger value of  $\sigma/J$ ) for light-ion induced reactions.

The  $\gamma$ -ray angular distribution has large dependence on the value of  $\sigma/J$ . The angular distributions calculated for an E2  $\gamma$ -ray is shown in Fig. 5.9 for different values of  $\sigma/J$  and also the corresponding angular coefficients ( $a_2, a_4$ ) and the DCO ratios are shown in Table 5.2. It can be seen that as the alignment decreases (the value of  $\sigma/J$  increases), the distribution becomes flatter and accordingly the value of  $a_2, a_4$  and DCO ratio changes. Therefore, it is important to know the value of  $\sigma/J$  i.e the degree of orientation if the angular distribution ( $W(\theta)$ ) and Directional Correlation of Oriented (DCO) state ratio are used to assign the  $J^\pi$  of a nuclear state.

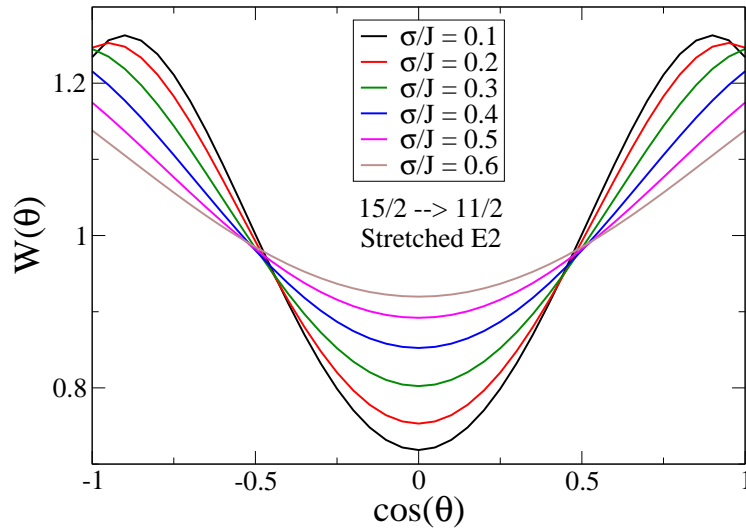


Figure 5.9: Calculated angular distribution of  $\gamma$ -ray for different  $\sigma/J$  values.

### Determination of $\sigma/J$ -value for $^{169}\text{Tm}(^{32}\text{S}, ^{32}\text{S}')^{169}\text{Tm}^*$ Inelastic Reaction

In the present thesis work, the excited states of the stable nucleus  $^{169}\text{Tm}$  has been studied by populating them in the reaction  $^{169}\text{Tm}(^{32}\text{S}, ^{32}\text{S}')^{169}\text{Tm}^*$ . In this reaction, the prompt  $\gamma$ -rays were detected but the excited states can be populated in various inelastic excitations. Therefore, it is not possible to get a-priori knowledge on the value of  $\sigma/J$  in order to do  $J^\pi$  assignment of the excited states.

The value of  $\sigma/J$  in this type of reaction was obtained from the knowledge of the transitions with known multipolarity in  $^{169}\text{Tm}$ . The angular distributions of 323-keV E2 and 337-keV M1+E2  $\gamma$ -transitions are shown in Fig. 5.10. It can be seen from these plot that good angular distribution is obtained, indicating a reasonably smaller value of  $\sigma/J$ .

To obtain the  $\sigma/J$  value, the angular distribution coefficients  $a_2$  and  $a_4$  corresponding to the 323-keV E2  $\gamma$ -transition are calculated for different values of the  $\sigma/J$ . The result of the calculations is shown in Fig. 5.11. In this calculation, the value of  $\sigma/J$  was varied from 0.05 to 1.0. The experimental data point in Fig. 5.11 is the values of the  $a_2$  and  $a_4$  coefficients obtained from the fitting of the experimental angular distribution data of 323-keV E2  $\gamma$ -transition. It can be

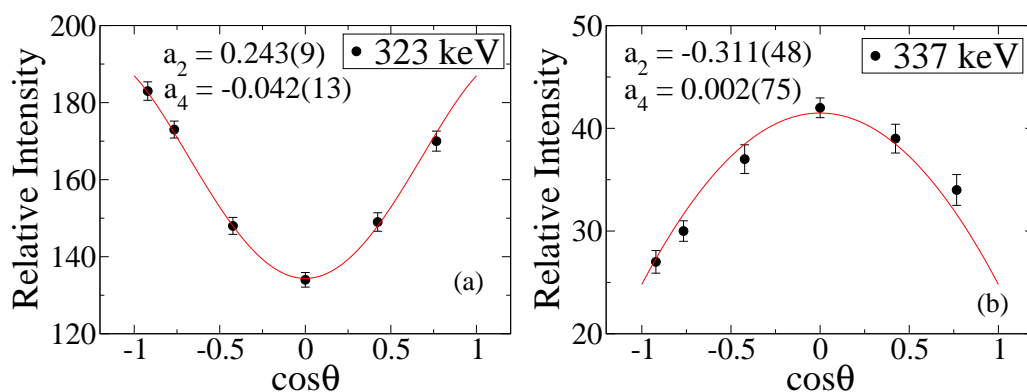


Figure 5.10: Angular distribution of (a) 323-keV and (b) 337-keV  $\gamma$ -transitions. The solid line (red) is the fitted curve to the experimental data points (circle).

seen that the experimental data point corresponds to  $\sigma/J = 0.42(3)$  which can be considered as the degree of alignment obtained in this inelastic types of reaction. This value is about 40% more than the ones in the heavy-ion fusion evaporation reaction and still good enough to perform angular distribution and DCO ratios measurements to get multipolarity and mixing ratios. Considering the  $\sigma/J = 0.42(3)$ , the mixing ratio ( $\delta$ ) has been determined as  $-0.13(4)$  from the fitted angular distribution coefficients of 337 keV (M1/E2)  $\gamma$ -transition (Fig. 5.10). This value of mixing ratio agrees well with  $-0.127(35)$  obtained by Taras et al. [4] and differ slightly with the value  $-0.199(20)$  reported by Robinson et al. [5].

### 5.3.3 Linear polarization of $\gamma$ -ray transitions

The clover detector, because of its geometry, has the advantage of using it as the Compton polarimeter. Out of the four crystals of a clover, any one crystal acts as a scatterer and the two adjacent crystals act as analyzers. Therefore, polarization of  $\gamma$ -ray transitions can be measured by the help of these detectors. From the polarization measurements, the type (E/M) of a  $\gamma$ -ray transition can be obtained and thereby, the parity of a nuclear excited state can be unambiguously assigned. In the present experiments, the Integrated Polarisation Directional

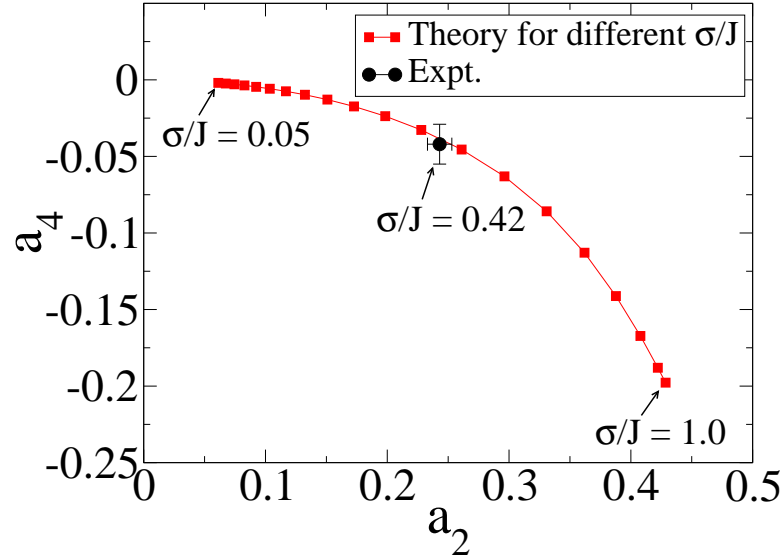


Figure 5.11: Calculated contour plot of  $a_2$  vs.  $a_4$  (red square) for different  $\sigma/J$  values in interval of 0.05 for 323 keV stretched quadrupole transition of  $^{169}\text{Tm}$  produced via  $^{169}\text{Tm}(^{32}\text{S},\text{S}')^{169}\text{Tm}^*$  inelastic reaction has been shown. The experimental angular distribution coefficients (black circle) are compared with the calculation.

Correlation (IPDCO) ratio were obtained following the prescription in Ref [97, 98]. In order to enhance the polarization, data only from the  $90^\circ$  detectors were used. According to the Klein Nishina formula [99], after Compton scattering at the detector, there is a maximum probability that the scattered  $\gamma$ -ray can go either perpendicular or parallel direction to the reaction plane (formed by the beam direction and the direction of emission of the  $\gamma$ -ray) depending on the type (E/M) of the  $\gamma$ -transition. The formula is given by

$$\frac{d\sigma}{d\Omega}(\nu, \xi) = \frac{r_0^2}{2} \left( \frac{E'_\gamma}{E_\gamma} \right)^2 \left[ \frac{E'_\gamma}{E_\gamma} + \frac{E_\gamma}{E'_\gamma} - 2 \sin^2 \nu \cos^2 \xi \right] \quad (5.25)$$

where,  $\nu$  is the Compton scattering angle with respect to the incident  $\gamma$ -ray direction and  $\xi$  is the angle between the electric field vector ( $\vec{E}$ ) of the incident  $\gamma$ -ray with respect to the scattering plane. Here,  $r_0$  is the classical electron radius.  $E_\gamma$  and  $E'_\gamma$  are the incident and scattered  $\gamma$ -ray energy. It is seen from the eq.(5.25) that the differential Compton scattering cross-section becomes maximum when  $\xi = 90^\circ$  i.e. in the direction perpendicular to the electric

field vector ( $\vec{E}$ ) of the incident  $\gamma$ -ray. Now, the experimental polarization asymmetry ( $\Delta_{IPDCO}$ ) is defined as

$$\Delta_{IPDCO} = \frac{a(E_\gamma)N_\perp - N_\parallel}{a(E_\gamma)N_\perp + N_\parallel} \quad (5.26)$$

where,  $N_\perp$  and  $N_\parallel$  are the perpendicular and parallel counts of a  $\gamma$ -transition in the  $90^\circ$  detectors with respect to the reaction plane.  $N_\perp$  and  $N_\parallel$  counts were obtained by forming two  $\gamma - \gamma$  matrices with either perpendicularly or parallelly scattered  $\gamma$ -rays (at  $90^\circ$  detectors) with respect to the reaction plane on one axis and with the coincident  $\gamma$ -rays from all the detectors on the other axis.  $a(E_\gamma)$  is a correction factor which takes care of the geometrical asymmetry of the detector array, asymmetry in placement of the four crystals of a clover with respect to the reaction plane and asymmetry in efficiency of the four crystals of a clover detector. It is defined as  $a(E_\gamma) = N_\parallel/N_\perp$  and its value has been obtained using the  $^{133}\text{Ba}$  and  $^{152}\text{Eu}$  radioactive sources. The asymmetric correction factor  $a(E_\gamma)$  of INGA and VENUS arrays as a function of  $\gamma$ -ray energy are shown in the Fig. 5.12(a) and Fig. 5.12(b) respectively. The experimental data points are fitted with the linear equation  $y = ax + c$ . In case of INGA, the fitted parameters are  $a = 1.0 \times 10^{-4}$  and  $c = 0.9613$  and the average value of  $a(E_\gamma)$  is 1.023(3). In case of VENUS, the fitted parameters are  $a = -2.5 \times 10^{-6}$  and  $c = 1.0180$  and the average value of  $a(E_\gamma)$  is 1.016(2). A positive or negative values of  $\Delta_{IPDCO}$  indicate that a transition is electric or magnetic type, respectively. The perpendicular ( $N_\perp$ ) and parallel ( $N_\parallel$ ) counts of the  $\gamma$ -ray transitions of  $^{196}\text{Tl}$  are shown in Fig. 5.13(a) and Fig. 5.13(b). It is seen from the figures that the 266-, 271-, 285- and 289-keV transitions are magnetic type and 663- and 681-keV are electric type.

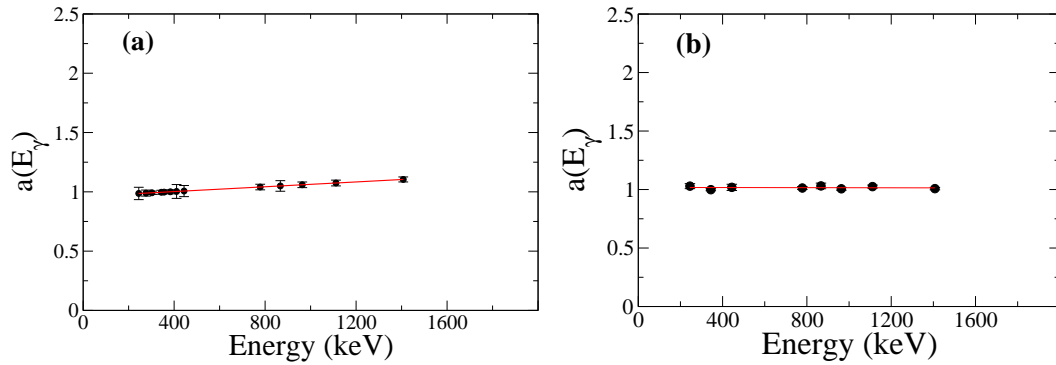


Figure 5.12: Asymmetry correction factor  $a(E_\gamma)$  of (a) INGA and (b) VENUS detector arrays. The solid line is the linear fit.

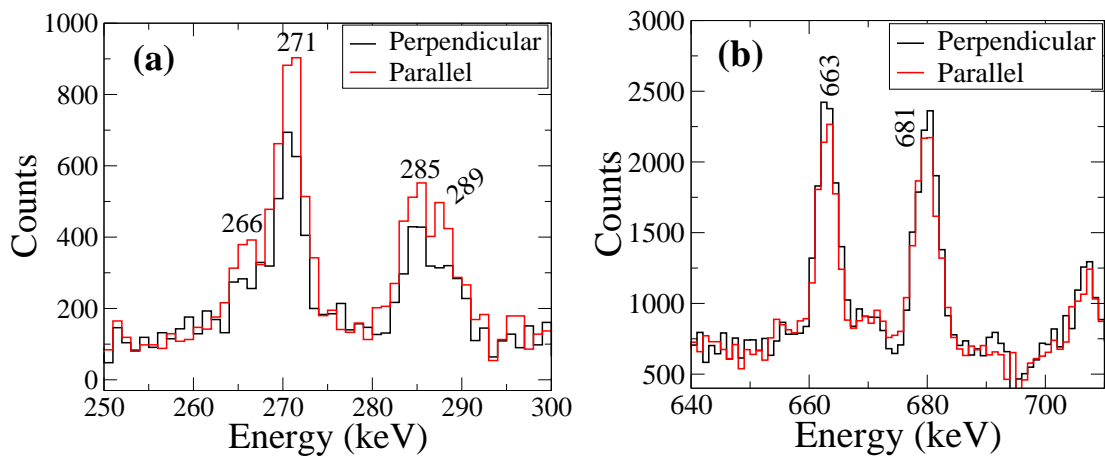


Figure 5.13: (a): Perpendicular counts (black solid line) are less than the parallel counts (red solid line) for 266-, 271-, 285- and 289-keV  $\gamma$ -transitions of  $^{196}\text{Tl}$  and therefore, these are magnetic in nature. (b): For 663- and 681-keV transitions of  $^{196}\text{Tl}$ , perpendicular counts are greater than the parallel counts and therefore, these are electric type.

The experimental  $\Delta_{IPDCO}$  is related to the linear polarization of  $\gamma$ -ray by the following relation

$$P = \frac{\Delta_{IPDCO}}{Q} \quad (5.27)$$

where,

$$Q = \frac{\frac{d\sigma}{d\Omega}(\nu = 90^\circ, \xi = 90^\circ) - \frac{d\sigma}{d\Omega}(\nu = 90^\circ, \xi = 0^\circ)}{\frac{d\sigma}{d\Omega}(\nu = 90^\circ, \xi = 90^\circ) + \frac{d\sigma}{d\Omega}(\nu = 90^\circ, \xi = 0^\circ)} \quad (5.28)$$

is the polarization sensitivity of the Compton polarimeter. It depends on the incident  $\gamma$ -ray energy and the geometry of the polarimeter. It is obtained for a point scatterer and point analyzer from the Klein-Nishina formula. However, the polarization sensitivity can be reduced to finite size of scatterer and analyzer by the parameterized equation as

$$Q(E_\gamma) = (A + BE_\gamma)Q_0(E_\gamma) \quad (5.29)$$

with

$$Q_0(E_\gamma) = \frac{\alpha + 1}{\alpha^2 + \alpha + 1} \quad (5.30)$$

where  $\alpha = E_\gamma/m_e c^2$ ,  $E_\gamma$  is the incident  $\gamma$ -ray energy and  $m_e c^2$  is the electron rest mass energy. The parameters,  $A$  and  $B$  in  $Q(E_\gamma)$  can be experimentally determined using  $\gamma$ -rays with known polarizations. In the present thesis work,  $A = 0.446(6)$  and  $B = -0.000099(7) \text{ keV}^{-1}$  are taken from Ref. [101]. Therefore, the linear polarization of the  $\gamma$ -rays can be obtained from the measured  $\Delta_{IPDCO}$  and  $Q(E_\gamma)$  values.

The angular distribution of linearly polarized  $\gamma$ -rays emitted from an axially oriented ensemble of nuclei is given by [96, 100, 101]

$$W(\theta, \phi) = \frac{d\Omega}{8\pi} \sum_{\lambda=even} B_\lambda U_\lambda \left[ A_\lambda P_\lambda(\cos \theta) + 2A_{\lambda 2} P_{\lambda 2}^{(2)}(\cos \theta)(\cos 2\phi) \right] \quad (5.31)$$

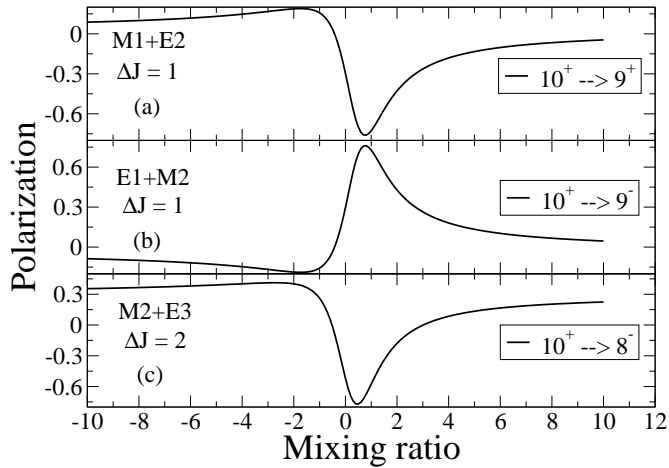


Figure 5.14: Calculated polarization of (a) (M1/E2) mixed  $\gamma$ -ray for  $\Delta J = 1$ , (b) (E1/M2) mixed  $\gamma$ -ray for  $\Delta J = 1$  and (c) (M2/E3) mixed  $\gamma$ -ray for  $\Delta J = 2$  as a function of mixing ratio.

where,  $\theta$  is the angle between the direction of the outgoing  $\gamma$ -ray with respect to the beam axis and  $\phi$  is the angle between the electric field vector  $\vec{E}$  of the  $\gamma$ -ray with respect to the scattering plane.  $B_\lambda$  are orientation tensors describing the degree of orientation of the parent nucleus and  $U_\lambda$  are deorientation coefficients.  $P_\lambda(\cos \theta)$  and  $P_{\lambda 2}^{(2)}(\cos \theta)$  are Legendre and associated Legendre polynomials respectively. The coefficients  $A_\lambda$  and  $A_{\lambda 2}$  can be obtained from Ref.[96, 100].

The degree of linear polarization can be defined as

$$P_{cal}(\theta) = \frac{W(\theta, \phi = 0^\circ) - W(\theta, \phi = 90^\circ)}{W(\theta, \phi = 0^\circ) + W(\theta, \phi = 90^\circ)} \quad (5.32)$$

where the normalization is such that  $-1 \leq P(\theta) \leq +1$ . For completely polarized  $\gamma$ -rays,  $P(\theta) = \pm 1$  and for the completely unpolarized  $\gamma$ -rays,  $P(\theta) = 0$ . In experiments, the angle  $\theta$  is chosen to be  $90^\circ$  to enhance the magnitude of polarization. Now putting eq.(5.31) into eq.(5.32), the following form of  $P_{cal}(\theta)$  [102] is obtained:

$$P_{cal}(\theta) = \frac{\sum_\lambda a_\lambda^{(2)} P_\lambda^{(2)}(\cos \theta)}{\sum_\lambda a_\lambda P_\lambda(\cos \theta)} \quad (5.33)$$

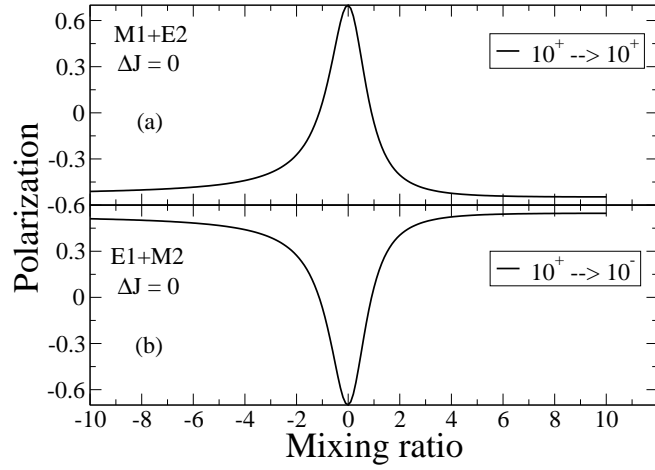


Figure 5.15: Calculated polarization of (a) (M1/E2) mixed  $\gamma$ -ray for  $\Delta J = 0$  and (b) (E1/M2) mixed  $\gamma$ -ray for  $\Delta J = 0$  as a function of mixing ratio.

where,

$$\begin{aligned}
 a_{\lambda}^{(2)} = \frac{1}{1 + \delta^2} & \left[ -k_{\lambda}(L_1 L_2) F_{\lambda}(J_f L_1 L_2 J_i) \right. \\
 & + 2\delta k_{\lambda}(L_1 L_2) F_{\lambda}(J_f L_1 L_2 J_i) \\
 & \left. + \delta^2 k_{\lambda}(L_1 L_2) F_{\lambda}(J_f L_1 L_2 J_i) \right]
 \end{aligned} \tag{5.34}$$

$a_{\lambda}^{(2)}$  are the linear polarization distribution coefficients,  $\delta$  is mixing ratio,  $F_{\lambda}(J_f L_1 L_2 J_i)$  function is defined in eq.(5.12) and  $k_{\lambda}(L_1 L_2)$  can be obtained from Ref. [103].  $a_{\lambda} = B_{\lambda} U_{\lambda} A_{\lambda}$  are the angular distribution coefficients. By introducing a linear polarization mixing coefficient  $H_{\lambda}(L_1, L_2)$  [104] as

$$H_{\lambda}(L_1, L_2) = \frac{2a_{\lambda}^{(2)}}{a_{\lambda}} \tag{5.35}$$

the polarization  $P_{cal}(\theta)$  for  $\theta = 90^{\circ}$  and  $\lambda_{even} \leq 4$  can be expressed as

$$P_{cal}(90^{\circ}) = \pm \frac{3a_2 H_2 - 7.5a_4 H_4}{2 - a_2 + 0.75a_4} \tag{5.36}$$

where  $+(-)$  sign is for the transition without (with) parity change.  $a_2$  and  $a_4$  are the angular distribution coefficients. For a pure M1 or E1 transition ( $\delta = 0$ ),  $H_2(L_1 = 1, L_2 = 2) = 1$  and  $H_4(L_1 = 1, L_2 = 2) = -\frac{1}{6}$ . For a dipole-quadrupole mixed transition  $H_\lambda$  can be expressed as

$$H_2(L_1 = 1, L_2 = 2) = \frac{F_2(11) - \frac{2}{3}\delta F_2(12) + \delta^2 F_2(22)}{F_2(11) + 2\delta F_2(12) + \delta^2 F_2(22)} \quad (5.37)$$

$$H_4(L_1 = 1, L_2 = 2) = -\frac{1}{6} \quad (5.38)$$

For a pure E2 or M2 transition,  $H_2(L_1 = 2, L_2 = 3) = -1$  and  $H_4(L_1 = 2, L_2 = 3) = \frac{1}{6}$ . For a quadrupole-octupole mixed transition  $H_\lambda$  can be expressed as

$$H_2(L_1 = 2, L_2 = 3) = \frac{-F_2(22) - \delta F_2(23) + \frac{2}{3}\delta^2 F_2(33)}{F_2(22) + 2\delta F_2(23) + \delta^2 F_2(33)} \quad (5.39)$$

$$H_4(L_1 = 2, L_2 = 3) = \frac{\frac{1}{6}F_4(22) - \frac{1}{15}\delta F_4(23) + \frac{2}{3}\delta^2 F_4(33)}{F_4(22) + 2\delta F_4(23) + \delta^2 F_4(33)} \quad (5.40)$$

Calculated polarizations ( $P_{cal}(\theta)$ ) of (M1/E2) mixed  $\gamma$ -transition, from  $J_i = 10^+$  to  $J_f = 9^+$ , and (E1/M2) mixed  $\gamma$ -transition, from  $J_i = 10^+$  to  $J_f = 9^-$ , for  $\Delta J = 1$  as a function of mixing ratio ( $\delta$ ) are shown in Fig. 5.14(a) and Fig. 5.14(b), respectively. Also that of (M2/E3) mixed  $\gamma$ -transition from  $J_i = 10^+$  to  $J_f = 8^-$  for  $\Delta J = 2$  are shown in Fig. 5.14(c). For  $\Delta J = 0$ , polarizations of (M1/E2) and (E1/M2)  $\gamma$ -ray transitions are shown in Fig. 5.15(a) and Fig. 5.15(b), respectively. Polarizations and DCO ratios of 337 keV (M1/E2) mixed transition and 235 keV E1 transition in  $^{169}\text{Tm}$  have been experimentally determined and compared with the calculated contour plots of polarization vs. DCO ratio as a function of mixing ratio, shown in Fig. 5.16(a) and Fig. 5.16(b).

### Development of the code ADRAP

All the above mentioned theoretical calculations have been performed in the present thesis work. For this, a new code, ADRAP, has been developed. This code has been written in the C++ language with graphical interface using GTK+. This code calculates the  $F_k$ ,  $B_k$  and  $U_k$

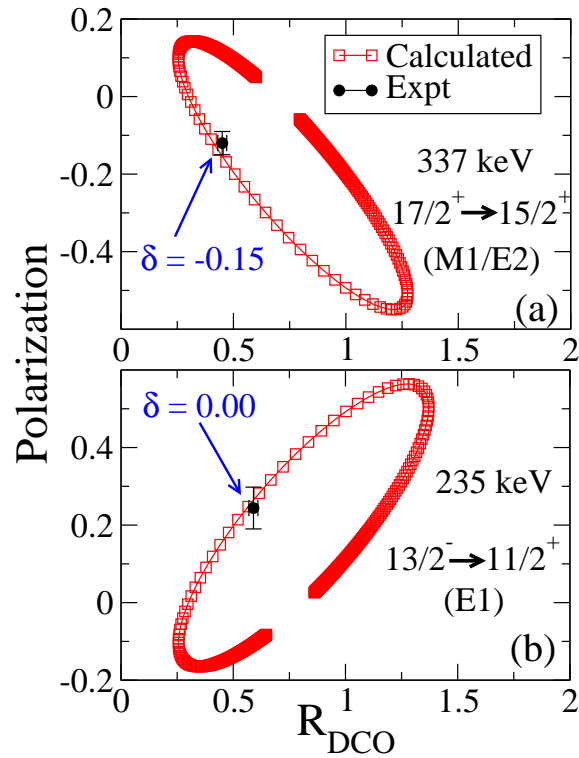


Figure 5.16: Contour plot of calculated  $R_{DCO}$  and polarization for the (a) 337-keV,  $17/2^+ \rightarrow 15/2^+$  transition in the band B1 and (b) 235-keV,  $13/2^- \rightarrow 11/2^+$  connecting transition between band B1 and B2 of  $^{169}\text{Tm}$ . The measured values are shown as experimental points. The values of mixing ratio  $\delta$  for the calculated points close to the experimental point are shown.

values from the user-supplied data of the multipolarity of the transition and the spins of the initial and final states. From these, it calculates the angular distribution coefficients  $a_k$  for a transition using a supplied value of  $\sigma/J$  to compare with the measured angular distribution co-efficients. The calculations can be repeated for different values of the mixing ratio ( $\delta$ ) for a mixed transition and the mixing ratio can be obtained from the comparison of calculated and measured values. The calculations can be performed up to hexadecapole multipolarity. The  $R_{DCO}$  values are calculated (up to octupole multipolarity) in this code by using equation 5.19. The polarization (P) is also calculated by this code which can be compared with the experimental values for unambiguous assignment of spin and parity of a state.

## 5.4 Some useful quantities for the interpretation of experimental data

To study rotational bands of nuclei, some deduced quantities like rotational frequency ( $\omega$ ), quasi-particle aligned angular momentum ( $i_x$ ), kinematic moment of inertia ( $J^{(1)}$ ), dynamic moment of inertia ( $J^{(2)}$ ), quasi-particle Routhian ( $e'$ ) and  $B(M1)/B(E2)$  ratio etc. play very important role.

Using a simple rotational model, the rotational frequency ( $\omega$ ) of a nucleus emitting  $\gamma$ -ray transition between the states of spin  $I + 1$  and  $I - 1$  can be extracted from the following the relation,

$$\begin{aligned}
 \omega(I) &= \frac{dE(I)}{dI_x(I)} \\
 &\approx \frac{E(I + 1) - E(I - 1)}{I_x(I + 1) - I_x(I - 1)} \\
 &= \frac{E_\gamma}{I_x(I + 1) - I_x(I - 1)}
 \end{aligned} \tag{5.41}$$

Where  $E_\gamma$  is the energy of the  $\gamma$ -ray decaying from the  $I + 1$  state to  $I - 1$  state.  $E(I)$  and  $I_x$  are the nuclear level energy and angular momentum along rotation axis at spin  $I$ , respectively.  $I_x$  can be calculated using Pythagoras theorem,

$$I_x(I) = \sqrt{I(I+1) - K^2} \approx \sqrt{\left(I + \frac{1}{2}\right)^2 - K^2} \quad (5.42)$$

Where  $K$  is the projection of angular momentum  $I$  on the nuclear symmetry axis. Using the above equation (5.42) in the expression of  $\omega$ , we get,

$$\begin{aligned} \omega(I) &\approx \frac{E_\gamma}{\sqrt{\left(I + \frac{3}{2}\right)^2 - K^2} - \sqrt{\left(I - \frac{1}{2}\right)^2 - K^2}} \\ &\approx \frac{E_\gamma}{2} (I \gg K) \end{aligned} \quad (5.43)$$

### 5.4.1 Quasi-particle aligned angular momentum

The quasi-particle aligned angular momentum,  $i_x$ , is the angular momentum generated by unpaired nucleons. The contribution to  $i_x$  can come from the odd-particle (proton / neutron) of an odd-A nucleus and also after the breaking of a pair of valence nucleons in time-reversed orbits from the core of a nucleus along the rotation axis. To obtain the  $i_x$  from the rotational angular momentum ( $I_x$ ) of the rotating nucleus, we need to subtract the core contribution ( $I_x^{ref}$ ) from the rotational angular momentum ( $I_x$ ).

$$i_x = I_x - I_x^{ref} \quad (5.44)$$

where,

$$I_x^{ref} = J_0\omega + J_1\omega^3 \quad (5.45)$$

Where  $J_0$  and  $J_1$  are the Harris parameters [105]. The alignment ( $i_x$ ) is an additive quantity [106] and therefore, it is useful for the interpretation of any band structure based on multi-

quasi-particle configuration. It is generally plotted as a function of rotational frequency. The variation of the aligned angular momentum ( $i_x$ ) with the rotational frequency can be used to determine the intrinsic structural properties of rotational bands (e.g. band crossing frequency, nature of pair alignment etc.).

### 5.4.2 Experimental quasi-particle Routhian

The experimental quasi-particle Routhian is expressed as,

$$e'(I) = E_{expt}^\omega(I) - E_{ref}^\omega(I) \quad (5.46)$$

where,

$$E_{expt}^\omega(I) = \frac{1}{2}[E(I+1) + E(I-1)] - \omega(I)I_x(I) \quad (5.47)$$

$$E_{ref}^\omega(I) = -\frac{1}{2}\omega^2 J_0 - \frac{1}{4}\omega^4 J_1 + \frac{1}{8}\frac{\hbar^2}{J_0} \quad (5.48)$$

This quantity is generally plotted as a function of rotational frequency. The nature of the Routhian depends on the quasi-particle orbitals involved. The band crossing frequency and interaction strength between g- and s-band can be understood from the experimental Routhian plot. The quantity is simply additive and can be compared with theoretical calculation.

### 5.4.3 Moment of inertia

Collective rotation of a nucleus can be described by the two moments of inertia, kinematic moment of inertia ( $\mathcal{J}^{(1)}$ ) and dynamic moment of inertia ( $\mathcal{J}^{(2)}$ ).

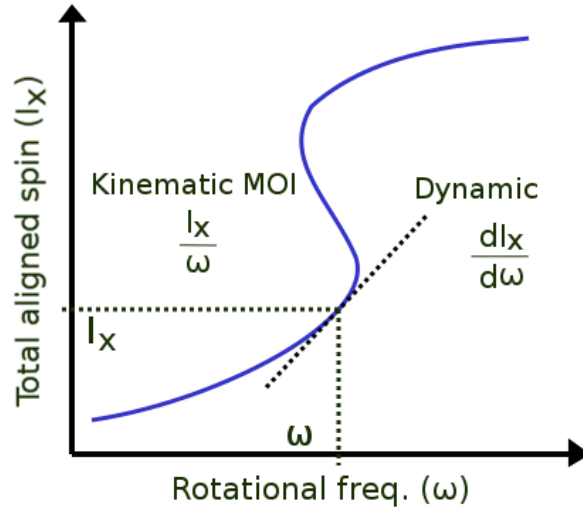


Figure 5.17: A schematic diagram illustrating the kinematic and dynamic moment of inertia.

#### Kinematic moment of inertia

$$\mathcal{J}^{(1)} = \frac{I_x}{\omega} \quad (5.49)$$

#### Dynamic moment of inertia

$$\begin{aligned} \mathcal{J}^{(2)} &= \frac{dI_x}{d\omega} \\ &\approx \frac{4\hbar}{\Delta E_\gamma} \end{aligned} \quad (5.50)$$

As  $\mathcal{J}^{(2)}$  has no spin dependence, it is therefore useful quantity to characterize a band whose level-spins are not known. The variation of the  $\mathcal{J}^{(1)}$  and  $\mathcal{J}^{(2)}$  as a function of spin or rotational frequency can be used to determine the intrinsic structural properties of rotational bands.

#### 5.4.4 Experimental B(M1)/B(E2) ratio

The B(M1)/B(E2) ratios of a band depend on single-particle configuration and structural properties of the band. The experimental B(M1)/B(E2) ratios can be extracted by using the M1

( $\Delta I = 1$ ) and E2 ( $\Delta I = 2$ )  $\gamma$ -ray intensities of the band and the ratio is defined by the following relation [107, 108]:

$$\frac{B(M1; I \rightarrow I - 1)}{B(E2; I \rightarrow I - 2)} = 0.697 \frac{I_\gamma(\Delta I = 1) E_\gamma^5(E2)}{I_\gamma(\Delta I = 2) E_\gamma^3(M1)} \frac{1}{1 + \delta^2} \left( \frac{\mu_N}{eb} \right)^2 \quad (5.51)$$

Here,  $I_\gamma$  ( $\Delta I = 1$ ) and  $I_\gamma$  ( $\Delta I = 2$ ), and  $E_\gamma$  (M1) and  $E_\gamma$  (E2) are the intensities and energies of the M1 ( $\Delta I = 1$ ) and E2 ( $\Delta I = 2$ )  $\gamma$ -ray transitions. Energy is in MeV unit. The quantity  $\delta$  determines the M1/E2 mixing ratio of the M1( $\Delta I = 1$ ) transition.

### 5.4.5 Calculated B(M1)/B(E2) ratio

Calculated B(M1)/B(E2) ratios are extremely sensitive to the single-particle configurations because of the involvement of the corresponding quasi-particle g-factors. Therefore, calculated B(M1)/B(E2) ratios are compared with experimental B(M1)/B(E2) ratios to assign band configuration. The calculated B(M1)/B(E2) ratios are obtained from the semiclassical Dönau-Frauendorf model using the following formula [109, 110, 111]:

$$\frac{B(M1; I \rightarrow I - 1)}{B(E2; I \rightarrow I - 2)} = \frac{12}{5Q_0^2 \cos^2(\gamma + 30^\circ)} \left( 1 - \frac{K^2}{(I - 1/2)^2} \right)^{-2} (A - B)^2 \left( \frac{\mu_N}{eb} \right)^2 \quad (5.52)$$

where,

$$A = \left( 1 - \frac{K^2}{I^2} \right)^{1/2} \left\{ \Omega_1(g_1 - g_R) \left( 1 \pm \frac{\Delta e}{\hbar\omega} \right) + \sum_n \Omega_n(g_n - g_R) \right\}$$

$$B = \frac{K}{I} \left\{ (g_1 - g_R)i_1 + \sum_n (g_n - g_R)i_n \right\}$$

Where  $g_n$  and  $g_R$  are the g-factors for quasi-particle and even-even core of a nucleus respectively, and  $i_n$  are the quasi-particle aligned angular momenta.  $K = \sum_n \Omega_n$  is total nuclear spin projection along nuclear symmetry axis.  $g_1$  and  $i_1$  stands for rotation-aligned quasi-particle

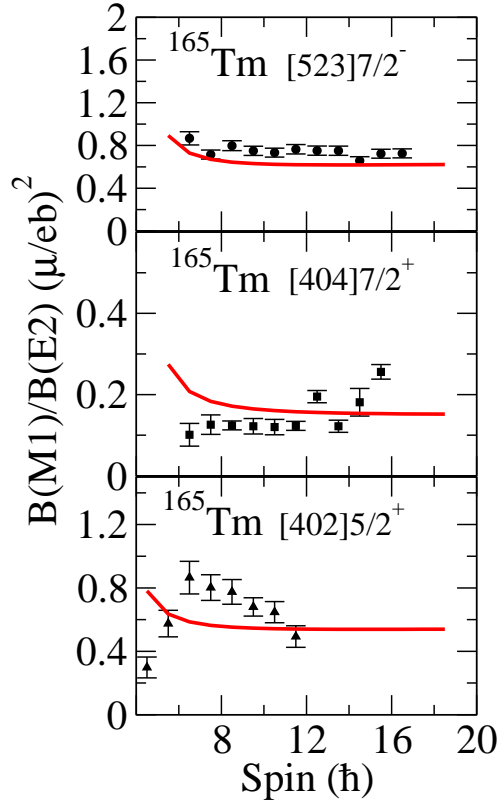


Figure 5.18:  $B(M1)/B(E2)$  ratios for the bands based on different configurations in  $^{165}\text{Tm}$ . The experimental data (black circle) are compared with calculated ones (red solid line). The experimental data are taken from Ref. [2].

which is responsible for signature splitting. Signature splitting term  $\Delta e$  can be extracted from experimental routhians of signature partners.  $\beta_2$  and  $\gamma$  are the deformation parameters.  $Q_0$  is the intrinsic quadrupole moment and obtained using the  $Q_0 = \frac{3}{\sqrt{5\pi}}R^2Z\beta_2(1 + 0.16\beta_2)$  relation. Experimental and calculated  $B(M1)/B(E2)$  ratios for the three bands in  $^{165}\text{Tm}$ , based on  $[402]5/2^+$ ,  $[404]7/2^+$  and  $[523]7/2^-$  Nilsson states, are shown in Fig. 5.18. The agreement of calculated and measured  $B(M1)/B(E2)$  ratios for  $[402]5/2^+$  band is not as good as the other two bands. However, the calculated values are closely matching with those in Ref. [2] where a good agreement has been claimed. In these calculations, same values of  $Q_0$  ( $= 7.2$  eb) and  $g_R$  ( $= 0.32$ ) have been assumed for all the bands which may not be the case and this may be responsible for the observed difference.

# Chapter 6

## Study of Band Structures in $^{169}\text{Tm}$

### 6.1 Introduction

The high spin structures of odd-A Tm ( $Z = 69$ ) nuclei around  $A \sim 170$  shows interesting features. The proton Fermi level lies near the mid-shell region of the two magic numbers at  $Z = 50$  and  $Z = 82$ . As they are situated in the deformed rare-earth region, these nuclei are well deformed. The lighter nuclei are reported to be triaxial [1, 112, 113, 114, 115, 116] and the heavier ones ( $A > 163$ ) are axially deformed [2, 3, 4, 5, 6]. For the heavier Tm isotopes the neutron Fermi level lies near the deformed shell gap at the neutron number  $N = 98$ . Several rotational bands based on different Nilsson states, originated from unique negative parity  $h_{11/2}$  and  $h_{9/2}$  proton orbitals as well as positive parity  $d_{3/2}$ ,  $d_{5/2}$ , and  $g_{7/2}$  proton orbitals, have been observed for the neutron deficient odd-A isotopes [2, 3, 4, 5, 6]. However, the band crossing and the band interaction phenomena for these isotopes are not well studied due to lack of high spin data above the band crossing except for a few of those isotopes. The band crossing in Tm isotopes occurs due to the alignment of neutron particles by pair breaking. The nature of a band crossing depends on the orbitals involved in the particle alignment and on the deformation of the nucleus. From the systematic study of the  $i_{13/2}$  neutron pair alignment in the ground

state band based on  $\pi[411]1/2^+$  Nilsson state in odd-A Thulium isotopes, it is observed that the band crossings of the two neighbouring isotopes,  $^{165}\text{Tm}$  [2] and  $^{167}\text{Tm}$  [3] show contrasting behavior. A sharp back-bending is observed in  $^{165}\text{Tm}$ , while a gradual or smooth up-bending is reported for  $^{167}\text{Tm}$ , as shown in Fig. 1.3 in Chapter 1. However, the very similar gain in alignment for these two isotopes indicates that the neutron pair alignments take place at the same orbitals. In case of  $^{169}\text{Tm}$  [4, 5] and heavier isotopes, the high spin data are limited to below the band crossing region. Therefore, a systematic investigation of the effect of the neutron Fermi level on the alignment process could not be extended to the heavier isotopes. In the present work, the level scheme of  $^{169}\text{Tm}$  has been extended to observe the band crossing in the ground state band based on  $\pi[411]1/2^+$  to shed some light on this issue.

The life-time measurements in Ref. [4] indicated a deformation of  $\beta_2 \sim 0.3$  in  $^{169}\text{Tm}$ . Assuming prolate deformation, the Nilsson diagram indicates that at  $\beta_2 \sim 0.3$ , the proton Fermi level for  $^{169}\text{Tm}$  lies near the  $[411]1/2^+$  Nilsson orbital originated from the  $d_{3/2}$  parentage while the  $[541]1/2^-$  orbital, originated from the  $h_{9/2}$  parentage, intrudes strongly from above the  $Z = 82$  shell gap and lies very close to it. These two orbitals differ by  $\Delta l = 3$  and  $\Delta j = 3$ , where  $l$  and  $j$  are orbital angular momentum and total angular momentum quantum numbers, respectively. The existence of such orbitals in close proximity induces octupole correlation in nuclei, such as in the Barium, Lanthanum, Cerium, Samarium, etc nuclei in  $A \sim 140$  region [40, 41, 42, 43, 44, 45]. In this region, the  $h_{11/2} - d_{5/2}$  pair of proton orbitals and  $i_{13/2} - f_{7/2}$  pair of neutron orbitals, both characterized by  $\Delta l = 3$  and  $\Delta j = 3$ , lie very close to each other near the proton and the neutron Fermi levels. In  $^{169}\text{Tm}$ , bands based on  $\pi[541]1/2^-$  and  $\pi[411]1/2^+$  Nilsson orbitals have been identified within about 400 keV to each other [117] but the  $i_{13/2} - f_{7/2}$  pair of neutron orbitals are not available in close proximity. Therefore, it would be interesting to investigate if and to what extent octupole correlation exists in  $^{169}\text{Tm}$  for which only proton Fermi level is situated close to a pair of  $\Delta l = 3$  and  $\Delta j = 3$  orbitals.

## 6.2 Experiment and Data Analysis

The excited states in  $^{169}\text{Tm}$  were produced using the reaction  $^{169}\text{Tm}(^{32}\text{S}, ^{32}\text{S}')^{169}\text{Tm}^*$  at the beam energy of 164 MeV from the 14-UD BARC-TIFR Pelletron, Mumbai on a self-supporting thick (8 mg/cm<sup>2</sup>) foil of  $^{169}\text{Tm}$ . The gamma rays were detected using 19 Compton-suppressed clover HPGe detectors of INGA (Indian National Gamma Array). The clover detectors were arranged at six different angles with three clovers each at  $\pm 40^\circ$  and  $\pm 65^\circ$  and  $-23^\circ$  while four clovers were at  $90^\circ$  angles during the experiment. For efficiency and energy calibration of the detectors,  $^{133}\text{Ba}$  and  $^{152}\text{Eu}$  radioactive sources were used.

A digital data acquisition (DDAQ) system, based on Pixie-16 modules [21, 22], has been used for the data collection with a sampling rate of 100 MHz for each detector in this experiment. Time-stamped  $\gamma - \gamma$  coincidence data were recorded when at least two clover detectors were fired at a time window of 150 ns in coincidence mode. Raw data sorting was done by Multi-pARameter time-stamped based COincidence Search (MARCOS) code [22], developed at TIFR, Mumbai. The  $\gamma - \gamma$  matrix and  $\gamma - \gamma - \gamma$  cube were formed by MARCOS and Radware [28] software packages.  $\pm 50$  ns time window was chosen for the above matrix and cube formation.

The spins and parities of the levels in  $^{169}\text{Tm}$  were known from the previous work [4, 5, 117] using  $\gamma$ -ray angular correlation studies. In this work, Directional Correlation from Oriented states (DCO) ratio and polarization of the  $\gamma$ -transitions have been obtained in order to assign spins and parities of the new levels and also to test the previous assignments. DCO and IPDCO ratio measurement processes have been described in Section 5.3.

## 6.3 Experimental Results

Table 6.1 shows the intensity, DCO ratio, IPDCO ratio, multipolarity and the other relevant parameters of the  $\gamma$ -rays observed in the present work which are placed in the proposed level

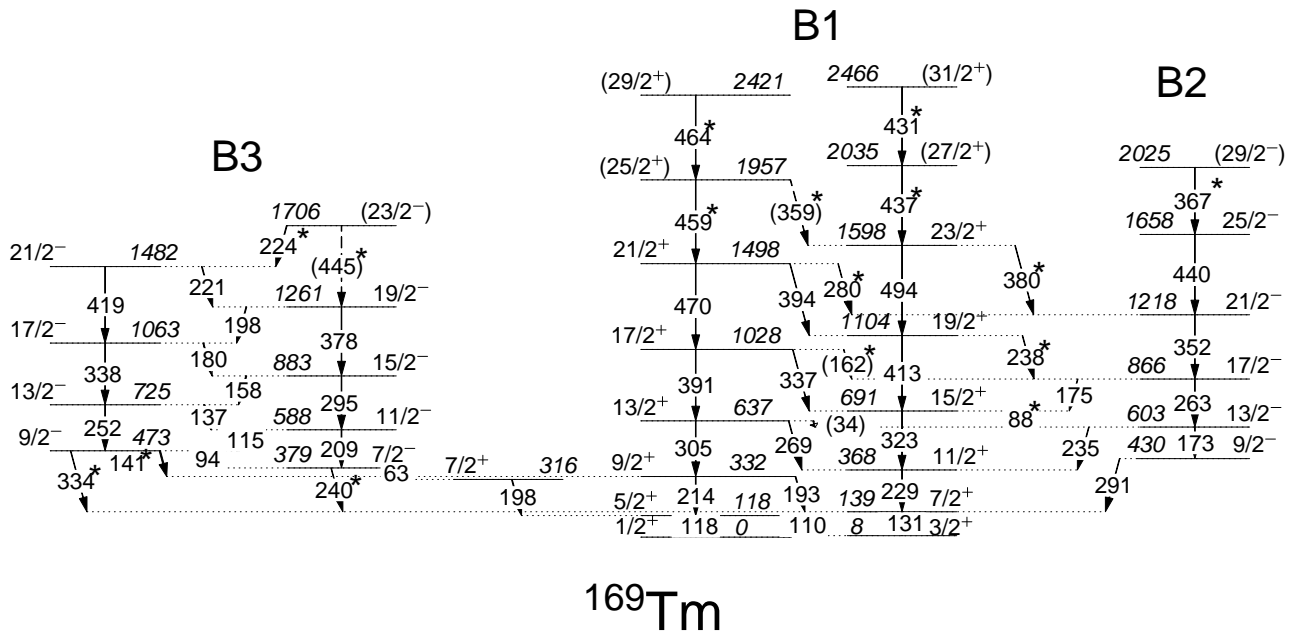


Figure 6.1: Proposed level scheme of  $^{169}\text{Tm}$ . The  $\gamma$ -rays marked by \* symbol are the newly placed transitions.

scheme in Fig. 6.1. In the present work, the proposed level scheme contains 16 new  $\gamma$ -ray transitions which are marked by asterisks (\*). With the placement of the new transitions, the level scheme has been extended up to an excitation energy of  $\sim 2.5$  MeV and a spin of  $31/2 \hbar$ . The DCO and the IPDCO ratios could not be obtained for some of the transitions because either of their low energy or low statistics. The multiplicities for these transitions were either adopted from the previous measurements or assumed based on whether they are in-band transition in the same signature partner band or is a connecting transition between the two signature partner bands.

The level scheme has been constructed by the  $\gamma - \gamma$  coincidence relation and intensity balance. The  $\gamma - \gamma$  coincidence relations have been established by analysing several single- and double-gated spectra projected from the matrix and the cube. The intensity of each  $\gamma$ -ray has been obtained by putting a single gate on the strong 110-keV transition decaying from the  $5/2^+$

state to the  $3/2^+$  state. Representative double and single gated spectra are shown in Fig. 6.2, Fig. 6.3 and Fig. 6.4.

Table 6.1: The energy ( $E_\gamma$ ) and intensity ( $I_\gamma$ ) of the  $\gamma$  rays of  $^{169}\text{Tm}$  along with the corresponding spin and parity of the initial ( $J_i^\pi$ ) and the final ( $J_f^\pi$ ) states and the energy of the initial state ( $E_i$ ). The measured values of  $R_{DCO}$  and  $\Delta_{IPDCO}$  of the corresponding  $\gamma$  rays are also shown.

$E_\gamma(keV)$ (in keV)	$E_i(keV)$ (in keV)	$J_i^\pi \rightarrow J_f^\pi$	$I_\gamma$ <sup>1</sup>	$R_{DCO}$	$\Delta_{IPDCO}$	Deduced Multipolarity
63.1 <sup>7</sup>	379	$7/2^- \rightarrow 7/2^+$				
87.7	691	$15/2^+ \rightarrow 13/2^-$	18.9(2)	0.66(9) <sup>5</sup>		E1
93.8	473	$9/2^- \rightarrow 7/2^-$	2.9(2)			(M1+E2)
109.6	118	$5/2^+ \rightarrow 3/2^+$	1000	0.86(1) <sup>3</sup>		M1+E2
115.0	588	$11/2^- \rightarrow 9/2^-$	9.8(3)			(M1+E2)
117.8	118	$5/2^+ \rightarrow 1/2^+$	101.3(3)	0.93(3) <sup>3</sup>		E2
130.6	139	$7/2^+ \rightarrow 3/2^+$	726.5(8)	0.92(1) <sup>3</sup>		E2
136.8	725	$13/2^- \rightarrow 11/2^-$	10.2(3)			(M1+E2)
141.2	473	$9/2^- \rightarrow 9/2^+$	1.2(4)			(E1)
157.8	883	$15/2^- \rightarrow 13/2^-$	3.3(2)			(M1+E2)
(162)	1028	$17/2^+ \rightarrow 17/2^-$	0.3(1)			(E1)
173.1	603	$13/2^- \rightarrow 9/2^-$	17.5(3)			(E2)
174.6	866	$17/2^- \rightarrow 15/2^+$	2.0(1)	0.58(12) <sup>4</sup>		E1
179.6	1063	$17/2^- \rightarrow 15/2^-$	2.0(2)			(M1+E2)
192.9	332	$9/2^+ \rightarrow 7/2^+$	614.9(7)	0.88(1) <sup>2</sup>		M1+E2
197.6	316	$7/2^+ \rightarrow 5/2^+$	17.2(2) <sup>6</sup>			(M1+E2)
197.6	1261	$19/2^- \rightarrow 17/2^-$				(M1+E2)

Table 6.1: Continued...

$E_\gamma(keV)$ (in keV)	$E_i(keV)$ (in keV)	$J_i^\pi \rightarrow J_f^\pi$	$I_\gamma$ <sup>1</sup>	$R_{DCO}$	$\Delta_{IPDCO}$	Deduced Multipolarity
209.0	588	$11/2^- \rightarrow 7/2^-$	2.1(2)			(E2)
213.6	332	$9/2^+ \rightarrow 5/2^+$	255.5(5)	0.96(1) <sup>3</sup>	0.05(2)	E2
221.1	1482	$21/2^- \rightarrow 19/2^-$	1.5(2)			(M1+E2)
223.8	1706	$(23/2^-) \rightarrow 21/2^-$	0.8(2)			(M1+E2)
228.6	368	$11/2^+ \rightarrow 7/2^+$	543.6(7)	0.99(1) <sup>2</sup>	0.04(1)	E2
235.0	603	$13/2^- \rightarrow 11/2^+$	29.9(3)	0.59(2) <sup>5</sup>	0.09(2)	E1
237.9	1104	$19/2^+ \rightarrow 17/2^-$	1.0(2)	0.55(6) <sup>4</sup>		(E1)
240.1	379	$7/2^- \rightarrow 7/2^+$	0.2(1)			(E1)
252.2	725	$13/2^- \rightarrow 9/2^-$	1.8(1)			(E2)
262.9	866	$17/2^- \rightarrow 13/2^-$	13.3(4)	0.94(14) <sup>2</sup>		E2
269.4	637	$13/2^+ \rightarrow 11/2^+$	250.1(4)	0.64(1) <sup>2</sup>	-0.03(1)	M1+E2
280.1	1498	$21/2^+ \rightarrow 21/2^-$	0.5(1)			(E1)
291.3	430	$9/2^- \rightarrow 7/2^+$	19.8(5)	0.60(5) <sup>2</sup>	0.02(1)	E1
295.4	883	$15/2^- \rightarrow 11/2^-$	2.2(1)			(E2)
304.9	637	$13/2^+ \rightarrow 9/2^+$	208.8(4)	1.06(1) <sup>2</sup>	0.09(1)	E2
322.9	691	$15/2^+ \rightarrow 11/2^+$	168.7(4)	1.01(1) <sup>2</sup>	0.08(1)	E2
334.2	473	$9/2^- \rightarrow 7/2^+$	0.5(1)			(E1)
336.8	1028	$17/2^+ \rightarrow 15/2^+$	45.5(2)	0.45(2) <sup>2</sup>	-0.04(1)	M1+E2
337.6	1063	$17/2^- \rightarrow 13/2^-$	1.0(1)			(E2)
352.4	1218	$21/2^- \rightarrow 17/2^-$	3.0(1)			(E2)
359.0	1957	$25/2^+ \rightarrow 23/2^+$				(M1+E2)
366.8	2025	$(29/2^-) \rightarrow 25/2^-$	0.8(2)			(E2)
378.3	1261	$19/2^- \rightarrow 15/2^-$	0.5(1)			(E2)

Table 6.1: Continued...

$E_\gamma(keV)$ (in keV)	$E_i(keV)$ (in keV)	$J_i^\pi \rightarrow J_f^\pi$	$I_\gamma$ <sup>1</sup>	$R_{DCO}$	$\Delta_{IPDCO}$	Deduced Multipolarity
380.0	1598	23/2 <sup>+</sup> $\rightarrow$ 21/2 <sup>-</sup>	0.8(2)			(E1)
390.7	1028	17/2 <sup>+</sup> $\rightarrow$ 13/2 <sup>+</sup>	94.9(3)	1.02(2) <sup>3</sup>	0.09(3)	E2
393.7	1498	21/2 <sup>+</sup> $\rightarrow$ 19/2 <sup>+</sup>	11.2(1)	0.47(3) <sup>4</sup>	-0.13(5)	M1+E2
412.7	1104	19/2 <sup>+</sup> $\rightarrow$ 15/2 <sup>+</sup>	48.9(2)	1.02(5) <sup>2</sup>	0.10(2)	E2
419.2	1482	21/2 <sup>-</sup> $\rightarrow$ 17/2 <sup>-</sup>	0.8(1)			(E2)
431.4	2466	(31/2 <sup>+</sup> ) $\rightarrow$ (27/2 <sup>+</sup> )	0.2(1)			(E2)
436.9	2035	(27/2 <sup>+</sup> ) $\rightarrow$ 23/2 <sup>+</sup>	0.5(1)			(E2)
440.0	1658	25/2 <sup>-</sup> $\rightarrow$ 21/2 <sup>-</sup>	1.4(2)			(E2)
(445)	1706	(23/2 <sup>-</sup> ) $\rightarrow$ 19/2 <sup>-</sup>				(E2)
459.4	1957	(25/2 <sup>+</sup> ) $\rightarrow$ 21/2 <sup>+</sup>	0.3(1)			(E2)
464.2	2421	(29/2 <sup>+</sup> ) $\rightarrow$ (25/2 <sup>+</sup> )	0.5(1)			(E2)
469.9	1498	21/2 <sup>+</sup> $\rightarrow$ 17/2 <sup>+</sup>	21.8(2)	1.01(5) <sup>3</sup>	0.06(2)	E2
494.5	1598	23/2 <sup>+</sup> $\rightarrow$ 19/2 <sup>+</sup>	1.2(2)			(E2)

Double-gated spectra with gates put on several known  $\gamma$  rays in  $^{169}\text{Tm}$  are shown in Fig. 6.2. All the known  $\gamma$  rays in the two signature partners of the [411]1/2<sup>+</sup> ground-state band in  $^{169}\text{Tm}$  [4, 5, 117] could be observed along with a few new  $\gamma$  lines. The placement of the new lines in the level scheme is based on the coincidence relation as depicted in Fig. 6.2. The top

<sup>1</sup>Relative  $\gamma$ -ray intensities are estimated from prompt spectra and normalized to 1000 for the total intensity of 109.6 keV  $\gamma$ -rays.

<sup>2</sup>From 130.6 keV (E2) DCO gate;

<sup>3</sup>From 304.9 keV (E2) DCO gate;

<sup>4</sup>From 322.9 keV (E2) DCO gate;

<sup>5</sup>From 228.6 keV (E2) DCO gate;

<sup>6</sup>Intensity of 197.6-keV doublet.

<sup>7</sup>Adopted from Ref. [117].

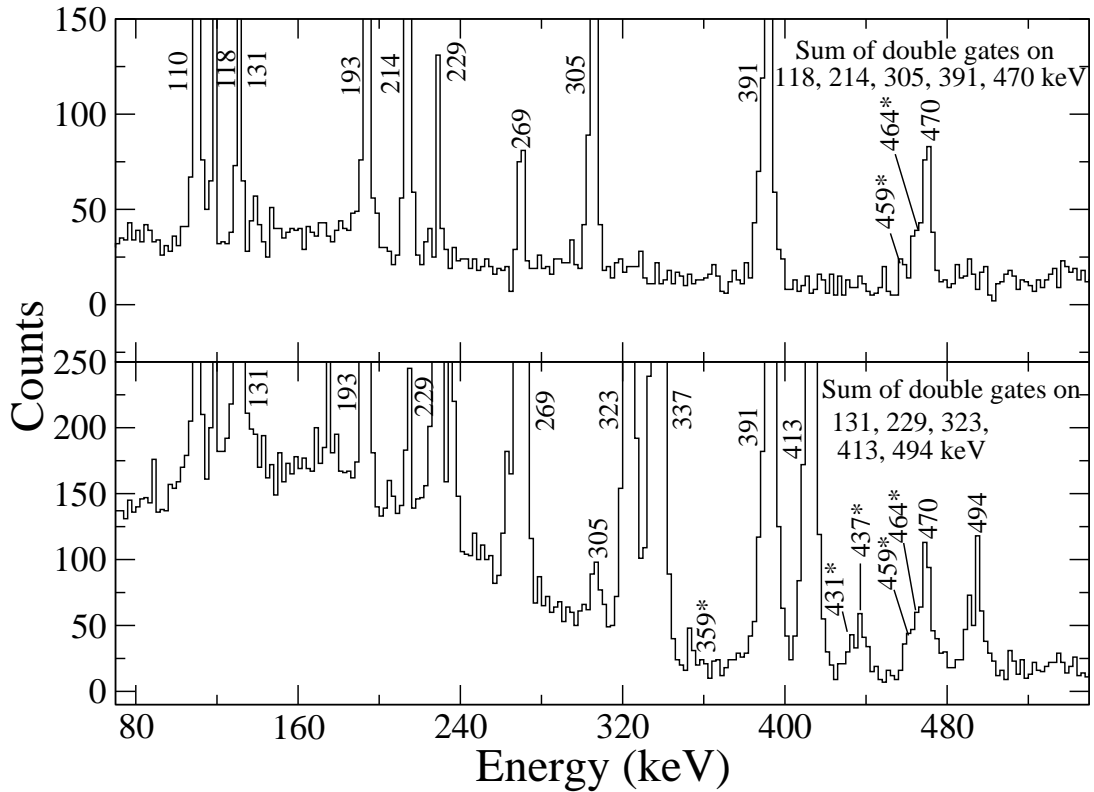


Figure 6.2:  $\gamma$ -ray spectra of  $^{169}\text{Tm}$  obtained by sum of double gates. The gates were put on the transitions in band B1. The new  $\gamma$  peaks are marked by asterisks (\*).

part in this figure is a sum double-gated spectrum for the  $\alpha = +1/2$  signature partner ( $1/2^+$ ,  $5/2^+$ ,  $9/2^+$ ,... sequence) whereas the bottom part is the same for  $\alpha = -1/2$  signature partner ( $3/2^+$ ,  $7/2^+$ ,  $11/2^+$ ,... sequence). It can be seen that all the new lines are clearly seen in the bottom spectrum but the 359-, 431- and 437-keV  $\gamma$  rays are not observed in the top spectrum in accordance with their placement in the level scheme in Fig. 6.1. No  $\gamma$ -ray above the  $29/2^+$  or  $31/2^+$  states are observed and hence the level scheme could not be extended further possibly because of the fact that almost the limit of high spin that can be excited by the inelastic excitation adopted in this work has been reached.

The spectrum in Fig. 6.3(a) is a double gated spectrum with gates put on 229-keV (in the band B1) and 235-keV (connecting transition between the bands B1 and B2)  $\gamma$  lines, whereas the spectrum in Fig. 6.4(a) is a single-gated spectrum with gate put on the 352-keV transition in

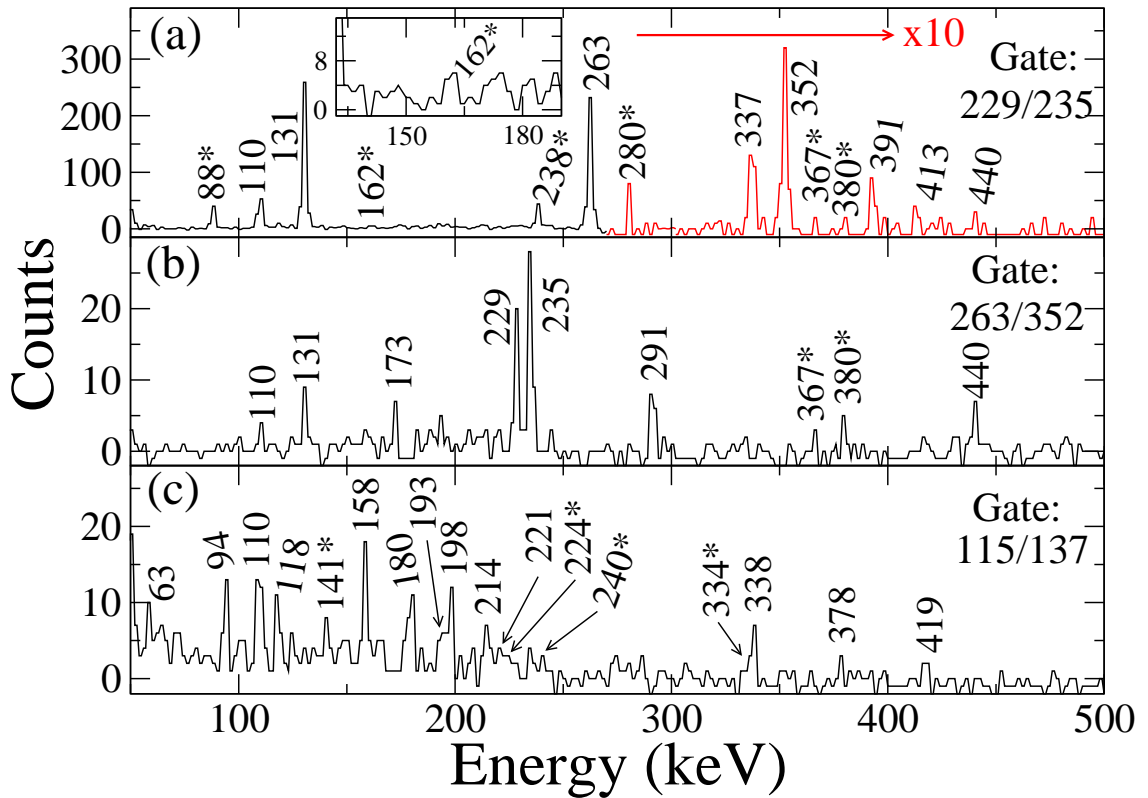


Figure 6.3:  $\gamma$ -spectra of  $^{169}\text{Tm}$  obtained by double gates. The gates were put on (a) the transition in band B1 and a connecting transition between bands B1 and B2, (b) the transitions in band B2 and (c) the transitions in band B3. The new  $\gamma$  transitions are marked by asterisks (\*).

band B2. These two spectra show all the transitions in the band B2 shown in the level scheme (Fig.6.1) along with the  $\gamma$  rays connecting the band B1 with the band B2. These connecting transitions have been observed for the first time in this work. The transitions connecting the band B2 with the band B1 (291, 235 and 175 keV) were already known [117]. The evidence of the 162-keV transition (shown in the inset in Fig.6.3(a)) is relatively poor so, we have marked it as a tentative transition in the level scheme. In the spectrum shown in Fig. 6.3(a), we could observe the 337 and 391 keV transitions which belong to the band B1. This clearly indicates that there must be a 34-keV transition from the  $13/2^+$  state in band B1 to the  $13/2^-$  state in band B2. However, our experimental setup was not suitable to observe such a low energy  $\gamma$  ray.

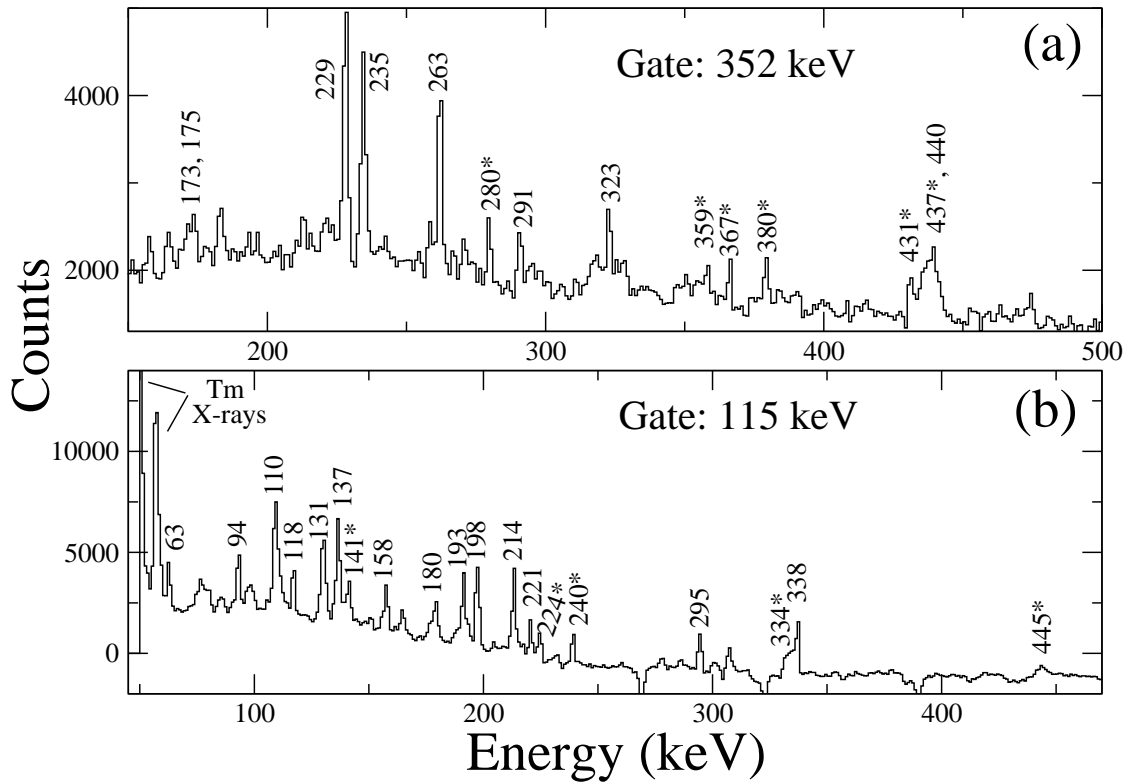


Figure 6.4:  $\gamma$ -ray spectra of  $^{169}\text{Tm}$  obtained by single gates. The gates were put on the transitions in band B2 (a) and in band B3 (b). The new  $\gamma$  transitions are marked by asterisks (\*).

The double gated spectrum in Fig. 6.3(b) with gates put on 263- and 352-keV  $\gamma$  transitions belonging to band B2, shows the other transitions in that band and the 380-keV interconnecting transition but not the 238-keV or 88-keV transitions. This confirms the placements of these newly observed transitions.

The band B2 was known to be a negative parity band from the earlier works [117, 118]. The spin and the parity of the 430-keV state has been fixed from the multipolarity of the 291-keV transition. The  $E1$  nature of this transition has been confirmed from the present work from the DCO and the polarization values (see Table-6.1). This assignment is also supported by the  $E1$  nature of the 235-keV transition decaying from the 603-keV state of this band from its measured polarization and  $R_{DCO}$  values (see Fig.5.16(b) in Section 5.3). All the transitions

decaying from both the signature partners in band B1 to the band B2 are observed for the first time in this work. The band B2 has been extended up to 2025-keV with tentative spin and parity assignment of  $29/2^-$ . Since the spin and parity of the states in bands B1 and B2 (except for the top most level) are already known, the multipolarity of the connecting transitions are, therefore, fixed as  $E1$ . Due to their low intensities, the DCO and polarization measurements could not be possible for most of these transitions except for the 238-keV transitions for which the DCO ratio could be measured. The measured  $R_{DCO}$  value for the 238-keV transition clearly indicates (see Table-6.1) that it is of dipole nature and provides support for the dipole nature of the interconnecting transitions between the bands B1 and B2.

The double-gated spectrum in Fig. 6.3(c) and the single-gated spectrum in Fig. 6.4(b) show the  $\gamma$  rays in band B3 and its connecting transitions to the band B1. This band has been observed up to 1706-keV with tentative spin and parity assignment of  $23/2^-$ . This band was known to decay to the ground state band B1 via an intermediate state at 316 keV [117]. Three new transitions, 141- and 334-keV from the 473-keV,  $9/2^-$  state and 240-keV from the 379-keV,  $7/2^-$  state, have been observed for the first time in this work which decay directly from the negative parity band B3 to the positive parity band B1.

## 6.4 Discussion

$^{169}\text{Tm}$  is a deformed nucleus with deformation  $\beta_2 \sim 0.3$  for the ground state band as obtained from the lifetime measurements [4]. The observed bands in  $^{169}\text{Tm}$  have been discussed in the light of the available Nilsson orbitals for the protons and the neutrons near the Fermi levels with deformation  $\beta_2 \sim 0.3$ . The observed bands have also been compared with the similar band structures observed in the neighboring nuclei.

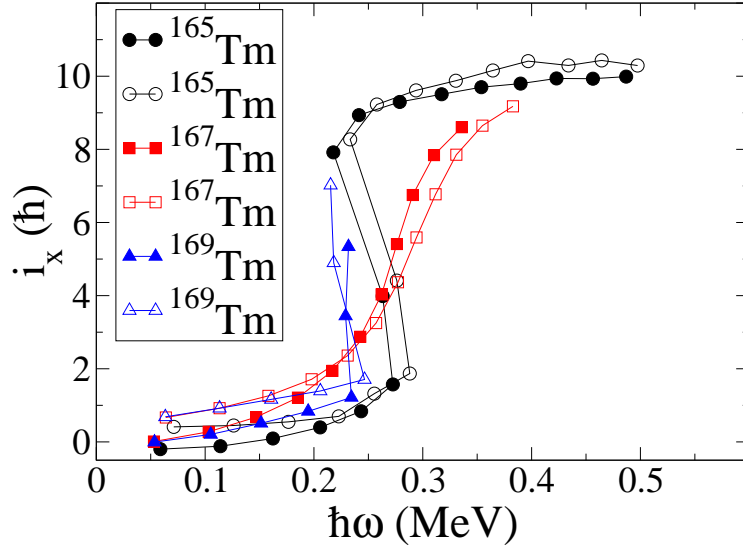


Figure 6.5: Quasi-particle aligned angular momenta ( $i_x$ ) as a function of rotational frequency ( $\hbar\omega$ ) for odd-A Tm isotopes. The solid and the open symbols represent signature  $\alpha = +1/2$  and  $-1/2$ , respectively. Haris parameters  $J_0 = 35 \hbar^2/MeV$  and  $J_1 = 43 \hbar^4/MeV^3$  are taken to subtract a rotor reference value.

#### 6.4.1 Band crossing in $^{169}\text{Tm}$

The aligned angular momentum ( $i_x$ ) for this band in  $^{169}\text{Tm}$  has been plotted as a function of rotational frequency ( $\hbar\omega$ ) in Fig. 6.5 along with those for the other neighboring odd-A Tm isotopes for the same configuration of  $\pi[411]1/2^+$ . It can be seen that with the observation of the new  $\gamma$ -rays in the present work, the particle (neutron) alignment could be well observed in  $^{169}\text{Tm}$  for the first time. The alignment of  $^{169}\text{Tm}$  can thus be compared with the neighboring  $^{165}\text{Tm}$  and  $^{167}\text{Tm}$  isotopes.

It can be seen in Fig. 6.5 that a sharp back-bending type of alignment is observed in  $^{169}\text{Tm}$ , similar to  $^{165}\text{Tm}$  and in contrast to the smooth up-bending in its immediate neighbor  $^{167}\text{Tm}$ . It can also be seen from this plot that with the increase in neutron number from  $N = 96$  to  $N = 100$ , the alignment frequency ( $\hbar\omega_c$ ) gradually decreases and the nature of the alignment also changes from sharp back-bending at  $N = 96$  to gradual alignment for  $N = 98$  and, interestingly, back to sharp back-bending at  $N = 100$ . The alignment or crossing frequency

depends on the orbitals involved in the alignment and on the deformation of the nucleus. The gain in alignment ( $\Delta i_x$ ) can be clearly estimated in  $^{165}\text{Tm}$  to be about  $10\hbar$  and in  $^{167,169}\text{Tm}$  it seems to approach this value, suggesting that the neutron pair alignments are taking place at  $i_{13/2}$  orbital for all these three isotopes.

The band crossing or particle alignment phenomenon in a nucleus is interpreted as the crossing of two bands, the g-band (ground band) and the s-band (super band). Where the s-band resulted from the alignment of a pair of particle, which is by breaking of a neutron pair in this case. As mentioned in Chapter 1, the nature of the band crossing depends on the interaction strength between the two bands. For smaller interaction strength, sharp back-bending occurs where as gradual alignment or smooth up-bending indicates a larger interaction strength. Under this assumption, it is evident that in the case of Tm isotopes around the stability line, the interaction strength between the 1- and the 3-quasiparticle bands is larger in case of the  $N = 98$  nucleus,  $^{167}\text{Tm}$  and decreases on either side of this neutron number.

### **Cranked Shell Model (CSM) calculations**

In order to understand the band crossing frequency and the difference in the nature of band crossings of the  $[411]1/2^+$  band in  $^{165,167,169}\text{Tm}$  isotopes, theoretical calculations were carried out using the principal axis cranking model as described in the Section 2.6. In these calculations, the quasi-particle energies (Routhians) have been calculated using deformed Woods-Saxon potential and BCS pairing. Coriolis term  $\omega j_x$  has been introduced to include the cranking, where  $\omega$  is the rotational frequency of the nucleus and  $j_x$  is the projection of the single particle total angular momentum on the rotation axis. The calculated single particle Routhians as a function of rotational frequency gives the idea about the alignment frequency as well as the interaction strengths between the g- and the s-bands.

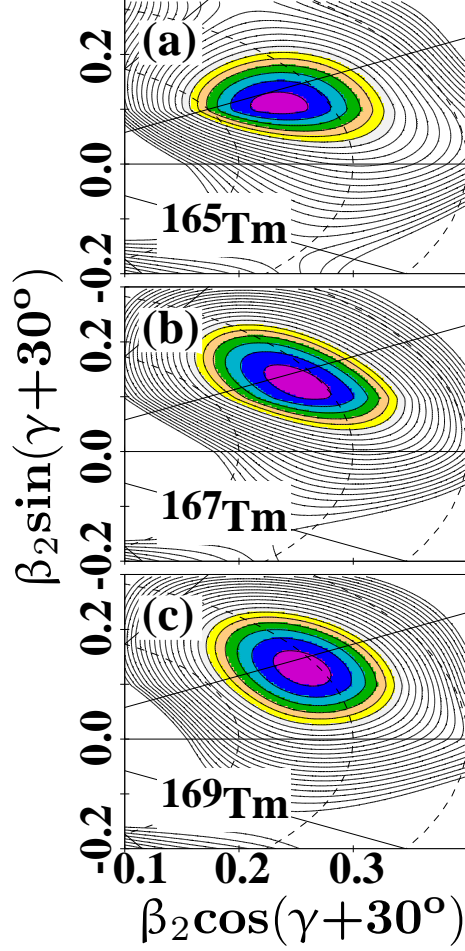


Figure 6.6: TRS calculations of  $^{165}\text{Tm}$  (a),  $^{167}\text{Tm}$  (b), and  $^{169}\text{Tm}$  (c) nuclei at  $\hbar\omega = 0.2$  MeV. The contours are 250 keV apart.

The Total Routhian Surface (TRS) calculations were also performed using the above model, for the nuclei in this region, using the Strutinsky shell correction method to get the quantitative idea about the shape of a nucleus in a particular configuration. The TRS code of Nazarewicz et al. [72, 73] was used for the calculations as described in Section 2.7.

The contour plots of the TRSs for  $^{165}\text{Tm}$ ,  $^{167}\text{Tm}$  and  $^{169}\text{Tm}$  isotopes in the  $[411]1/2^+$  configuration are shown in Figs. 6.6(a), 6.6(b) and 6.6(c), respectively. These surfaces were calculated at  $\hbar\omega = 0.2$  MeV which is just below the crossing frequencies. As seen in Fig. 6.6, the minimum of the TRS comes out to be at prolate shape with  $\gamma \sim 0^\circ$  for all the three isotopes. The

Table 6.2: Deformation parameters  $\beta_2$ ,  $\beta_4$  and  $\gamma$  obtained from TRS calculations for the  $[411]1/2^+$  band in Tm isotopes.

A	$\beta_2$	$\beta_4$	$\gamma$
165	0.274	0.035	0.5
167	0.284	0.005	1.1
169	0.292	-0.095	0.8

calculated deformation parameters are presented in Table 6.2 which shows a small increase of the quadrupole deformation  $\beta_2$  with neutron number in these isotopes and there is a relatively large variation in the values of  $\beta_4$ .

The deformed shapes are realized in these nuclei as the proton Fermi surface lies in the mid-shell region and also there would be deformation driving effect of the deformed shell gap at neutron number  $N = 98$ . However, the observation of rotational bands in all the lighter Tm isotopes up to  $^{157}\text{Tm}$  [1] indicates that the deformed shape persists even upto  $N = 88$  [1]. Deformed shape is also obtained in our TRS calculations for the negative parity band in lighter Tm isotopes up to  $^{155}\text{Tm}$  ( $N = 86$ ). It suggests that the structure in Tm nuclei, away from  $N = 98$ , are still deformed mostly because the proton Fermi level lies in the mid-shell.

The single particle Routhians are also obtained in this work from the cranked shell model (CSM) calculation. In case of the  $\pi[411]1/2^+$  band in Tm isotopes the first band crossing is due to the alignment of a pair of neutrons in the  $i_{13/2}$  orbital. The calculated quasi-particle energies for neutron levels for  $N = 96, 98$  and  $100$  corresponding to  $^{165}\text{Tm}$ ,  $^{167}\text{Tm}$  and  $^{169}\text{Tm}$  nuclei are shown in Figs. 6.7(a), 6.7(b) and 6.7(c), respectively, as a function of rotational frequency  $\hbar\omega$ . In these calculations, the deformation parameters obtained from the minimum of TRSs as shown in Table 6.2 are taken. In this model, the crossing frequency  $\omega_c(cal)$  corresponds to the value of rotational frequency at which the Routhians from above and below the Fermi level come close together and the interaction strength at the crossing corresponds to half the distance of closest approach of the Routhians. The calculated values of  $\omega_c(cal)$  and the interaction strength (V)

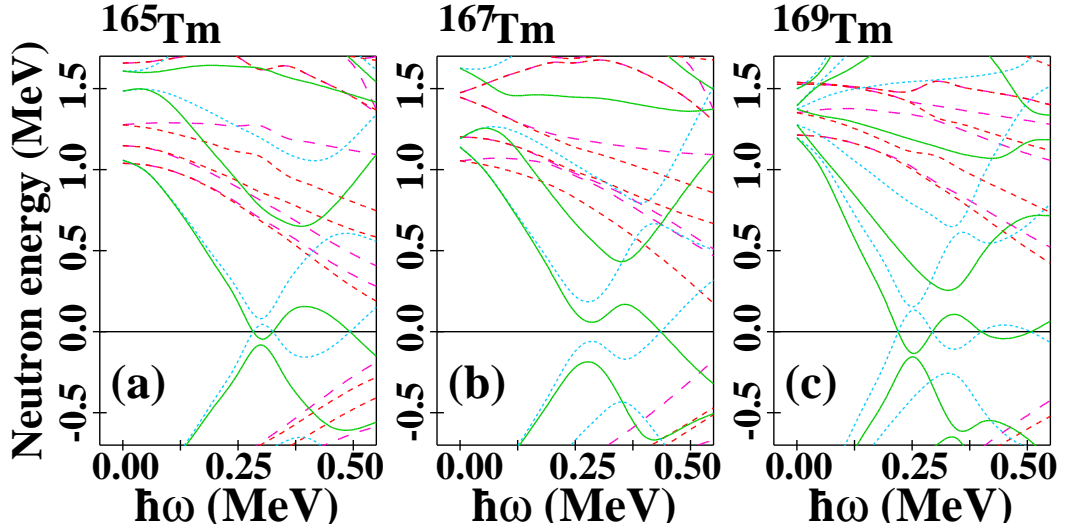


Figure 6.7: Calculated quasi-neutron energy levels for  $N = 96, 98$  and  $100$  corresponding to  $^{165}\text{Tm}$ ,  $^{167}\text{Tm}$  and  $^{169}\text{Tm}$  nuclei.

are presented in Table 6.3 along with the experimental values of crossing frequencies ( $\omega_c(\text{exp})$ ) for the three isotopes. It can be seen from Fig. 6.7 and Table 6.3 that the calculated crossing frequencies are in excellent agreement with the measured ones.

The differences in the nature of the alignments as depicted in Fig. 6.5 can also be understood from the CSM calculations. A much larger interaction strength ( $V = 125$  keV) is obtained for  $^{167}\text{Tm}$  compared to the other two isotopes (see Table 6.3) which clearly supports the observed smooth up-bend in this  $N = 98$  isotope in contrast to the back-bend in  $^{165}\text{Tm}$  and  $^{169}\text{Tm}$ . A larger interaction strength is realized for a larger energy gap in the single particle diagram. As mentioned earlier, in the Nilsson diagram, there is a gap at  $N = 98$  for deformation  $\beta_2 \sim 0.28$ . It is, therefore, suggested that the smooth up-bend in  $^{167}\text{Tm}$  may be because of this deformed gap. This is also supported by the observed smooth up-bend in the neighboring  $N = 98$  isotones of even-even  $^{166}\text{Er}$  [127] and odd-A  $^{169}\text{Lu}$  [128].

The calculations are extended for  $^{171}\text{Tm}$  with  $N = 102$  and an interaction strength  $V = 75$  keV has been obtained, which is smaller than in  $^{167}\text{Tm}$  possibly because the deformed shell gap at

Table 6.3: Experimental & calculated crossing frequencies ( $\omega_c$ ) and calculated interaction strengths (V) at the band crossings for the  $[411]1/2^+$  band in Tm isotopes.

A	$\omega_c(exp)$ (MeV)	$\omega_c(cal)$ (MeV)	V (keV)
165	0.29	0.30	20
167	$\sim 0.27$	0.28	125
169	0.24	0.25	10

$N = 102$  is smaller than at  $N = 98$ . This indicates that an alignment, similar to  $^{167}\text{Tm}$ , with less smooth up-bend is expected in  $^{171}\text{Tm}$ . Experimental data, however, are not available yet for this nucleus to test this prediction.

### 6.4.2 Possible octupole correlation in $^{169}\text{Tm}$

The negative parity band B2 is a decoupled band and only one signature partner is observed, indicating that it is based on the  $\Omega = 1/2$  component of a high- $j$  orbital which provides the required large Coriolis force. Therefore, it was assigned a configuration of  $\pi[541]1/2^-$  with  $h_{9/2}$  parentage [117]. The  $\Omega = 1/2$  component of the  $h_{9/2}$  proton orbital comes down in energy sharply with deformation from above the  $Z = 82$  shell closure and intrudes into the region of the proton Fermi level of  $^{169}\text{Tm}$  and close to the  $\pi[411]1/2^+$  orbital for a deformation of  $\beta_2 \sim 0.3$ .

Interwined  $E1$  transitions between the positive parity band B1 and the negative parity band B2 have been observed in this work. These resemble the parity-doublet states generally observed between the octupole correlated bands. Such octupole correlated bands are reported in Ba, La, Ce and Sm isotopes with neutron numbers close to  $N = 90$  [40, 41, 42, 43, 44, 45]. For these nuclei, the Fermi level of protons lie close to the  $\pi h_{11/2}$  and  $\pi d_{5/2}$  orbitals and the Fermi level of neutrons lie close to the  $\nu i_{13/2}$  and  $\nu f_{7/2}$  orbitals. Both these pairs of proton and neutron orbitals are characterized by  $\Delta l = 3$  and  $\Delta j = 3$ , a condition which is believed to be responsible for the observation of parity-doublet octupole correlated bands characterized by enhanced  $E1$

transitions for the above nuclei in  $A \sim 140$  region. In case of  $^{169}\text{Tm}$  ( $Z = 69$ ), the proton Fermi level is close to the  $h_{9/2} - d_{3/2}$  pair of orbitals for prolate deformation with  $\beta_2 \sim 0.3$ . These two orbitals are also characterized by  $\Delta l = 3$  and  $\Delta j = 3$ , similar to those for the Ba, La, Ce and Sm isotopes in mass  $A \sim 140$  region. But with neutron number  $N = 100$ , the  $i_{13/2} - f_{7/2}$  neutron pair of orbitals do not lie close to the Fermi level of  $^{169}\text{Tm}$  at that deformation. Therefore, the favorable condition for the observation of octupole correlation is only partially fulfilled in case of  $^{169}\text{Tm}$ , through the proton orbitals. However, it has been observed that the bands B1 and B2 in  $^{169}\text{Tm}$ , based on the  $\pi[411]1/2^+$  and  $\pi[541]1/2^-$  configurations, originated from the  $d_{3/2}$  and  $h_{9/2}$  proton orbitals, respectively, are connected by several  $E1$  transitions, similar to the octupole correlated bands observed in nuclei in  $A \sim 140$  region. In the following we have verified if this indicates the presence of octupole correlation in  $^{169}\text{Tm}$  for which no prior prediction is available to the best of our knowledge.

In octupole correlated nuclei, the parity doublet bands are characterized with simplex quantum numbers [44, 119, 120]  $s = \pm 1$  and  $s = \pm i$  for even-A and odd-A nuclei, respectively. The energy differences  $\delta E$  between the octupole correlated  $\pi = +$  and  $\pi = -$  bands can be obtained from the following relation [121]:

$$\delta E = E(I^-) - \frac{(I+1)E(I-1)^+ - IE(I+1)^+}{2I+1}, \quad (6.1)$$

where the superscripts indicate the parities of the levels. The values of  $\delta E(I)$  as obtained for  $^{169}\text{Tm}$  in the present work has been plotted as a function of spin ( $I$ ) in Fig. 6.8 and are compared with those for a few odd-A (Fig. 6.8(a)) and even-even (Fig. 6.8(b)) nuclei in  $A \sim 140$  region for which octupole correlation has been reported. In the limit of stable octupole deformation,  $\delta E$  should be close to zero. The figure shows that  $\delta E(I)$  of  $^{169}\text{Tm}$  decreases and tends towards zero with increasing spin in a way similar to what has been observed in the other octupole correlated nuclei shown in the figure.

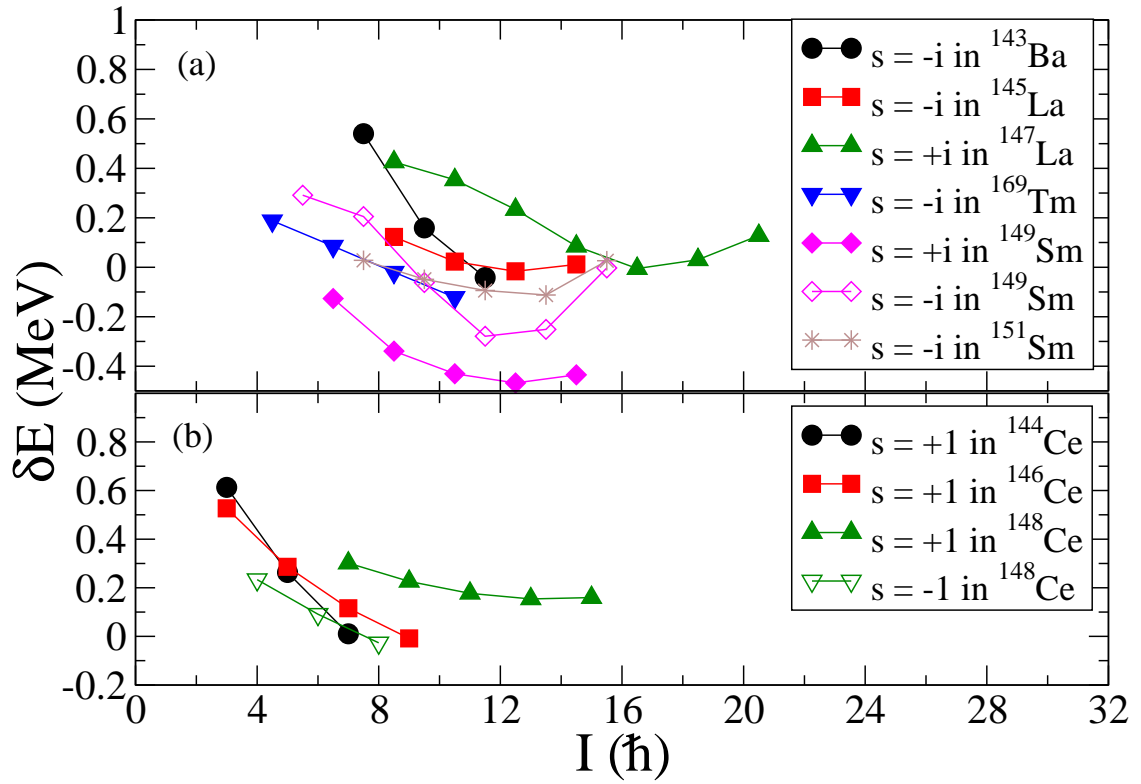


Figure 6.8: Plot of the energy difference ( $\delta E$ ) between the positive and negative parity states in bands B1 and B2 in  $^{169}\text{Tm}$  compared with that in the parity doublet bands in odd-A nuclei (a) and even-even nuclei (b).

The experimental  $B(E1)/B(E2)$  branching ratios are obtained from the following expression:

$$\frac{B(E1)}{B(E2)} = 0.771 \frac{I_\gamma(E1)}{I_\gamma(E2)} \frac{E_\gamma^5(E2)}{E_\gamma^3(E1)} (10^{-6} fm^{-2}) \quad (6.2)$$

where the energy unit of  $E_\gamma$  is MeV. In case of the reported octupole correlated bands in Ba, La, Ce isotopes the  $B(E1)/B(E2)$  ratios vary from  $\sim 0.2 \times 10^{-6}$  to  $\sim 2 \times 10^{-6} fm^{-2}$  [40, 42, 43, 44]. However, in the present case, the average value of  $B(E1)/B(E2)$  ratios has been found to be  $\sim 0.12 \times 10^{-6} fm^{-2}$  with a maximum value of  $\sim 0.44 \times 10^{-6} fm^{-2}$  near the bottom of the bands and  $\sim 0.28 \times 10^{-6} fm^{-2}$  near the top of the bands in case of  $^{169}\text{Tm}$ . Therefore, the strength of the octupole correlation, if present, would be much smaller in case of  $^{169}\text{Tm}$  and the bands are predominantly characterized by quadrupole deformation. This may be understood from the fact that only the protons contribute to the octupole correlation in case of  $^{169}\text{Tm}$  whereas, both protons and neutrons contribute to the correlation for the other nuclei in  $A \sim 140$  region with neutron number close to  $N = 90$ . The octupole state has the lowest energy around this neutron number [122]. The energy of the octupole state increases with both increase and decrease of this neutron number. Therefore, the nuclei with  $N \sim 90$  are considered as the most likely candidates for octupole correlation.

In the present work, our results show that the  $B(E1)$  strength decreases by a factor of about 5 when moving from the  $N = 90$  nuclei in  $A \sim 140$  region to the  $N = 100$  nucleus  $^{169}\text{Tm}$ , assuming that the effect of protons remains similar because of the involvement of similar proton orbitals in both the regions. However, it needs more experimental and theoretical works to establish this. In particular, it would be interesting to search for octupole correlation in neutron deficient Tm isotopes with neutron number  $N \sim 90$ . In case of these neutron deficient Tm isotopes, favorable orbitals for octupole correlation would be available both for protons and neutrons.

The band B3 is again a negative parity band with very little signature splitting indicating that it is based on a high- $\Omega$  orbital. Considering the available Nilsson orbitals around the proton

Fermi level in  $^{169}\text{Tm}$  for the prolate deformation of  $\beta_2 \sim 0.3$ , a configuration of  $\pi[523]7/2^-$ , with  $h_{11/2}$  parentage has been suggested for this band.

## 6.5 Conclusion

The excited states in  $^{169}\text{Tm}$  have been investigated by populating them in the reaction  $^{169}\text{Tm}(^{32}\text{S}, ^{32}\text{S}')^{169}\text{Tm}^*$  at the beam energy of 164 MeV using Indian National Gamma Array (INGA) with 19 clover HPGe detectors. A new level scheme of  $^{169}\text{Tm}$  with three bands has been proposed from the present work with the placement of 16 new transitions. All the observed bands have been extended to higher excitation energies and angular momenta. The ground state band, based on  $\pi[411]1/2^+$ , has been extended to observe the neutron pair alignment in this nucleus for the first time and the same has been compared with those in its neighboring isotopes around  $N = 98$  deformed shell gap. Apart from a slightly different crossing frequency, a sharp backbending, similar to  $^{165}\text{Tm}$ , has been observed in  $^{169}\text{Tm}$  which is in sharp contrast to its immediate neighbor  $^{167}\text{Tm}$  in which smooth up-bending has been observed for the same configuration. The crossing frequencies and the band crossing behavior have been interpreted in the cranked shell model approach in which the single particle Routhians and the total Routhian surface (TRS) were calculated. The observed crossing frequencies in the three isotopes could be very well reproduced by the calculations. The difference in the alignment behavior of  $^{167}\text{Tm}$  compared to  $^{165,169}\text{Tm}$  is well understood from the large interaction strength between the ground- and the s-bands calculated for  $N = 98$ . The calculations predict that if one moves towards  $N = 82$  spherical shell closure, the deformed shape persists for neutron number as low as  $N = 86$  in  $^{155}\text{Tm}$ . Therefore, it may be concluded that the shapes of the Tm nuclei are mostly determined by the proton Fermi level and has only limited effect of the  $N = 98$  deformed shell gap. However, this deformed shell gap significantly affects the nature of the alignment of the nuclei in the  $A \sim 170$  region. It is also predicted that the interaction

strength for  $^{171}\text{Tm}$  is less than in  $^{167}\text{Tm}$  but still large enough to show up-bending due to neutron alignment.

Several intertwined  $E1$  transitions between the yrast positive parity and a negative parity band have been observed. These transitions resemble the octupole correlated parity-doublet bands as observed for the nuclei with  $Z \sim 60$  and  $N \sim 90$  in mass  $A \sim 140$  region. However, the  $B(E1)/B(E2)$  ratios are much smaller in case of  $^{169}\text{Tm}$ , indicating predominance of quadrupole deformation in this nucleus. It is opined that although the proton  $h_{9/2}$  and  $d_{3/2}$  orbitals contribute to the octupole correlation but as the neutron Fermi level moves up, the contributions coming from the pair of neutron orbitals with  $\Delta l = 3$  and  $\Delta j = 3$  becomes very small which results in to a factor of  $\sim 5$  less in observed  $B(E1)/B(E2)$  ratios for  $^{169}\text{Tm}$  compared to the Ba, La and Ce nuclei in  $A \sim 140$  region

# Chapter 7

## High spin nuclear structures in odd-odd $^{196}\text{Tl}$

### 7.1 Introduction

In the Thallium nuclei with proton number  $Z = 81$ , the proton Fermi level lies near the  $3s_{1/2}$  orbital just below the  $Z = 82$  spherical shell closure and, hence, due to the proximity of the shell closure, the ground state of the Tl isotopes are near-spherical. However, due to the large shape driving effect of the  $\pi h_{9/2}$  orbital, the Nilsson states with high (low)  $\Omega$  components originating from this orbital come down in energy in the oblate (prolate) deformation side in the Nilsson diagram and intrude near the proton Fermi level of Tl below the  $Z = 82$  shell gap. On the other hand, in case of Tl isotopes in  $A \sim 190$  mass region, the unique positive parity  $\nu i_{13/2}$  orbital, available near the neutron Fermi level, also has a large shape driving effect. Hence, due to the combined effect of these two shape-driving orbitals, rotational bands based on the  $\pi h_{9/2} \otimes \nu i_{13/2}$  configuration, indicating induced deformation, have been observed in the odd-odd Tl isotopes in this region [7, 8, 9, 10] at moderate excitation energies. The prolate and oblate shape driving

effect of the  $\nu i_{13/2}$  orbital depends on whether the neutron Fermi level is close to the low or high- $\Omega$  components of  $i_{13/2}$  orbital. Therefore, it is important to identify and determine the nature of the band structures built on different configurations in the Tl isotopes. However, data on the odd-odd Tl nuclei are very limited. Moreover, the complex and exotic modes of generation of angular momentum have been reported in some of the odd-odd Tl nuclei. For neutron number  $N = 113$ , a triaxial shape is indicated at higher excitation energy from the observation of Chiral doublet bands in  $^{194}\text{Tl}$  [11] for the 4-quasiparticle (qp) configuration. This is possibly due to the opposite shape driving effects of the proton and the neutron orbitals. On the other hand, Magnetic Rotational (MR) band based on 6-quasiparticle configuration has also been identified in the same nucleus [12]. In  $^{198}\text{Tl}$  [13, 14], the chiral band is reported for the 2-quasiparticle configuration,  $\pi h_{9/2} \otimes \nu i_{13/2}$ , at relatively lower spin compared to the chiral band in  $^{194}\text{Tl}$ . Therefore, in order to get a better understanding on the band structures based on different configurations, the high-spin states in odd-odd  $^{196}\text{Tl}$  nucleus have been studied. The existing data on the high-spin states in  $^{196}\text{Tl}$  are very scarce. In the previous work [9], the ground-state band based on  $\pi h_{9/2} \otimes \nu i_{13/2}$  configuration was reported with uncertainty in spin and excitation energy. Moreover, the spin-parity assignments for the states of the two side bands are not known, so configuration assignment could not be done. In the present thesis work, the study of the high spin spectroscopy of  $^{196}\text{Tl}$  provides improved information to get a new insight about the odd-odd Tl nuclei.

## 7.2 Experiment and Data Analysis

The excited states in  $^{196}\text{Tl}$  has been populated using  $^{185,187}\text{Re}(^{13}\text{C}, xn)^{196}\text{Tl}$  fusion evaporation reaction at a beam energy of 75 MeV from 14-UD BARC-TIFR Pelletron at Mumbai, India. According to PACE-IV calculation,  $^{196}\text{Tl}$  nucleus is predominantly produced in the 4n channel from the  $^{187}\text{Re}$  target at this energy. Self-supporting target of natural rhenium of 18.5 mg/cm<sup>2</sup>

thickness was used so that the produced recoiling nuclei are stopped inside the target. Isotopic ratio of  $^{185}\text{Re}$  and  $^{187}\text{Re}$  in the target was 37:63. The  $\gamma - \gamma$  coincidence data were collected from the  $\gamma$ -ray detector array INGA (Indian National Gamma Array) consisting of 15 HPGe clovers with BGO anti-Compton shields during the experiment. Four clovers were at  $90^\circ$ , two clovers each at  $\pm 40^\circ$  and  $\pm 65^\circ$  while three were at  $-23^\circ$  angles. For energy efficiency and calibration of the clover detectors, radioactive sources  $^{133}\text{Ba}$  and  $^{152}\text{Eu}$  were used.

A digital data acquisition (DDAQ) system, based on Pixie-16 modules [21, 22], has been used for the data collection with a sampling rate of 100 MHz for each detector in this experiment. Time-stamped  $\gamma - \gamma$  coincidence data were recorded when at least two clover detectors were fired at a time window of 150 ns in coincidence mode. Raw data sorting was done by Multi-pARameter time-stamped based COincidence Search (MARCOS) code [22], developed at TIFR, Mumbai. The  $\gamma - \gamma$  matrix and  $\gamma - \gamma - \gamma$  cube were formed by MARCOS and Radware [28] software packages.  $\pm 50$  ns time window was chosen for the above matrix and cube formation.

The present level scheme has been constructed using the  $\gamma - \gamma$  coincidence relations and the  $\gamma$ -ray intensity balance. The  $\gamma - \gamma$  coincidence relations have been obtained from  $\gamma - \gamma$  matrix and  $\gamma - \gamma - \gamma$  cube. Spins and parities of the nuclear levels in  $^{196}\text{Tl}$  have been assigned by the measurement of the directional correlation from oriented states (DCO) ratio and integrated polarization directional correlation (IPDCO) ratio of the corresponding  $\gamma$  rays decaying from the levels. The DCO and IPDCO ratio measurement processes have been described in Section 5.3.

## 7.3 Experimental Results

The level scheme of  $^{196}\text{Tl}$ , obtained in the present work, has been shown in the Fig. 7.1. The level scheme contains 38 new  $\gamma$ -lines indicated by asterisk (\*). The yrast band B1 and two side bands B2 and B3, which were reported in the previous work [9], have been considerably extended in the present work. Besides the three bands, several non-yrast levels have been

observed in the present work. The excitation energy, spin and parity of the nuclear excited states and the multipolarity of the  $\gamma$  rays including the other relevant deduced quantities, have been shown in Table 7.1. The DCO and IPDCO ratios of most of the observed  $\gamma$  rays are shown in Fig. 7.2 as a function of  $\gamma$ -ray energy. The low spin states  $7^+$ ,  $3^-$ , and ground state  $2^-$  in the  $^{196}\text{Tl}$  nucleus, populated by electron capture decay of  $^{196}\text{gPb}$ , are adopted from Ref. [9] and are shown in the proposed level scheme. In the present work, the deduced excitation energies of the nuclear states have been measured with respect to the  $2^-$  ground state. Prior to the present work, the level scheme of  $^{196}\text{Tl}$  was known up to  $\sim 3.6$  MeV of excitation energy and  $20\hbar$  of spin. The proposed level scheme from the present work has been extended up to an excitation energy of  $\sim 5.1$  MeV and a spin of  $22\hbar$ .

The  $\gamma - \gamma$  coincidence relations have been established by analysing several single- and double-gated spectra projected from the  $\gamma - \gamma$  matrix and the  $\gamma - \gamma - \gamma$  cube. The relative intensities of most of the observed  $\gamma$ -rays have been obtained by putting a single gate on the 344-keV strong transition, decaying from the  $8^-$  to the  $7^+$  state. Representative single- and double-gated spectra are shown in Fig. 7.3, Fig. 7.4, and Fig. 7.5.

In the yrast band B1, all the known  $\gamma$ -ray transitions have been observed in the present work. A few new  $\gamma$  rays, 170-, 518-, 477-, 693-, 389-, 577- and 304-keV, in the band B1 have been observed in the present work and with the placement of these transitions, the band B1 has been extended up to an excitation energy of  $\sim 4.3$  MeV and a spin of  $22^- \hbar$ . The new  $\gamma$ -ray transitions are shown in the single- and double-gated spectra in Fig. 7.3 and 7.4(a), respectively. A 170-keV cross-over E2  $\gamma$  ray has been observed in the present work which is in coincidence with the known 271-keV  $\gamma$  ray decaying from the  $12^-$  to the  $10^-$  state and the 344-keV  $\gamma$  ray from the  $8^-$  state to the  $7^+$  state, as can be seen from Fig. 7.3 and Fig. 7.4(a). The cross-over transition ( $108\text{-keV} + 62\text{-keV} = 170\text{-keV}$ ) has been fitted between the  $10^-$  and  $8^-$  state. Therefore, with the observation of this transition, the uncertainty in spin ( $I_0$ ) and level energy ( $X$ ), as previously reported in Ref. [9], has been removed in the present work by putting  $I_0 = 0$

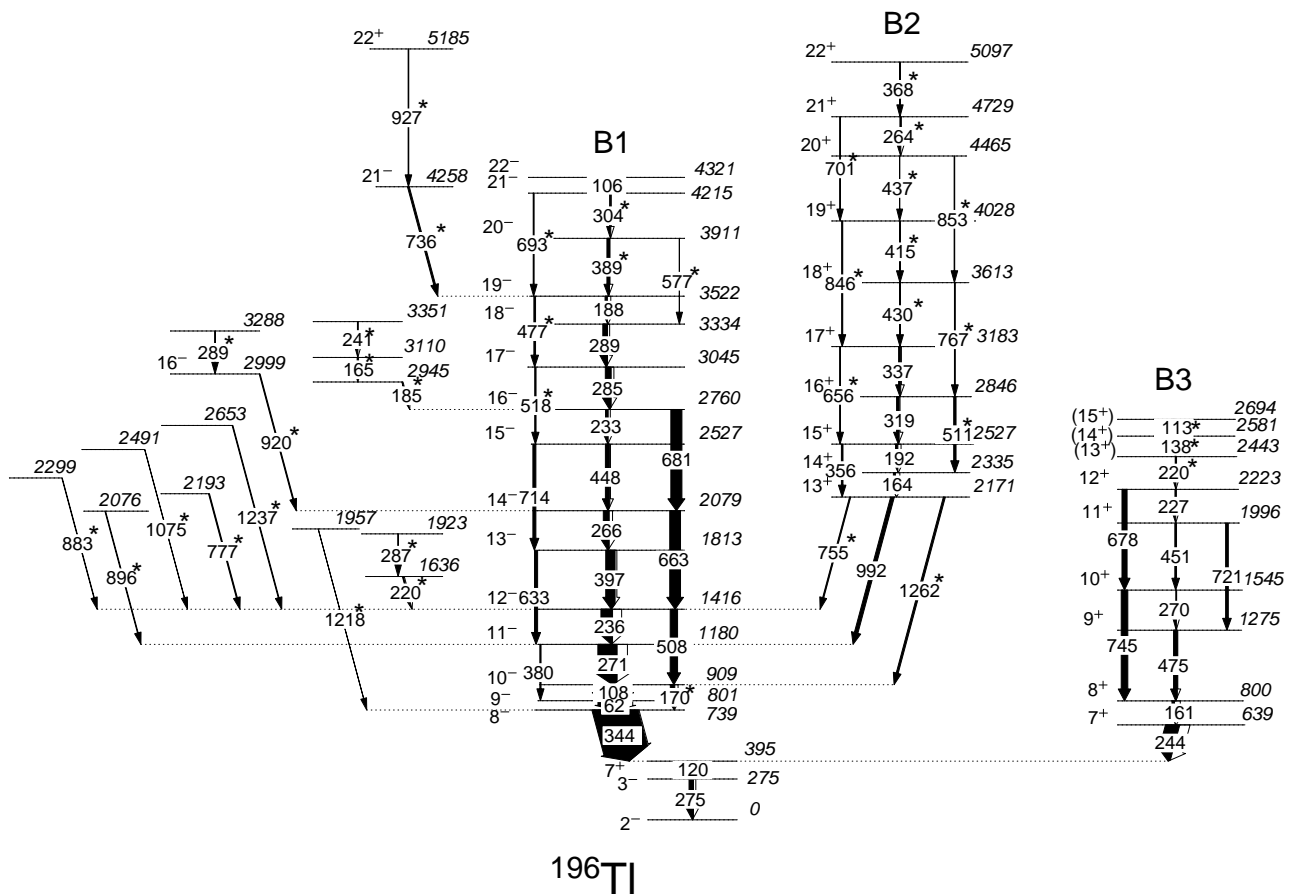


Figure 7.1: Proposed level scheme of  $^{196}\text{Tl}$ . The  $\gamma$ -rays marked by \* symbol are the newly placed transitions.

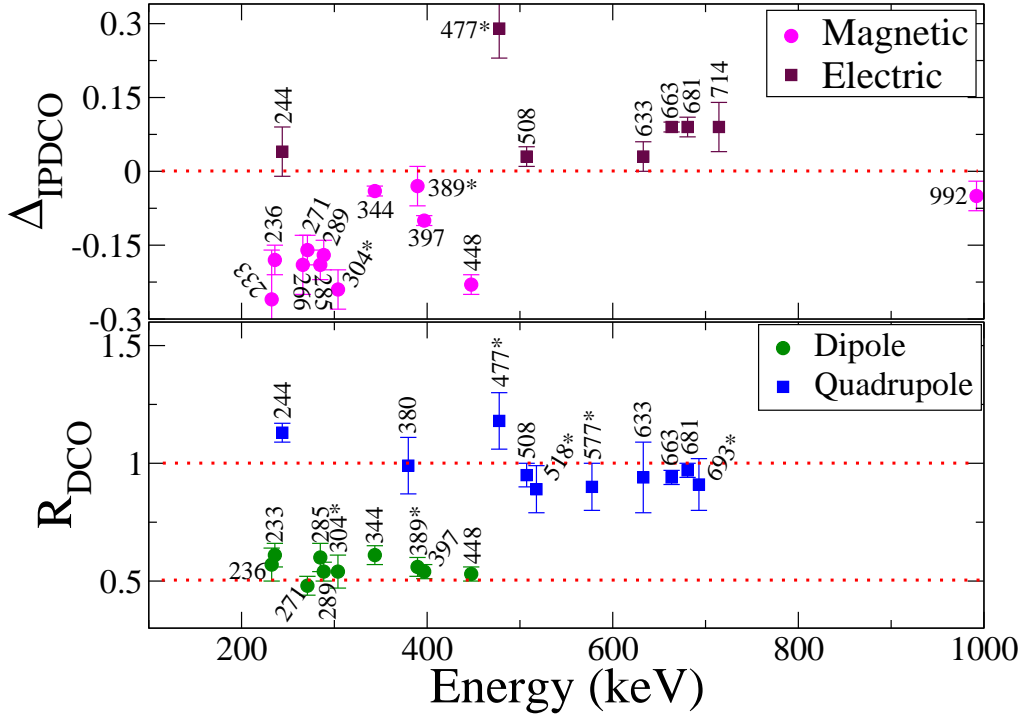


Figure 7.2: DCO and IPDCO ratios plots as a function of  $\gamma$ -ray energy of the known as well as new  $\gamma$  rays in  $^{196}\text{Tl}$ . The DCO ratios of the  $\gamma$  rays have been obtained with stretched E2 transition gate.

and  $X = 0$ . The 106-keV  $\gamma$  ray of multipolarity M1+E2 was tentatively placed on top of the 188-keV M1+E2  $\gamma$  ray from the  $19^-$  to the  $18^-$  state in the previous work [9]. In the present work, two new 389- and 304-keV M1+E2  $\gamma$  rays have been observed in coincidence with the 188-keV  $\gamma$  ray in this band. The ordering and placement of these  $\gamma$  rays above the 188-keV  $\gamma$  ray have been fixed by the observed 577- and 693-keV cross-over E2 transitions, as can be seen from the level scheme in Fig. 7.1. Therefore, in the present work, the 106-keV  $\gamma$  ray has been placed on top of the 304-keV  $\gamma$  ray. The placement of these  $\gamma$  rays are also consistent with their relative intensities.

The spin-parity of the band B2 was not assigned in the previous work. This band is connected with the band B1 by the 992-keV  $\gamma$ -ray transition decaying from the  $E_i = 2171$  keV to the  $E_f = 1180$  keV state. The multipolarity of this connecting transition was not reported in the

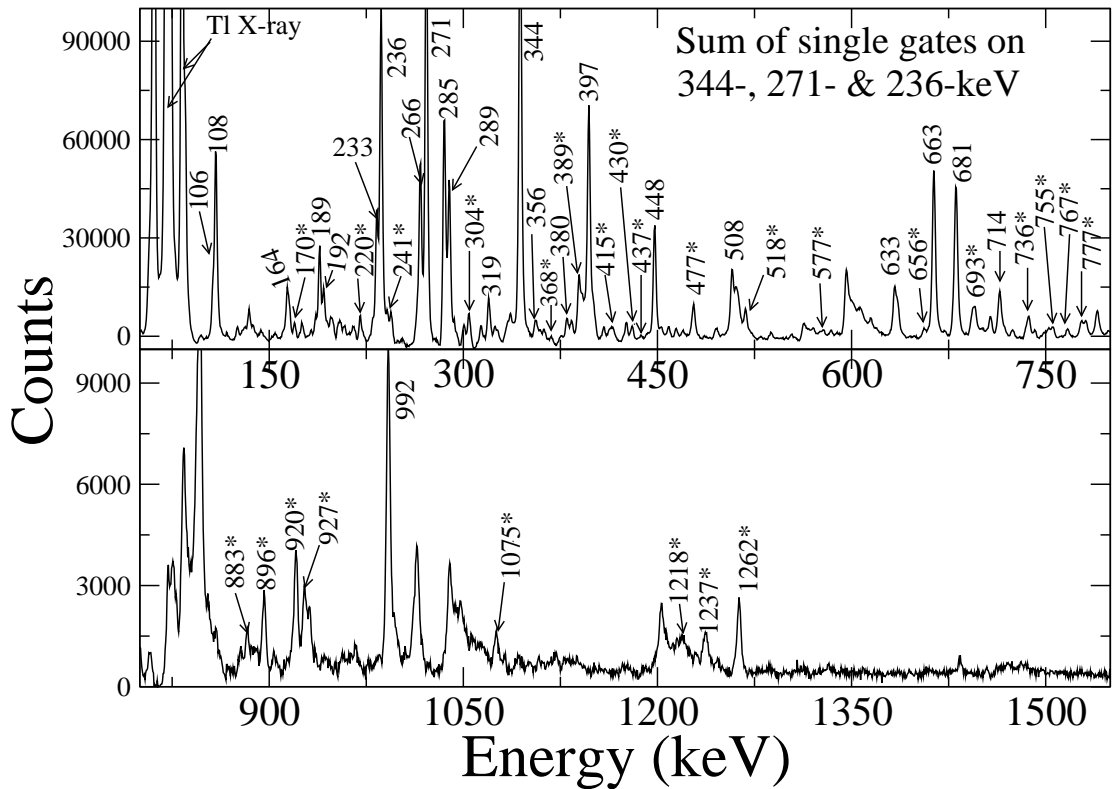


Figure 7.3: Coincidence  $\gamma$ -spectra corresponding to sum of single gates on 344-, 271- and 236-keV. The upper panel spectrum up to 800 keV and lower panel spectrum is from 800 keV to 1600 keV. New  $\gamma$ -transitions are marked by \*.

previous work. In order to find the multipolarity, DCO and IPDCO ratio for this  $\gamma$  ray has been obtained in the present work (see Table 7.1). The spectra for the perpendicular scattering counts ( $N_{\perp}$ ) and the parallel scattering counts ( $N_{\parallel}$ ) are shown in Fig. 7.6. The negative value of the IPDCO ratio suggests that the transition is magnetic in nature. The DCO ratio for the  $\gamma$  ray has been obtained as 1.53(1) by gating on 344-keV stretched E1  $\gamma$ -ray transition from the  $8^-$  to the  $7^+$  state. This value of DCO ratio is little bit away from the value  $\sim 2$  for a pure quadrupole transition. This suggests a small admixture of octupole multipolarity with the quadrupole nature of the 992-keV transition. Therefore, M2+ E3 character of the 992-keV  $\gamma$ -ray transition has been proposed in the present work. This suggests the spin and parity of  $13^+$  for the 2171-keV level that is the band head of the band B2. In order to confirm this assignment, the DCO ratio and the polarization (P) of the 992 keV transition have been

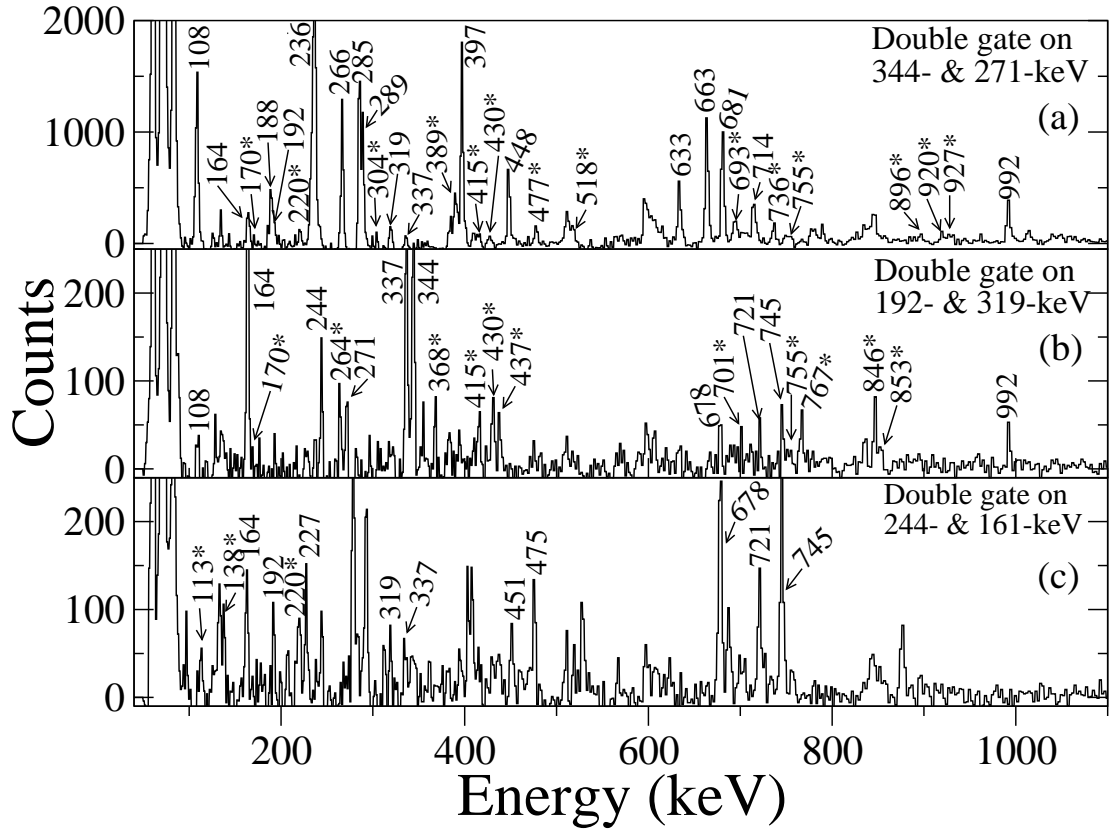


Figure 7.4: Double gated  $\gamma$ -spectra. Top panel: double gate on 344- and 271-keV, middle panel: double gate on 192- and 319-keV and lower panel: double gate on 244- and 161-keV.

calculated using the ADRAP code (as described in chapter 5) and were compared with the measured values for different possible spin and parity assignments of the 2171-keV level. The DCO ratio and P for the  $J_i^\pi \rightarrow J_f^\pi$  assignments,  $11^+ \rightarrow 11^-$ ,  $11^- \rightarrow 11^-$ ,  $12^+ \rightarrow 11^-$ ,  $12^- \rightarrow 11^-$ ,  $13^+ \rightarrow 11^-$  and  $13^- \rightarrow 11^-$ , were calculated as a function of mixing ratio ( $\delta$ ), where ever applied, and are shown in Fig. 7.7. From the figure, it is clearly seen that for the  $13^+ \rightarrow 11^-$  spin-parity assignment, the calculated DCO ratio and polarization match with the experimental DCO ratio and polarization values for the mixing ratio  $\delta \approx -0.2$ , which suggests that there is a small admixture of E3 transition with the M2 multipolarity of 992-keV transition. 755-keV and 1262-keV two new connecting  $\gamma$ -ray transitions between the bands B1 and B2 are also observed in the present work. With the assignment of  $J^\pi = 13^+$  for the 2171-keV level, the 755-keV becomes an E1 transition and the 1262-keV becomes an E3 transition. The measured

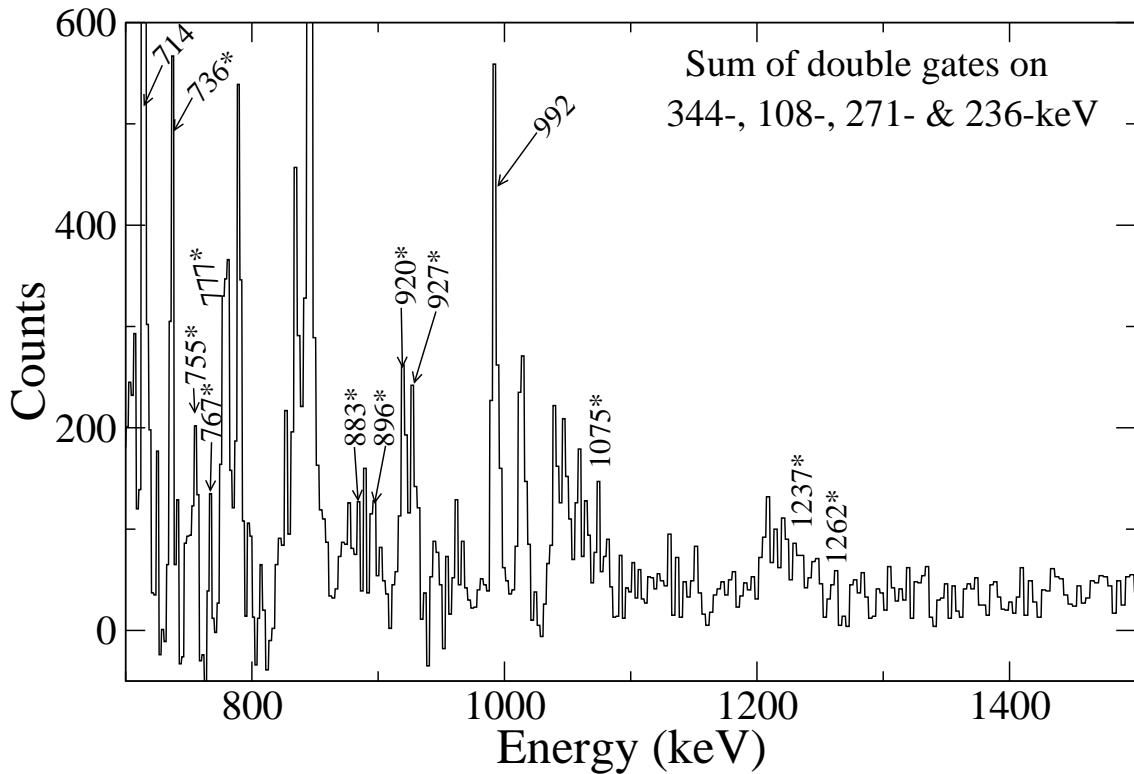


Figure 7.5: Coincidence spectrum generated by double gate list of 344-, 108-, 271- and 236-keV  $\gamma$  rays. The new  $\gamma$ -transitions are marked by \*.

DCO ratios of these two transitions are consistent with this assignment. The calculated half-life (Weisskopf estimate) of the  $13^+$  level considering 992-keV  $\gamma$ -ray transition as pure M2 is 1 ns and for E3 transition is 545 ns. Therefore, the half-life of the  $13^+$  level for the (M2/E3) mixed 992-keV transition is 0.99 ns. So, the level is not expected to be a long-lived isomer. However, considering the uncertainty in the data point in Fig. 7.7, the possibility of a lower multipolarity (M1) of the 992-keV transition with  $12^-$  assignment for the 2171 keV level can not be completely ruled out.

All the  $\gamma$ -rays of band B2, except the 316.7 keV  $\gamma$  ray, as reported in the previous work [9], have been observed in the present work. The tentatively placed 356.0 keV  $\gamma$  ray has been confirmed in the present work. In this band, a few new  $\gamma$ -ray transitions, 511-, 656-, 430-, 767-, 846-, 415-, 701-, 853-, 437-, 264- and 368-keV have been observed and are shown in Fig. 7.3 and Fig. 7.4(b).

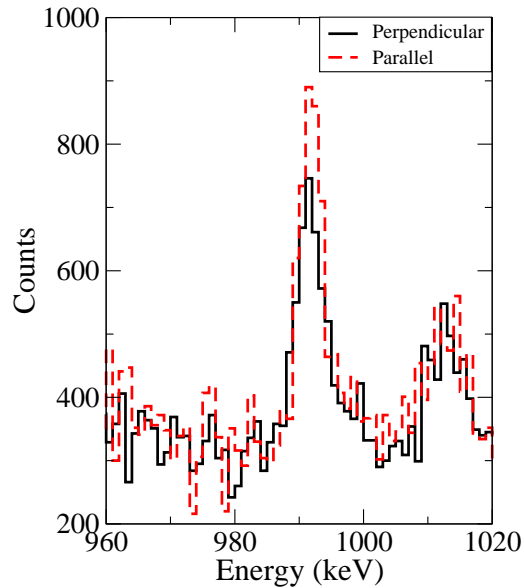


Figure 7.6: Perpendicular (solid) and parallel (dashed) components of 992-keV  $\gamma$  ray are shown. The higher parallel scattering counts than the perpendicular one indicates magnetic type transition.

These  $\gamma$  rays are placed in the band according to their coincidence and intensity relation. For a few of these new  $\gamma$ -rays, though DCO ratios have been measured, but the IPDCO ratios could not be obtained due to low statistics (see Table 7.1). With the placement of these new  $\gamma$  rays in the level scheme, band B2 has been extended up to an excitation energy of  $\sim 5.1$  MeV and a spin of  $22^+ \hbar$ .

Along with the known  $\gamma$  rays of band B3, as reported in Ref. [9], 3 new  $\gamma$  rays, 220-, 138- and 113-keV have been observed in the present work and are shown in Fig. 7.4(c). The new  $\gamma$  rays have been placed in the band above the 227-keV  $\gamma$  ray decaying from the 2223-keV state. The spins and parities of the levels of this band were not assigned in the previous work [9]. In order to assign the spin-parity of this band, a cross-over transition 678-keV from the 2223-keV to 1545-keV state has been chosen and the angular distribution of this transition has been obtained, which is shown in Fig 7.8. The figure suggests the quadrupole nature of this transition. IPDCO ratio for this transition has been obtained. The positive value of the IPDCO ratio (see Table 7.1) suggests that the transition is electric type. Therefore, it is confirmed that

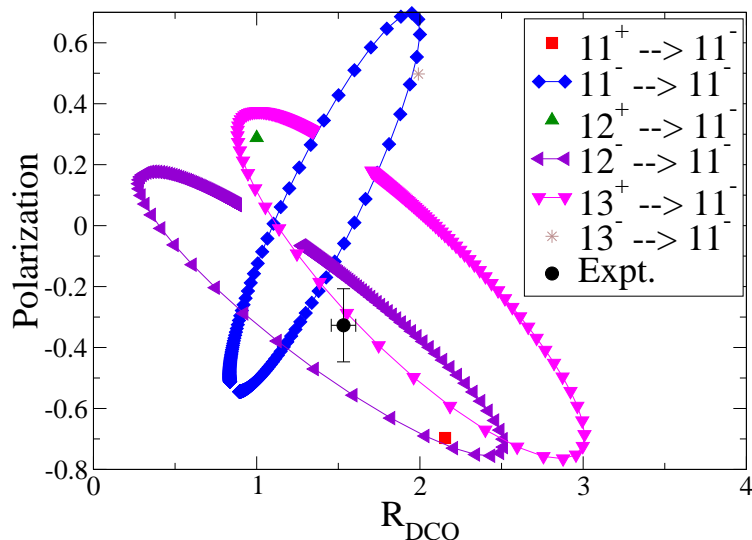


Figure 7.7: Theoretical contour plots of DCO ratio vs. polarization for different possible spin-parity  $J_i^\pi \rightarrow J_f^\pi$  assignments as a function of mixing ratio ( $\delta$ ) for the 992-keV  $\gamma$  ray. The theoretical calculations are compared with the experimentally measured values.

the transition has stretched E2 multipolarity. The low lying  $7^+$  state at 395-keV excitation energy, is connected with the band B3 by the 244-keV  $\gamma$  ray decaying from the 639-keV state. By gating on the 678-keV  $\gamma$ -ray transition, the DCO ratio of the 244-keV  $\gamma$  ray was obtained as 1.11(11). The IPDCO ratio for this transition was obtained as 0.04(5). In order to assign the spin-parity of the 639-keV state, theoretical contour plots of DCO ratio vs. polarization for different possible spin-parity  $J_i^\pi \rightarrow J_f^\pi$  assignments as a function of mixing ratio ( $\delta$ ) for the 244-keV  $\gamma$  ray have been done and compared with the experimentally measured values, as shown in Fig. 7.9. The experimentally measured DCO ratio and polarization data point (marked by filled circle) lies close to the calculated values for the  $9^- \rightarrow 7^+$  and  $7^+ \rightarrow 7^+$  spin-parity assignments in Fig. 7.9. In case of  $9^- \rightarrow 7^+$  assignment, multipolarity of the 244-keV  $\gamma$  ray decaying from that state will be M2+E3. In that case, half-life of the 639-keV state will be in the order of  $\mu$ s to ms. However, the half-life of this state has been reported as 2.5 ns in the previous work [9]. Therefore, the suitable spin-parity configuration for the 244-keV  $\gamma$  ray is  $7^+ \rightarrow 7^+$  which suggests the spin-parity of the 639-keV state as  $7^+$ .

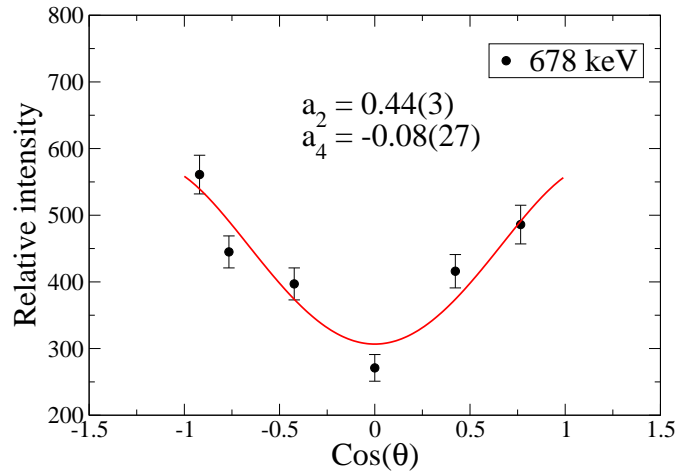


Figure 7.8: Angular distribution of 678-keV  $\gamma$  ray decaying from the 2223-keV to 1545-keV state in band B3. Solid line is the fitted curve of the data.

A few of the  $\gamma$ -ray transitions in band B3 are seen in the gated spectrum of band B2 and vice versa (see Fig. 7.4(b) and Fig. 7.4(c)). This indicates that the bands B2 and B3 are connected. However, no connecting  $\gamma$ -ray transition between the bands could be observed in the present work. With the observation of the  $\gamma$  rays of band B3 in different gated spectra of band B2 and vice versa, it is suggested that the connecting transitions between the bands could be very low-energy transitions. However, the experimental setup for the present work is not suitable for identifying such low-energy transitions.

Table 7.1: The energy ( $E_\gamma$ ) and intensity ( $I_\gamma$ ) of the  $\gamma$  rays of  $^{196}\text{Tl}$  along with the corresponding spin and parity of the initial ( $J_i^\pi$ ) and the final ( $J_f^\pi$ ) states and the energy of the initial state ( $E_i$ ). The measured values of  $R_{DCO}$  and  $\Delta_{IPDCO}$  of the corresponding  $\gamma$  rays are also shown in the following table.

$E_\gamma(\text{keV})$ (in keV)	$E_i(\text{keV})$ (in keV)	$J_i^\pi \rightarrow J_f^\pi$	$I_\gamma$ <sup>1</sup>	$R_{DCO}$	$\Delta_{IPDCO}$	Deduced Multipolarity
61.5 <sup>9</sup>	801	$9^- \rightarrow 8^-$	-	-	-	(M1+E2)

Table 7.1: Continued....

$E_\gamma(keV)$ (in keV)	$E_i(keV)$ (in keV)	$J_i^\pi \rightarrow J_f^\pi$	$I_\gamma$ <sup>1</sup>	$R_{DCO}$	$\Delta_{IPDCO}$	Deduced Multipolarity
106.3	4321	$22^- \rightarrow 21^-$	2.30(4)	$0.71(13)$ <sup>2</sup>	-	M1+E2
108.4	909	$10^- \rightarrow 9^-$	9.85(14)	$0.73(12)$ <sup>2</sup>	-	M1+E2
113.3	2694	$(15^+) \rightarrow (14^+)$	1.23(10)	-	-	-
137.6	2581	$(14^+) \rightarrow (13^+)$	1.74(10)	-	-	-
161.4	800	$8^+ \rightarrow 7^+$	5.66(31)	$0.59(5)$ <sup>6</sup>	-	M1+E2
163.6	2335	$14^+ \rightarrow 13^+$	4.54(7)	$0.91(7)$ <sup>4</sup>	-	M1+E2
165.0	3110	-	-	-	-	-
170.0	909	$10^- \rightarrow 8^-$	0.90(2)	-	-	E2
185.0	2945	-	-	-	-	-
188.3	3522	$19^- \rightarrow 18^-$	5.88(9)	$0.68(9)$ <sup>2</sup>	-	M1+E2
192.2	2527	$15^+ \rightarrow 14^+$	5.72(8)	$1.07(13)$ <sup>4</sup>	-	M1+E2
219.5	2443	$(13^+) \rightarrow 12^+$	1.81(10)	-	-	-
220.0	1636	-	2.11(3)	-	-	-
226.8	2223	$12^+ \rightarrow 11^+$	1.73(10)	-	-	M1+E2
232.5	2760	$16^- \rightarrow 15^-$	5.90(9)	$0.57(6)$ <sup>5</sup>	-0.26(10)	M1+E2
235.9	1416	$12^- \rightarrow 11^-$	26.01(37)	$0.61(2)$ <sup>2</sup>	-0.18(3)	M1+E2
241.0	3351	-	2.58(4)	-	-	-
243.9	639	$7^+ \rightarrow 7^+$	31.02(13)	$1.11(11)$ <sup>6</sup>	0.04(5)	M1+E2
263.7	4729	$21^+ \rightarrow 20^+$	1.97(8)	-	-	M1+E2
266.1	2079	$14^- \rightarrow 13^-$	13.25(19)	$0.57(2)$ <sup>3</sup>	-0.19(6)	M1+E2
269.6	1545	$10^+ \rightarrow 9^+$	1.09(7)	-	-	M1+E2
271.0	1180	$11^- \rightarrow 10^-$	43.16(62)	$0.48(1)$ <sup>2</sup>	-0.16(3)	M1+E2
284.9	3045	$17^- \rightarrow 16^-$	13.12(19)	$0.60(2)$ <sup>2</sup>	-0.19(3)	M1+E2

Table 7.1: Continued....

$E_\gamma(keV)$ (in keV)	$E_i(keV)$ (in keV)	$J_i^\pi \rightarrow J_f^\pi$	$I_\gamma$ <sup>1</sup>	$R_{DCO}$	$\Delta_{IPDCO}$	Deduced Multipolarity
287.0	1923	-	-	-	-	-
288.6	3334	$18^- \rightarrow 17^-$	10.57(16)	$0.54(2)^3$	-0.17(3)	M1+E2
289.0	3288	-	-	-	-	-
303.9	4215	$21^- \rightarrow 20^-$	2.58(4)	$0.54(3)^3$	-0.24(4)	M1+E2
319.4	2846	$16^+ \rightarrow 15^+$	5.74(8)	$0.81(8)^4$	-0.09(6)	M1+E2
336.7	3183	$17^+ \rightarrow 16^+$	4.09(6)	$0.90(9)^4$	-	M1+E2
343.6	739	$8^- \rightarrow 7^+$	100	$0.61(1)^2$	-0.04(2)	E1(+M2)
356.3	2527	$15^+ \rightarrow 13^+$	3.02(5)	$1.60(31)^4$	-	E2
368.0	5097	$22^+ \rightarrow 21^+$	0.74(1)	$1.04(31)^4$	-	M1+E2
379.7	1180	$11^- \rightarrow 9^-$	2.45(4)	$0.99(17)^2$	-	E2
389.4	3911	$20^- \rightarrow 19^-$	5.75(9)	$0.56(3)^3$	-0.03(4)	M1+E2
396.8	1813	$13^- \rightarrow 12^-$	20.94(30)	$0.54(2)^3$	-0.10(1)	M1+E2
415.1	4028	$19^+ \rightarrow 18^+$	1.85(3)	$0.82(11)^4$	-0.03(1)	M1+E2
430.3	3613	$18^+ \rightarrow 17^+$	1.78(3)	$1.02(19)^4$	-0.26(7)	M1+E2
437.0	4465	$20^+ \rightarrow 19^+$	0.37(1)	$0.93(30)^4$	-	M1+E2
447.6	2527	$15^- \rightarrow 14^-$	9.94(15)	$0.53(2)^2$	-0.23(2)	M1+E2
450.8	1996	$11^+ \rightarrow 10^+$	3.31(26)	-	-	M1+E2
475.4	1275	$9^+ \rightarrow 8^+$	8.43(45)	$0.24(2)^7$	-	M1+E2
477.4	3522	$19^- \rightarrow 17^-$	3.60(5)	$1.28(19)^2$	0.29(6)	E2
507.6	1416	$12^- \rightarrow 10^-$	16.14(24)	$0.95(5)^2$	0.03(2)	E2
510.8	2846	$16^+ \rightarrow 14^+$	8.23(12)	-	-	E2
517.8	3045	$17^- \rightarrow 15^-$	2.82(5)	$0.89(16)^2$	-	E2
577.4	3911	$20^- \rightarrow 18^-$	0.60(2)	$0.90(20)^3$	-	E2

Table 7.1: Continued....

$E_\gamma(keV)$ (in keV)	$E_i(keV)$ (in keV)	$J_i^\pi \rightarrow J_f^\pi$	$I_\gamma$ <sup>1</sup>	$R_{DCO}$	$\Delta_{IPDCO}$	Deduced Multipolarity
632.9	1813	$13^- \rightarrow 11^-$	6.79(11)	$0.94(15)$ <sup>3</sup>	0.03(3)	E2
656.4	3183	$17^+ \rightarrow 15^+$	1.85(3)	$1.69(27)$ <sup>4</sup>	-	E2
663.4	2079	$14^- \rightarrow 12^-$	23.78(34)	$0.94(3)$ <sup>3</sup>	0.09(1)	E2
678.4	2223	$12^+ \rightarrow 10^+$	11.22(60)	-	0.09(1)	E2 <sup>8</sup>
680.7	2760	$16^- \rightarrow 14^-$	24.46(35)	$0.97(3)$ <sup>2</sup>	0.09(2)	E2
692.9	4215	$21^- \rightarrow 19^-$	1.93(22)	$0.91(11)$ <sup>3</sup>	-	E2
700.7	4729	$21^+ \rightarrow 19^+$	0.87(2)	$1.73(32)$ <sup>4</sup>	-	E2
714.4	2527	$15^- \rightarrow 13^-$	6.60(10)	$1.59(10)$ <sup>4</sup>	0.09(5)	E2
720.8	1996	$11^+ \rightarrow 9^+$	5.92(33)	-	-	E2
736.4	4258	$21^- \rightarrow 19^-$	3.97(6)	$0.89(3)$ <sup>2</sup>	0.11(1)	E2
745.2	1545	$10^+ \rightarrow 8^+$	14.57(80)	$0.95(3)$ <sup>6</sup>	0.15(2)	E2
755.2	2171	$13^+ \rightarrow 12^-$	2.45(4)	$1.06(9)$ <sup>4</sup>	-	E1
766.8	3613	$18^+ \rightarrow 16^+$	1.81(3)	$1.65(45)$ <sup>4</sup>	-	E2
777.4	2193	-	2.04(6)	-	-	
846.4	4028	$19^+ \rightarrow 17^+$	-	-	-	E2
853.0	4465	$20^+ \rightarrow 18^+$	1.24(6)	$1.53(92)$ <sup>4</sup>	-	E2
883.1	2299	-	0.94(3)	-	-	-
895.9	2076	-	1.43(3)	-	-	-
920.4	2999	$16^- \rightarrow 14^-$	1.95(4)	$0.94(12)$ <sup>2</sup>	0.17(3)	E2
927.3	5185	$22^+ \rightarrow 21^-$	1.42(4)	$0.64(12)$ <sup>2</sup>	0.03(1)	E1
991.7	2171	$13^+ \rightarrow 11^-$	7.71(12)	$1.53(7)$ <sup>4</sup>	-0.05(2)	M2+E3
1075.3	2491	-	0.55(3)	-	-	-
1217.7	1957	-	0.31(3)	-	-	-

Table 7.1: Continued....

$E_\gamma(keV)$ (in keV)	$E_i(keV)$ (in keV)	$J_i^\pi \rightarrow J_f^\pi$	$I_\gamma$ <sup>1</sup>	$R_{DCO}$	$\Delta_{IPDCO}$	Deduced Multipolarity
1237.4	2653	-	1.66(4)	-	-	-
1262.3	2171	$13^+ \rightarrow 10^-$	4.31(7)	$0.77(6)$ <sup>4</sup>	0.05(2)	(E3)

## 7.4 Discussion

In Tl isotopes, the proton Fermi level lies below the  $Z = 82$  spherical shell closure near the  $3s_{1/2}$  and  $2d_{3/2}$  orbitals, whereas in  $A \sim 190$  mass region, the neutron Fermi level lies close to the  $1i_{13/2}$ ,  $3p_{3/2}$  and  $2f_{5/2}$  orbitals. The high (low)  $\Omega$  components of the negative parity proton Nilsson states originating from the  $h_{9/2}$  parentage come down in energy in oblate (prolate) deformation side in the Nilsson diagram. Therefore, a band structure above the  $8^-$  isomeric state in all odd-odd Tl isotopes in the  $A = 190 - 200$  mass region, has been interpreted as a 2-quasiparticle band (band B1) with  $\pi h_{9/2} \otimes \nu i_{13/2}$  configuration. The spins and parities of the  $2^-$ ,  $3^-$  and  $7^+$  low-lying states in  $^{196}\text{Tl}$ , can be obtained from the  $\pi s_{1/2} \otimes \nu p_{3/2}$ ,  $\pi s_{1/2} \otimes \nu f_{5/2}$  and  $\pi s_{1/2} \otimes \nu i_{13/2}$  possible configurations, respectively. The positive parity band B2 is built on the  $13^+$  state. This band is connected with the negative parity ground-state band B1 by three  $\gamma$ -ray transitions. This band has developed at relatively high excitation energy and spin. Therefore,

<sup>1</sup>Relative  $\gamma$ -ray intensities are estimated from prompt spectra and normalized to 100 for the total intensity of 343.9-keV  $\gamma$ -rays.

<sup>2</sup>From 663.4 keV (E2) DCO gate;

<sup>3</sup>From 680.7 keV (E2) DCO gate;

<sup>4</sup>From 343.6 keV (E1) DCO gate;

<sup>5</sup>From 507.6 keV (E2) DCO gate;

<sup>6</sup>From 678.4 keV (E2) DCO gate;

<sup>7</sup>From 243.9 keV (M1+E2,  $\Delta J = 0$ ) DCO gate;

<sup>8</sup>Multipolarity obtained from angular distribution;

<sup>9</sup>Adopted from Ref. [9]

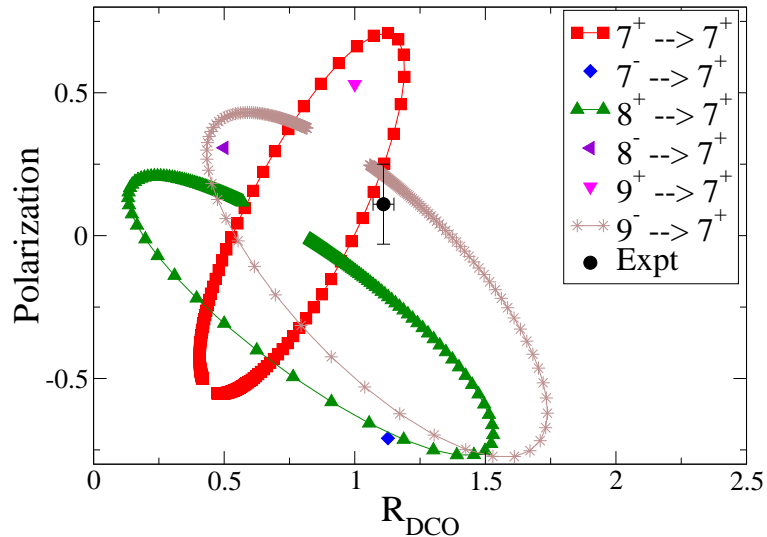


Figure 7.9: Theoretical contour plots of DCO ratio vs. polarization for different possible spin-parity  $J_i^\pi \rightarrow J_f^\pi$  assignments as a function of mixing ratio ( $\delta$ ) for the 244-keV  $\gamma$  ray in band B3. The theoretical calculations are compared with the experimentally measured values.

this could be a four-quasiparticle band. A possible band configuration  $\pi h_{9/2} \otimes \nu(i_{13/2}^{-2}j)$  has been suggested for this band, where  $j$  stands for either the  $f_{5/2}$  or the  $p_{3/2}$  orbital. This is based on the available single particle orbitals near the Fermi levels, systematics of the neighboring even-even and odd-A nuclei and considering the spin, parity and excitation energy of the band head of the band B2. The above configuration involves the alignment of a pair of neutrons in the  $\nu i_{13/2}$  and  $\nu(f_{5/2}/p_{3/2})$  orbitals. Such 2 neutron configurations have been already reported in odd-A  $^{195,197}\text{Tl}$  nuclei. The excitation energy of the band head of band B2 (2171 keV) is very similar to the 3-qp band with same neutron configuration in its nearest neighbor  $^{197}\text{Tl}$  (2114 keV). However, the band B3 with  $7^+$  band-head spin, has developed at relatively low excitation energy and spin. Therefore, this could be a 2-quasiparticle band and a possible band configuration  $\pi d_{3/2} \otimes \nu i_{13/2}$  has been suggested. In order to study the high-spin band structure in  $^{196}\text{Tl}$ , systematics of B(M1)/B(E2) ratio, aligned angular momentum ( $i_x$ ), kinetic moment of inertia ( $J^{(1)}$ ) and signature splitting have been discussed below.

Experimental B(M1)/B(E2) ratios and its comparison with theoretical calculations can be used to get information about the involved orbitals. In the present work, a systematic study of the

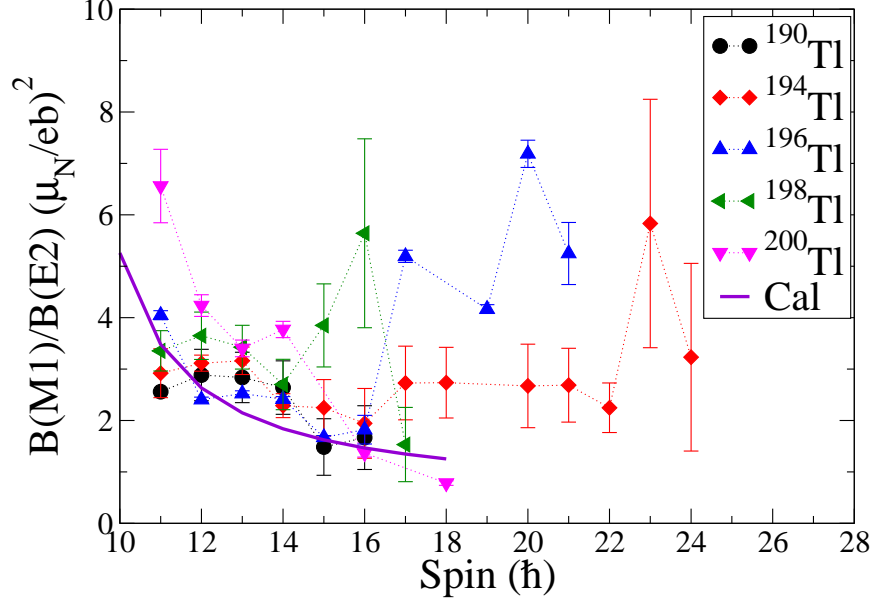


Figure 7.10: Experimental  $B(M1)/B(E2)$  ratios (filled symbols) as a function of spin for the  $\pi h_{9/2} \otimes \nu i_{13/2}$  yrast band in  $^{196}\text{Tl}$  nucleus along with the neighboring odd-odd Tl isotopes. The experimental values are compared with theoretical calculation (solid line) from geometrical model for the  $\pi h_{9/2} \otimes \nu i_{13/2}$  configuration in  $^{196}\text{Tl}$ .

$B(M1)/B(E2)$  ratios of the 2-quasiparticle ground-state band (band B1) in  $^{196}\text{Tl}$  along with the neighboring odd-odd Tl isotopes has been performed. The experimental  $B(M1)/B(E2)$  ratios can be obtained from the following relation [125]:

$$\frac{B(M1; I \rightarrow I - 1)}{B(E2; I \rightarrow I - 2)} = 0.697 \frac{I_\gamma(\Delta I = 1)}{I_\gamma(\Delta I = 2)} \frac{E_\gamma^5(\Delta I = 2)}{E_\gamma^3(\Delta I = 1)} \frac{1}{1 + \delta^2} \left[ \frac{\mu_N^2}{e^2 b^2} \right] \quad (7.1)$$

Where  $\delta$  is the mixing ratio in  $\Delta I = 1$  transition and its values are taken from Ref. [9] in the experimental  $B(M1)/B(E2)$  calculation.  $I_\gamma$  are the experimentally measured  $\gamma$ -ray intensities for the competing transitions.  $E_\gamma$  are the  $\gamma$ -ray energies in MeV unit. The theoretical  $B(M1)/B(E2)$  ratios have been obtained for the ground-state band (B1) considering  $\pi h_{9/2} \otimes \nu i_{13/2}$  band configuration using the semiclassical Dönau-Frauendorf model [109, 110, 111]:

$$\frac{B(M1; I \rightarrow I - 1)}{B(E2; I \rightarrow I - 2)} = \frac{12}{5Q_0^2 \cos^2(\gamma + 30^\circ)} \left( 1 - \frac{K^2}{(I - 1/2)^2} \right)^{-2} (A - B)^2 \left[ \frac{\mu_N^2}{e^2 b^2} \right] \quad (7.2)$$

where,

$$A = \left(1 - \frac{K^2}{I^2}\right)^{1/2} \left\{ \Omega_1(g_1 - g_R)(1 \pm \frac{\Delta e}{\hbar\omega}) + \sum_n \Omega_n(g_n - g_R) \right\}$$

$$B = \frac{K}{I} \left\{ (g_1 - g_R)i_1 + \sum_n (g_n - g_R)i_n \right\}$$

Where  $g_n$  are the g-factors for quasi-particles,  $g_R$  is the rotational g-factor of the even-even core of a nucleus,  $i_n$  are quasi-particle aligned angular momenta, and  $K = \sum_n \Omega_n$  is total nuclear spin projection along the nuclear symmetry axis.  $g_1$  and  $i_1$  stands for rotation-aligned quasi-particle which is responsible for signature splitting. Signature splitting term  $\Delta e$  can be extracted from experimental routhians of signature partners. In case of B(M1)/B(E2) ratio calculations for the  $\pi h_{9/2} \otimes \nu i_{13/2}$  yrast band in  $^{196}\text{Tl}$ , the values used for the parameters have been mentioned here. The aligned angular momenta  $i_p = 1.5$  and  $i_n = 6.5$  for proton and neutron, respectively, were taken for the calculation. Here,  $g_R$  was assumed to be 0.3, obtained from g-factor measurements in the  $A \sim 190$  mass region [129]. The measured odd-proton g-factor  $g_p$  of 0.86 for the  $(\pi h_{9/2})_{9/2^-}$  state in  $^{189}\text{Tl}$  and odd-neutron g-factor  $g_n$  of -0.16 for the  $(\nu i_{13/2})_{13/2^+}$  state in  $^{189}\text{Hg}$  [129] were used for the calculation. The measurement of g-factor for the neighboring odd-A isotopes are not available in the literature. However, the same orbitals are involved in these two nuclei as that of  $^{196}\text{Tl}$ . The  $K$ -value for this band was chosen to be  $K = 7$ . The choice of  $K = 7$  for the ground state band in  $^{196}\text{Tl}$  is based on the comparison of calculated and measured B(M1)/B(E2) ratios. This ratio has been calculated for different  $K$  values ( $5\hbar$ ,  $6\hbar$ ,  $7\hbar$  and  $8\hbar$ ). Out of these, the one with  $K = 7$  matches well with the experimental B(M1)/B(E2) values. The deformation parameters  $\beta_2 = 0.16$  and  $\gamma = -60^\circ$  were used. The deformation parameters  $\beta_2$  and  $\gamma$  were taken from the TRS calculations. The intrinsic quadrupole moment  $Q_0$  was obtained using the relation  $Q_0 = \frac{3}{\sqrt{5\pi}} R^2 Z \beta_2 (1 + 0.16\beta_2)$ . B(M1)/B(E2) ratios as a function of spin of the ground-state rotational band of  $^{196}\text{Tl}$ , along with the neighboring odd-odd Tl isotopes ( $A = 190 - 200$ ), have been shown in Fig. 7.10. The

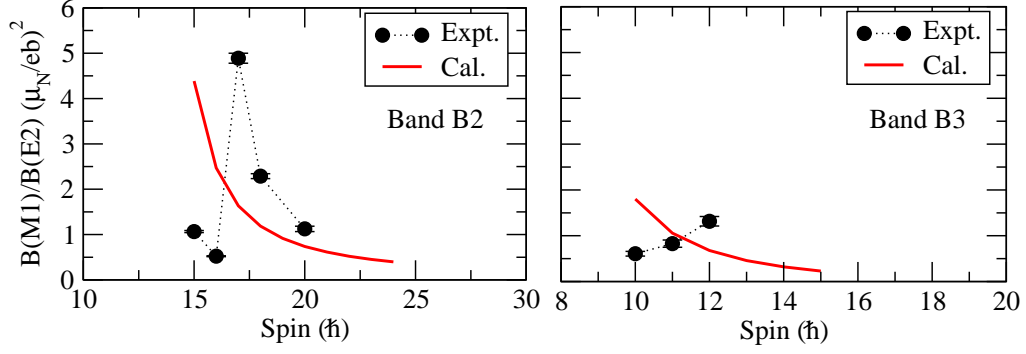


Figure 7.11: Experimental  $B(M1)/B(E2)$  ratios (filled symbols) as a function of spin for the bands B2 and B3 in  $^{196}\text{Tl}$ . The experimental values are compared with calculations (red solid lines) from geometrical model.

systematic trend of the experimental  $B(M1)/B(E2)$  ratios for all the odd-odd Tl isotopes before band crossing (for all the isotopes band crossing occurs after a spin of  $15\hbar$ ) are similar. A good agreement between the experimental and calculated results (solid line) has been achieved for the 2-quasiparticle band and this again confirms the configuration assigned for the ground-state band. It is clearly seen from the figure that after band crossing, the experimental  $B(M1)/B(E2)$  ratios as a function of spin show different trends for all the odd-odd Tl isotopes.

For bands B2 and B3, based on  $\pi h_{9/2} \otimes \nu(i_{13/2}^{-2}j)(j = f_{5/2}/p_{3/2})$  and  $\pi d_{3/2} \otimes \nu i_{13/2}$ , respectively,  $B(M1)/B(E2)$  ratios have also been calculated using the semiclassical Dönau-Frauendorf model. For the 4-qp band B2, the parameters  $K = 12$ ,  $g_R = 0.3$ ,  $g_p = 0.86$ ,  $g_n(\nu i_{13/2}) = -0.16$ ,  $g_n(\nu f_{5/2}) = 0.33$ ,  $i_p = 1.5$ ,  $i_n = 6.5$ ,  $i_n + i_n = 7$ ,  $\beta_2 = 0.14$  and  $\gamma = -55^\circ$  were used for the calculations. For the 2-qp band B3, the parameters  $K = 6$ ,  $g_R = 0.3$ ,  $g_p(\pi d_{3/2}) = 0.53$ ,  $g_n(\nu i_{13/2}) = -0.16$ ,  $i_p = 0.5$ ,  $i_n = 6.5$ ,  $\beta_2 = 0.07$  and  $\gamma = -30^\circ$  were used for the calculations. The calculated values have been compared with the measured  $B(M1)/B(E2)$  values and are shown in Fig. 7.11. In case of band B3, the agreement of calculated and measured  $B(M1)/B(E2)$  values is not good. For band B3, the nucleus can not be treated as a good rotor because of its very small deformation. This may be responsible for the observed difference.

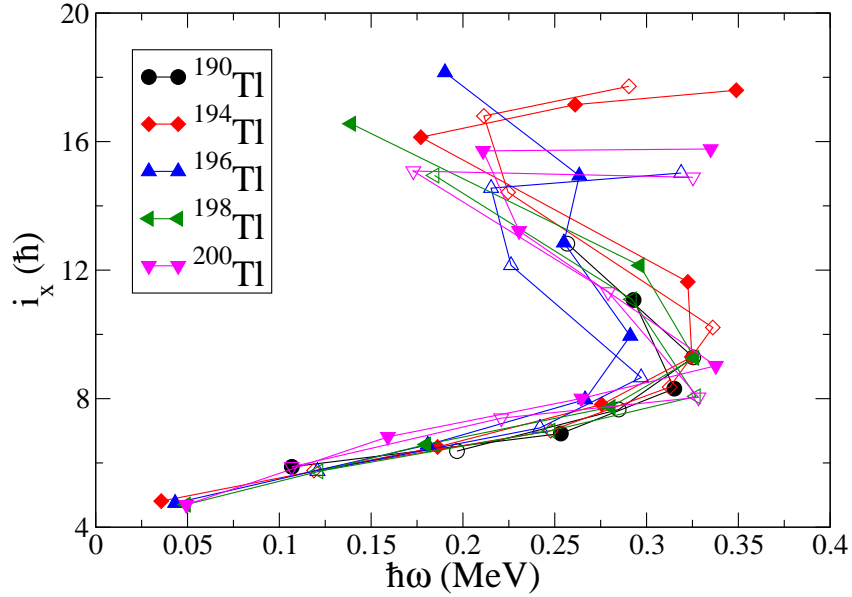


Figure 7.12: Aligned angular momenta ( $i_x$ ) as a function of rotational frequency ( $\hbar\omega$ ) for the  $\pi h_{9/2} \otimes \nu i_{13/2}$  bands in odd-odd Tl isotopes. The Harris reference parameters are chosen to be  $J_0 = 8.0 \hbar^2/\text{MeV}$  and  $J_1 = 40.0 \hbar^4/\text{MeV}^3$ .

The particle aligned angular momentum ( $i_x$ ) as a function of the rotational frequency ( $\hbar\omega$ ) for the ground-state band (band B1) of  $\pi h_{9/2} \otimes \nu i_{13/2}$  configuration in  $^{196}\text{Tl}$  along with the neighboring odd-odd Tl isotopes for the same configuration are shown in Fig. 7.12. It can be seen from the figure that the first band crossing in the band B1 in  $^{196}\text{Tl}$  occurs at a rotational frequency of  $\hbar\omega_c \sim 0.27 \text{ MeV}$ . The initial alignment is  $\sim 5\hbar$  and the gain in alignment ( $\Delta i_x$ ) is  $\sim 8\hbar$ . It is interesting to notice that the initial alignment, crossing frequency ( $\hbar\omega_c$ ) and gain in alignment ( $\Delta i_x$ ) in  $^{196}\text{Tl}$  are almost similar to those in the neighboring odd-odd Tl isotopes, as can be seen from Fig. 7.12. The alignment or crossing frequency and gain in alignment depends on the orbitals involved in the alignment and on the deformation of the nucleus. Therefore, from the  $i_x$  plots, it is expected that the neutron pair alignments due to band crossing are taking place at same orbital for all these Tl isotopes. The band crossing in the Tl isotopes in  $A \sim 190$  mass region are attributed to the alignment of a pair of neutrons in the  $i_{13/2}$  orbital, based on the availability of the  $i_{13/2}$  orbital near the neutron Fermi level and the observed large gain in alignment. The nature of the aligned angular momentum plots for all the Tl isotopes are

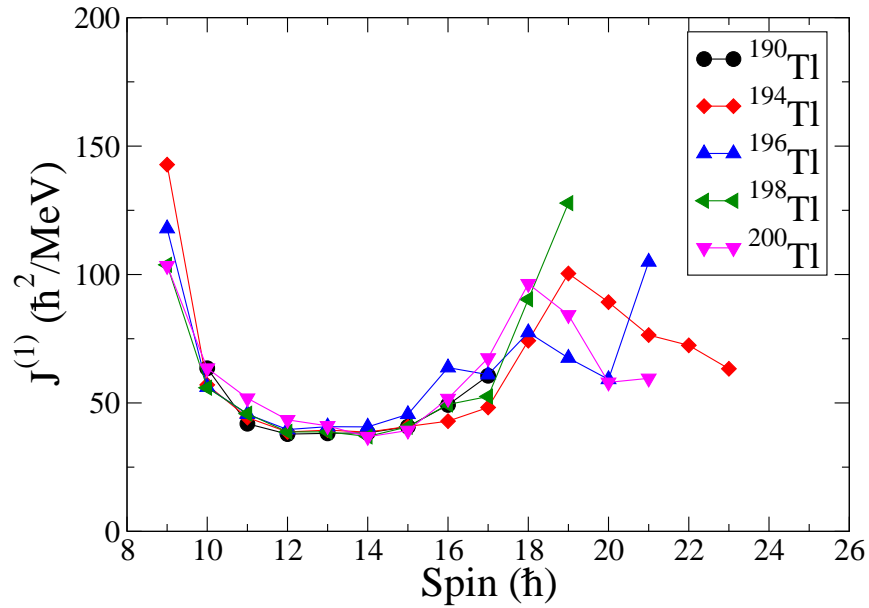


Figure 7.13: Comparison of kinetic moment of inertia ( $J^{(1)}$ ) as a function of spin ( $I$ ) of  $\pi h_{9/2} \otimes \nu i_{13/2}$  rotational bands in odd-odd Tl isotopes.

very much similar up to the band crossing. However, after band crossing, the nature of the  $i_x$  plots deviates from each other with increasing rotational frequency (i.e. with increasing spin). This different behaviour after the band crossing can be interpreted as the different collective features involved in the Tl isotopes. The kinetic moments of inertia ( $J^{(1)}$ ) for the ground-state bands for the Tl isotopes are also plotted as a function of spin and shown in Fig. 7.13. The similarity between these odd-odd Tl isotopes is also reflected in their kinetic moments of inertia values up to a spin  $I = 16\hbar$ , which corresponds to the crossing frequency. However, at higher spin region, they start to behave differently.

The signature splitting, defined as  $S(I) = [E(I) - E(I-1)]/2I$ , where  $E(I)$  is the level energy of spin  $I$ , for the band B1 in  $^{196}\text{Tl}$  along with the neighboring odd-odd Tl isotopes has been plotted as a function of spin  $I$  and shown in Fig. 7.14. It can be seen that the signature splitting for all the Tl isotopes are very similar up to spin  $I = 16\hbar$ . All the isotopes show a low-spin signature inversion at  $11\hbar$ . This signature inversion was explained in Ref. [130] by considering the J-dependence residual p-n interaction. At the higher spin  $I > 16$  (i.e. after particle alignment),

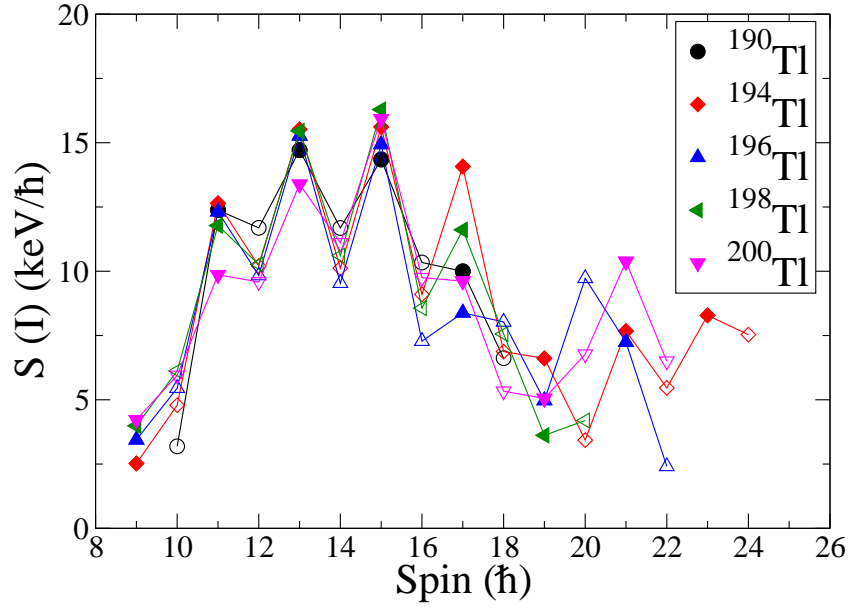


Figure 7.14: Comparison of signature splitting  $S(I)$  as a function of spin ( $I$ ) of  $\pi h_{9/2} \otimes \nu i_{13/2}$  rotational bands in odd-odd Tl isotopes.

all the Tl isotopes start to behave differently. This indicates that the residual p-n interaction is almost similar for all the Tl isotopes before particle alignment. However, at  $19\hbar$ , a second signature inversion has been observed in all the Tl isotopes except  $^{190}\text{Tl}$  (due to lack of high spin data as shown in Fig. 7.14) and  $^{194}\text{Tl}$ . In the present work, the uncertainty in spin of the ground-state band B1 in  $^{196}\text{Tl}$  has been removed and extended up to a spin of  $22\hbar$  as compared to the previous work [9]. Therefore, the second signature inversion and thereafter the trend of the signature splitting in  $^{196}\text{Tl}$  is clearly observed. In case of  $^{200}\text{Tl}$ , the second inversion is quickly recovered and follows the trend as in the  $^{194}\text{Tl}$ . However, in case of  $^{196}\text{Tl}$ , after the second signature inversion, the signature splitting follows the trends opposite as in  $^{200}\text{Tl}$  and  $^{194}\text{Tl}$ .

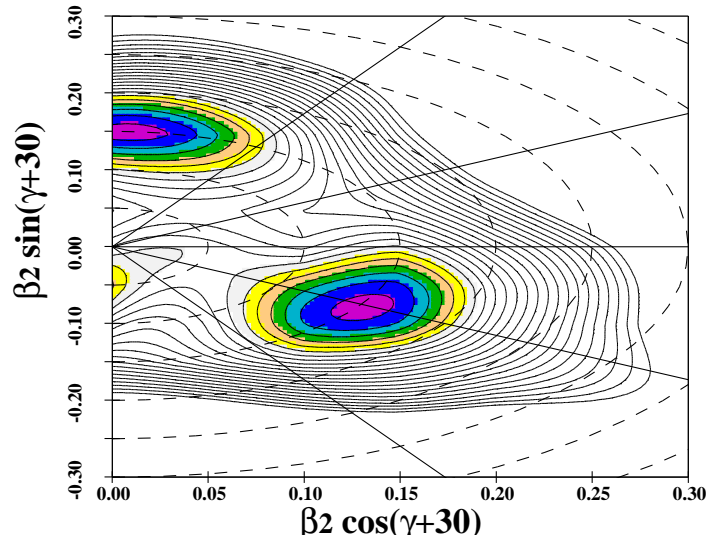


Figure 7.15: TRS calculations of  $^{196}\text{Tl}$  for the ground-state band B1 near band head at  $\hbar\omega = 0.11$  MeV. The contours are 250 keV apart.

## 7.5 TRS calculations

In order to get the quantitative idea about the shape of  $^{196}\text{Tl}$  nucleus for different band structures, the Total Routhian Surface (TRS) calculations were performed using the Strutinsky shell correction method. In these calculations, the quasi-particle energies were calculated using the Cranked Shell Model in which deformed Woods-Saxon potential with BCS pairing was incorporated. Coriolis term  $\omega j_x$  was introduced to include the cranking, where  $\omega$  is the rotational frequency of the nucleus and  $j_x$  is the projection of the single particle total angular momentum on the rotation axis. The TRS code of Nazarewicz et al. [72, 73] was used for the calculations as described in Section 2.7.

The contour plots of the TRSs calculated for  $^{196}\text{Tl}$  in the configurations, corresponding to the bands B1, B2 and B3 are shown in Fig. 7.15, Fig. 7.16 and Fig. 7.17, respectively. For the ground-state band B1, the surface was calculated near the band head ( $\hbar\omega = 0.11$  MeV), below its band crossing. Also for the two side bands B2 and B3, the surfaces were calculated near the band heads ( $\hbar\omega = 0.16$  MeV), below their band crossings. The contours are 250 keV apart.

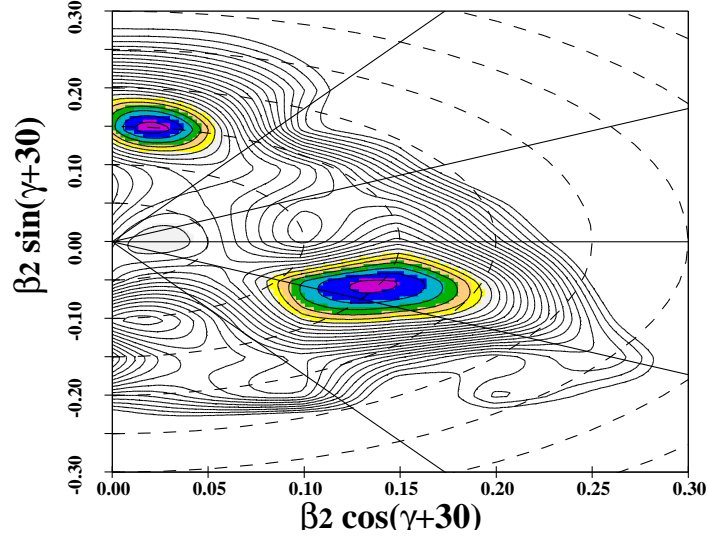


Figure 7.16: TRS calculations of  $^{196}\text{Tl}$  for the side band B2 near band head at  $\hbar\omega = 0.16$  MeV. The contours are 250 keV apart.

The spin values are well reproduced in the calculations for the three configurations. For the band B1, the band-head spin comes out as  $7\hbar$ , for B2,  $14\hbar$  and for B3,  $6\hbar$ . The TRS plots clearly show minima at oblate deformations with  $\beta_2 \sim 0.16$  and  $\gamma \sim -60^\circ$ , and  $\beta_2 \sim 0.14$  and  $\gamma \sim -55^\circ$  for bands B1 and B2, respectively. However, for band B3, the minimum of the TRS comes out to be  $\beta_2 \sim 0.07$  and  $\gamma \sim -30^\circ$  which indicate triaxiality with small deformation. The energies of the E2  $\gamma$ -rays in a rotational band of a deformed nucleus is inversely proportional to the moment of inertia according to the rotational model formula  $E = \frac{\hbar^2}{2\mathcal{J}}I(I + 1)$ , where  $E$  and  $I$  are the excitation energy and spin of the rotational level, respectively and  $\mathcal{J}$  is the moment of inertia. The moment of inertia of a nucleus would be smaller for smaller deformation and hence, the E2  $\gamma$ -ray energy would be larger for the same spin value. Therefore, the small deformation is in compliance with the experimentally obtained large E2 transition energy in band B3.

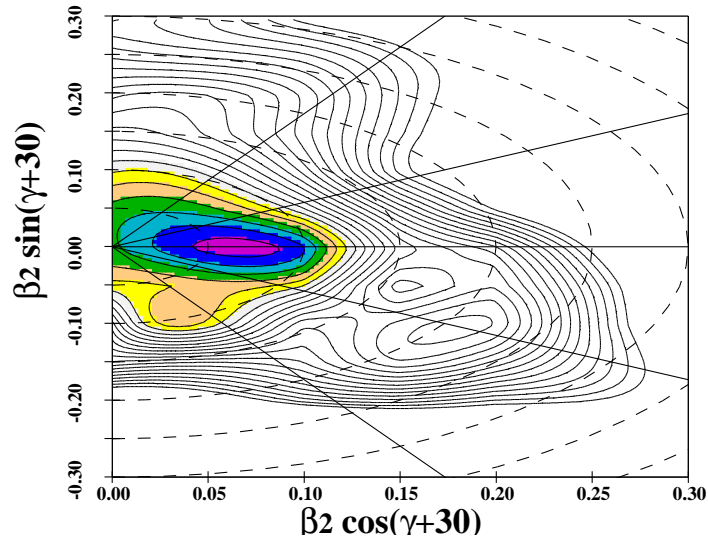


Figure 7.17: TRS calculations of  $^{196}\text{Tl}$  for the side band B3 near band head at  $\hbar\omega = 0.16$  MeV. The contours are 250 keV apart.

## 7.6 Conclusion

The high-spin states in the odd-odd nucleus  $^{196}\text{Tl}$  have been populated using  $^{185,187}\text{Re}(^{13}\text{C}, xn)^{196}\text{Tl}$  fusion evaporation reaction at a beam energy of 75 MeV. Total 38 new  $\gamma$ -ray transitions have been observed in this work. The level scheme of  $^{196}\text{Tl}$  has been extended up to an excitation energy of  $\sim 5.1$  MeV and a spin of  $22\hbar$  with the placement of the newly observed  $\gamma$  rays in this work compared to those reported in Ref. [9]. Moreover, definite spin and parity assignments were done in this work for the side bands B2 and B3 and hence, proper configurations have been assigned to these bands. With the new observation, the  $\pi h_{9/2} \otimes \nu i_{13/2}$  band (B1) has been extended beyond the band crossing and a systematic comparison of aligned angular momentum, B(M1)/B(E2) ratio, signature splitting and kinetic moment of inertia has been done for the odd-odd Tl isotopes. It has been observed that the behaviour of the odd-odd Tl nuclei remain almost identical before the band crossing but they behave differently after the band crossing. For the side bands B2 and B3, B(M1)/B(E2) ratios have been calculated considering the proposed single-particle configurations and compared with the measured values. It is also interesting

that no clear indication of chirality or MR band could be observed in  $^{196}\text{Tl}$ , where as these were reported for the isotopes  $^{194,198}\text{Tl}$ .

# Chapter 8

## High spin $\gamma$ -spectroscopy of $^{207}\text{Po}$

### 8.1 Introduction

For Po nuclei, the proton number (84) is close to the  $Z = 82$  spherical shell closure, therefore, for the heavier isotopes of Po, for which the neutron number is close to the  $N = 126$  spherical shell closure, are expected to be spherical in nature. Rotational bands, characterizing deformed shape, have indeed been reported for the lighter Po isotopes with  $N < 114$ . A plot of excitation energy vs. spin, shown in Fig. 8.1, for the ground state bands of the odd-A Po isotopes clearly shows that the lighter Po isotopes follow the rotational-like behaviour while the heavier isotopes ( $N > 114$ ) do not. The excited states of these heavier Po isotopes are, therefore, mostly generated by single particle excitations [15, 16, 17, 18, 19]. In the present thesis work,  $^{207}\text{Po}$  has been studied which is considered to be heavier isotope as the neutron number is  $N > 114$ . The properties of the excited states of the heavier Po isotopes are interpreted by the coupling of the doubly closed  $^{208}\text{Pb}$  ( $Z = 82$ ,  $N = 126$ ) core with the valence proton particles and neutron holes outside the core [16, 17, 18, 19]. Systematic investigations of the effect of the coupling of the high-j orbitals with the doubly closed Pb core can be carried out for these nuclei. In case of  $^{207}\text{Po}$  nucleus with  $Z = 84$  and  $N = 123$ , the proton and the neutron Fermi levels lie just above

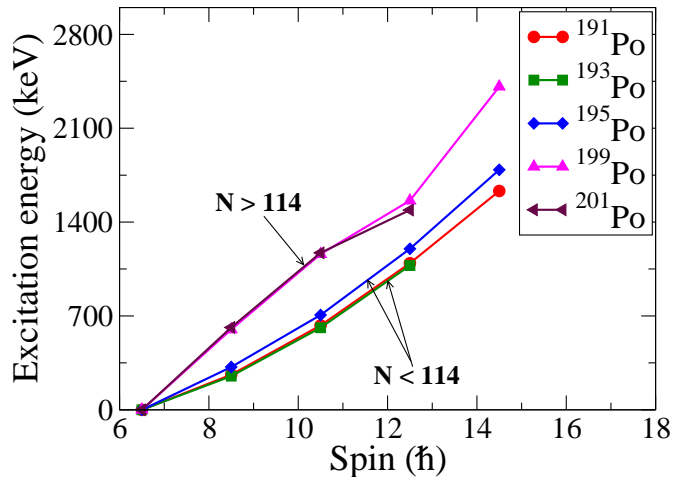


Figure 8.1: A plot of excitation energy vs. spin for the ground state bands of the odd-A Po isotopes. The data are taken from Ref. [36].

and below the heaviest known shell closures at  $Z = 82$  and  $N = 126$ , respectively. Therefore, this nucleus has two valence proton particles and three neutron holes outside the  $^{208}\text{Pb}$  core. The available high- $j$  orbitals near the Fermi levels are  $f_{5/2}$ ,  $f_{7/2}$ ,  $h_{9/2}$  and  $i_{13/2}$ .

The valence proton particles and the neutron holes can access the high- $j$  orbitals like  $\pi h_{9/2}$ ,  $\pi i_{13/2}$ ,  $\nu i_{13/2}$  etc. around their Fermi levels in this near-spherical shape nucleus. Again, such particle-hole orbitals are favorable for Magnetic Rotational (MR) bands which have been reported in different isotopes of Pb, Bi, Tl etc. in the  $A \sim 200$  mass region [134, 135, 136]. Therefore, one of the aims in this work was to look for MR band at high excitation energy.

## 8.2 Experiment and Data Analysis

The excited states in  $^{207}\text{Po}$  were populated using  $^{208}\text{Pb}(\alpha, 5n)^{207}\text{Po}$  fusion evaporation reaction at a beam energy of 60 MeV from K-130 cyclotron at VECC, Kolkata. The  $\gamma - \gamma$  coincidence data were collected using the  $\gamma$ -ray detector array VENUS (VECC array for NUClear Spectroscopy) consisting of 6 HPGe clovers with BGO anti-Compton shields during the exper-

iment. The detectors were placed in 4 angles with 2 each at  $\pm 30^\circ$  (backward) and  $\pm 90^\circ$ , the other two detectors were at the forward  $45^\circ$  and  $55^\circ$  angles with respect to the beam direction, in median plane.

A VME data acquisition system was used for recording the  $\gamma-\gamma$  coincidence data. The analysis of the data was done using the LAMPS [27] and RADWARE [28] software packages.  $^{133}\text{Ba}$  and  $^{152}\text{Eu}$  radioactive sources were used for energy efficiency and calibration of the detectors.

The present level scheme of  $^{207}\text{Po}$  was constructed by using relative  $\gamma$ -ray intensity and  $\gamma-\gamma$  coincidence relation.  $\gamma-\gamma$  coincidence relation was obtained from the  $\gamma-\gamma$  matrix. As described in Section 5.3, the spin-parity assignments of the excited states were done using DCO and IPDCO measurement. DCO matrix was constructed using data from  $-30^\circ$  and  $90^\circ$  detectors. For IPDCO ratio,  $90^\circ$  detectors were used for parallel and perpendicular scattering events.

### 8.3 Results and Discussion

Level scheme of  $^{207}\text{Po}$ , obtained from the present work, is shown in Fig. 8.2. A total of 8 new  $\gamma$  transitions have been identified and placed in the proposed level scheme. The new transitions are marked by asterisk (\*) in the level scheme. Table 8.1 shows the intensity, DCO and IPDCO ratios of the  $\gamma$  rays observed in the present work, along with the other relevant deduced quantities. By placing the new transitions, the level scheme has been extended from  $\sim 4.3$  MeV to  $\sim 6.9$  MeV of excitation energy and a spin from  $35/2\hbar$  to  $49/2\hbar$  compared to its previously known level scheme reported in Ref. [16]. The DCO and the IPDCO ratios could not be obtained for some of the transitions because of their low energy or less counts.

The  $\gamma-\gamma$  coincidence relations have been established by analysing several gated spectra projected from the  $\gamma-\gamma$  matrix. Representative single-gated spectra are shown in Fig. 8.3, Fig. 8.4

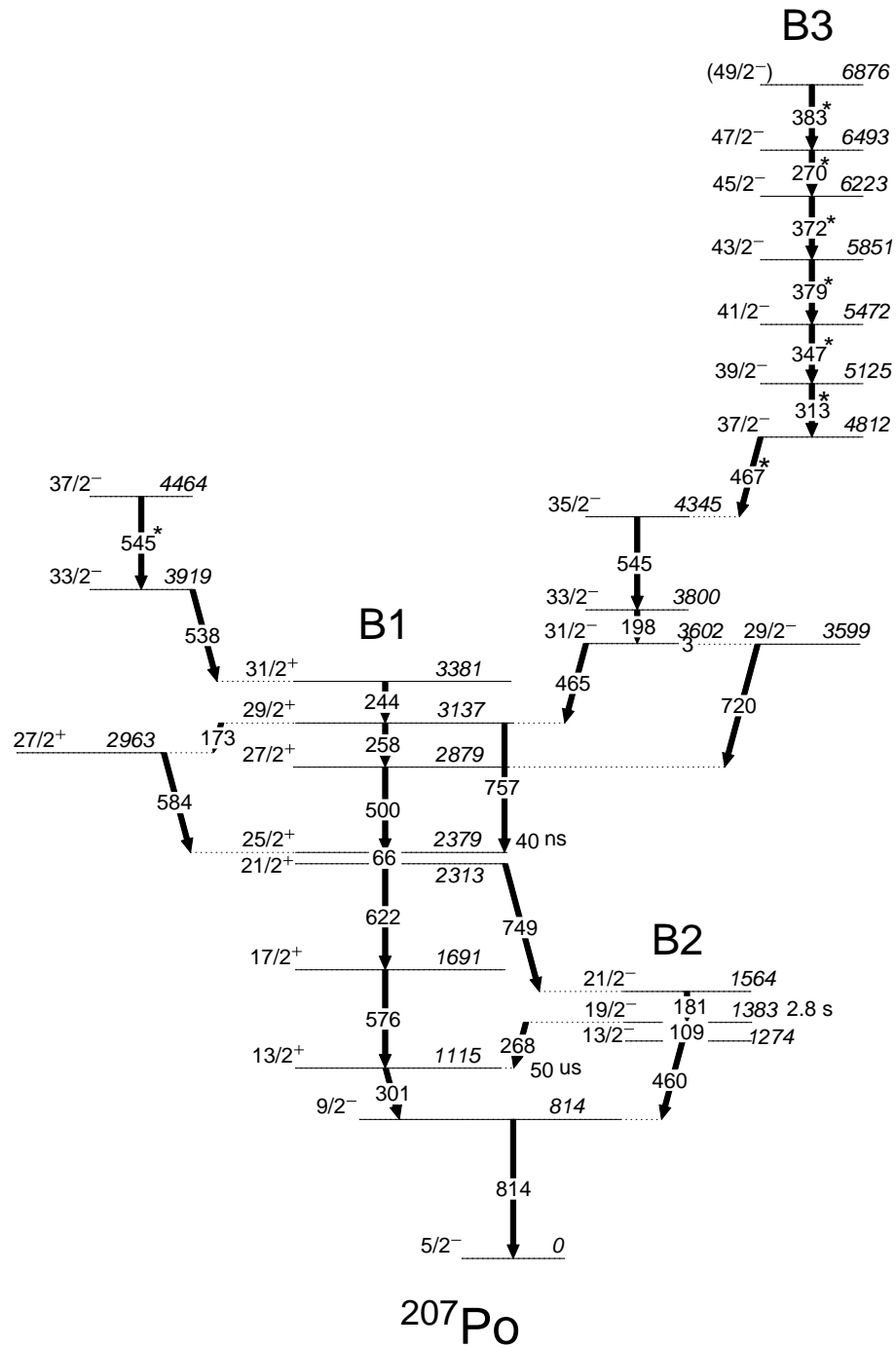


Figure 8.2: Level scheme of  $^{207}\text{Po}$  obtained from the present work.

and Fig. 8.5. Relative intensities of all the  $\gamma$  rays placed in the proposed level scheme, except 460-, 814-, 301-, 268-, 109-, 181- and 66-keV transitions, have been obtained by putting a single gate on a strong transition 576-keV, decaying from the  $17/2^+$  to the  $13/2^+$  state. The  $13/2^+$  state at 1115 keV is an isomeric state with a half life of 50  $\mu s$ , which decays to the  $5/2^-$  ground state through the  $9/2^-$  state. Therefore, the relative intensities of the transitions have been obtained with respect to the strong 576-keV transition decaying from the  $17/2^+$  state to the 50  $\mu s$   $13/2^+$  isomeric state. The 268-keV  $\gamma$ -ray, decaying from the  $19/2^-$  state at 1383 keV, and the 460-keV  $\gamma$  ray, decaying from the  $13/2^-$  state at 1274-keV, have been adopted from the previous work reported in Ref. [16]. The  $19/2^-$  state at 1383-keV is an isomeric state with a half life of 2.8 s. The state decays to the  $13/2^+$  state at 1115-keV and  $13/2^-$  state at 1274 keV through 268-keV and 109-keV  $\gamma$  rays, respectively. The 109-keV of M3 type transition could not be observed as a  $\gamma$ -ray transition, this transition was confirmed by the conversion electron measurement in the previous work [16]. The low energy 66-keV known  $\gamma$  ray decaying from the  $25/2^+$  isomeric state of 40 ns half life to the  $21/2^+$  state could not be observed using our experimental set up. In the present level scheme, the 109- and 66-keV transitions have also been adopted from Ref. [16].

Table 8.1: The energy ( $E_\gamma$ ) and intensity ( $I_\gamma$ ) of the  $\gamma$  rays of  $^{207}\text{Po}$  along with the corresponding spin and parity of the initial ( $J_i^\pi$ ) and the final ( $J_f^\pi$ ) states and the energy of the initial state ( $E_i$ ). The measured values of  $R_{DCO}$  and  $\Delta_{IPDCO}$  of the corresponding  $\gamma$  rays are also shown in the following table.

$E_\gamma(keV)$ (in keV)	$E_i(keV)$ (in keV)	$J_i^\pi \rightarrow J_f^\pi$	$I_\gamma$ <sup>1</sup>	$R_{DCO}$	$\Delta_{IPDCO}$	Deduced Multipolarity
66.2 <sup>7</sup>	2379	$25/2^+ \rightarrow 21/2^+$	-	-	-	E2
109.1 <sup>7</sup>	1383	$19/2^- \rightarrow 13/2^-$	-	-	-	M3

Table 8.1: Continued....

$E_\gamma(keV)$ (in keV)	$E_i(keV)$ (in keV)	$J_i^\pi \rightarrow J_f^\pi$	$I_\gamma^1$	$R_{DCO}$	$\Delta_{IPDCO}$	Deduced Multipolarity
173.4	3137	$29/2^+ \rightarrow 27/2^+$	1.82(2)	-	-	-
181.0	1564	$21/2^- \rightarrow 19/2^-$	-	-	-	$M1^7$
198.1	3800	$33/2^- \rightarrow 31/2^-$	9.76(3)	$0.59(1)^2$	-0.07(9)	M1+E2
244.0	3381	$31/2^+ \rightarrow 29/2^+$	5.14(2)	$0.58(2)^2$	-0.19(8)	M1+E2
257.6	3137	$29/2^+ \rightarrow 27/2^+$	6.95(4)	$0.48(2)^2$	-0.09(5)	M1+E2
268.1 <sup>7</sup>	1383	$19/2^- \rightarrow 13/2^+$	-	-	-	E3
270.0	6493	$47/2^- \rightarrow 45/2^-$	2.17(2)	$0.497(59)^3$	-	(M1+E2)
300.7	1115	$13/2^+ \rightarrow 9/2^-$	-	-	-	$M2^7$
313.4	5125	$39/2^- \rightarrow 37/2^-$	2.64(2)	$0.59(4)^2$	-0.20(9)	M1+E2
347.4	5472	$41/2^- \rightarrow 39/2^-$	2.72(2)	$0.54(5)^2$	-0.03(6)	M1+E2
371.7	6223	$45/2^- \rightarrow 43/2^-$	2.17(2)	$0.52(4)^2$	-0.07(6)	M1+E2
379.4	5851	$43/2^- \rightarrow 41/2^-$	2.46(2)	$0.46(5)^2$	-0.08(7)	M1+E2
383.0	6876	$(49/2^-) \rightarrow 47/2^-$	1.08(3)	-	-	(M1+E2)
459.6 <sup>7</sup>	1274	$13/2^- \rightarrow 9/2^-$	-	-	-	E2
465.1	3602	$31/2^- \rightarrow 29/2^+$	5.43(13)	$0.44(2)^2$	0.05(3)	E1
467.3	4812	$37/2^- \rightarrow 35/2^-$	3.43(18)	$0.89(6)^5$	-0.09(9)	M1+E2
499.6	2879	$27/2^+ \rightarrow 25/2^+$	24.27(6)	$0.46(2)^2$	-0.06(2)	M1+E2
538.3	3919	$33/2^- \rightarrow 31/2^+$	4.22(3)	$0.47(3)^2$	0.06(5)	E1
544.7	4464	$37/2^- \rightarrow 33/2^-$	3.97(3)	$1.64(3)^6$	0.20(6)	E2
544.9	4345	$35/2^- \rightarrow 33/2^-$	10.93(4)	$1.01(3)^5$	-0.09(2)	M1+E2
575.8	1691	$17/2^+ \rightarrow 13/2^+$	100	$0.98(5)^3$	0.13(3)	E2
583.7	2963	$27/2^+ \rightarrow 25/2^+$	6.69(4)	$0.43(3)^3$	-0.11(4)	M1+E2
621.9	2313	$21/2^+ \rightarrow 17/2^+$	99.58(13)	$1.01(4)^2$	0.11(2)	E2

Table 8.1: Continued....

$E_\gamma(keV)$ (in keV)	$E_i(keV)$ (in keV)	$J_i^\pi \rightarrow J_f^\pi$	$I_\gamma$ <sup>1</sup>	$R_{DCO}$	$\Delta_{IPDCO}$	Deduced Multipolarity
719.6	3599	$29/2^- \rightarrow 27/2^+$	8.66(4)	$0.53(3)$ <sup>2</sup>	0.13(3)	E1
749.0	2313	$21/2^+ \rightarrow 21/2^-$	9.84(5)	$1.04(12)$ <sup>4</sup>	-	E1
757.4	3137	$29/2^+ \rightarrow 25/2^+$	3.59(3)	$1.16(7)$ <sup>2</sup>	0.25(7)	E2
814.0	814	$9/2^- \rightarrow 5/2^-$	-	-	-	E2 <sup>7</sup>

The 538-keV  $\gamma$  ray from the  $33/2^-$  to the  $31/2^+$  state in  $^{207}\text{Po}$  was known but its multipolarity was tentative. The multipolarity of the 538-keV  $\gamma$  ray was reported [16] either as E1 or E2. Therefore, spin-parity of the 3919-keV state, from which the 538-keV  $\gamma$  ray decays, was not assigned in the previous work. In the present work, this  $\gamma$  ray has been observed and shown in Fig. 8.3 and Fig. 8.4. The DCO ratio and the positive value of the IPDCO ratio (see Table 8.1) for this transition, obtained in the present work, confirmed its E1 multipolarity. Therefore, spin-parity of the 3919-keV state has been assigned as  $33/2^-$  based on the deduced multipolarity of the 538-keV  $\gamma$  ray.

A new 545-keV  $\gamma$  ray, decaying from the 4464-keV state, has been observed in the present work which is in coincidence with the known 244-keV  $\gamma$  ray from the  $31/2^+$  to the  $29/2^+$  state, shown in Fig. 8.4. Since the known 545-keV  $\gamma$  ray decaying from the  $35/2^-$  to the  $33/2^-$  state is parallel to the 244-keV  $\gamma$  ray, the 244-keV transition, which is predominantly dipole type (M1), has been chosen for DCO gate to obtain DCO ratio for the new 545-keV  $\gamma$  ray. The value

<sup>1</sup>Relative  $\gamma$ -ray intensities are estimated from prompt spectra and normalized to 100 for the total intensity of 575.8-keV  $\gamma$ -rays.

<sup>2</sup>From 575.8 keV (E2) DCO gate;

<sup>3</sup>From 621.9 keV (E2) DCO gate;

<sup>4</sup>From 757.4 keV (E2) DCO gate;

<sup>5</sup>From 719.6 keV (E1) DCO gate;

<sup>6</sup>From 244.0 keV (M1) DCO gate;

<sup>7</sup>Adopted from Ref. [16]

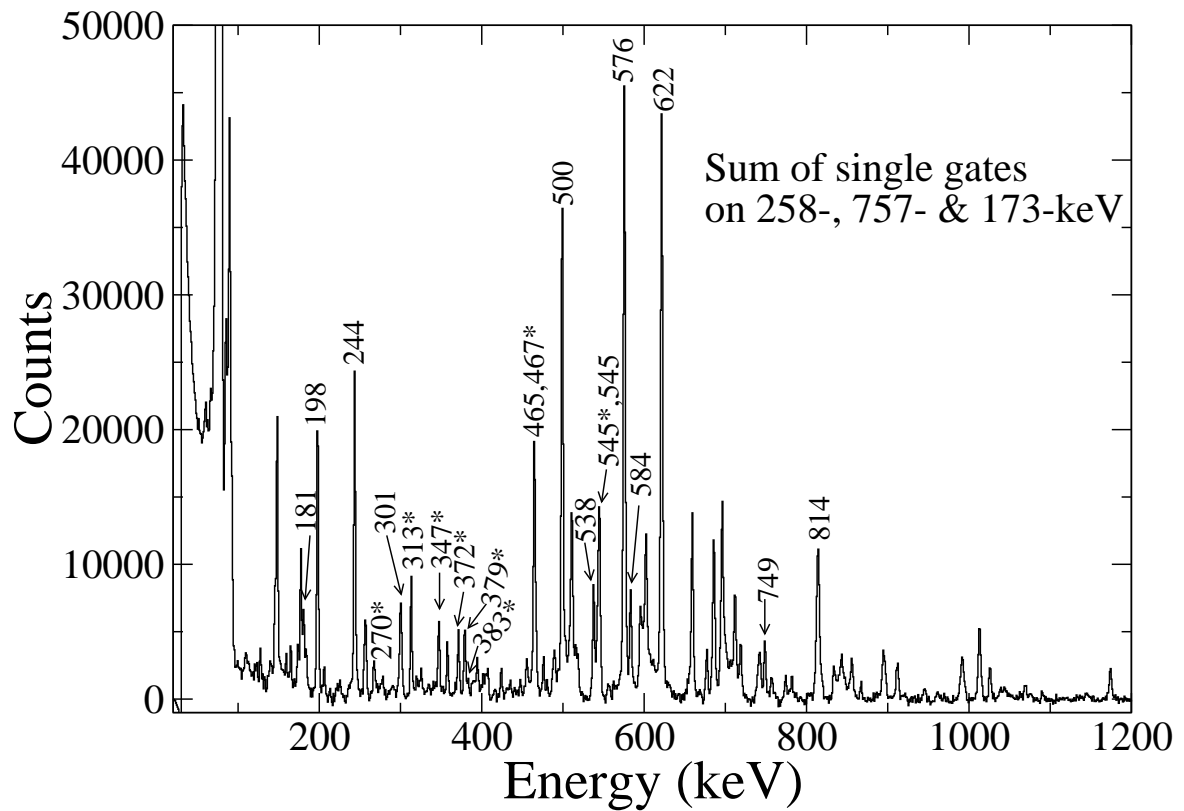


Figure 8.3: Coincidence  $\gamma$ -spectrum corresponding to sum of single gates on 258-, 757- and 173-keV. New  $\gamma$ -transitions are marked by \*.

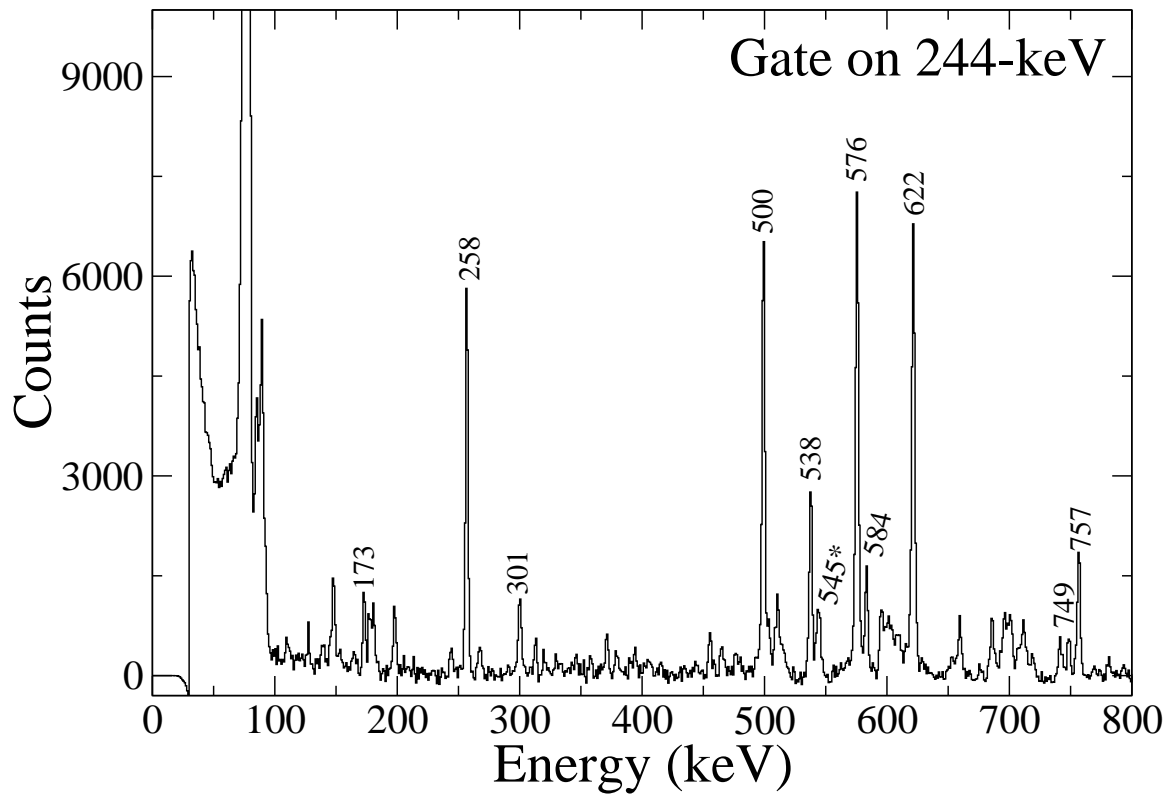


Figure 8.4: Coincidence spectrum generated by single gate on 244-keV. The new  $\gamma$ -transitions are marked by \*.

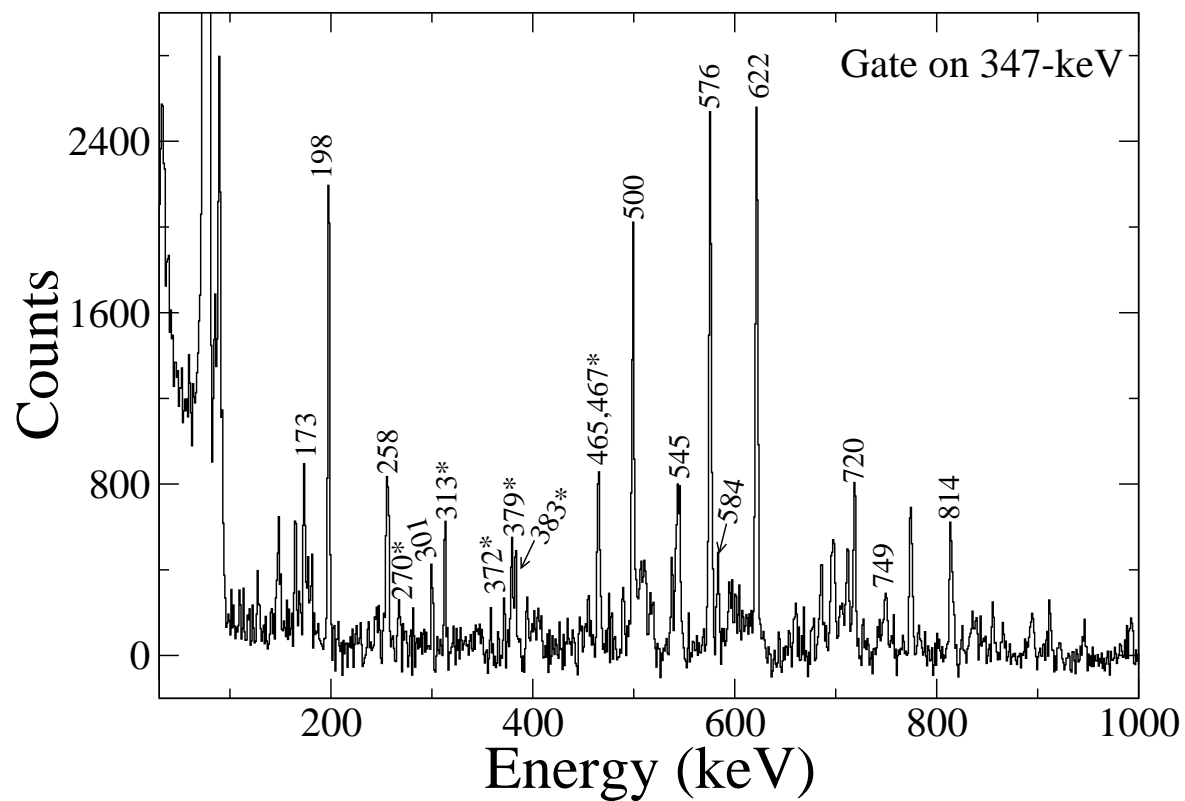


Figure 8.5: Coincidence spectrum generated by single gate on 347-keV. The new  $\gamma$ -transitions are marked by \*.

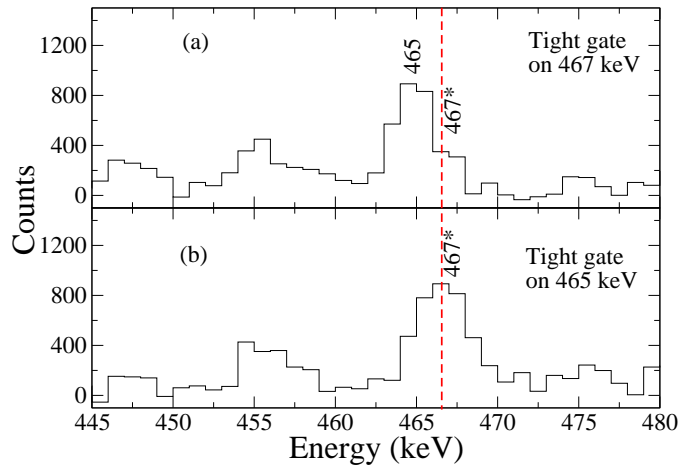


Figure 8.6: Coincidence spectrum of top panel (a) generated by tight gate on 467-keV and lower panel (b) by tight gate on 465-keV.

of the DCO ratio has been obtained as 1.64(3) (see Table 8.1), which indicates the stretched quadrupole nature of the 545-keV  $\gamma$  ray. The positive value of the IPDCO ratio (see Table 8.1) indicates electric nature of the 545-keV  $\gamma$  ray. Therefore, the multipolarity of this transition has been assigned as stretched E2. As a result, the spin-parity of the 4464-keV state has become  $37/2^-$ .

The spectrum in Fig. 8.3 is a sum of single-gated spectra with gates put on 258-, 757- and 173-keV known  $\gamma$  rays. The spectrum shows most of the known  $\gamma$  rays reported in Ref.[16]. A cascade of 467-, 313-, 347-, 379-, 372-, 270-, and 383- keV M1+E2  $\gamma$  rays above the 4345-keV state in band B3 has been observed (see spectrum in Fig. 8.3) in the present work. No cross-over E2 transition has been observed in this cascade. The ordering of the new  $\gamma$  rays in this cascade are fixed by their relative intensities. As there are no cross-over E2 transitions in this cascade, the ordering may be considered somewhat tentative. A spectrum gated by the new 347-keV  $\gamma$  ray, shown in Fig. 8.5, shows most of the known as well as the new  $\gamma$  rays in  $^{207}\text{Po}$  in the present work. As the known 465-keV transition from the  $31/2^-$  to the  $29/2^+$  state are in coincidence with the new  $\gamma$  rays in the cascade, this transition and the 467-keV new  $\gamma$  ray from the  $37/2^+$  to the  $35/2^+$  state can be separated from each other by tight gate on 467-keV

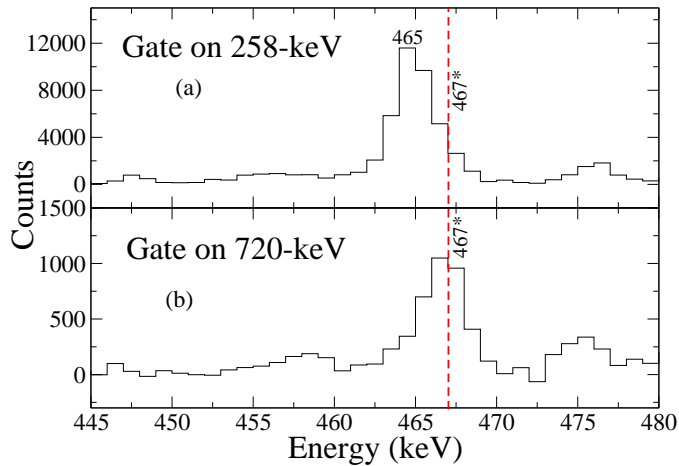


Figure 8.7: Coincidence spectrum of top panel (a) generated by gate on 258-keV and lower panel (b) by gate on 720-keV.

and 465-keV (see Fig. 8.6). The spectrum with tight gate on 467-keV  $\gamma$  ray, in Fig. 8.6(a), clearly shows the 465-keV transition, whereas the spectrum with tight gate on 465-keV  $\gamma$  ray, in Fig. 8.6(b), also clearly shows a peak at 467-keV. The 720-keV  $\gamma$  ray from the  $29/2^-$  to the  $27/2^+$  state is parallel to the 465-keV  $\gamma$  ray. A strong coincidence relation between the  $\gamma$ -ray transitions (e.g. 198-keV, 545-keV etc.  $\gamma$  rays) above the 3602-keV state and the 720-keV transition has been observed in the present work. Therefore, a low-energy  $\gamma$ -ray transition of 3-keV between the  $31/2^-$  and  $29/2^-$  state has been inferred. This was also reported in the previous work [16]. Therefore, the placement of the 467-keV transition in the cascade in band B3 has also been confirmed by its appearance in the 720-keV gated spectrum in Fig. 8.7(b). However, the spectrum (see Fig. 8.7(a)) gated by the 258-keV transition decaying from the  $29/2^+$  to the  $27/2^+$  state, which is in coincidence with the 465-keV  $\gamma$  ray, shows a peak at 467-keV at the tail of the 465-keV transition. This suggests that the 465-keV and 467-keV  $\gamma$  rays are in coincidence. The DCO ratios for all the  $\gamma$  rays, except 383-keV  $\gamma$  ray, in the band B3 have been obtained and are shown in Fig. 8.8 and in Table 8.1. The values of the DCO ratios confirmed the dipole nature of these transitions. The IPDCO ratios for most of the  $\gamma$  rays have been obtained. The negative values of the IPDCO ratios suggest magnetic nature of

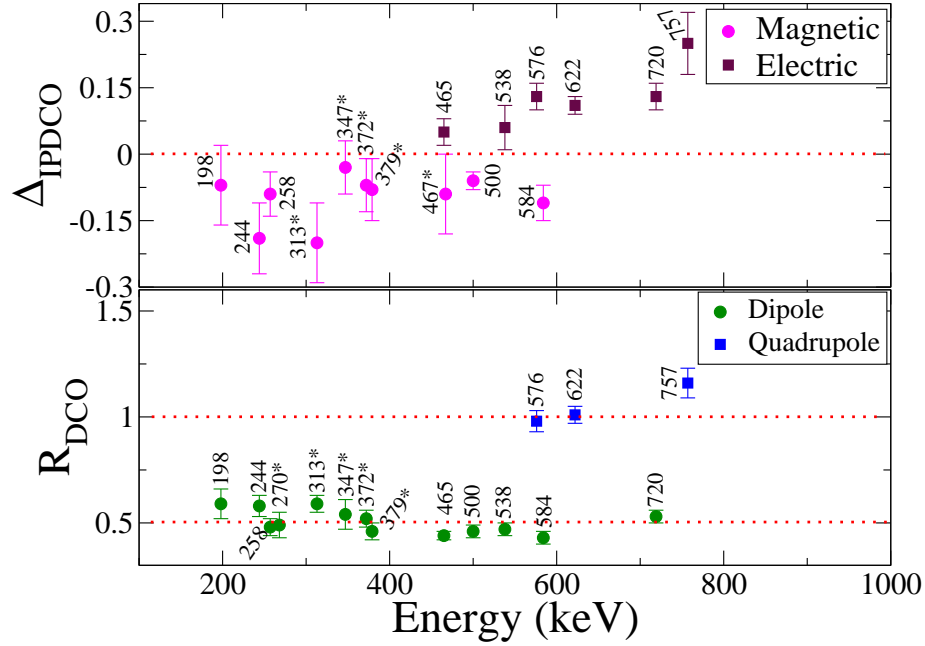


Figure 8.8: DCO (gated by stretched E2 transitions) and IPDCO ratios are plotted as a function of  $\gamma$ -ray energy.

these  $\gamma$  rays (see Table 8.1 and Fig. 8.8). According to their regular sequence, relative intensity and coincidence relations with the known 198-keV and 545-keV  $\gamma$  rays in band B3, the spins and parities of the levels, from which the new  $\gamma$  rays decay, have been assigned.

### 8.3.1 Low lying states

The lower-lying excited states in  $^{207}\text{Po}$  nucleus could be interpreted by the coupling of the odd neutron hole orbital with the states in even-even  $^{206}\text{Po}$  core. The ground state of  $^{207}\text{Po}$  is  $5/2^-$  which can be obtained by the coupling of the odd neutron hole in  $f_{5/2}$  orbital with the  $\pi(h_{9/2}^2)_{0+}$  state in even-even  $^{206}\text{Po}$ . The  $9/2^-$  and  $13/2^-$  states are due to the coupling of the odd neutron hole,  $\nu p_{1/2}^{-1}$ , with the  $\pi(h_{9/2}^2)_{4+}$  and the  $\pi(h_{9/2}^2)_{6+}$  state, respectively. For the  $19/2^-$  and  $21/2^-$  states, the odd neutron hole,  $\nu f_{5/2}^{-1}$ , is coupled with the  $\pi(h_{9/2}^2)_{8+}$  state in  $^{206}\text{Po}$ . The state  $13/2^+$  in  $^{207}\text{Po}$  can be obtained by the coupling of the odd neutron hole in  $i_{13/2}$  orbital with the  $\pi(h_{9/2}^2)_{0+}$  state in even-even  $^{206}\text{Po}$ . The states  $25/2^+$  and  $29/2^+$  in  $^{207}\text{Po}$

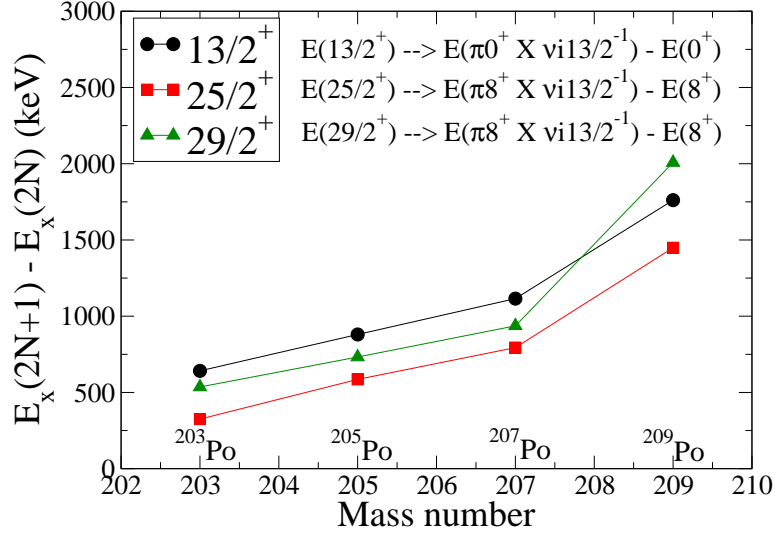


Figure 8.9: Excitation energies of  $13/2^+$ ,  $25/2^+$  and  $29/2^+$  spin-states in odd-A  $^{203-209}\text{Po}$  isotopes relative to the excitation energies of the neighboring even-even core Po isotopes.

may be interpreted as the coupling of the odd neutron hole in  $i_{13/2}$  orbital with the  $\pi(h_{9/2}^2)_{8+}$  state in even-even  $^{206}\text{Po}$  nucleus. The assigned configurations of the states are obtained from the systematics from Ref. [16] based on the empirical shell model calculations performed for the neighboring odd-A isotope  $^{209}\text{Po}$  in Ref. [19]. The configuration of the  $25/2^+$  state has been taken from Ref. [16]. This was based on the agreement of the measured  $B(E2)$  value of 2.9 W.U for the  $25/2^+ \rightarrow 21/2^+$  transition with the expected value for a  $\pi(h_{9/2}^2)_{8+} \rightarrow \pi(h_{9/2}^2)_{6+}$  transition as given in Ref. [20]. A comparison with the other isotopes provides the information on the position of the  $i_{13/2}$  orbital as a function of neutron number in Po isotopes. A systematic investigation of the coupling of the odd-neutron hole involving the  $i_{13/2}$  orbital in odd-A  $^{203-209}\text{Po}$  isotopes with the even-even core of the neighboring Po isotopes has been performed and shown in Fig. 8.9. It is seen from the figure that the relative excitation energies and the trends of the plots corresponding to the  $13/2^+$ ,  $25/2^+$  and  $29/2^+$  states are similar. This suggests that the simple coupling of the odd neutron in Po with the even-even Po core remains valid up to the spin as high as  $29/2\hbar$ .

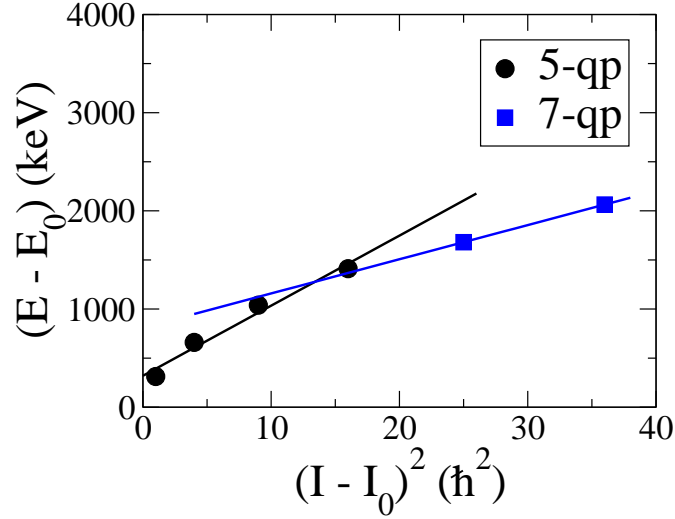


Figure 8.10: Relative level energy  $(E - E_0)$  has been plotted as a function of  $(I - I_0)^2$ .  $E_0$  and  $I_0$  are the band-head energy and spin of band B3. The data points indicated by filled circles are from 5-qp band and the data indicated by filled squares are from 7-qp band. The solid lines are the fitting curves of the data points.

### 8.3.2 Possible Magnetic Rotational band

The negative parity band B3 in  $^{207}\text{Po}$  has been extended up to spin of  $49/2\hbar$  and an excitation energy of 6876-keV with the placement of a cascade of 313-, 347-, 379-, 372-, 270-, and 383-keV new  $\gamma$  rays of M1(+ E2) type above the 4812-keV state. There is a regular pattern of the states above the  $37/2\hbar$  state at 4812-keV and up to the  $45/2\hbar$  state at 6223-keV. The 4812-keV state seems to be the likely band head of band B3. There is a slight irregularity in this band around  $45/2\hbar$  similar to the band crossing observed in normal deformed nuclei. Using the level energies ( $E$ ) and the spins ( $I$ ) of this band, a plot of  $(E - E_0)$  as a function of  $(I - I_0)^2$ , where  $E_0$  and  $I_0$  are the energy and spin of the band head, respectively, has been shown in Fig. 8.10. The straight line fits indicate the parabolic behaviour of the levels. It is indeed observed clearly in this plot that the two top most levels in band B3 are not part of the other levels. This strongly suggests a band crossing at around  $45/2\hbar$ . The data indicated by filled circles are before band crossing and the data indicated by filled squares are after band crossing in band B3. The solid

lines are the fitting curves of the data before and after the band crossing. The good fitting of the data in both cases clearly indicates that there are rotational like behaviour of the states before and after the band crossing in band B3. The extrapolation of the second curve gives the precise band crossing point. The possible particle-hole configuration of the negative parity band B3 before crossing with band-head spin  $I = 37/2\hbar$  and excitation energy  $E_x = 4812$  keV is  $\pi i_{13/2}^2 \otimes \nu(i_{13/2}^{-2} p_{3/2}^{-1})$ . Moreover, the particle-hole configuration of the band after crossing in band B3 has been suggested as  $\pi i_{13/2}^2 \otimes \nu(i_{13/2}^{-2} f_{5/2}^{-2} p_{3/2}^{-1})$ . Both the 5-quasiparticle and the 7-quasiparticle configurations of these two bands involve proton particles and neutron holes in high-j orbitals and therefore these are favorable configurations for Magnetic Rotation (MR) bands. It can be seen from Fig. 8.10 that the two curves (solid lines) corresponding to the 5-qp and 7-qp bands intersect at  $(I - I_0)^2 = 13.5\hbar^2$  which corresponds to  $I = 22\hbar$  considering band-head spin  $I_0 = 18.5\hbar$ . The crossing point of the curves indicates that the band crossing occurs around  $45/2\hbar$  (see Fig. 8.10).

In case of MR band, the excited states and spins are generated by shears mechanism. The shears mechanism of the 5-qp band can be investigated by a semiclassical description of the effective interaction between the proton and the neutron angular momentum vectors [131, 132, 133]. The shears angle  $\theta$  between the proton angular momentum  $j_\pi$  and the neutron angular momentum  $j_\nu$  can be obtained for each energy level of the band using the following relation

$$\begin{aligned} \cos \theta &= \frac{I(I+1) - j_\pi(j_\pi+1) - j_\nu(j_\nu+1)}{2\sqrt{j_\pi(j_\pi+1)j_\nu(j_\nu+1)}} \\ &\approx \frac{I^2 - j_\pi^2 - j_\nu^2}{2j_\pi j_\nu} \end{aligned} \quad (8.1)$$

where  $I$  is the total angular momentum. For the proposed particle-hole configuration  $\pi i_{13/2}^2 \otimes \nu(i_{13/2}^{-2} p_{3/2}^{-1})$  of the 5-qp band, the proton angular momentum  $j_\pi$  and the neutron angular momentum  $j_\nu$  are  $12\hbar$  and  $13.5\hbar$ , respectively. The minimum spin corresponding to the band-head spin  $I_{min} = 18\hbar$  is calculated for the configuration for the perpendicular coupling of the

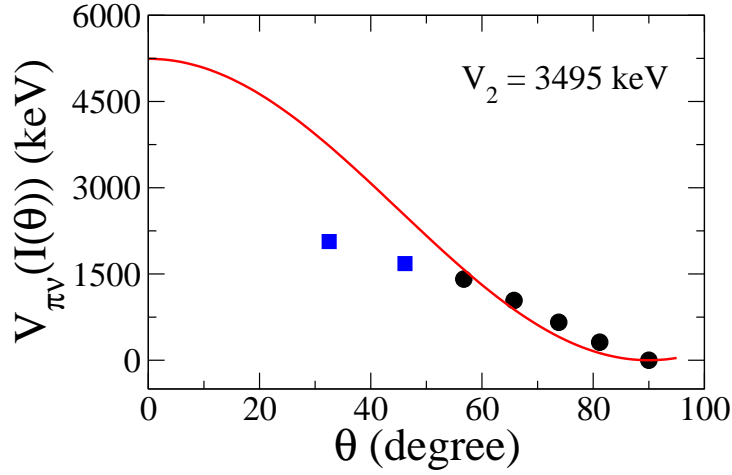


Figure 8.11: The interaction between the proton particle and neutron hole angular momenta as a function of shears angle for the 5-qp band (B3) based on  $\pi i_{13/2}^2 \otimes \nu(i_{13/2}^{-2} p_{3/2}^{-1})$  configuration, obtained from semiclassical formalism.

proton and neutron angular momenta (for shears angle  $\theta = 90^\circ$ ). The experimentally observed band-head spin of the 5-qp band is  $37/2\hbar$  which is very close to the calculated band-head spin. Here, the influence of the collective rotation of the core to the band-head spin is negligible ( $\sim 0.5\hbar$ ). The maximum spin for this configuration has been calculated as  $I_{max} = 25.5\hbar$ , corresponding to termination of the band with  $\theta = 0^\circ$ . This is also consistent with the band B3, however, there is a crossing of a 7-qp band before it attains its maximum spin value. Therefore, the main contribution to the angular momentum generation along this band seems to come from the shears mechanism.

An effective interaction between the proton blade and the neutron blade of a shears band is given by

$$V_{\pi\nu}(I(\theta)) = E(I) - E_0 = \frac{3}{2}V_2 \cos^2 \theta \quad (8.2)$$

where  $E_0$  is the band-head energy.  $E(I)$  is the level energy of spin  $I$  and  $\theta$  is the corresponding shears angle as given in Eq. 8.1.  $V_2$  is the effective interaction between the proton and the

neutron blades of the shears. If  $V_2$  is positive then, the interaction is of a particle-hole type whereas for negative value of  $V_2$  corresponds to a particle-particle interaction.  $V_{\pi\nu}(I(\theta)) = E(I) - E_0$  is plotted as a function of  $\theta$  in Fig. 8.11. The effective interaction  $V_2$  has been extracted by fitting the data (black filled circles) with eq. (8.2). Two data points (blue filled squares) shown in Fig. 8.11 corresponding to states of spin  $47/2^+$  and  $49/2^+$  belong to the states of the 7-qp band. From the Fig. 8.11,  $V_2$  has been extracted as 3495 keV. There are 6 particle-hole pairs in the particle-hole configuration  $\pi i_{13/2}^2 \otimes \nu(i_{13/2}^{-2} p_{3/2}^{-1})$  of the 5-qp band. Therefore, the effective interaction  $V_2$  per particle-hole pair for the proposed configuration of this band is 582 keV, which is in good agreement with the typical value of 400 – 600 keV observed for the MR bands in Pb nuclei in  $A \sim 200$  region [134, 132]. However, due to lack of data, the 7-qp band could not be explained by this semiclassical model.

To interpret the crossing of the 5-qp MR band with the 7-qp MR band in  $^{207}\text{Po}$ , as can be seen from Fig. 8.10, more experimental data to extend the 7-qp band and theoretical calculations (like TAC calculations) are required. Similar crossing of MR band having large multi-qp configuration has been observed in  $^{198}\text{Bi}$  by H. Pai et al. [135], in which crossing of 6-qp with 8-qp and 4-qp with 6-qp MR bands have been reported.

## 8.4 Conclusion

The high-spin excited states in  $^{207}\text{Po}$  have been populated by the  $^{208}\text{Pb}(\alpha, 5n)^{207}\text{Po}$  fusion-evaporation reaction at a beam energy of 60 MeV. The  $\gamma$  rays have been detected using the VENUS array. In this work, total 8 new  $\gamma$ -ray transitions have been observed. A new and improved level scheme of  $^{207}\text{Po}$  has been proposed which extends up to an excitation energy of  $\sim 6.9$  MeV and a spin of  $49/2\hbar$ . The DCO and IPDCO ratios have been obtained to assign the spins and parities of the levels. The lower-lying excited states could be interpreted as the odd-neutron in  $i_{13/2}$  orbital coupled with the different states in even-even  $^{206}\text{Po}$  nucleus. A

comparison with the other isotopes provides the information on the position of this  $i_{13/2}$  orbital as a function of neutron number. The higher lying states are generated due to the multi-particle excitations in the single-particle orbitals. No evidence of collective states could be observed at higher excitations. However, a MR band has been identified for the first time in this nucleus with 5-qp configuration at  $E_x = 4.8$  MeV with the observation of a regular sequence of M1(+E2) transitions. This band has been interpreted by a semiclassical approach. A possible crossing with a 7-qp MR band is suggested. More experimental data to extend this band and TAC calculations are required to establish this fact.

# Chapter 9

## Summary and Future Outlook

### 9.1 Summary

In the present thesis work, the high-spin states in  $^{169}\text{Tm}$  ( $Z = 69$ ),  $^{196}\text{Tl}$  ( $Z = 81$ ) and  $^{207}\text{Po}$  ( $Z = 84$ ) nuclei were experimentally investigated using the gamma-ray spectroscopic technique. The  $^{169}\text{Tm}$  nucleus is situated in the deformed rare-earth region and it is a well deformed nucleus. The other two nuclei are near-spherical in their ground state because of the proximity of their neutron and/or proton Fermi levels close to the  $Z = 82$  and  $N = 126$  spherical shell closures. The modes of the generation of high angular momentum states in these nuclei have been experimentally investigated. The level schemes for these nuclei have been improved considerably with the observation of several new  $\gamma$  rays, new levels, new band structures, band crossings and the definite spin-parity assignments for the levels. The high-spin band structures observed in these nuclei have been interpreted using the systematics of neighboring nuclei and theoretical calculations.

To study the high-spin states in  $^{169}\text{Tm}$  and  $^{196}\text{Tl}$  nuclei, the experiments were carried out at the Pelletron LINAC accelerator facility at TIFR, Mumbai using the Indian National Gamma Array

(INGA) facility. The heavy-ion induced reactions  $^{169}\text{Tm}(^{32}\text{S}, ^{32}\text{S}')^{169}\text{Tm}^*$  and  $^{185,187}\text{Re}(^{13}\text{C}, xn)^{196}\text{Tl}$  at the beam energies of 164 and 75 MeV were used to populate the high spin states in these nuclei. The light-ion induced fusion evaporation reaction  $^{208}\text{Pb}(\alpha, 5n)^{207}\text{Po}$  was used to study the  $^{207}\text{Po}$  nucleus. The 60-MeV alpha beam was delivered from the K-130 cyclotron at VECC, Kolkata and the VECC array for Nuclear Spectroscopy (VENUS) was used to detect the gamma rays. The INGA and the VENUS consisted of 19 (for  $^{169}\text{Tm}$  experiment), 15 (for  $^{196}\text{Tl}$  experiment) and 6 (for  $^{207}\text{Po}$  experiment) Compton Suppressed clover HPGe detectors. The  $\gamma-\gamma$  and  $\gamma-\gamma-\gamma$  coincidence relations, generated from the  $\gamma-\gamma$  matrix and the  $\gamma-\gamma-\gamma$  cube, were used to establish the level schemes in these nuclei. For spin-parity assignments of the levels, DCO ratio and polarization measurements were done using the angle-dependent asymmetric  $\gamma-\gamma$  matrices.

In order to understand and interpret the data on the deformed rotational bands in  $^{169}\text{Tm}$  and  $^{196}\text{Tl}$ , theoretical model calculations in the frame work of Cranked Shell Model (CSM) formalism with BCS pairing have been performed. The single particle energies for protons and neutrons were calculated in the deformed mean field basis using deformed Woods-Saxon potential.

**The study of  $^{169}\text{Tm}$  nucleus provides the following important information:**

- A total of 16 new  $\gamma$ -ray transitions have been observed and placed in the level scheme in the present work. With these new placements, the level scheme has been improved considerably. The ground state ( $[411]1/2^+$ ) band has been extended beyond the band crossing and thereby, the particle alignment has been established for the first time in this nucleus.
- A back-bending type of particle alignment has been observed in  $^{169}\text{Tm}$ , which is similar to that in  $^{165}\text{Tm}$  but in sharp contrast to its nearest neighbor  $^{167}\text{Tm}$ . This result, for the first

time, clearly identifies a larger interaction strength between the 1- and the 3-quasiparticle bands for neutron number  $N = 98$  in the case of Tm isotopes.

- The mean field calculations very well reproduces this experimental results and show the effect of the deformed shell gap at  $N = 98$  in determining the interaction strength. The calculations also predict a moderate interaction strength between the two bands for  $^{171}\text{Tm}$ , which awaits experimental verification. The Total Routhian Surface (TRS) calculations show that the neutron deficient Tm isotopes remain deformed even up to the neutron number as low as  $N = 86$  in  $^{155}\text{Tm}$  while moving towards  $N = 82$  magic number. These calculations also predict triaxial shape for the high spin states in  $^{165,167,169}\text{Tm}$  after the particle alignment.
- Some indication of the presence of octupole correlation in  $^{169}\text{Tm}$  has been found for the first time in this work. A comparison with the nuclei in the  $A \sim 140$  region which shows octupole correlation, indicates that the  $B(E1)/B(E2)$  value in  $^{169}\text{Tm}$  is about a factor of 5 less. The contribution from only protons and not from the neutron levels are considered as the reason for this low strength of octupole correlation. More experimental investigations are required to establish this.

**The study of  $^{196}\text{Tl}$  nucleus provides the following important information:**

- A total of 38 new  $\gamma$ -ray transitions have been observed in the present work including several low-lying non-yrast states, which have been identified for the first time.
- Definite spins and parities have been assigned for the bands B2 and B3 for which no spin parity assignment was reported. With these new information, the possible particle-hole configurations for these two bands (B2 and B3) have also been suggested in the present work. The ambiguity of the excitation energy and the spin of the band B1 has been removed in the present work.

- The ground state band (B1), based on  $\pi h_{9/2} \otimes \nu i_{13/2}$ , has been extended considerably beyond its band crossing. In order to study the collective features involved in this nucleus, a systematic comparison of aligned angular momentum, B(M1)/B(E2) ratio, signature splitting and kinetic moment of inertia has been done along with the neighboring odd-odd Tl isotopes for this band. All the isotopes show a low-spin signature inversion at  $11\hbar$ . A second signature inversion in  $^{196}\text{Tl}$  at  $19\hbar$  similar to  $^{198}\text{Tl}$  [13] and  $^{200}\text{Tl}$  [10] has been observed; however,  $^{194}\text{Tl}$  [11] nucleus does not show the second signature inversion up to spin of  $24\hbar$ . It has been observed that the behaviour of the odd-odd Tl nuclei remain almost identical before the band crossing but they behave differently after the band crossing.
- The TRS calculations show oblate shapes with deformation  $\beta_2 \sim 0.15$  for the 2-qp (B1) and the 4-qp (B2) bands involving  $\pi h_{9/2}$  as well as  $\nu i_{13/2}$  orbital. A triaxial shape with small deformation of  $\beta_2 \sim 0.07$  is obtained for the other 2-qp band (B3) having  $\pi d_{3/2} \otimes \nu i_{13/2}$  configuration.
- It is interesting that no clear indication of chirality or MR band could be observed in  $^{196}\text{Tl}$ , whereas these were reported for the  $^{194,198}\text{Tl}$  isotopes [11, 12, 13].

**The study of  $^{207}\text{Po}$  nucleus provides the following important information:**

- A total of 8 new  $\gamma$ -ray transitions have been observed in the present work.
- The lower lying excited states in this nucleus could be interpreted as the odd-neutron in  $i_{13/2}$  orbital coupled with the different states in even-even  $^{206}\text{Po}$  nucleus. A comparison with the other isotopes provides the information on the evolution of the  $\nu i_{13/2}$  orbital as a function of neutron number in Po isotopes. A systematic investigation of the coupling of the odd-neutron hole involving the  $i_{13/2}$  orbital in odd-A  $^{203-209}\text{Po}$  isotopes with the even-even core of the neighboring Po isotopes has been performed. It has been observed

from the systematics that the simple coupling of the odd neutron in Po with the even-even Po core remains valid up to the spin as high as  $29/2\hbar$ .

- The higher lying states are generated due to the multi-quasiparticle excitations in the single-particle orbitals. No evidence of collective states could be observed at higher excitations.
- A Magnetic Rotational (MR) band has been identified for the first time in this nucleus with 5-quasiparticle (qp) configuration at  $\sim 4.8$  MeV excitation energy with the observation of a regular sequence of M1(+E2) transitions. This band has been interpreted by a semiclassical approach. An indication of a possible crossing with a 7-qp MR band has been observed. However, more experimental data and detailed calculations are required to establish this fact.

In short, different aspects of the generation of angular momenta in nuclei have been investigated in this thesis work. It has been found that the individual nucleonic orbitals and the shell gaps play crucial roles in determining the low as well as the high spin level structures in a nucleus. It has been seen how the deformed shell gap affect the band crossing phenomena in Tm isotopes. On the other hand, it is also seen how the shape driving effects of the high-j proton and neutron orbitals ( $h_{9/2}$  and  $i_{13/2}$ ) breaks the spherical symmetry in  $^{196}\text{Tl}$  nucleus and generates several rotational band characteristics of deformed nucleus. In case of more robust spherical shape in  $^{207}\text{Po}$ , regular sequence of levels are generated by the novel mode of magnetic rotation at higher excitation energies when several particles (protons and neutrons) are excited in the high-j  $i_{13/2}$  orbital.

## 9.2 Future outlook

The present thesis work, provides several new information on the high spin states in the nuclei which are deformed and spherical in their ground state. The experimental results and the interpretation of these with the theoretical calculations in this work also help to understand various aspect of the high spin phenomena in these nuclei. However, this work also identifies several new interesting aspect which should be addressed in future works. Some of these are given below.

In the study of Tm isotopes, close to the stability line, a larger interaction strength between the g- and s-bands has been calculated for  $^{167}\text{Tm}$  (compared to its two neighboring isotopes) which explains the contrasting nature of band crossing in this isotope compared to  $^{165}\text{Tm}$  and  $^{169}\text{Tm}$ . The same calculations predict that the alignment of the  $\pi[411]1/2^+$  band in  $^{171}\text{Tm}$  would be similar to  $^{167}\text{Tm}$ , but with somewhat less smooth up-bend. Experimental data, however, are not available yet for this nucleus to test this prediction. Therefore, it will be interesting to study the high spin states in  $^{171}\text{Tm}$  beyond the particle alignment to establish the nature of its band crossing.

Octupole correlation in nuclei in  $A \sim 140$  region with neutron number close to  $N = 90$  has been reported [40, 41, 42, 43, 44, 45]. In these nuclei, pairs of  $\Delta l = 3$  and  $\Delta j = 3$  orbitals lie in close proximity near the Fermi levels of both protons and neutrons which contribute to the correlation. The octupole state has the lowest energy around the neutron number  $N = 90$  [122]. The energy of the octupole state increases with both increase and decrease of this neutron number. Therefore, the nuclei with  $N \sim 90$  are considered as the most likely candidates for octupole correlation. In case of  $^{169}\text{Tm}$  with  $N = 100$ , due to the presence of the  $[411]1/2^+$  (B1) and the  $[541]1/2^-$  (B2) bands whose particle-configurations are originated from the  $\pi d_{3/2}$  and the  $\pi h_{9/2}$  orbitals, respectively, the octupole correlation has been suggested based on the systematic study with the above octupole correlated bands. However, in this

case, only the protons with a pair of  $\Delta l = 3$  and  $\Delta j = 3$  orbitals contribute to the octupole correlation. Therefore, the strength of the octupole correlation has been found to be much smaller. However, it will be interesting to investigate the more lighter Tm isotopes for which neutron number approaches  $N = 90$  in which the octupole correlations are expected to be larger.

The TRS calculations for the ground state bands in  $^{165}\text{Tm}$ ,  $^{167}\text{Tm}$  and  $^{169}\text{Tm}$  isotopes have been performed in the present work. The calculations predict that after the alignment of a pair of neutrons, the shapes of all the three isotopes change from prolate to a triaxial one with  $\gamma \sim -26^\circ$  and  $\beta_2 \sim 0.32$ . To confirm this, the life-time measurements of the states beyond the band crossing are necessary. Therefore, more experimental investigations for these nuclei are needed for the observation of this structural change.

Moreover, the complex and exotic modes of generation of angular momentum have been reported in some of the odd-odd Tl nuclei. For neutron number  $N = 113$ , a triaxial shape is indicated at higher excitation energy from the observation of chiral doublet bands in  $^{194}\text{Tl}$  [11] for the 4-quasiparticle configuration. On the other hand, Magnetic Rotational (MR) band based on 6-quasiparticle configuration has also been identified in the same nucleus [12]. In  $^{198}\text{Tl}$  [13, 14], the chiral band is reported for the 2-quasiparticle configuration,  $\pi h_{9/2} \otimes \nu i_{13/2}$ , at relatively lower spin compared to the chiral band in  $^{194}\text{Tl}$ . The life-time measurements of the states in  $^{198}\text{Tl}$  have not been done. However, for the confirmation of chirality and MR nature of bands, an extensive support of the transition probability strengths ( $B(M1)$  and  $B(E2)$ ) through the life-time measurements of the states are required. In the study of  $^{196}\text{Tl}$ , no indication of chiral band has been observed in the present work. The reasons for this could be that a stable triaxial minimum is not realized in  $^{196}\text{Tl}$  as indicated by the TRS calculations for the 2-qp band in  $^{196}\text{Tl}$  or it could be that the chiral band is weakly populated in this nucleus. Therefore, more experimental data are required to investigate the weakly populated chiral partner band

in  $^{196}\text{Tl}$  as well as life-time measurements and detailed theoretical calculations are needed for the interpretation of these band structures.

A MR band has been identified in  $^{207}\text{Po}$ , for the first time among the Po isotopes in its 5-quasiparticle configuration at  $\sim 4.8$  MeV excitation energy. Also a possible crossing with a 7-quasiparticle MR band has been suggested. These bands have been interpreted by semiclassical approach. The life-time measurements for the states of these bands have not been done in the present work. In order to characterize these bands properly, it is important to have information about B(M1) and B(E2) transition probability strengths of the states through life-time measurement. At the same time, TAC calculation is also required for the interpretation of these bands. In case of the neighboring  $^{205}\text{Po}$  nucleus, with two protons and five neutron holes outside the doubly closed shell  $^{208}\text{Pb}$  core, it is possible to excite the same quasi-particle configuration similar to that of the MR band in  $^{207}\text{Po}$ . Therefore, it will be interesting to study the high spin states in  $^{205}\text{Po}$  nucleus for the search of MR band structure. This will provide the important information on the universality of the MR bands and their correlation with a particular configuration. The variation of the strength of the particle-hole interaction in a chain of isotopes can also be studied with this.

# Bibliography

- [1] M.A. Riley et al., Phys. Rev. C **51**, 1214 (1995).
- [2] H.J. Jensen et al., Nucl. Phys. A **695**, 3 (2001).
- [3] M J Burns et al., J. Phys. G: Nucl. Part. Phys. **31**, S1827 (2005).
- [4] P. Taras et al., Nucl. Phys. A **289**, 165 (1977).
- [5] M.P. Robinson et al., Nucl. Phys. A **647**, 175 (1999).
- [6] S. Drissi et al., Nucl. Phys. A **483**, 153 (1988).
- [7] C. Y. Xie et al., Phys. Rev. C **72**, 044302 (2005)
- [8] A.J. Kreiner et al., Phys. Rev. C **21**, 3 (1980)
- [9] A.J. Kreiner et al, Nucl. Phys. A **308**, 147 (1978).
- [10] Soumik Bhattacharya et al., Phys. Rev. C **95**, 014301 (2017)
- [11] P.L. Masiteng et al., PLB **719**, 83 (2013)
- [12] H. Pai et al., Phys. Rev. C **85**, 064313 (2012)
- [13] E. A. Lawrie et al., Phys. Rev. C **78**, 021305 (2008)
- [14] E. A. Lawrie et al., Eur. Phys. J. A **45**, 39 (2010)

- [15] T. Weckström et al., Z. Phys. A **321**, 231 (1985)
- [16] V. Rahkonen et al, Nucl. Phys. A **441**, 11 (1985).
- [17] A.M. Baxter et al, Nucl. Phys. A **515**, 493 (1990).
- [18] A.R. Poletti et al, Nucl. Phys. A **615**, 95 (1997).
- [19] A.R. Poletti et al, Nucl. Phys. A **665**, 318 (2000).
- [20] G. Astner et al., Nucl. Phys. A **182**, 219 (1972).
- [21] H. Tan et al., in Nuclear Science Symposium Conference Record 2008 (IEEE, Washington, DC, 2008), p. 3196.
- [22] R. Palit et al., Nucl. Instrum. Methods Phys. Res., Sect. A **680**, 90 (2012).
- [23] Soumik Bhattacharya et al., Proc. of the DAE-BRNS Symp. on Nucl. Phys. Vol **61**, 98 (2016).
- [24] S. Agostinelli et al., Nucl. Instrum. Methods Phys. Res., Sect. A **506**, 250 (2003).
- [25] Md. A. Asgar et al., Proc. of the DAE-BRNS Symp. on Nucl. Phys. Vol **60**, 960 (2015).
- [26] Md. A. Asgar et al., Proc. of the DAE-BRNS Symp. on Nucl. Phys., Vol **61**, 950 (2016).
- [27] A. Chatterjee, Priv. comm. (2001); <http://www.tifr.res.in/pell/lamps.html>.
- [28] D.C. Radford, Nucl. Instrum. Methods Phys. Res. A **361**, 297 (1995).
- [29] D.J. Hartley et al., Phys. Rev. Lett. **120**, 182502 (2018).
- [30] Md. A. Asgar et al., Phys. Rev. C **95**, 031304(R) (2017).
- [31] Md. A. Asgar et al., Proc. of the DAE-BRNS Symp. on Nucl. Phys. Vol **60**, 172 (2015).
- [32] D. Ward et al., Nucl. Phys. A **332**, 433 (1979).

- [33] D. Ward et al., Nucl. Phys. A **600**, 88 (1996).
- [34] H. Beuscher et al., Z.Phys. **263**, 201 (1973).
- [35] A. Johnson et al., Nucl. Phys. A **179**, 753 (1972).
- [36] <https://www.nndc.bnl.gov/ensdf/>
- [37] M.A. Riley et al., J. Phys. G: Nucl. Part. Phys. **16**, L67 (1990).
- [38] M. Lipoglavsek, et al., Phys. Lett. B **593**, 61 (2004).
- [39] Rejmund et al., Eur. Phys. J. A **8**, 161 (2000).
- [40] M.A. Jones et al., Nucl. Phys. A **605**, 133 (1996).
- [41] S.J. Zhu et al., Phys. Lett. B **357**, 273 (1995).
- [42] W. Urban et al., Phys. Rev. C **54**, 945 (1996).
- [43] S.J. Zhu et al., Phys. Rev. C **59**, 1316 (1999).
- [44] Y.J. Chen et al., Phys. Rev. C **73**, 054316 (2006).
- [45] Somapriya Basu et al., Phys. Rev. C **49**, 650 (1994).
- [46] W. Reviol et al., Physica Scripta T**56**, 167 (1995).
- [47] W. Reviol et al., Nucl. Phys A **548**, 331 (1992).
- [48] H. Pai et al., Phys. Rev. C **88**, 064302 (2013).
- [49] N. Mărginean et al., Eur. Phys. J. A **46**, 329 (2010).
- [50] S. Das Gupta et al., Phys. Rev. C **88**, 044328 (2013)
- [51] G. Baldsiefen et al., Phys. Lett. B **275**, 252 (1992).

- [52] G. Baldisiefen et al., Nucl. Phys. A **574**, 521 (1994).
- [53] M. Neffgen et al., Nucl. Phys. A **595**, 499 (1995).
- [54] <https://www.nndc.bnl.gov>
- [55] N. Bohr and F. Kalckar, Kgl. Danske Videnskabernes Selskab, Math.Fys. Meddelser 14, No. 10 (1937).
- [56] C.F.Von Weizsäcker, Z. Phys. **96**, 431 (1936).
- [57] H.A. Bethe, Rev. Mod. Phys. **8**, 82 (1936).
- [58] P. Ring and P. Schuck, The Nuclear Many-Body Problem, Springer-Verlag Berlin Heidelberg (1980).
- [59] M. G. Mayer, Phys. Rev. **75**, 1969 (1949).
- [60] O. Haxel, J.H.D. Jensen and H.E. Suess, Phys. Rev. **75**, 1766 (1949).
- [61] A. Bohr, Mat. Fys. Medd. Dan. Vid. Selsk. **26**, No. 14 (1952).
- [62] G. Andersson et al., Nucl. Phys. A **268**, 205 (1976).
- [63] D. L. Hill and J. A. Wheeler, Phys. Rev. **89**, 1102 (1953).
- [64] R. B. Firestone, et al., Table of Isotopes (John Wiley and Sons, Inc., New York (1999)).
- [65] S. G. Nilsson, Mat. Fys. Medd. Dan. Vid. Selsk. **29**, 16 (1955).
- [66] C. Gustafson et. al., Arkiv Fysik **36**, 613 (1967).
- [67] V. M. Strutinski Nucl. Phys. A **95**, 420 (1967).
- [68] V. M. Strutinski Nucl. Phys. A **122**, 1 (1968).
- [69] D.R.Inglis, Phys. Rev. **96**, 1059 (1954).

- [70] D.R.Inglis, Phys. Rev. **103**, 1786 (1956).
- [71] A. Bohr and B. R. Mottelson: Nuclear Structure, vol. II (W. A. Benjamin, Inc., New York, 1975)
- [72] W. Nazarewicz et al., Nucl. Phys. A **435**, 397 (1985).
- [73] W. Nazarewicz et al., Nucl. Phys. A **512**, 61 (1990).
- [74] G. Mukherjee, H. C. Jain, R. Palit, P. K. Joshi, S. D. Paul, and S. Nagraj, Phys. Rev. C **64**, 034316 (2001).
- [75] G. Mukherjee et al., Nucl. Phys. A **829**, 137 (2009).
- [76] H. Ejiri and M.J.A. de Voigt, Gamma-ray and Electron Spectroscopy in Nuclear Physics, Clarendon Press, Oxford (1989).
- [77] Subhendu Rajbanshi's Thesis (Generation of Angular momentum for Weakly Deformed Nuclei in Mass  $\sim 140$  Region).
- [78] Experiments in Nuclear Science, High-Resolution Gamma-Ray Spectroscopy published by EG and G ORTEC.
- [79] G.F. Knoll, Radiation Detection and Measurement, John Wiley & Sons, Inc.
- [80] T. Szücs et al., Eur. Phys. J. A **44**, 513 (2010).
- [81] I.Y. Lee, Nucl. Phys. A **520**, 641c (1990).
- [82] R.K. Bhowmik, in: Proceedings of Fourth International Conference on Fission and Properties of Neutron-Rich Nuclei, World Scientific, p. 258 (2007); H.C. Jain, Pramana **57** (1), 21 (2001); S. Muralithar, et al., Nuclear Instruments and Methods in Physics Research Section A **622**, 281 (2010).

- [83] C.W. Beausang, et al., Nuclear Instruments and Methods in Physics Research Section A **313**, 37 (1992).
- [84] J. Simpson, et al., Heavy Ion Physics **11**, 159 (2000).
- [85] R.T. Newman, et al., Balkan Physics Letters 182 (1998).
- [86] C.E. Svensson, et al., Journal of Physics G: Nuclear and Particle Physics **31**, S1663 (2005).
- [87] Soumik Bhattacharya, VECC, Priv. comm. (2018).
- [88] <https://www.root.cern.ch>
- [89] D. Mahato, Report of Summer Training Project at VECC (2015).
- [90] S. Bhutani, Report of Summer Training Project at VECC (2015).
- [91] Soumik Bhattacharya, et al., Proc. DAE Symp. on Nucl. Phys. **58**, 906 (2013)
- [92] T. Yamazaki, Nucl. Data, Section A **Vol.3** (1967).
- [93] E. Der Mateosian and A.W. Sunyar, Atomic Data and Nuclear Data Tables **13**, 391 (1974).
- [94] A. Krämer-Flecken et al., Nucl. Instrum. Methods Phys. Res. A **275**, 333 (1989).
- [95] Chr. Bargholtz and P.-E. Tegnér, NIM A **256**, 513 (1987)
- [96] R.M. Steffen and K. Alder, in: The Electromagnetic Interaction in Nuclear Spectroscopy, ed., W.D. Hamilton (North Holland, Amsterdam, 1975) p. 505.
- [97] K. Starosta et al., Nucl. Instrum. Methods Phys. Res., Sect. A **423**, 16 (1999).
- [98] Ch. Droste et al., Nucl. Instrum. Methods Phys. Res., Sect. A **378**, 518 (1996).
- [99] O. Klein and Y. Nishina. Z. Physik **52**, 853 (1929).
- [100] J.K. Deng et al., Nucl. Instrum. Methods in Phys. Res. A **317**, 242 (1992).

- [101] R. Palit et al., *Pramana – J. Phys.*, **54**, 347 (2000).
- [102] P.J. Twin, in: *The Electromagnetic Interaction in Nuclear Spectroscopy*, ed., W.D. Hamilton (North Holland, Amsterdam, 1975) p. 701.
- [103] L.W. Fagg and S.S. Hanna, *Rev. Mod. Phys.*, **31**, 711 (1959).
- [104] Takayoshi Aoki et al., *At. Data and Nucl. Data Tables*, **23**, 349 (1979).
- [105] S.M. Harris, *Phys. Rev.* **138**, B509 (1965).
- [106] S. Frauendorf, *Physica Scripta* **24**, 349 (1981).
- [107] P.H. Regan et al. *Nucl. Phys. A* **586**, 351 (1995).
- [108] A.P. Byrne et al. *Nucl. Phys. A* **548**, 131 (1992).
- [109] F. Dönau and S. Frauendorf, in *Proceedings of the Conference on High Angular Momentum Properties of Nuclei*, OakRidge, edited by N. R. Johnson (Harwood, New York, 1983), p. 143.
- [110] F. Dönau, *Nucl. Phys. A* **471**, 469 (1987).
- [111] H.J. Li, et al., *Phys. Rev. C* **91**, 054314 (2015)
- [112] G. Gascon et al., *Nucl. Phys. A* **467**, 539 (1987).
- [113] C. Foin et al., *Nucl. Phys. A* **417**, 511 (1984).
- [114] S.J. Warburton et al., *Nucl. Phys. A* **591**, 323 (1995).
- [115] N. S. Pattabiraman et al., *Phys. Lett. B* **647**, 243 (2007).
- [116] X. Wang et al., *Phys. Rev. C* **75**, 064315 (2007).
- [117] D. Barnéoud et al., *Nucl. Phys. A* **230**, 445 (1974)

- [118] C.M. Baglin, Nuclear data sheet, **109**, 2033 (2008).
- [119] W. Nazarewicz, G. A. Leader, and J. Dudek, Nucl. Phys. A **467**, 437 (1987).
- [120] W. Nazarewicz, P. Olanders, I. Ragnarsson, J. Dudek, and G. A. Leander, Phys. Rev. Lett. **52**, 1272 (1984).
- [121] W. Nazarewicz and P. Olanders, Nucl. Phys. A **441**, 420 (1985).
- [122] P.D. Cottle and N.V. Zamfir, Phys. Rev. C **54**, 176 (1996).
- [123] E. S. Macias et al., Comput. Phys. Commun. **11**, 75 (1976).
- [124] P.M. Walker et al., Phys. Rev. C **79**, 044321 (2009).
- [125] C. W. Beausang, L. Hildingsson, E. S. Paul, W. F. Piel Jr., N. Xu, and D. B. Fossan, Phys. Rev. C **36**, 1810 (1987).
- [126] S. Olbrich, V. Ionescu, J. Kern, C. Nordman and W. Reichart, Nucl. Phys. A **342**, 133 (1980).
- [127] C. Fahlander et al., Nucl. Phys. A **537**, 183 (1992).
- [128] C. Foin, D. Barneoud, S.A. Hjorth and R. Bethoux, Nucl. Phys. A **199**, 129 (1973).
- [129] P. Raghavan, At. Data Nucl. Data Tables **42**, 189 (1989).
- [130] C. Y. Xie et al., Phys. Rev. C **72**, 044302 (2005).
- [131] A.O. Macchiavelli et al., Phys. Rev. C **57**, R1073 (1998).
- [132] A.O. Macchiavelli et al., Phys. Rev. C **58**, R621 (1998).
- [133] A.O. Macchiavelli et al., Phys. Rev. C **58**, 3746 (1998).
- [134] A. Gorgen et al, Nucl. Phys. A **683**, 108(2001).

[135] H. Pai et al., Phys. Rev. C **90**, 064314 (2014).

[136] H. Pai et al., Phys. Rev. C **85**, 064313 (2012).